ANALYTICAL INVESTIGATIONS IN MAGNETIC RECORDING

BY

STEPHEN J. C. BROWN

A THESIS SUBMITTED TO

THE UNIVERSITY OF PLYMOUTH

IN PARTIAL FULFILMENT FOR THE DEGREE OF

DOCTOR OF PHILOSOPHY

DEPARTMENT OF MATHEMATICS AND STATISTICS

THE FACULTY OF TECHNOLOGY

AUGUST, 2003

STEPHEN JAMES CHARLES BROWN

Analytical Investigations in Magnetic Recording

Abstract

The Fourier method is used to provide new analytic solutions for idealized mathematical models of double-element shielded magnetoresistive (MR) recording heads. The general two-dimensional model allows analysis of various recording head configurations; a single pole head, a ring head, a dual stripe head and a differential head. The analysis accommodates both longitudinal recording (with no soft magnetic underlayer present) and perpendicular recording (in the presence of a soft underlayer). Typical field, spectral response function and output voltage pulse plots for double-element MR heads are given and compared to published, approximate solutions. The integrals arising in the determination of the Fourier series coefficients, magnetic potential and magnetic field components are expressed either as rapidly convergent infinite series or in terms of special functions to provide a more efficient means of evaluation than numerical integration. It is shown that, in many situations, it is only necessary to take the first Fourier coefficient in the calculation of output voltage pulse shapes in order to achieve sufficiently accurate results. Bi-variate regression techniques are used to provide a convenient method to approximate the first Fourier series coefficient for a broad range of typical head dimensions.

The thesis goes on to examine high speed switching behaviour in two classes of recording media by considering two different particle orientation distributions; 2D random media - intended to simulate a modern thin film rigid disk, and 3D oriented media - simulating a single domain particulate tape media. The gyromagnetic switching constant of a medium is calculated directly from the Landau - Lifshitz - Gilbert (L-L-G) equation of motion, which is solved numerically. The switching constants produced are discussed and compared with published experimental values for different media.

TABLE OF CONTENTS

LIST OF ILLUSTRATIONS

LIST OF TABLES

ACKNOWLEDGEMENTS

Firstly, I would like to thank my supervisor, Dr. David Wilton, for his guidance and support during my graduate studies. I could not have wished for a better advisor and mentor for my PhD. Without his knowledge, perceptiveness and common sense I would never have finished. Thank you for providing me with enough flexibility to maintain my commitments to my family and my academic career. Thank you to Professor Des Mapps, my co-supervisor who always gave me the support needed to conduct this research. I have also been fortunate to have the support of Dr. Hazel Shute throughout the development of the thesis. Hazel made her expertise available to me seven days a week and also took on the role of LaTeX troubleshooter. I am indebted to Dr. John Mallinson, a larger than life figure, who has been my pilot through the subject of gyromagnetic switching. John has patiently dealt with a very large number of questions - both on his visits to Plymouth and via endless transatlantic faxes.

To my family and friends, thank you for your understanding and encouragement over the years of my candidature, and to my dogs Gyp and Kanger, thank you for responding with a waggy tail regardless of my mood.

Finally, for being so patient with me and for providing more support than she could ever imagine, I am dedicating this work to my wife, Gail.

AUTHOR'S DECLARATION

At no time during the registration for the degree of Doctor of Philosophy has the author been registered for any other University award. The study was carried out in collaboration with the Centre for Research in Information Storage Technology (CRIST) at Plymouth. Relevant scientific seminars and conferences were attended at which work was presented and the following papers were published:

- S. J. C. Brown, J. C. Mallinson, D. T. Wilton and H. A. Shute "Calculation of the switching constant of magnetic recording media", *IEEE Trans. Magn.*, vol. 38, pp. 271-278, Jan. 2002.

- S. J. C. Brown, D. T. Wilton, H. A. Shute and D. J. Mapps "Analytic solutions for double-element shielded MR heads", *IEEE Trans. Magn.*, vol. 30, pp. 2180-2186, September. 1999.

- D. T. Wilton, S. J. C. Brown, H. A. Shute and D. J. Mapps "Integrals arising in models of shielded mgnetoresistive heads", *IEEE Trans. Magn*, vol. 37, pp. 565-570, Jan. 2001.

- D. T. Wilton, H. A. Shute, S. J. C. Brown and D. J. Mapps "Approximation of shielded MR head output for perpendicular media", *J. Magn. Magn. Mater.*, vol. 235, pp. 393-397, 2001.

Copies of these papers can be found at the end of this thesis.

Signed.....

Date.....05:04:04.....

LIST OF ABBREVIATIONS AND SYMBOLS

A	.....	subscript region A
a	.....	magnetization transition parameter
α	.....	Gilbert damping constant
α_L	.....	Landau-Lifshitz damping constant
$\mathbf{B}$	.....	magnetic flux density
BAR	.....	bit aspect ratio
$C_i(x)$	.....	the cosine integral
d	.....	head to medium spacing
∇	.....	vector operator (del) $\equiv \mathbf{i}\frac{\partial}{\partial x} + \mathbf{j}\frac{\partial}{\partial y} + \mathbf{k}\frac{\partial}{\partial z}$
$\delta(\mathbf{x})$	.....	the three-dimensional Dirac delta function
δ	.....	medium thickness
$E_1(z)$	.....	the complex exponential integral
G	.....	inter-element length
g	.....	semi inter-element length
Gb	.....	gigabit
GB	.....	gigabyte
γ	.....	gyromagnetic ratio
H	.....	element to shield length
h	.....	semi element to shield length
$\mathbf{H}$	.....	magnetic field
$\widehat{\mathbf{H}}$	.....	Fourier transform of magnetic field
$\mathbf{H_T}$	.....	total applied magnetic field
$\mathbf{H_K}$	.....	anisotropy field
i	.....	$\sqrt{-1}$
i_A	.....	current in coil A
Im	.....	imaginary part
$\mathbf{J}$	.....	current density
L	.....	element length
$\mathbf{M}$	.....	magnetization
$\widehat{\mathbf{M}}$	.....	Fourier transform of magnetization
$\mathbf{M}^*$	.....	complex conjugate of magnetization
M	.....	magnitude of magnetization
Mb	.....	megabit
MB	.....	megabyte
μm	.....	micrometer

μ_0	.....	permeability of free space
nm	.....	nanometer
Oe	.....	Oersted
φ	.....	magnetic scalar potential
φ_A	.....	flux in coil A, reciprocity
$\widehat{\varphi}$	.....	Fourier transform of φ
Re	.....	real part
$S_i(x)$	.....	the sine integral
S_w	.....	switching constant
T_s	.....	switching time
τ	.....	reduced switching time
τ_s	.....	reciprocal of reduced switching time
t	.....	head to medium spacing
x	.....	subscript x component
y	.....	subscript y component
$++$	.....	superscript dual stripe head
$-+$	.....	superscript differential head
I	.....	subscript region I
II	.....	subscript region II
III	.....	subscript region III

CHAPTER 1

THE EVOLUTION OF MASS DATA STORAGE TECHNOLOGY

1.1. Introduction

There exist a wide variety of magnetic recording media and recording heads. The aim of this chapter is to discuss some of the underlying technologies that are common to many forms of magnetic recording. This is often done using as an example the basic hard disk drive found in personal computers today. Section 1.2 gives a brief history of magnetic recording with particular reference to mass data storage applications. The aim of section 1.3 is to describe the design considerations of a basic hard disk drive. In section 1.4 the writing and reading processes are detailed and the inductive read/write head is presented and discussed. The anisotropic magnetoresistive effect is detailed in section 1.5 and its application to MR and GMR read heads is examined. Section 1.6 looks at perpendicular recording and discusses the possibility of an industry switch to this method in order to fulfill the ever growing mass data needs that are imposed by the continuing information revolution.

1.2. History

Even before the first commercial electronic computers appeared in the 1950's, 'mass' data storage, although miniscule measured by today's standards, was a necessity. In the mid-nineteenth century punched cards were used to input data into early mechanical calculators. By the end of that century - in 1898, Valdemar Poulsen, a Danish telephone engineer, had demonstrated magnetic recording for the first time using his telegraphone, successfully recording telephone conversations onto steel wire. His device was hailed as a sensation at the Universelle in Paris in 1900, where the few words spoken into it by the Austrian emperor Franz-Joseph survive as what is

generally accepted as the earliest example of magnetic recording [1]. In the 1920's and 30's German scientists pioneered the development of magnetic tape rather than steel wire as a recording medium. However it was not until the early 1950's that tape drives replaced the punched cards and vacuum tube technology that were widely used for mass storage applications until then. Magnetic drums quickly followed and, in 1957, the first hard disk drive (HDD) was introduced by IBM. The random access method of accounting and control (RAMAC) consisted of 50 magnetic disks (platters) of 24 inches diameter each spinning at 1200 rotations per minute. Magnetic hard disk drives have been the primary means of storing information on computers ever since. By the late 1980's hard drives with disks of 3.5 inch diameter were gaining acceptance, and they quickly became the standard for desktop and portable computers. Modern hard drives come in different sizes or form factors as well as 3.5 inch, such as 2.5 inch, 1.8 inch, 1 inch and others. The smaller form factor drives were developed as a direct response to the need to further reduce size and weight for laptop computers and hand held electronic devices. The 1 inch form factor Microdrive produced by Hitachi is about the size of two credit cards stacked, one on top of the other, and weighs just 16 grammes while delivering gigabyte capacity. The RAMAC drive with it's fifty 24 inch platters in 1957 was housed in a cabinet the size of a refrigerator and could store the equivalent of about 2,500 pages of double-spaced typed information. The typical drive today has perhaps three 3.5 inch platters and can store about 60 million pages of information - the surface area of the disks has shrunk by a factor of almost 80 while their capacity to store information has increased 24,000 times. It follows that the areal density (the number of bits of information per square inch) has grown by a factor of approximately 19 million. The immense advances that have been made in drive capacity, performance and size over the past forty odd years have fueled the information technology revolution that we are experiencing. The trend toward high-end graphics, multimedia, networking (including internet) and communications applications is driving the need for magnetic disk drives with ever higher capacities and performance. As an example, to store 'true motion' video requires about 500 megabits per second, which means that a modern 120 gigabyte drive would be exhausted after just 32 minutes. An obvious evolutionary step is to increase the storage

capacity of the HDD by increasing the packing density of bits on each disk surface, and reading and writing these data bits at the maximum rate. The next section looks at a basic hard drive design and examines the key factors to be considered in the pursuit of such goals.

1.3. The Basic Disk Drive

The first magnetic media was called 'particulate media' (as used in IBM's RAMAC) because it included particles of iron oxide as the magnetic medium, deposited in a brown film along with aluminium oxide to resist abrasion. Particulate hard disks are now largely confined to applications using large diameter disks. Modern hard disks use 'thin-film magnetic media' which consists of very thin layers of different materials as illustrated in Fig. 1.

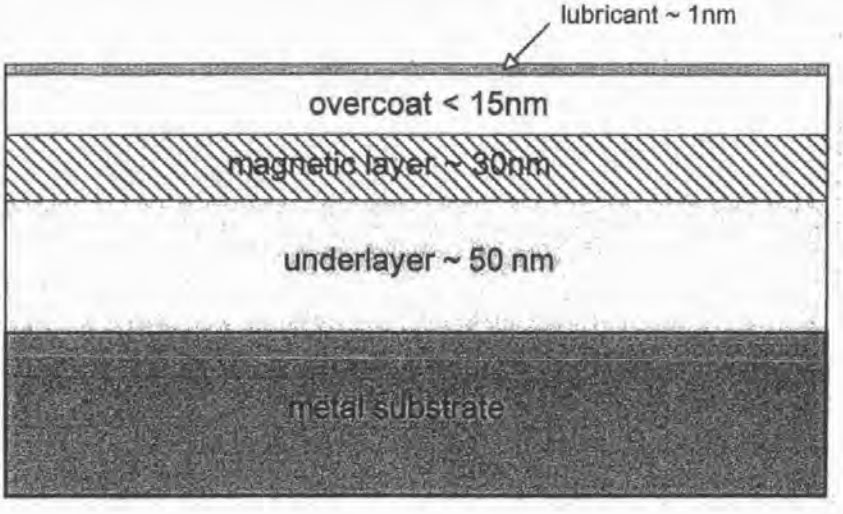

Figure 1. Schematic diagram of typical thin-film media used in hard disks.

In hard disk media an underlayer is usually deposited on the substrate first to improve the impact resistance of the whole disk and a carbon overcoat is applied after the magnetic layer to provide abrasion resistance. Finally, the diamond-like carbon overcoat is treated with a film of lubricant so finely dispersed that the average thickness is less than one molecule. The chief advantage of a thin film medium is the higher magnetization, which allows the use of thinner recording layers which in turn leads to a better defined magnetization reversal and consequently higher recording/areal densities.

A disk drive records information in a pattern of magnetized regions on the surface of the disk. The magnetic regions are arranged on the disk in tracks (concentric circular sets). A binary 1 is represented by a transition between opposite states of magnetization when moving along a track, and a 0 is the absence of such a flux reversal, as shown in Fig. 2.

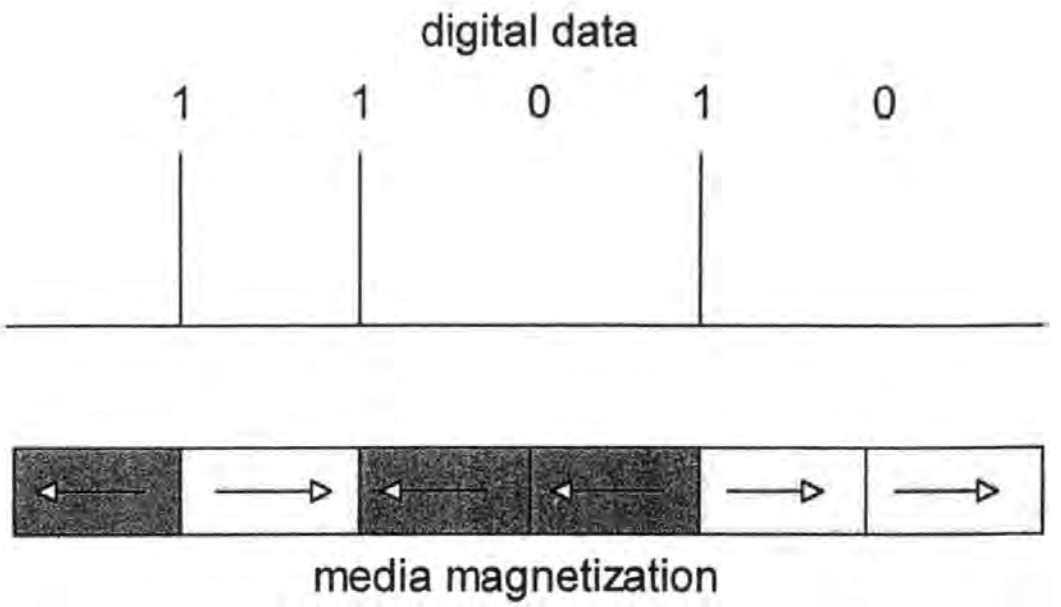

Figure 2. The binary representation of media magnetization.

Each spot where a transition might or might not be found is a bit cell. Boosting the areal density of a disk is a matter of making the bit cells smaller and packing adjacent tracks closer together. The width and length of bit cell (usually quoted as the bit cell aspect ratio - BAR, calculated as trackwidth/bit length) that is needed to achieve various areal densities are shown in Fig. 3. The magnetized regions employed on the early RAMAC disks are not included on the graph for good reason since, to the same rough scalings, the equivalent bit cell would need to be drawn over 500 metres tall (track width) and in excess of 200 metres wide (bit cell length).

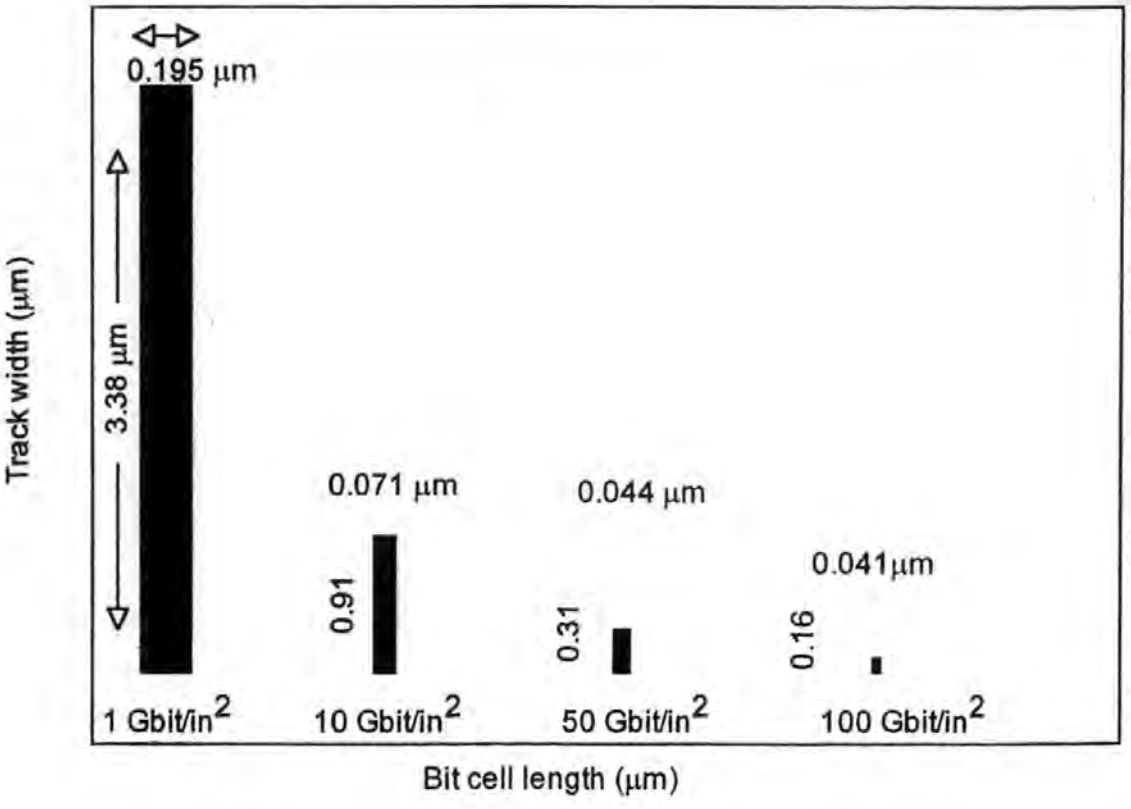

Figure 3. The shrinking bit cell related to various areal densities.

As the bit size shrinks and the bits are packed more and more tightly, the associated magnetic fields become weaker, requiring smaller and more efficient recording heads to perform the writing and reading of data to and from the disk. Continued advancements in recording head technology are essential to maintain consistent and rapid areal density growth in the coming years and the remainder of this chapter will

largely focus on the progress made in this vital area of HDD design. However before moving on to this there is one more factor worthy of consideration. It is important that the heads themselves must be brought very close to the disk surface, so that the effects of the magnetic fields are felt more strongly. The closer the drive head is to the platter the more sensitive it is to variations in the disk's magnetic field. The first hard disk experiments employed heads in contact with the magnetic media but the design was changed due to the unacceptable wear that contact caused at high rotation rates. Other applications that do not have to worry about very high head/media interface speeds do use read/write heads in contact, for example: floppy disks, video cassette recorders and tape decks.

Modern drive heads float over the surface of the disk and perform their tasks without ever touching the platters that they are writing to or reading from. The head is bonded to a metal suspension, which is a small arm that holds the head in position above or beneath a disk (in fact most drives employ two heads for each disk - one above and one beneath). The heads themselves are housed in a self-pressurized air-bearing design slider. When the drive is turned on, the disk starts spinning up to operating speed and air pressure builds up between the slider and the disk surface. The aerodynamic properties of the slider ensure that the tension of the head suspension arm is overcome and it starts to 'fly'. The head, slider and suspension collectively are called the head-gimbal assembly or HGA (see Fig. 4).

The RAMAC drive operated with a head to media gap of 25 micrometers or 25,000 nanometers and, in contrast to today's drives, had a dedicated compressor which jetted air on to the flat surface of the heads to provide a cushioned hovering effect. In comparison, current flying heights in the region of a miniscule 10 nanometers are being achieved. To put this into perspective, a human hair has a diameter of about 50 micrometers or 50,000 nanometers - 5,000 times the magnitude of the flying height. Consequently it is necessary that the hard disk is assembled in a clean room containing air specially filtered to remove all but the tiniest particles. The disk's internal environment is also kept free from contamination by a breather filter that allows the drive to adjust to changes in air pressure, ensuring a uniform flying height. Even so, as the flying height of drives continues to decrease, the point may soon be

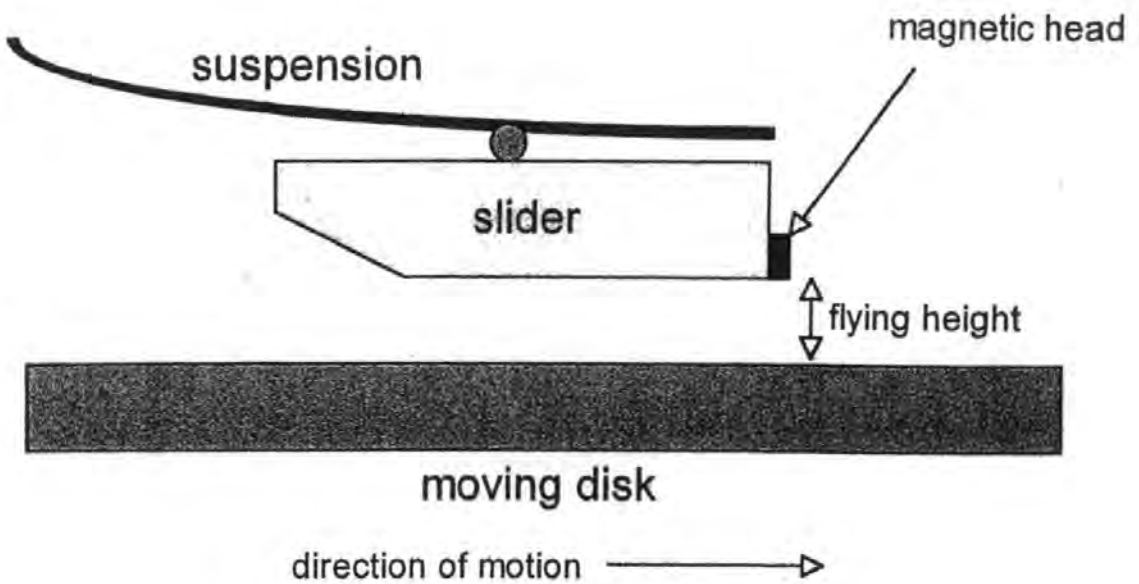

Figure 4. A head-gimbal assembly.

reached where it cannot be reduced any further without skimming the surface of the platter.

1.4. Inductive Heads

Much of the progress that has been achieved in obtaining higher and higher areal densities can be attributed to scaling considerations, that is, by simply making everything smaller and then adjusting parameters such as velocities and flying heights to suit. However, as far as the evolution of recording heads is concerned, there have been some radical transitions in the technology over the past decade.

The read/write head technology that sustained the early hard disk drive development is based on the inductive voltage produced when a permanent magnet (the disk) moves past a wire-wrapped magnetic core (the head). The oldest design

is the ferrite head - a U-shaped iron core much like a child's horseshoe magnet, with each end representing one of the poles. To write to the hard disk, the drive's controller sends an electrical current through the wires wrapping the head to induce a magnetic field within the core. This field is focused on the spinning disk through a narrow gap (the open end of the 'U') cut into the magnetic core of the head. The direction of the field produced depends on the direction of the current flow through the coil. A simplified drawing of a write head is shown in Fig. 5.

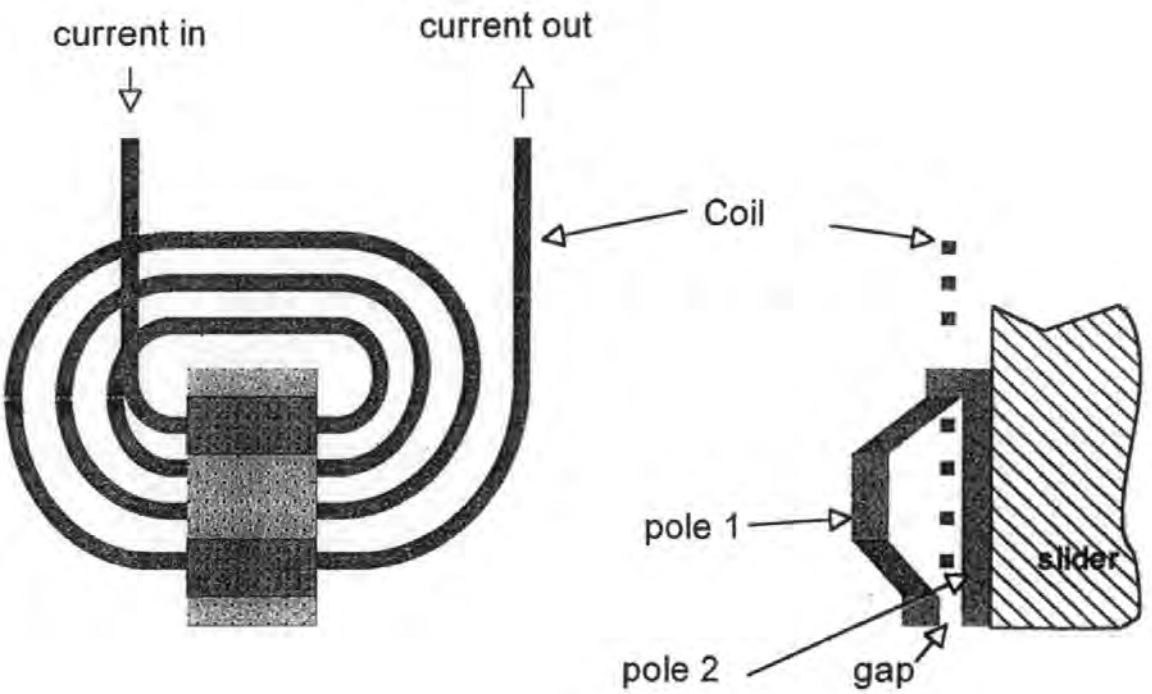

Figure 5. A write head.

As discussed earlier, the data are written on the disk in the form of binary digits, transmitted to the disk drive in a corresponding time sequence of binary 1's or 0's. In order to write these to the disk they are converted into an electric waveform that is delivered by wires to the head coil. The whole process is represented in Fig. 6, where it can be seen that a moving disk is magnetized in the positive (north) direction for positive current and is magnetized in the negative (south) direction for negative

current flow. A timing clock is synchronized to the spinning of the disk and bit cells exist for each tick of the clock, enabling each of them to be identified as either a 1 (a magnetic flux reversal) or a 0 (an absence of a flux reversal). Once written, the magnetized pattern on the disk remains unchanged until it is overwritten with a new data pattern.

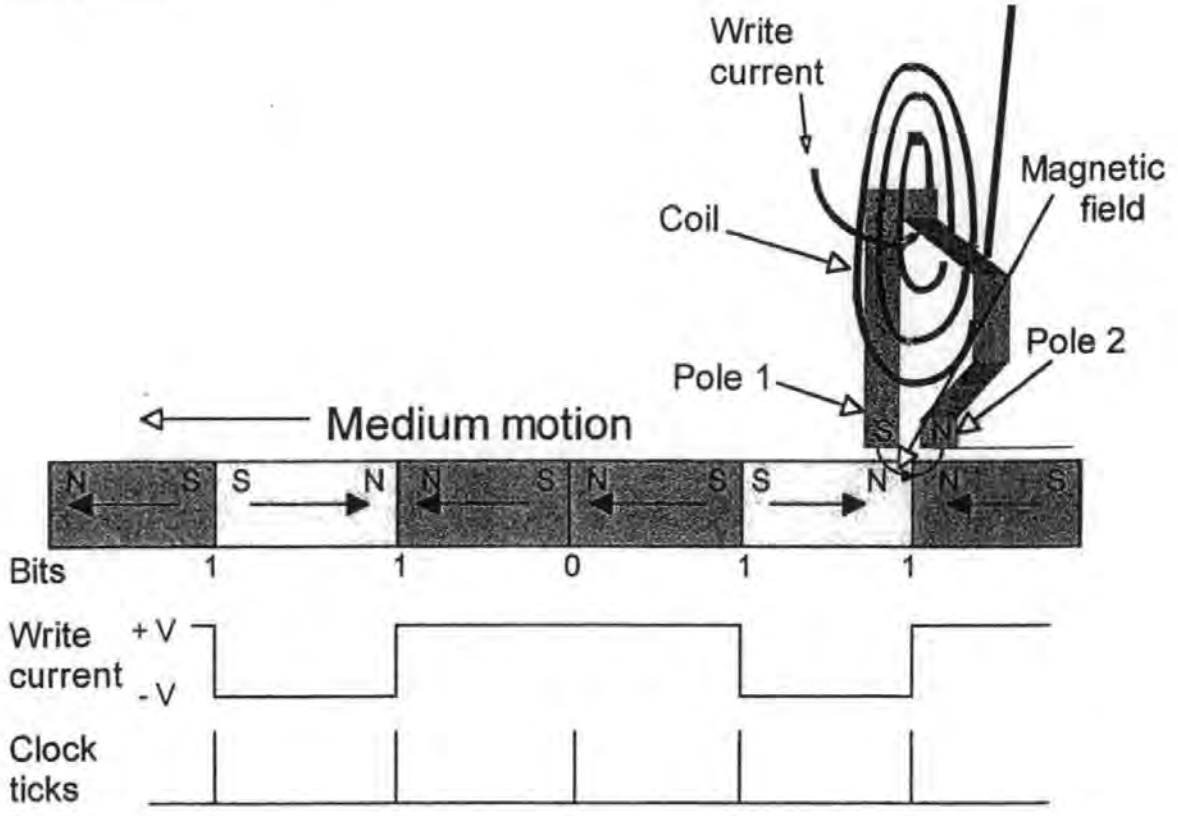

Figure 6. The writing process.

During a data read, the process is reversed: the head is passed over the magnetic fields on the disk and the flux changes induce a current of one direction or another in the coil of the head, depending on the polarity of the magnetic field. The read voltage pulses are then translated into sequences of bits equal to 0's and 1's by the drive's controller. The older type heads are usually called 'read/write heads' since they perform both the reading and the writing operation using the same element. However, using a single dual-function inductive head for both reading and writing imposes some specific limitations on their performance with modern, very high

density recording media. One way to improve the head's sensitivity to smaller, weaker magnetic fields is to increase the number of turns in the coil, since the strength of the read signal is directly proportional to the number of turns in the coil. Unfortunately, increasing the number of turns also increases the head's inductance, and there is a limit to the amount of inductance that a head can tolerate and still perform successful writes. As higher areal densities are sought, the increase in inductance associated with the number of turns limits the frequency with which the current reversals can occur for write operations. Another possibility is to improve the read signal strength by increasing the linear speed at which the magnetic transitions pass under the head: the faster the speed, the stronger the signal. But high inductance heads, as stated previously, cannot handle the high data frequencies that accompany faster rotational speeds and once more the task of designing a read/write inductive head becomes one of striking a careful balance between the two distinct operations that it must carry out.

Early ferrite read/write heads suffer from being large and cumbersome, working at relatively large flying heights and requiring reasonably large and strong magnetic fields to function efficiently. As a result, they are no longer in general use with thin film recording media and are typically found in PC hard drives under 50 megabytes in size. Some of the major evolutionary advances to read/write head technology include; the composite ferrite head, the metal-in-gap (MIG) head, and the thin-film head. The composite ferrite head (a ferrite head with a glass-filled gap) and the metal-in-gap head (where as the name suggests, the gap is filled with a metal alloy) both exhibited a markedly improved sensitivity over the older 'ordinary' ferrite head. The thin-film head differs from these in that it is produced in a process using vacuum deposition and photolithography. The coil winding is deposited onto a ceramic base, creating very small heads with a precise gap between the magnetic pole-pieces of the magnetic material and these heads represented a substantial improvement in performance. But magnetic recording research continued to aim for higher areal density by a combination of increases in linear and track densities [2], and by the late 1980's it became evident that inductive heads can only do so much to

improve areal density and that a radically new technology was needed to overcome the limitations of the read/write head due to it's inherent 'inductance compromise'.

1.5. Magnetoresistive (MR) Heads

The solution, first developed in the early 1990's, was the magnetoresistive head which was based on the ability of certain metals to change their electrical resistivity in the presence of a magnetic field. This phenomenon is called the anisotropic magnetoresistance effect (AMR) and was originally discovered by Lord Kelvin in 1857. As a result, first generation MR heads are more correctly termed anisotropic magnetoresistive (AMR) heads, but traditionally they have been called simply magnetoresistive (MR).

A basic MR read head consists of a read element located in the space between two highly permeable magnetic shields. The element itself is actually a minute stripe of a ferromagnetic alloy (an alloy of Nickel and Iron, 81%/19%, is widely used and is called Permalloy). The shields' purpose is to reject stray magnetic fields from the MR element. During an MR head read, a small direct current, called a sense current, is generated through the alloy stripe and as the head passes over the surface of the disk, the stripe changes resistance by a few percent as the magnetic fields change corresponding to the stored patterns on the disk. The resultant change in amperage of the sense current is measured and a read signal corresponding to each data bit, whose voltage is proportional to the change in resistance of the MR stripe, is generated. Unfortunately, the voltage change across the stripe is non linear with the disk magnetic field, and designing an efficient electronics system to interpret the magnetic transitions is difficult. To address this problem, a second, magnetically soft but non-magnetoresistive film is placed in proximity to the stripe but magnetically separated from it by a high resistance spacer layer. When the sense current flows through the MR stripe a magnetic field is generated, which magnetizes the soft-adjacent-layer (SAL). This magnetized soft layer produces a magnetic field which, in turn, biases the magnetization in the MR stripe so that it is maintained near to 45° and the voltage change is approximately linear and a maximum. Other methods

of linearizing exist, but the SAL technique has gained wide acceptance because it is simple to process and is suitable for high areal density applications.

An important feature of MR heads is that the MR technology is used for reading the data only. For writing, a separate thin-film inductive head is used. This means that MR heads do not suffer as a consequence of the inductance compromise since the MR read head allows the thin-film inductive head to be optimized solely for the writing operation. The MR stripe automatically senses flux, enabling the reading of smaller bit cells and narrower track widths which, in turn, allows the write head to be less powerful with lower inductance. The lower inductance permits the writing of data at very high frequencies. Although the read and write processes are different functions, it is important that the two heads are in close proximity to the recording medium, and that the write gap and the MR element are close to each other. To achieve this the top shield of the MR read head may be fabricated to also serve as the bottom magnetic pole of the thin-film inductive write head. Such a head is usually called a merged head, and the basic design is shown in Fig. 7.

Successive generations of MR heads have reduced in size to allow even greater areal density. Such heads are often referred to as extended MR heads or MRX heads. Even so, as areal density continues to increase, MR heads eventually reach the point (at about 5 gigabits/in^2) when they are not sensitive enough to detect the tiny magnetic fields that are generated by the transitions on the disk. This results in a reduction in the voltage changes produced by the head and lower signal amplitudes. The natural successor to MR is GMR (giant magnetorestance). The descriptor 'giant' does not refer to the size of the GMR head; they are actually smaller than their MR predecessors. Rather, the giant magnetoresistive effect is an advanced application of magnetoresistive technology that is characterized by the 'giant' changes in resistance exhibited in comparison with ordinary MR heads. The effect was first discovered, independently, by Peter Gruenberg and Albert Fert, who noticed very large resistance changes in thin layers of metals when they were subjected to magnetic fields.

The GMR head structure consists of a stack of four thin films, as shown in Fig. 8; a 'sensing' or 'free' layer - free to rotate in response to the magnetic patterns on the disk, a non-magnetic spacer layer - located between the free and pinned layers

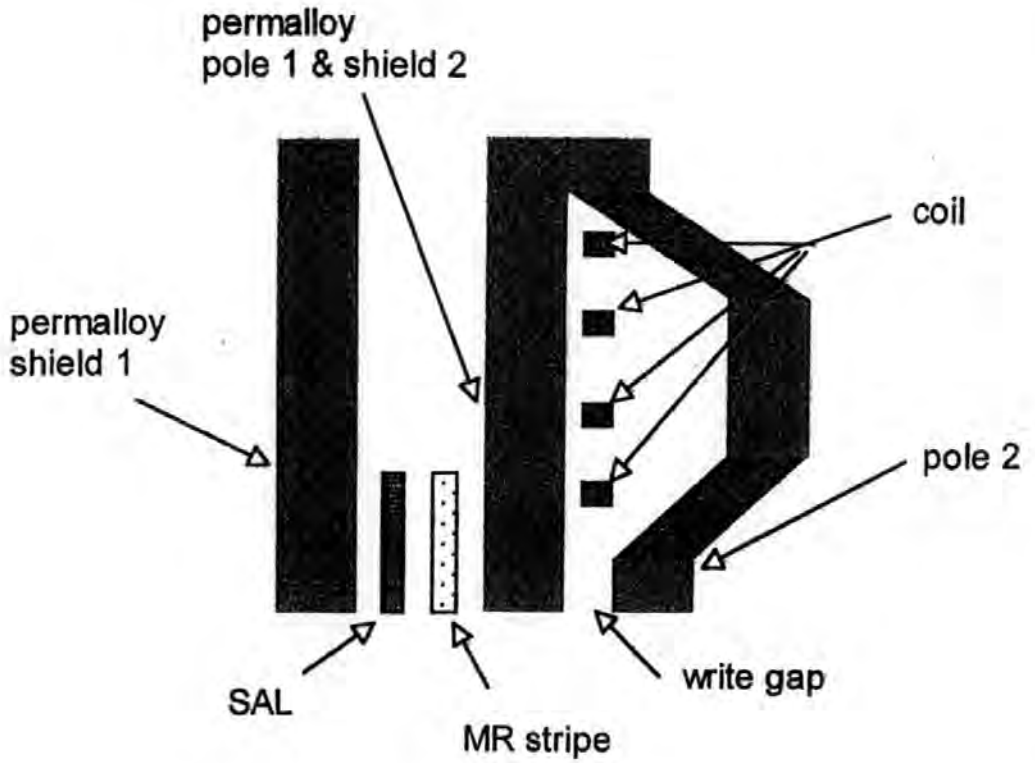

Figure 7. A merged MR head.

to separate them magnetically, a magnetic 'pinned' layer - held in a fixed magnetic orientation by virtue of its proximity to the exchange layer, and an 'exchange' layer - this fixes the pinned layer's magnetic orientation.

When, during a read, the head passes over a flux reversal, the orientation of the magnetization in the free layer is changed and the electrons rotate so that they are not aligned with those in the pinned layer, whose magnetization orientation is fixed. This non-alignment causes an increase in the resistance of the overall structure. When both free and pinned layers have a parallel magnetic orientation the resistance of the structure is lowered. The rotation of the free film's orientation caused by the magnetic transitions on the surface of the hard disk have led to these structures being labeled spin-valve GMR heads. Spin-valve GMR heads typically exhibit a resistance change when passing from one polarity to another of anything up to 15% [2]. This compares with a resistance change of only a few percent for MR heads.

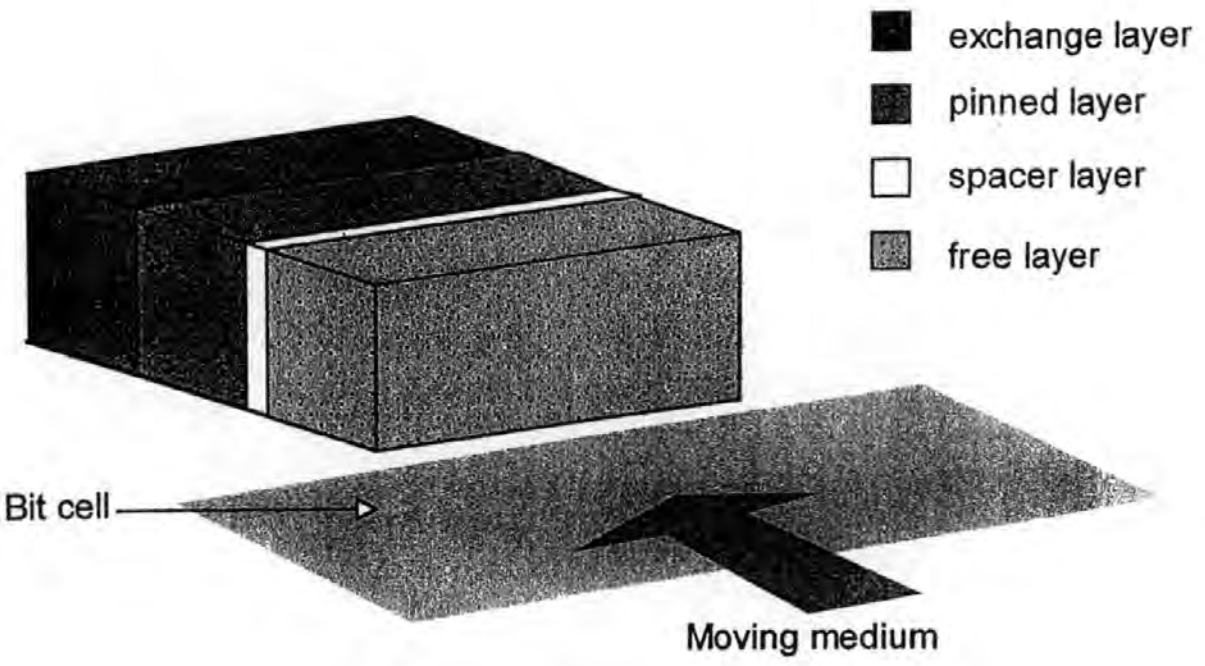

Figure 8. A schematic drawing of a GMR head structure.

1.6. Perpendicular Recording

The process outlined in Fig. 6, which is used almost exclusively today by the recording industry, is known as longitudinal recording: the medium has a preferred magnetic orientation, or easy axis, in a direction parallel to its plane. Another approach is to use perpendicular recording, when the medium's preferred orientation is in a direction normal to its plane. Perpendicular recording was first studied over 20 years ago, by Iwasaki, as a result of his study on the circular mode of magnetization in short-wavelength recording [3], [4]. It has often been put forward as superior to longitudinal recording, but the industry has not switched to it because, at areal densities below a few hundred gigabits/in^2, it is essentially equal in capability to longitudinal recording. However, as areal density rises towards 1 terabit/in^2 the superparamagnetic effect will at some point become the limiting factor. This effect arises because,

as the data bits get smaller, the magnetic energies holding the bits in place also decrease and inherent thermal energies can cause demagnetism of the bit cells over time, leading to data loss. The phenomenon is also referred to as the thermal fluctuation after-effect problem. The major advantage of perpendicular recording compared to longitudinal recording is illustrated in Fig. 9. In both cases, an alternating pattern of magnetizations in the recording medium is drawn. In the longitudinal case this will lead to a severe demagnetization in every cell, due to the opposite magnetization directions in the adjacent cells. This effect will increase at higher densities, leading to a decreasing net magnetization in each cell. In perpendicular recording, two adjacent cells magnetize rather than demagnetize each other. As a result of the demagnetizing field-free transitions, significantly higher areal densities are more thermally stable for perpendicular recording.

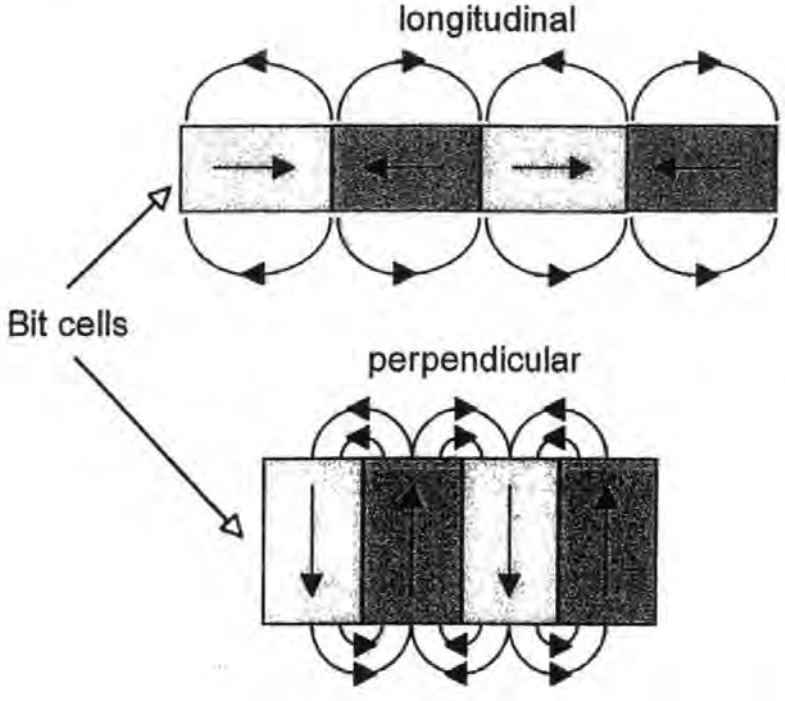

Figure 9. Illustration of the advantage of perpendicular recording over longitudinal recording.

The current preferred approach of longitudinal magnetic recording can likely reach areal densities of over 100 gigabits/in^2 [5]. However it is expected that higher densities of 500 to 1000 gigabits/in^2 (1 terabit/in^2), will require a switch to perpendicular recording [6], [7].

1.7. Summary

In this chapter:

- A brief history of the development of magnetic recording is given.
- The major considerations in the design of the modern hard disk drive are discussed.
- The read and write processes are presented and the fundamentals of the inductive read/write recording head are investigated.
- The anisotropic magnetoresistive effect is discussed and its use in MR and GMR read heads is presented.
- Perpendicular magnetic recording is outlined and the method is compared to longitudinal recording.

CHAPTER 2

THEORETICAL METHODS

2.1. Introduction

In this chapter the concepts and definitions that are required for later discussion are introduced along with the essential mathematical techniques. The theory underlying the relationships used in the analysis of magnetic recording heads is developed in section 2.2 from basic physical principles [8], in particular using as a starting point the Biot and Savart law of magnetostatics. Also, the modeling assumptions that are employed in this thesis to study the magnetic recording process are given and evaluated in section 2.2. In section 2.3, the Fourier method of analysis, which is later applied to new head geometries, is described with reference to the classic case of an unshielded single pole head [9] in the presence of a soft magnetic underlayer. The reciprocity formulas, which form the basis for the study of the reproduce process, are derived in section 2.4 using the principle of reciprocity. Section 2.5 contains a description of the Landau-Lifshitz-Gilbert equation [10], which is the general equation of motion employed in Chapter 6 to study the magnetization reversal of two different classes of recording media.

2.2. Mathematical Model

2.2.1. Biot and Savart Law and Laplace's Equation

Early in the nineteenth century Biot and Savart, through a series of experiments, established the relationship between the magnetic flux density $\mathbf{B}$ (sometimes called the magnetic induction) and charges in motion (currents) and formulated the

law of force between one current and another. They showed that the elemental flux density $d\mathbf{B}$ at an observation point P as shown in Fig. 10. may be expressed as

$$d\mathbf{B} = kI\frac{(d\mathbf{I} \times \mathbf{x})}{|\mathbf{x}|^3} \quad , \tag{2.1}$$

where $d\mathbf{I}$ is an element of length (pointing in the direction of current flow) of a wire which carries a current I, $\mathbf{x}$ is the coordinate vector from $d\mathbf{I}$ to the point P and k is a constant that depends upon the system of units employed.

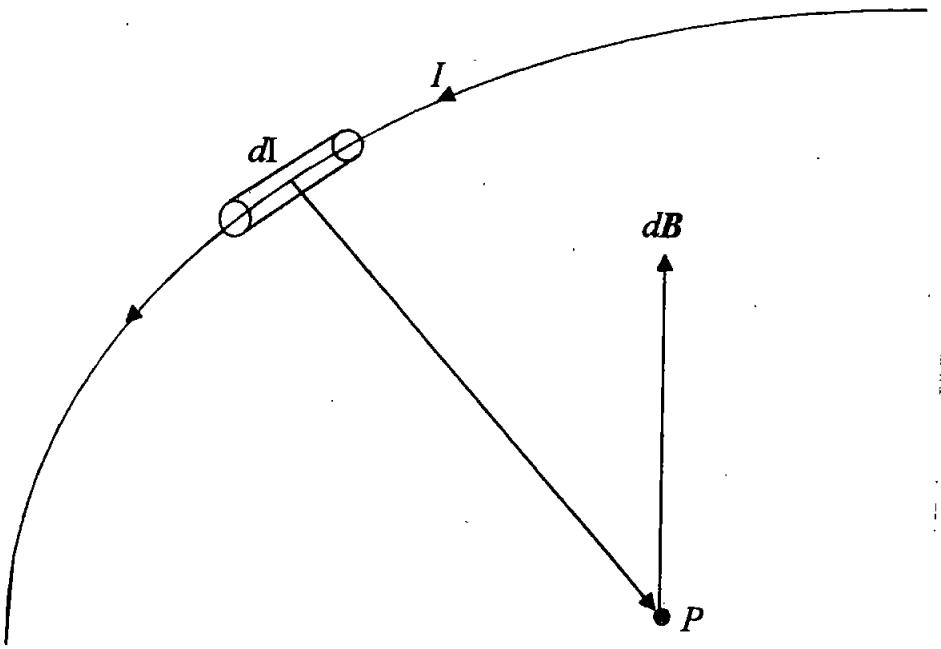

Figure 10. Elemental magnetic induction $d\mathbf{B}$ due to current element $I\ d\mathbf{I}$.

If the charges in motion (currents) are so small and numerous that they can be described by a current density $\mathbf{J}(\mathbf{x})$, then the basic inverse square law (2.1) can be replaced by an integral for $\mathbf{B}(\mathbf{x})$, the magnetic flux density at $\mathbf{x}$ due to a current density at $\mathbf{x}'$:

$$\mathbf{B}(\mathbf{x}) = k\int \mathbf{J}(\mathbf{x}') \times \frac{(\mathbf{x}-\mathbf{x}')}{|\mathbf{x}-\mathbf{x}'|^3}\, d^3x' \quad , \tag{2.2}$$

where d^3x' is a volume element at $\mathbf{x}'$. As a function of $\mathbf{x}$, the vector factor in the integrand is the negative gradient of the scalar $1/|\mathbf{x}-\mathbf{x}'|$:

$$\frac{(\mathbf{x}-\mathbf{x}')}{|\mathbf{x}-\mathbf{x}'|^3} = -\nabla\left(\frac{1}{|\mathbf{x}-\mathbf{x}'|}\right) \quad , \tag{2.3}$$

from which it follows that the magnetic flux density can be written as

$$\mathbf{B}(\mathbf{x}) = k\nabla \times \int \frac{\mathbf{J}(\mathbf{x}')}{|\mathbf{x}-\mathbf{x}'|} d^3x' \quad , \tag{2.4}$$

since the gradient operator can be taken outside of the integration as it does not involve the variable of integration. Since the divergence of the curl of any well behaved scalar function of position vanishes it follows immediately that

$$\nabla \cdot \mathbf{B} = 0 \quad , \tag{2.5}$$

which is the first differential law of magnetostatics. In free space the magnetic flux density $\mathbf{B}$ is identical to the magnetic field, $\mathbf{H}$, since in free space there is no magnetization and it follows that (2.5) becomes $\nabla \cdot \mathbf{H} = 0$.

Using the vector identity $\nabla \times (\nabla \times \mathbf{A}) = \nabla(\nabla \cdot \mathbf{A}) - \nabla^2\mathbf{A}$ for an arbitrary vector field $\mathbf{A}$ and taking the curl of expression (2.4) for $\mathbf{B}$ gives

$$\nabla \times \mathbf{B} = k\nabla \int \mathbf{J}(\mathbf{x}') \cdot \nabla\left(\frac{1}{|\mathbf{x}-\mathbf{x}'|}\right) d^3x' - k\int \mathbf{J}(\mathbf{x}')\, \nabla^2\left(\frac{1}{|\mathbf{x}-\mathbf{x}'|}\right) d^3x' \tag{2.6}$$

and using the relationships

$$\nabla\left(\frac{1}{|\mathbf{x}-\mathbf{x}'|}\right) = -\nabla'\left(\frac{1}{|\mathbf{x}-\mathbf{x}'|}\right) \tag{2.7}$$

where ∇' is the vector operator ∇ applied with respect to $\mathbf{x}'$ and

$$\nabla^2\left(\frac{1}{|\mathbf{x}-\mathbf{x}'|}\right) = -4\pi\delta(\mathbf{x}-\mathbf{x}') \tag{2.8}$$

where $\delta(\mathbf{x}-\mathbf{x}')$ is the three-dimensional Dirac delta function, the integrals in (2.6) can be written

$$\nabla \times \mathbf{B} = k\nabla \int \mathbf{J}(\mathbf{x}') \cdot \nabla'\left(\frac{1}{|\mathbf{x}-\mathbf{x}'|}\right) d^3x' + 4k\pi\, \mathbf{J}(\mathbf{x}) \quad . \tag{2.9}$$

Integration by parts produces

$$\nabla \times \mathbf{B} = 4k\pi\, \mathbf{J}(\mathbf{x}) + k\nabla \int \frac{\nabla' \cdot \mathbf{J}(\mathbf{x}')}{|\mathbf{x} - \mathbf{x}'|}\, d^3x' \quad . \tag{2.10}$$

The continuity equation that relates charge density $\rho(\mathbf{x})$ and current density using the principle of conservation of charge is

$$\frac{\partial \rho}{\partial t} + \nabla \cdot \mathbf{J} = 0 \quad . \tag{2.11}$$

Consequently, for charges and fields that do not vary with time (2.11) reduces to $\nabla \cdot \mathbf{J} = 0$ and (2.10) becomes

$$\nabla \times \mathbf{B} = 4k\pi \mathbf{J} \quad , \tag{2.12}$$

which is the second differential law of magnetostatics. If, in the region of interest the current density is zero, then

$$\nabla \times \mathbf{B} = \mathbf{0} \quad . \tag{2.13}$$

In free space, it follows that $\nabla \times \mathbf{H} = \mathbf{0}$ which allows the magnetic field $\mathbf{H}$ to be expressed as the gradient of a magnetic scalar potential, $\mathbf{H} = -\nabla\varphi$, and equation (2.5) becomes a partial differential equation for the magnetic scalar potential:

$$\nabla^2\varphi \equiv \frac{\partial^2\varphi}{\partial x^2} + \frac{\partial^2\varphi}{\partial y^2} + \frac{\partial^2\varphi}{\partial z^2} = 0 \quad , \tag{2.14}$$

which is Laplace's equation in three dimensions. The solution of Laplace's equation in the region exterior to a recording head therefore permits computation of the magnetic field $\mathbf{H}$ in that region.

2.2.2. The Modeling Assumptions

For each of the head geometries considered, the following modeling assumptions are made.

A. Modeling the Head Dimensions

- The head is infinitely wide so that a two-dimensional model results and it is therefore only necessary to solve Laplace's equation in two dimensions:

$$\frac{\partial^2\varphi}{\partial x^2} + \frac{\partial^2\varphi}{\partial y^2} = 0 \quad . \tag{2.15}$$

- The pole piece(s) are semi-infinite (in the y direction).
- Shields, where present, are semi-infinite in both the horizontal and vertical directions.
- An underlayer, where present, is infinitely long (in the x direction).

A two dimensional analysis is appropriate for the modeling of read heads since the track width on which the magnetizations are written is large compared with the other significant dimensions in the model. The shields and pole pieces are assumed to be infinitely high within the two dimensional model because their heights are much greater than the head/underlayer separation. Similarly, the shields and underlayer are taken to be of semi-infinite and infinite length respectively in the model because they are significantly longer than the pole pieces and the gaps between the poles and between the poles and shields. Thus, the magnetic scalar potential satisfies the two-dimensional Laplace equation in the region exterior to the recording head and below the underlayer if one is present. To perform a Fourier analysis the region must be subdivided into rectangular regions some of which may necessarily be semi-infinite. Solutions to the partial differential equations in each region which satisfy the relevant boundary conditions are obtained using the technique of separation of variables [11]. Semi-infinite regions permit an integral solution which contains an unknown function within the integrand, while finite regions produce a solution in the form of an infinite series with unknown harmonic coefficients. The unknown function and sets of coefficients are then found by matching the solutions and the normal derivatives along their common boundary. This method allows the unknown function in the integrand to be expressed in terms of the harmonic coefficients which are in turn defined by infinite systems of linear algebraic equations.

B. Modeling the Head Materials

- Each pole piece has a constant magnetic potential distribution (implied by assuming an infinite permeability).

This is a valid assumption because, in practice, the pole pieces are constructed from very high permeability magnetic alloys.

- An underlayer, where present, is infinitely permeable and at zero potential.

- The pole pieces have perfectly rectangular corners.

Mathematically, the **B** field becomes logarithmically infinite at the pole tip corners whereas in reality the pole(s) saturate in these regions and the field can not exceed $\mathbf{B_S}$, the maximum flux density of the magnetic material of the pole [12]. Fields higher than the average deep gap field can be found close to the corners at distances of less than about one tenth of the gap dimension. However, the increased field strength in these regions is only of importance in the case of wide gaps reading thin media at a very close spacing [13].

- The effect on the field exterior to the pole pieces due to the recording medium, other than the possible presence of an underlayer, is negligible.

Relative to the pole and the underlayer, the permeability of the medium is only slightly greater than that of air, which is also only slightly greater than the permeability of a vacuum. The underlayer, which is usually a part of the recording medium, is made of a very high permeability material such as nickel-iron.

2.3. The Fourier Method

Fourier techniques were first used in the study of magnetic recording heads by Fan [9] to calculate the head field distribution of an unshielded single pole. Exact analytic solutions in the form of infinite series have subsequently been obtained for various head configurations by the application of the Fourier method to the relevant idealized models. The method is particularly useful for areas of research which require an analytic solution, such as the design analysis of a head/disk system. The infinite series solution to Laplace's equation permits each of the head's dimensions to be taken into account and provides an explicit expression which is relatively easy to apply to design work [12]. Fan followed his study of a single pole head with an analysis of a ring head [13], which has been the subject of further investigation [14], [15], [16]. Solutions for both the shielded single pole in the presence of an underlayer (keeper layer)[17]

and a ring head in the presence of an underlayer [18] have also been presented. All of the above analyses can be considered special cases of the new general results for double-element heads that are presented in Chapter 3.

2.3.1. The Single Pole Head

The Fourier method is demonstrated here by giving Fan's solution for a single pole head [9] in a coordinate system and notation consistent with that used in this thesis. Fig. 11. shows Fan's idealized two-dimensional model of the single pole head with an underlayer [9]. A semi-infinite pole of width $2L$ is perpendicular to and at a distance t from an infinitely long, highly permeable underlayer at zero potential. The pole is assumed to have a constant potential V and the negative potential pole is effectively the reflection of the positive pole, in the underlayer. Due to symmetry it is only necessary to solve Laplace's equation for $x \geq 0$ and the area is further subdivided into two regions, A and B as shown. The general solutions to Laplace's equation which satisfy the boundary conditions in these two regions are, with the subscript denoting the region,

$$\varphi_A(x,y) = V\frac{t-y}{t} + \sum_{n=1}^{\infty} A_n \sin\left(\frac{n\pi(t-y)}{t}\right)\cosh\left(\frac{n\pi x}{t}\right) \qquad 0 \leq x \leq L \qquad (2.16)$$

and

$$\varphi_B(x,y) = \int_0^{\infty} B(k)\sin\left(\frac{k(t-y)}{t}\right)e^{-kx/t}\,dk\,. \qquad (2.17)$$

Matching the solutions at $x = L$ gives:

$$B(k) = \frac{2V}{\pi}e^{kL/t}\frac{\sin(k)}{k^2} + e^{kL/t}\sum_{n=1}^{\infty} A_n 2n(-1)^n \cosh\left(\frac{n\pi L}{t}\right)\frac{\sin(k)}{k^2-(n\pi)^2}\,. \qquad (2.18)$$

So that in region B

$$\varphi_B(x,y) = \frac{2V}{\pi}I_0 + \sum_{n=1}^{\infty} A_n 2n(-1)^n \cosh\left(\frac{n\pi L}{t}\right) I_n \qquad (2.19)$$

where

$$I_n = \int_0^{\infty} \frac{\sin(k)\sin\left(k(t-y)/t\right)}{k^2-(n\pi)^2}e^{-k(x-L)/t}\,dk\,. \qquad (2.20)$$

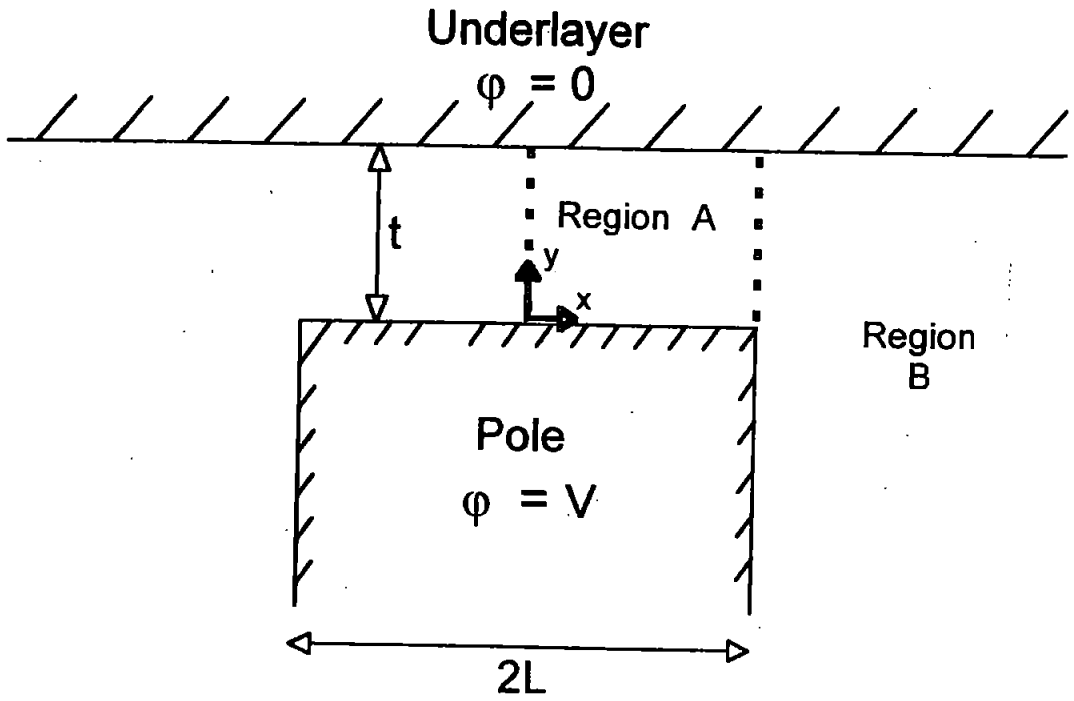

Figure 11. The single pole head.

Now matching the x derivatives of both solutions at $x = L$ gives

$$\frac{\pi}{4} A_m \sinh\left(\frac{m\pi L}{t}\right) + \sum_{n=1}^{\infty} A_n n\pi (-1)^{m+n} \cosh\left(\frac{n\pi L}{t}\right) I_{mn} = V(-1)^{m+1} I_{m0}\,, \quad (2.21)$$

for $m = 1, 2, 3, \cdots$ where

$$I_{mn} = \int_0^{\infty} \frac{k \sin^2(k)}{[k^2 - (m\pi)^2][k^2 - (n\pi)^2]}\, dk \quad (2.22)$$

which is an infinite set of linear algebraic equations for the coefficients A_m depending on the ratio L/t only. Normalized coefficients, $A_m^{'} = A_m \cosh(m\pi L/t)/V$, are computed by truncating the system of equations to some finite size $N \times N$. Fan gives no further information on how he evaluated the constants, in [15] $N = 6$ was used and in [16] systems up to 640×640 were solved and extrapolation using library routines [19] was used to obtain coefficients correct to 6dp.

The normalized horizontal field component $H_x = -\partial\varphi/\partial x$ and vertical field component $H_y = -\partial\varphi/\partial y$ follow by partial differentiation,

$$\frac{H_x}{V} = \begin{cases} -\sum_{n=1}^{\infty} A_n' \frac{n\pi}{t} \sin\left(\frac{n\pi(t-y)}{t}\right) \sinh\left(\frac{n\pi x}{t}\right) \Big/ \cosh\left(\frac{n\pi L}{t}\right) & 0 \le x \le L \\ \frac{2}{\pi t} J_0 + \sum_{n=1}^{\infty} A_n' \frac{2n}{t} (-1)^n J_n & L \le x < \infty \end{cases} \tag{2.23}$$

$$\frac{H_y}{V} = \begin{cases} \frac{1}{t} + \sum_{n=1}^{\infty} A_n' \frac{n\pi}{t} \cos\left(\frac{n\pi(t-y)}{t}\right) \cosh\left(\frac{n\pi x}{t}\right) \Big/ \cosh\left(\frac{n\pi L}{t}\right) & 0 \le x \le L \\ \frac{2}{\pi t} K_0 + \sum_{n=1}^{\infty} A_n' \frac{2n}{t} (-1)^n K_n & L \le x < \infty \end{cases} \tag{2.24}$$

where

$$J_n = \int_0^{\infty} \frac{k \sin(k) \sin\left(k(t-y)/t\right)}{k^2 - (n\pi)^2} e^{-k(x-L)/t}\, dk \tag{2.25}$$

$$K_n = \int_0^{\infty} \frac{k \sin(k) \cos\left(k(t-y)/t\right)}{k^2 - (n\pi)^2} e^{-k(x-L)/t}\, dk\,. \tag{2.26}$$

It is possible to write all of the integrals that appear in Fan's solution in terms of special functions, in particular the exponential integral Ei, the sine integral Si, and the cosine integral Ci. All of these functions are defined in Appendix A.1.1. The integrals I_{m0} and I_{mn} are given in closed form by Fan [9]. They are,

$$\text{when } n = 0, \quad I_{m0} = \frac{1}{2(m\pi)^2} \left[\gamma + \ln(2m\pi) - \mathrm{Ci}(2m\pi)\right] \tag{2.27}$$

$$\text{else} \qquad I_{mn} = \begin{cases} \frac{1}{2m\pi} \mathrm{Si}(2m\pi), & m = n \\ \frac{1}{2\pi^2(n^2-m^2)} \left[\ln\left(\frac{m}{n}\right) - \mathrm{Ci}(2m\pi) + \mathrm{Ci}(2n\pi)\right], & m \ne n, \end{cases} \tag{2.28}$$

which differs in sign from the result given by Fan in the case when $m \neq n$. Analytic expressions for the integrals I_n, J_n and K_n are given in [14].

For I_n,

$$I_0 = \frac{1}{2t}\left[\frac{x-L}{2}\ln\left(\frac{y^2+(x-L)^2}{(2t-y)^2+(x-L)^2}\right)\right.$$
$$\left.+(2t-y)\arctan\left(\frac{2t-y}{x-L}\right)-y\arctan\left(\frac{y}{x-L}\right)\right] \tag{2.29}$$

$$I_n = \frac{1}{4n\pi}\mathrm{Re}[e^{-a}\mathrm{Ei}(a)-e^{a}\mathrm{Ei}(-a)-e^{-b}\mathrm{Ei}(b)+e^{b}\mathrm{Ei}(-b)]$$
$$+\frac{1}{2n}e^{-n\pi(x-L)/t}(-1)^n\sin\left(\frac{n\pi(t-y)}{t}\right) \tag{2.30}$$

for $0 < (t-y)/t < 1$, where

$$a = \frac{n\pi}{t}[(x-L)-(2t-y)i] \qquad \text{and} \qquad b = \frac{n\pi}{t}[(x-L)-yi]\,. \tag{2.31}$$

For J_n,

$$\text{when } n=0,\ J_0 = \frac{1}{4}\left[\ln\left(\frac{(x-L)^2+(2t-y)^2}{(x-L)^2+y^2}\right)\right] \tag{2.32}$$

$$\text{else} \qquad J_n = -\frac{1}{4}\mathrm{Re}\left[e^{a}\mathrm{E}_1(a)+e^{-a}\mathrm{E}_1(-a)-e^{b}\mathrm{E}_1(b)-e^{-b}\mathrm{E}_1(-b)\right]+R \tag{2.33}$$

where a and b are given by (2.31) and

$$R = \begin{cases} \frac{\pi}{2}(-1)^n e^{-n\pi(x-L)/t}\sin\left(\frac{n\pi q}{r}\right) & 0 \le (t-y) \le t \\ 0 & y > t \end{cases}$$

For K_n,

$$\text{when } n=0,\ K_0 = \frac{1}{2}\left[\arctan\left(\frac{2t-y}{x-L}\right)+\arctan\left(\frac{y}{x-L}\right)\right] \tag{2.34}$$

$$\text{else} \qquad K_n = \frac{1}{4}\mathrm{Im}\left[e^{a}\mathrm{E}_1(a)+e^{-a}\mathrm{E}_1(-a)+e^{b}\mathrm{E}_1(b)+e^{-b}\mathrm{E}_1(-b)\right]+S \tag{2.35}$$

where a and b are given by (2.31) and

$$S = \begin{cases} \frac{\pi}{2}(-1)^n e^{-n\pi(x-L)/t}\cos\left(\frac{n\pi(x-L)}{t}\right) & 0 \le (t-y) \le t \\ 0 & y > t. \end{cases}$$

2.4. The Reciprocity Principle

When a writing head is driven by a current in its coil, it produces flux in the region above it. Conversely, when the same head is used in the reading process, the magnetizations in the recorded medium produces flux in the coil [20]. To illustrate this principle consider two coils A and B linked by a mutual inductance L_m. A current i_A in coil A will cause a flux $\varphi_B = L_m i_A$ to thread coil B. Similarly, a current i_B in coil B will generate a reciprocal relationship with the flux φ_A threading coil A so that $\varphi_A = L_m i_B$, where the mutual inductance L_m is common to both relations. Thus,

$$\frac{\varphi_A}{i_B} = \frac{\varphi_B}{i_A} \quad . \tag{2.36}$$

Now take coil A to represent the coil of the reproduce head and coil B to carry a solenoidal current i_B representing a magnetized element of the recording medium. The x component of the magnetization, at point x' in the recording medium, is represented by

$$i_B = M_x(x')dx' = M_x(x - \bar{x})dx \quad . \tag{2.37}$$

Considering only x components of the head field $H_x(x, y)$, the flux in coil B is given by

$$\varphi_B = \mu_0 H_x(x, y)\, dy\, dz \quad , \tag{2.38}$$

where μ_0 is the permeability of free space and $dy\, dz$ is the area enclosed by coil B. Substituting (2.38) and (2.37) in (2.36) gives

$$\frac{\mu_0 H_x(x, y)\, dy\, dz}{i_A} = \frac{\varphi_A}{M_x(x - \bar{x})dx} \quad , \tag{2.39}$$

from which it is easy to obtain an expression for the flux in the reproduce head

$$\varphi_A = \frac{\mu_0}{i_A} H_x(x, y)\, M_x(x - \bar{x})dx\, dy\, dz \quad . \tag{2.40}$$

Integration over the volume of the recording medium gives the total flux in the head coil

$$\varphi_A = \frac{\mu_0}{i_A} \int_{z=-\infty}^{z=\infty} \int_{y=d}^{d+\delta} \int_{x=-\infty}^{\infty} H_x(x + \bar{x}, y) M_x(x, y) dx\, dy\, dz \quad . \tag{2.41}$$

In an inductive head the output voltage is proportional to the rate of change of flux. In magnetoresistive heads, which are under consideration in this thesis, the output voltage $e_x(\bar{x})$ is directly proportional to the flux.

$$e_x(\bar{x}) = \frac{\mu_0}{i_A} \int_{z=-\infty}^{z=\infty} \int_{y=d}^{d+\delta} \int_{x=-\infty}^{\infty} H_x(x+\bar{x}, y) M_x(x, y) dx\, dy\, dz \quad . \tag{2.42}$$

Similarly, the output voltage arising from the y component magnetization in the recording medium is

$$e_y(\bar{x}) = \frac{\mu_0}{i_A} \int_{z=-\infty}^{z=\infty} \int_{y=d}^{d+\delta} \int_{x=-\infty}^{\infty} H_y(x+\bar{x}, y) M_y(x, y) dx\, dy\, dz \quad . \tag{2.43}$$

Combining Eq. (2.42) and Eq. (2.43) and considering a recording medium with track width w produces an output voltage of

$$\mathbf{e}(\bar{x}) = \frac{\mu_0}{i_A} \int_{z=-w/2}^{z=w/2} \int_{y=d}^{d+\delta} \int_{x=-\infty}^{\infty} \mathbf{H}(x+\bar{x}, y) \cdot \mathbf{M}(x, y) dx\, dy\, dz \quad . \tag{2.44}$$

Thus, performing the integration over the track width the reciprocity theorem gives the output voltage $e(\bar{x})$ for the 2-D model of a double-element MR head shown in Fig. 12. as the correlation integral

$$e(\bar{x}) = C^{MR} \int_{y=d}^{d+\delta} \int_{x=-\infty}^{\infty} \mathbf{H}(x+\bar{x}, y) \cdot \mathbf{M}(x, y) dx dy \quad , \tag{2.45}$$

where $C^{MR} = w\mu_0/i_A$.

Calculation of the integrals (2.42) and (2.43) for longitudinally and perpendicularly recorded media respectively is achieved by using Fourier transform methods, which can be done fully analytically for the magnetization considered in Chapter 5 where the output voltages for shielded double-element MR heads are presented.

2.5. The Landau-Lifshitz-Gilbert Equation

In Chapter 6, the high speed switching behaviour of two different classes of magnetic recording media is investigated. To do this the media are assumed to consist of single domain ferromagnetic grains/particles. The magnetization reversal process of the individual grains by rotation is described by the gyromagnetic precession equation

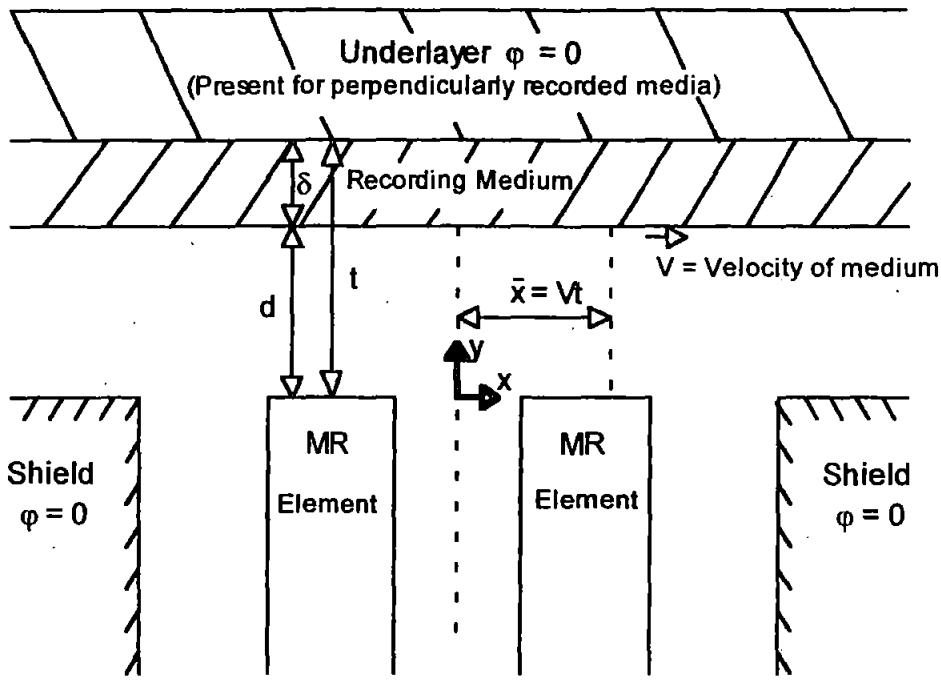

Figure 12. Double-element shielded MR head.

$$\frac{d\mathbf{M}}{dt} = \gamma(\mathbf{M} \times \mathbf{H}_T), \tag{2.46}$$

where $d\mathbf{M}/dt$ is the time rate of change of the magnetization vector $\mathbf{M}$, $\mathbf{H}_T$ is the total effective field acting on $\mathbf{M}$ and γ is the magnetomechanical or gyromagnetic ratio. The term $\gamma(\mathbf{M} \times \mathbf{H})$ is a (torque) vector that drives the precessional motion. However, for the magnetization to switch irreversibly, a damping term is required since the absence of such a term results in the precession continuing for an infinite time. The damped gyromagnetic precession equation

$$\frac{d\mathbf{M}}{dt} = -\gamma(\mathbf{M} \times \mathbf{H}_T) + \frac{\alpha_L}{M}(\mathbf{M} \times (\mathbf{M} \times \mathbf{H}_T)), \tag{2.47}$$

first given in 1937 by two Russian physicists Landau and Lifshitz [21], introduced a damping term from a simple geometric argument [22]. In this equation M is the

magnitude of the magnetization vector and α_L is the phenomenological damping constant. The existence of a damping term was, and remains, a hypothesis, but the presence of such a term is a reasonable theoretical assumption. The Landau-Lifshitz (L-L) equation may be readily visualized as a vector diagram on the surface of a sphere of radius equal to the magnetization, as shown in Fig. 13. Point A represents the tip of the magnetization vector on the surface of the sphere.

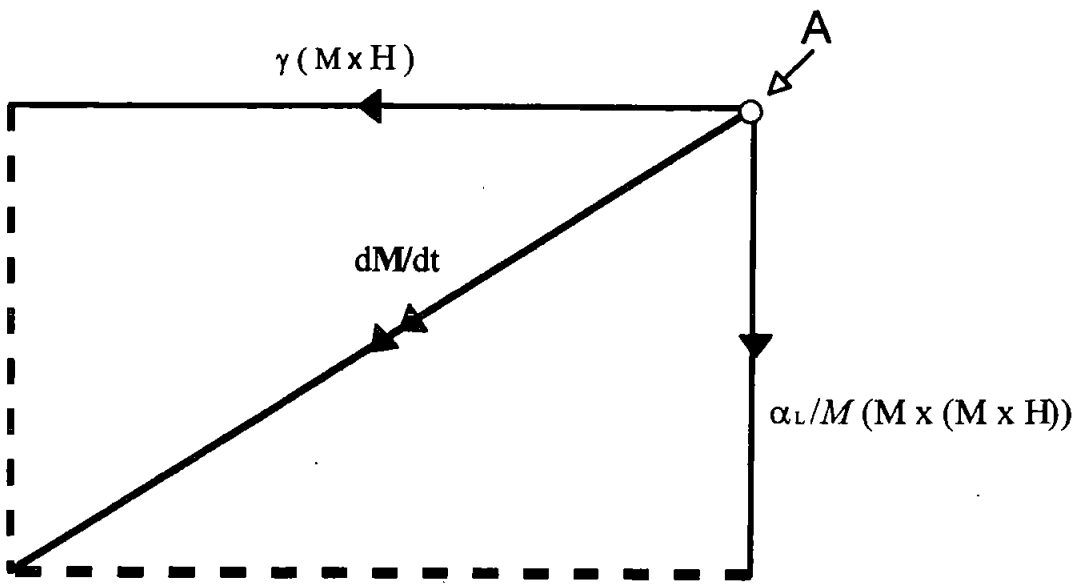

Figure 13. Visualization of the Landau-Lifshitz (L-L) equation.

The time evolution of the magnetization vector, $d\mathbf{M}/dt$, is easily identified as the resultant of the (torque) vector, $\gamma(\mathbf{M} \times \mathbf{H})$, and the (dissipation) vector, α_L/M $(\mathbf{M} \times (\mathbf{M} \times \mathbf{H}_T))$ [22]. The L-L equation, however, can only be considered physically consistent for low values of the constant α_L. This is because it predicts that $d\mathbf{M}/dt$ increases without limit as α_L is increased. It is clear that a system in which switching gets arbitrarily faster as damping increases is not physically plausible [22]. In 1955,

Gilbert [10] proposed an alternative formulation of the L-L equation that does not suffer from this fault. The Landau-Lifshitz-Gilbert (L-L-G) equation

$$\frac{d\mathbf{M}}{dt} = -\gamma(\mathbf{M} \times \mathbf{H}_T) + \frac{\alpha}{M}(\mathbf{M} \times \frac{d\mathbf{M}}{dt}) \tag{2.48}$$

leads to a reversal time that does become infinite for both infinite damping and zero damping, as it should. Again, this may be visualized as a vector diagram on the surface of a sphere with constant M radius (Fig. 14.).

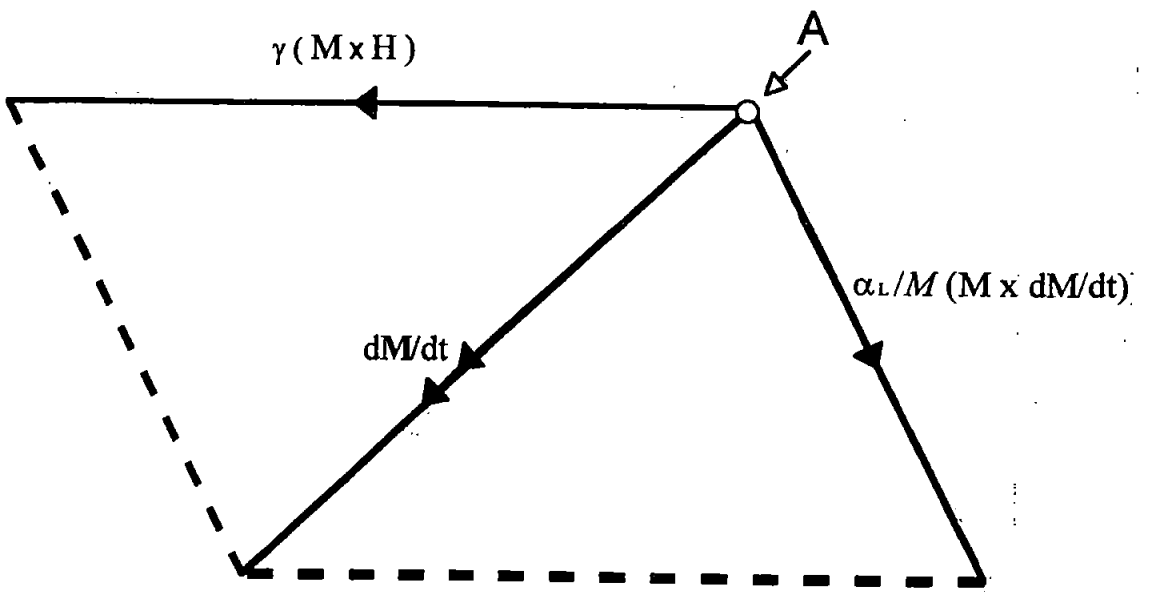

Figure 14. Visualization of the Landau-Lifshitz-Gilbert (L-L-G) equation.

The time rate of change of the magnetization vector is the resultant of the (torque) vector, $\gamma(\mathbf{M} \times \mathbf{H})$, and the Gilbert (dissipation) vector, $\alpha/M\ (\mathbf{M} \times d\mathbf{M}/dt)$. The Gilbert formulation of the L-L equation can be manipulated algebraically into a form that resembles the Landau-Lifshitz form mathematically [22], but they express completely different physics and the Gilbert form will be used exclusively in this thesis.

2.6. Summary

In this chapter:

- Laplace's equation for the magnetic potential is derived starting from the Biot and Savart law of magnetostatics [8].
- The modeling assumptions employed for the Fourier method are presented and discussed.
- An example of the use of Fourier method is given applied to a single pole head with an underlayer.
- Previously published Fourier results are reviewed.
- A derivation of the reciprocity principle is presented.
- The Landau-Lifshitz-Gilbert equation for gyromagnetic switching is presented.

CHAPTER 3

ANALYTIC SOLUTIONS FOR DOUBLE-ELEMENT SHIELDED MAGNETORESISTIVE HEADS

3.1. Introduction

Magnetoresistive (MR) heads are in common use today as reading sensors in the area of high density longitudinal magnetic recording [23], [24]. It has also been suggested that MR heads are likely to have a strong influence on the future development of perpendicular recording [25]. Double-element heads offer advantages over single-element heads in terms of increased robustness against thermal spikes, the reduction of pulse amplitude asymmetry, and alleviating the electrical shorting to disk problem [24]. In this chapter new analytic solutions are presented for idealized mathematical models of double-element shielded magnetoresistive (MR) magnetic recording heads. Section 3.2 describes the geometry and notation of the idealized mathematical model. Two types of heads are modeled, represented by poles of either equal or opposite magnetic potentials, each in the presence of an infinitely permeable underlayer. The model is also used to generate solutions for heads without underlayers by considering special cases of the more general results. In section 3.3, the Fourier method, introduced in Chapter 2, is used to obtain full analytic solutions for the different head configurations, for both longitudinal and perpendicular recording. Expressions for the magnetic potential and magnetic fields are given, and the results of typical magnetic field calculations are presented in section 3.4. In section 3.5, the results are compared with previously published approximate solutions and, in section 3.6, explicit spectral response functions are developed and typical spectral response results are presented and discussed.

3.2. The Mathematical Model

The idealized mathematical model of a symmetrically shielded, double-element MR head is shown in Fig. 15. Two semi-infinite MR elements each of length L are separated by a gap of $G = 2g$ and are perpendicular to and at a distance t from an infinite plane (the underlayer) at zero potential. The right hand pole has potential $+V$, while the left hand pole may be taken as either having a potential of $+V$ or $-V$ to enable the modeling of different head types. The shields are semi-infinite in both the horizontal and vertical directions with element/shield gaps of $H = 2h$. The shields each have potential αV, although the case $\alpha = 0$ is of most practical interest. The shields, MR sensors and the underlayer are all assumed to have infinite permeability and the recorded medium has unit permeability.

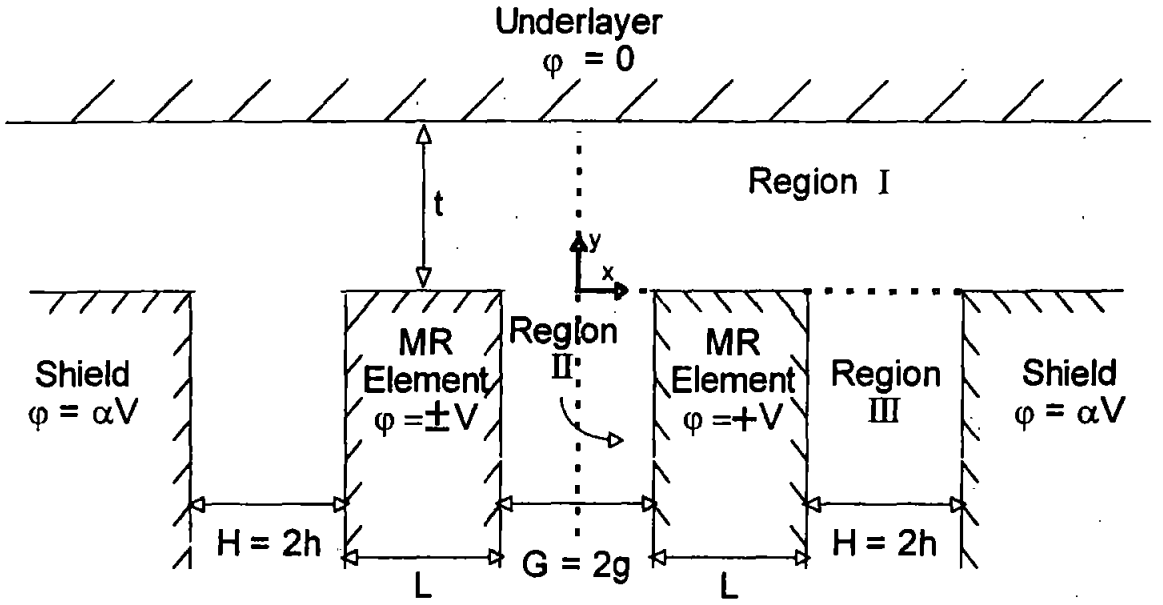

Figure 15. Double-element shielded MR head :
dual stripe head, φ = +V on the left-hand element;
differential head, φ = -V on the left-hand element.

Various configurations of the two elements are possible, depending on the magnetization direction in each element due to the bias field, the directions of the sens-

ing currents and whether the output voltages are added or subtracted [26], [27], [28]. There are however only two basic output pulse shapes, which, when the head response is linear, may be determined by assigning magnetic potentials to the two MR elements and applying the reciprocity principle. The appropriate 'reciprocity potentials' are either equal potentials ($+V$) on each pole or opposite potentials ($-V$ on the left hand pole, $+V$ on the right hand pole). The problem is then to solve Laplace's equation for the magnetic scalar potential φ in the region below the underlayer and exterior to the elements. Following [29], the name 'dual stripe' refers to a head with MR elements at the same potential, while 'differential' is used when the elements have opposite potential. The superscript '++' denotes results for the dual stripe head, while '−+' refers to the differential head.

3.3. Magnetic Field

3.3.1. Dual Stripe MR Head with an Underlayer

The idealized mathematical model of a dual stripe head with a keeper layer present is represented in Fig. 15. by assigning equal potentials ($\varphi = +V$) to both poles. By symmetry, only $x \geq 0$ needs to be considered, which is subdivided into regions I, II and III as shown. The general solution of Laplace's equation in region I which is symmetric in x and zero at $y = t$ is

$$\varphi_I^{++}(x,y) = \int_0^\infty D(k)\cos[kx]\sinh[k(t-y)]dk. \tag{3.1}$$

In region II the solution which is symmetric in x, takes the value $\varphi_{II}^{++} = V$ at $x = g$ and has the correct behavior as $y \to -\infty$ is

$$\varphi_{II}^{++}(x,y) = V + \sum_{n=1}^{\infty} A_n \cos[(n-1/2)\pi x/g]e^{(n-1/2)\pi y/g}, \tag{3.2}$$

while in region III the appropriate solution is

$$\begin{aligned}\varphi_{III}^{++}(x,y) &= V[1+(\alpha-1)(x-g-L)/H] + \sum_{n=1}^{\infty} B_n \sin[n\pi(x-g-L-h)/h]e^{n\pi y/h} \\ &\quad + \sum_{n=1}^{\infty} C_n \cos[(n-1/2)\pi(x-g-L-h)/h]e^{(n-1/2)\pi y/h}.\end{aligned} \tag{3.3}$$

Matching the potential at $y = 0$

$$\varphi_I^{++}(x,y) = \begin{cases} \varphi_{II}^{++}(x,0) & 0 \le x \le g \\ V & g \le x \le g+L \\ \varphi_{III}^{++}(x,0) & g+L \le x \le g+L+H \\ \alpha V & g+L+H \le x < \infty \end{cases} \tag{3.4}$$

and taking a Fourier cosine transform

$$F_c[f(x)] = \int_0^\infty \cos[\omega x] f(x) dx \tag{3.5}$$

gives $D(k)$ in terms of the Fourier coefficients A_n, B_n and C_n and hence

$$\begin{aligned} \varphi_I^{++}(x,y) &= \frac{2Vh(1-\alpha)}{\pi} J_0^{++} + \frac{\alpha V(t-y)}{t} + \sum_{n=1}^{\infty} A_n 2(n-1/2)g(-1)^n I_n^{++} \\ &\quad + \sum_{n=1}^{\infty} B_n 4nh(-1)^{n+1} J_n^{++} + \sum_{n=1}^{\infty} C_n 4(n-1/2)h(-1)^n K_n^{++}. \end{aligned} \tag{3.6}$$

I_n^{++}, J_n^{++} and K_n^{++} are integrals which are functions of x and y and are given in Appendix B.1.

Matching the potential gradient $\partial\varphi/\partial y$ at $y = 0$ in $0 \le x \le g$ and $g+L \le x \le g+L+H$, and using the orthogonality properties of the sine and cosine functions in (3.2) and (3.3) in their appropriate intervals, results in three coupled infinite sets of linear simultaneous equations for the coefficients A_n, B_n and C_n.

$$\begin{aligned} &A_m + \sum_{n=1}^{\infty} A_n 4(n-1/2)g^2(-1)^{m+n} I_{mn}^{++} + \sum_{n=1}^{\infty} B_n 8ngh(-1)^{m+n+1} J_{mn}^{++} \\ &+ \sum_{n=1}^{\infty} C_n 8(n-1/2)gh(-1)^{m+n} K_{mn}^{++} \\ &= \frac{4V(\alpha-1)gh}{\pi}(-1)^m J_{m0}^{++} + \frac{2V\alpha g}{t[(m-1/2)\pi]^2}(-1)^m \end{aligned} \tag{3.7}$$

$$\begin{aligned} &\sum_{n=1}^{\infty} A_n 4(n-1/2)gh(-1)^{m+n+1} J_{nm}^{++} + B_m + \sum_{n=1}^{\infty} B_n 8nh^2(-1)^{m+n} L_{mn}^{++} \\ &+ \sum_{n=1}^{\infty} C_n 8(n-1/2)h^2(-1)^{m+n+1} M_{mn}^{++} \\ &= \frac{4V(\alpha-1)h^2}{\pi}(-1)^{m+1} L_{m0}^{++} \end{aligned} \tag{3.8}$$

$$\sum_{n=1}^{\infty} A_n 4(n-1/2)gh(-1)^{m+n}K_{nm}^{++} + \sum_{n=1}^{\infty} B_n 8nh^2(-1)^{m+n+1}M_{nm}^{++}$$
$$+C_m + \sum_{n=1}^{\infty} C_n 8(n-1/2)h^2(-1)^{m+n}N_{mn}^{++}$$
$$= \frac{4V(\alpha-1)h^2}{\pi}(-1)^m M_{0m}^{++} + \frac{2V\alpha h}{t[(m-1/2)\pi]^2}(-1)^m, \qquad (3.9)$$

for $m = 1, 2, 3, \ldots$ in each case where the integrals I_{mn}^{++}, J_{mn}^{++}, K_{mn}^{++}, L_{mn}^{++}, M_{mn}^{++} and N_{mn}^{++} are given in Appendix B.2. Normalized coefficients A_n/V, B_n/V and C_n/V depend on the ratios g/L, h/L and t/L.

The recording medium lies in region I and here the magnetic field components are

$$H_x^{++}(x,y) = -\frac{\partial \varphi_I^{++}}{\partial x}(x,y) = \frac{2Vh(1-\alpha)}{\pi}M_0^{++} + \sum_{n=1}^{\infty} A_n 2(n-1/2)g(-1)^n L_n^{++}$$
$$+ \sum_{n=1}^{\infty} B_n 4nh(-1)^{n+1}M_n^{++} + \sum_{n=1}^{\infty} C_n 4(n-1/2)h(-1)^n N_n^{++} \qquad (3.10)$$

and

$$H_y^{++}(x,y) = -\frac{\partial \varphi_I^{++}}{\partial y}(x,y) = \frac{2Vh(1-\alpha)}{\pi}Q_0^{++} + \frac{\alpha V}{t} + \sum_{n=1}^{\infty} A_n 2(n-1/2)g(-1)^n P_n^{++}$$
$$+ \sum_{n=1}^{\infty} B_n 4nh(-1)^{n+1}Q_n^{++} + \sum_{n=1}^{\infty} C_n 4(n-1/2)h(-1)^n R_n^{++}, \qquad (3.11)$$

where the integrals L_n^{++}, M_n^{++}, N_n^{++}, P_n^{++}, Q_n^{++} and R_n^{++} are given in Appendix B.3.

The result given in [30] for a single element symmetrically placed between shields is consistent with the above more general result in regions I and III if the inter-element separation distance G, is set to zero.

3.3.2. Dual Stripe MR Head without an Underlayer

The solution for the head shown in Fig. 15 with equal potentials but with no underlayer follows immediately from the previous solution as the special case of $t \to \infty$. In (3.1), $\sinh[k(t-y)]$ is replaced by e^{-ky}which leads to the representation (3.6) for $\varphi_I^{++}(x,y)$ with $\sinh[k(t-y)]/\sinh[kt]$ in each of the integrals I_n^{++},

J_n^{++} and K_n^{++} becoming e^{-ky}. In the linear equations (3.7) -(3.9) the $\coth[kt]$ term in I_{mn}^{++}, J_{mn}^{++}, K_{mn}^{++}, L_{mn}^{++}, M_{mn}^{++} and N_{mn}^{++} becomes unity. For the horizontal field $\sinh[k(t-y)]/\sinh[kt]$ becomes e^{-ky} in each of L_n^{++}, M_n^{++} and N_n^{++} and for the vertical field $\cosh[k(t-y)]/\sinh[kt]$ becomes e^{-ky} in each of P_n^{++}, Q_n^{++} and R_n^{++}.

The result in [31] for a single shielded element is the particular case of this solution when the inter-element distance, G, is zero and $\alpha = 0$.

3.3.3. Differential MR Head with an Underlayer

This head geometry is modelled in Fig. 15 by assigning a negative potential ($\varphi = -V$) to the left-hand MR element, that is, the MR element potentials are equal in magnitude but opposite in sign. In this case

$$\varphi_I^{-+}(x,y) = \int_0^\infty D(k)\sin[kx]\sinh[k(t-y)]dk, \tag{3.12}$$

$$\varphi_{II}^{-+}(x,y) = \frac{Vx}{g} + \sum_{n=1}^{\infty} A_n \sin(n\pi x/g)e^{n\pi y/g}, \tag{3.13}$$

and $\varphi_{III}^{-+}(x,y)$ is as given in (3.3). Following the same method as described in section 3.3.1 leads to

$$\begin{aligned}\varphi_I^{-+}(x,y) \;=\; & \frac{2Vh}{\pi}(\alpha-1)J_0^{-+} + \frac{2Vg}{\pi}I_0^{-+} + \sum_{n=1}^{\infty} A_n 2ng(-1)^n I_n^{-+} \\ & + \sum_{n=1}^{\infty} B_n 4nh(-1)^n J_n^{-+} + \sum_{n=1}^{\infty} C_n 4(n-1/2)h(-1)^n K_n^{-+},\end{aligned} \tag{3.14}$$

with I_n^{-+}, J_n^{-+} and K_n^{-+} given in Appendix B.4.

The coefficients A_n, B_n and C_n are obtained by solving

$$\begin{aligned}& A_m + \sum_{n=1}^{\infty} A_n 4ng^2(-1)^{m+n} I_{mn}^{-+} + \sum_{n=1}^{\infty} B_n 8ngh(-1)^{m+n} J_{mn}^{-+} \\ & + \sum_{n=1}^{\infty} C_n 8(n-1/2)gh(-1)^{m+n} K_{mn}^{-+} \\ & = \frac{4V(1-\alpha)gh}{\pi}(-1)^m J_{m0}^{-+} + \frac{4Vg^2}{\pi}(-1)^{m+1} I_{m0}^{-+}\end{aligned} \tag{3.15}$$

$$\sum_{n=1}^{\infty} A_n 4ngh(-1)^{m+n} J_{nm}^{-+} + B_m + \sum_{n=1}^{\infty} B_n 8nh^2(-1)^{m+n} L_{mn}^{-+}$$
$$+ \sum_{n=1}^{\infty} C_n 8(n-1/2)h^2(-1)^{m+n} M_{mn}^{-+}$$
$$= \frac{4V(1-\alpha)h^2}{\pi}(-1)^m L_{m0}^{-+} + \frac{4Vgh}{\pi}(-1)^{m+1} J_{0m}^{-+} \tag{3.16}$$

$$\sum_{n=1}^{\infty} A_n 4ngh(-1)^{m+n} K_{nm}^{-+} + \sum_{n=1}^{\infty} B_n 8nh^2(-1)^{m+n} M_{nm}^{-+}$$
$$+C_m + \sum_{n=1}^{\infty} C_n 8(n-1/2)h^2(-1)^{m+n} N_{mn}^{-+}$$
$$= \frac{4V(1-\alpha)h^2}{\pi}(-1)^m M_{0m}^{-+} + \frac{4Vgh}{\pi}(-1)^{m+1} K_{0m}^{-+}, \tag{3.17}$$

for $m = 1, 2, 3, \ldots$ in each case where the integrals are given in Appendix B.5. The magnetic field components in region I are

$$H_x^{-+}(x,y) = -\frac{2Vh}{\pi}(\alpha-1)M_0^{-+} - \frac{2Vg}{\pi}L_0^{-+} - \sum_{n=1}^{\infty} A_n 2ng(-1)^n L_n^{-+}$$
$$- \sum_{n=1}^{\infty} B_n 4nh(-1)^n M_n^{-+} - \sum_{n=1}^{\infty} C_n 4(n-1/2)h(-1)^n N_n^{-+} \tag{3.18}$$

and

$$H_y^{-+}(x,y) = \frac{2Vh}{\pi}(\alpha-1)Q_0^{-+} + \frac{2Vg}{\pi}P_0^{-+} + \sum_{n=1}^{\infty} A_n 2ng(-1)^n P_n^{-+}$$
$$+ \sum_{n=1}^{\infty} B_n 4nh(-1)^n Q_n^{-+} + \sum_{n=1}^{\infty} C_n 4(n-1/2)h(-1)^n R_n^{-+}, \tag{3.19}$$

where the integrals are given in Appendix B.6. Here, if $L \to \infty$, the geometry becomes that of a ring head with an underlayer and the solution in regions I and II reduces to that given in [18].

3.3.4. Differential MR Head without an Underlayer

Again, this solution is a special case of the previous one with $t \to \infty$. In (3.12) $\sinh[k(t-y)]$ is replaced by e^{-ky} giving e^{-ky} in each of I_n^{-+}, J_n^{-+} and K_n^{-+} in place of $\sinh[k(t-y)]/\sinh[kt]$ for the representation (14). In the equations (3.15) – (3.17) the $\coth[kt]$ term in each of I_{mn}^{-+}, J_{mn}^{-+}, K_{mn}^{-+}, L_{mn}^{-+}, M_{mn}^{-+} and N_{mn}^{-+} becomes unity. For the integrals L_n^{-+}, M_n^{-+} and N_n^{-+} in the horizontal field, $\sinh[k(t-y)]/\sinh[kt]$ becomes e^{-ky} as does $\cosh[k(t-y)]/\cosh[kt]$ in the integrals P_n^{-+}, Q_n^{-+} and R_n^{-+} for the vertical field. Here, if $L \to \infty$, the solution for a ring head without an underlayer [13] is obtained in regions I and II.

3.4. Results

3.4.1. Magnetic Field Calculations

The normalized Fourier coefficients A_n/V, B_n/V and C_n/V for the dual stripe head and differential head, in each case with an underlayer present, satisfy the three coupled infinite systems of linear algebraic equations (3.7) – (3.9), and (3.15) – (3.17), respectively. For each head configuration the three coupled infinite systems may be solved approximately by restricting each system to some finite size N, the normalized coefficients satisfying the resulting $3N \times 3N$ square system. The integrals appearing within the coupled systems and the other integrals appearing in Appendix B have been evaluated using numerical integration [32], since it has not yet proved possible to find closed form analytic expressions for them. This places a restriction on the size of N it has been possible to consider. All coefficients reproduced in this thesis were computed using coupled systems truncated to a size of 60×60 ($N = 20$).

Table 1 shows the first six normalized coefficients A_n/V, B_n/V and C_n/V for the dual stripe head with an underlayer present with $\alpha = 0$, $g/L = t/L = 1$ and a range of gap ratios h/L.

As the pole to pole gap width, G, of the dual stripe head decreases the geometry approaches that of a shielded single pole head with an underlayer [30], providing

h/L	0.5	1.0	1.5	2.0	2.5
A_1/V	-0.4116	-0.4111	-0.4109	-0.4108	-0.4108
A_2/V	0.0572	0.0571	0.0570	0.0570	0.0570
A_3/V	-0.0232	-0.0231	-0.0231	-0.0231	-0.0231
A_4/V	0.0128	0.0128	0.0128	0.0128	0.0128
A_5/V	-0.0083	-0.0083	-0.0083	-0.0083	-0.0083
A_6/V	0.0058	0.0058	0.0058	0.0058	0.0058
B_1/V	0.0504	0.0670	0.0866	0.1058	0.1233
B_2/V	-0.0166	-0.0209	-0.0261	-0.0315	-0.0369
B_3/V	0.0085	0.0106	0.0130	0.0155	0.0181
B_4/V	-0.0053	-0.0065	-0.0079	-0.0094	-0.0109
B_5/V	0.0038	0.0045	0.0054	0.0064	0.0074
B_6/V	-0.0027	-0.0033	-0.0040	-0.0047	-0.0054
C_1/V	-0.1138	-0.2059	-0.2756	-0.3277	-0.3674
C_2/V	0.0156	0.0287	0.0401	0.0506	0.0603
C_3/V	-0.0063	-0.0116	-0.0162	-0.0203	-0.0242
C_4/V	0.0035	0.0064	0.0089	0.0112	0.0133
C_5/V	-0.0023	-0.0042	-0.0058	-0.0072	-0.0085
C_6/V	0.0016	0.0029	0.0041	0.0051	0.0060

Table 1. Coefficients A_n/V, B_n/V and C_n/V for a dual stripe head with an underlayer with $\alpha = 0$, $g : L : t = 1 : 1 : 1$ and computed with $N = 20$.

a useful measure of the accuracy of the coefficients given in Table 1. Comparison of the coefficients obtained using the dual stripe head with $g/L = 0$ with those obtained for the shielded pole head in [30] confirms the expected correspondence, accurate to at least three decimal places. Consequently this is the expected level of accuracy for the coefficients given in Table 1 and the other tables in this paper.

Table 2 shows the first six normalized coefficients for the differential head with an underlayer present with $\alpha = 0$, $g/L = t/L = 1$ and a range of gap ratios h/L.

As the pole width, L, of the differential head with an underlayer increases relative to the head to medium separation, t, the geometry approaches that of the idealized model of a ring head with an underlayer [18]. For ratios of $L/t > 5$ agreement with the coefficients for a ring head with an underlayer [18] is to about three decimal

h/L	0.5	1.0	1.5	2.0	2.5
A_1/V	-0.1330	-0.1328	-0.1327	-0.1326	-0.1326
A_2/V	0.0414	0.0414	0.0414	0.0414	0.0414
A_3/V	-0.0210	-0.0210	-0.0210	-0.0210	-0.0210
A_4/V	0.0129	0.0129	0.0129	0.0129	0.0129
A_5/V	-0.0089	-0.0089	-0.0089	-0.0089	-0.0089
A_6/V	0.0065	0.0065	0.0065	0.0065	0.0065
B_1/V	0.0502	0.0667	0.0863	0.1056	0.1231
B_2/V	-0.0165	-0.0208	-0.0260	-0.0315	-0.0369
B_3/V	0.0085	0.0105	0.0130	0.0155	0.0181
B_4/V	-0.0053	-0.0065	-0.0079	-0.0095	-0.0110
B_5/V	0.0037	0.0045	0.0054	0.0064	0.0074
B_6/V	-0.0027	-0.0033	-0.0040	-0.0047	-0.0054
C_1/V	-0.1136	-0.2059	-0.2756	-0.3277	-0.3674
C_2/V	0.0155	0.0287	0.0402	0.0507	0.0604
C_3/V	-0.0063	-0.0116	-0.0162	-0.0204	-0.0243
C_4/V	0.0035	0.0064	0.0090	0.0113	0.0134
C_5/V	-0.0023	-0.0042	-0.0058	-0.0072	-0.0086
C_6/V	0.0016	0.0029	0.0041	0.0051	0.0060

Table 2. Coefficients A_n/V, B_n/V and C_n/V for a differential head with an underlayer with $\alpha = 0$, $g : L : t = 1 : 1 : 1$ and computed with $N = 20$.

places. The normalized coefficients for the dual stripe head and differential head without an underlayer present are shown in Tables 3 and 4, respectively.

Representative horizontal and vertical field components for the dual stripe head and the differential head, both with an underlayer present, are shown in Figs. 16-19, in each case all distances have been normalized by half of the shield to shield gap, $g + L + H$. Typical head dimension ratios of $g/L = t/L = 1$ and $h/L = 2$ have been chosen in line with experimental head dimensions given in [29] and [33]. Figs. 20-23 show the corresponding field components for the dual stripe head and differential head without an underlayer present. All results were obtained by truncating the appropriate infinite series to 10 terms only.

h/L	0.5	1.0	1.5	2.0	2.5
A_1/V	-0.1259	-0.1074	-0.0949	-0.0856	-0.0784
A_2/V	0.0187	0.0157	0.0138	0.0124	0.0114
A_3/V	-0.0076	-0.0064	-0.0056	-0.0051	-0.0047
A_4/V	0.0042	0.0035	0.0031	0.0028	0.0026
A_5/V	-0.0027	-0.0023	-0.0020	-0.0018	-0.0017
A_6/V	0.0019	0.0016	0.0014	0.0013	0.0012
B_1/V	0.0444	0.0461	0.0474	0.0486	0.0495
B_2/V	-0.0148	-0.0152	-0.0154	-0.0157	-0.0160
B_3/V	0.0077	0.0079	0.0080	0.0081	0.0082
B_4/V	-0.0048	-0.0049	-0.0050	-0.0051	-0.0051
B_5/V	0.0033	0.0034	0.0035	0.0035	0.0036
B_6/V	-0.0025	-0.0025	-0.0026	-0.0026	-0.0026
C_1/V	-0.0198	-0.0312	-0.0391	-0.0450	-0.0497
C_2/V	0.0029	0.0045	0.0056	0.0064	0.0072
C_3/V	-0.0012	-0.0018	-0.0023	-0.0026	-0.0029
C_4/V	0.0006	0.0010	0.0013	0.0015	0.0016
C_5/V	-0.0004	-0.0006	-0.0008	-0.0009	-0.0010
C_6/V	0.0003	0.0005	0.0006	0.0007	0.0007

Table 3. Coefficients A_n/V, B_n/V and C_n/V for a dual stripe head without an underlayer with $\alpha = 0$, $g : L = 1 : 1$ and computed with $N = 20$.

h/L	0.5	1.0	1.5	2.0	2.5
A_1/V	-0.0990	-0.0962	-0.0946	-0.0936	-0.0928
A_2/V	0.0327	0.0319	0.0314	0.0312	0.0310
A_3/V	-0.0169	-0.0165	-0.0163	-0.0162	-0.0161
A_4/V	0.0105	0.0103	0.0102	0.0101	0.0101
A_5/V	-0.0073	-0.0071	-0.0070	-0.0070	-0.0070
A_6/V	0.0054	0.0053	0.0052	0.0052	0.0052
B_1/V	0.0463	0.0518	0.0573	0.0623	0.0669
B_2/V	-0.0154	-0.0171	-0.0188	-0.0206	-0.0223
B_3/V	0.0080	0.0088	0.0097	0.0105	0.0114
B_4/V	-0.0050	-0.0055	-0.0060	-0.0065	-0.0070
B_5/V	0.0035	0.0038	0.0041	0.0045	0.0048
B_6/V	-0.0026	-0.0028	-0.0030	-0.0033	-0.0036
C_1/V	-0.0497	-0.0818	-0.1051	-0.1230	-0.1375
C_2/V	0.0071	0.0123	0.0166	0.0204	0.0237
C_3/V	-0.0029	-0.0050	-0.0068	-0.0085	-0.0099
C_4/V	0.0016	0.0028	0.0038	0.0047	0.0055
C_5/V	-0.0010	-0.0018	-0.0024	-0.0030	-0.0036
C_6/V	0.0007	0.0013	0.0017	0.0021	0.0025

Table 4. Coefficients A_n/V, B_n/V and C_n/V for a differential head without an underlayer with $\alpha = 0$, $g : L = 1 : 1$ and computed with $N = 20$.

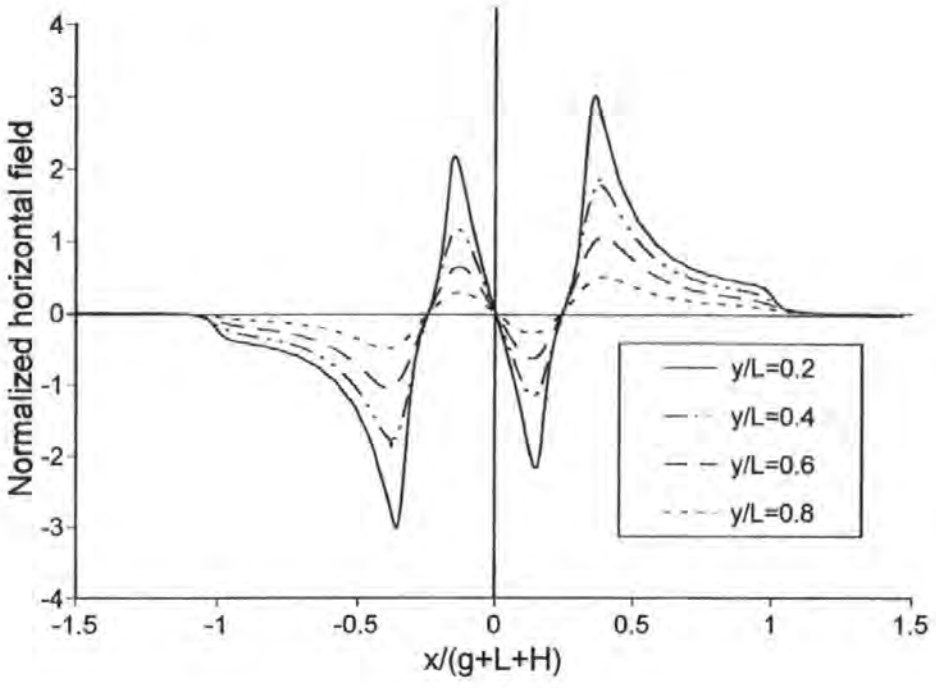

Figure 16. Horizontal field component for a dual stripe head with an underlayer, g/L=t/L=1.0, h/L=2.0

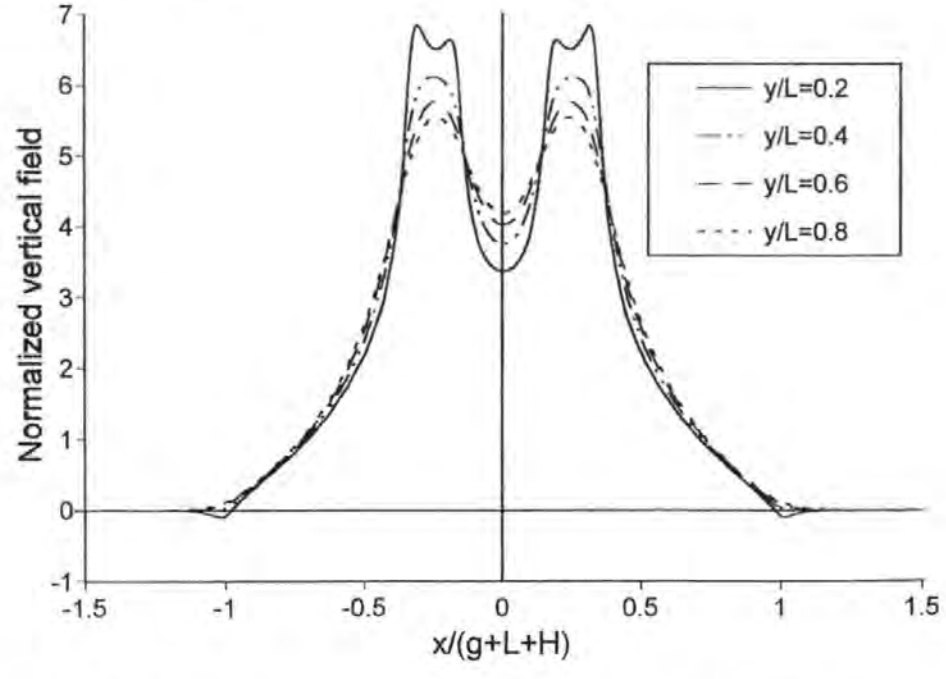

Figure 17. Vertical field component for a dual stripe head with an underlayer, g/L=t/L=1.0, h/L=2.0

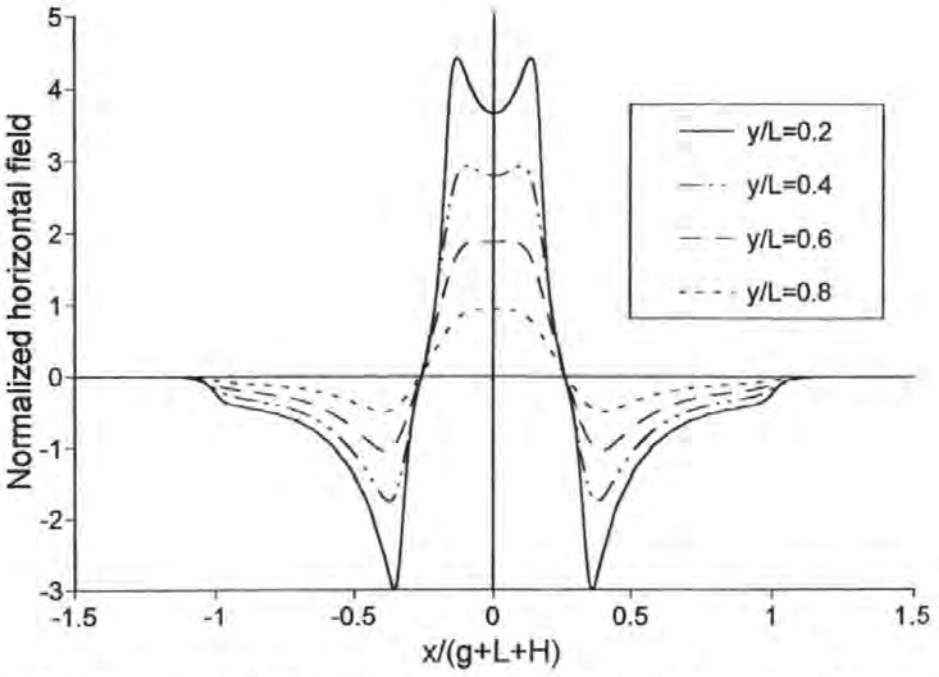

Figure 18. Horizontal field component for a differential head with an underlayer, g/L=t/L=1.0, h/L=2.0

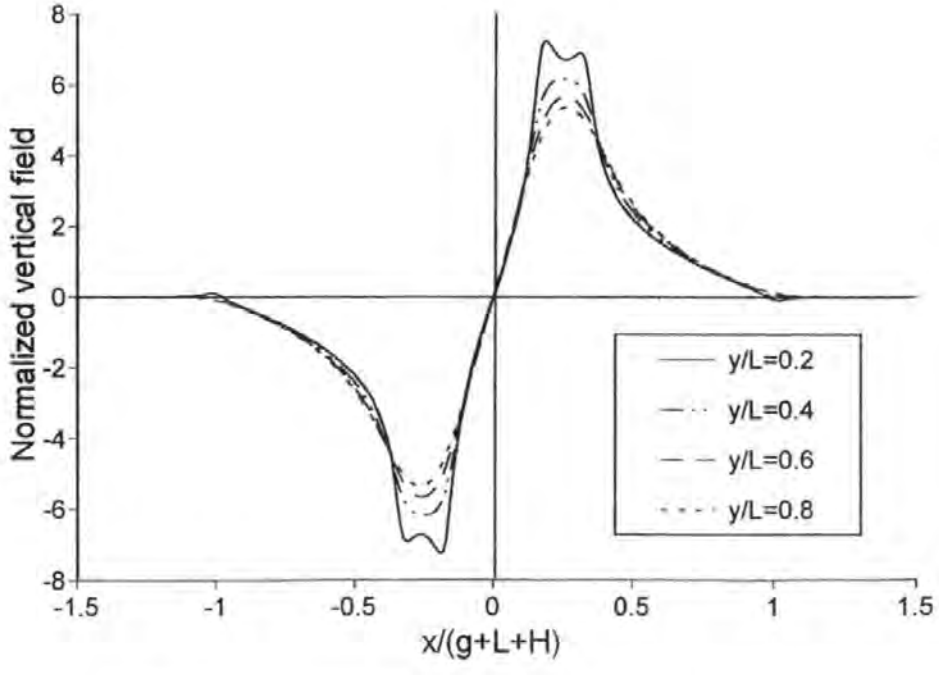

Figure 19. Vertical field component for a differential head with an underlayer, g/L=t/L=1.0, h/L=2.0

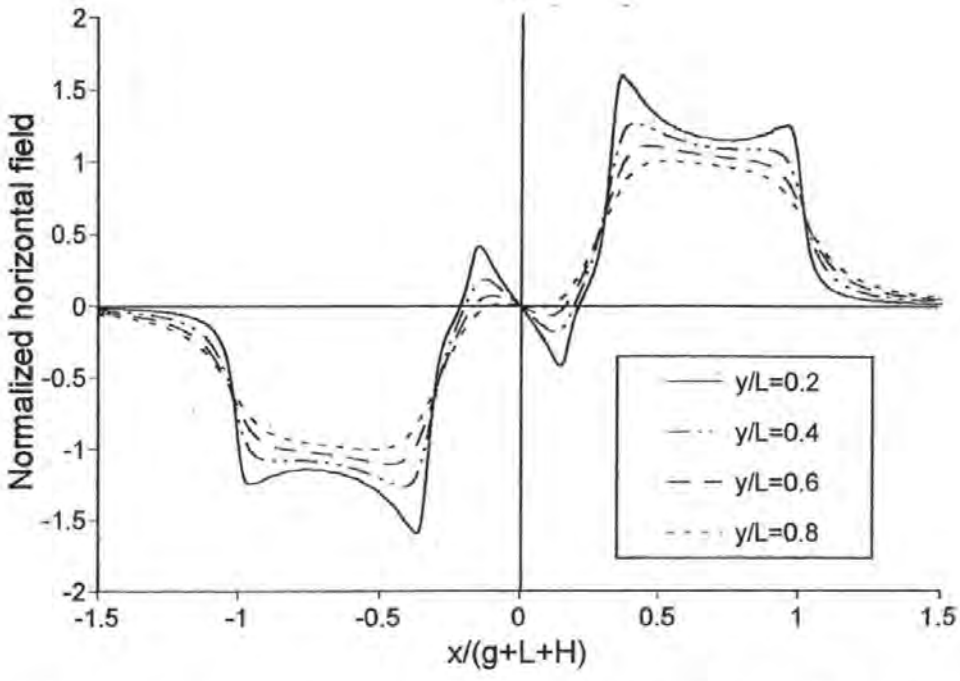

Figure 20. Horizontal field component for a dual stripe head without an underlayer, g/L=1.0, h/L=2.0

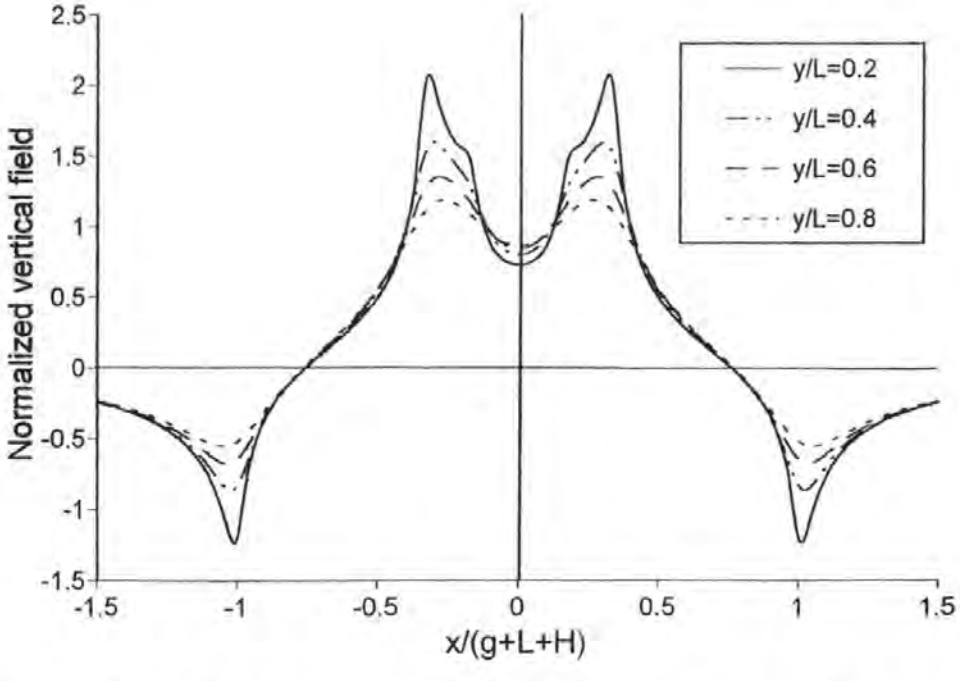

Figure 21. Vertical field component for a dual stripe head without an underlayer, g/L=1.0, h/L=2.0

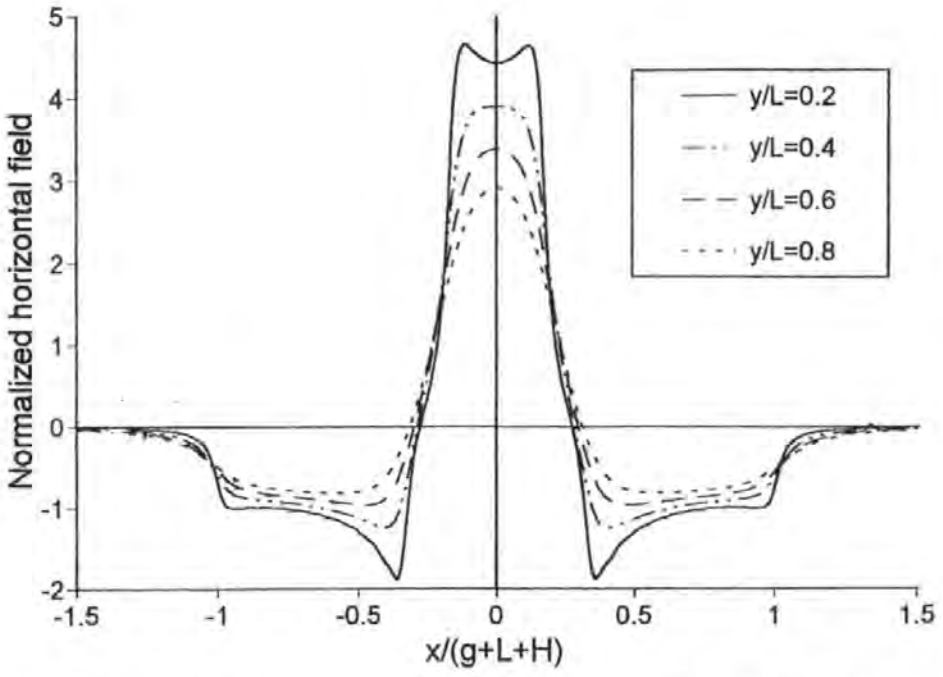

Figure 22. Horizontal field component for a differential head without an underlayer, g/L=1.0, h/L=2.0

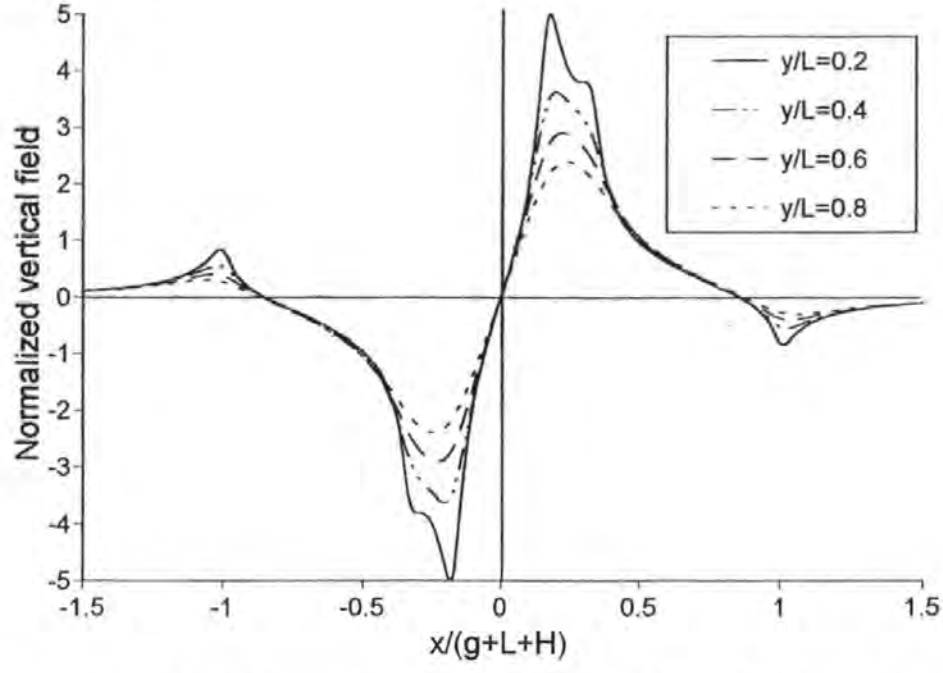

Figure 23. Vertical field component for a differential head without an underlayer, g/L=1.0, h/L=2.0

Figs. 16-19 clearly show how the presence of an underlayer gives an enhanced peak value for the vertical component of the magnetic field in comparison with that of the horizontal component. Moreover, the vertical field maintains a high value as the distance from the head increases while the horizontal field, as expected, decays rapidly to zero. With no underlayer (Figs. 20-23) the peak horizontal and vertical fields are of comparable magnitude and the decay in each component with distance from the head is similar. The shield, the edge of which is at $x/(g+L+H)=1$, is seen here to be significantly less effective in reducing the fields to zero in the gap region than when an underlayer is present.

3.5. Comparison with Approximate Results

In section 3.3 a full explicit solution for the magnetic field of double-element shielded heads is given. Although only a small number of terms is required to give excellent accuracy, it is necessary to first compute the harmonic coefficients A_n, B_n and C_n. For many practical purposes an approximate solution is acceptable, as exemplified by the Karlqvist approximations to the field components of a ring head, which, despite their known limitations, have proved popular for over 35 years. Here, previously published approximations which are applicable to double-element heads are compared with the new exact solutions.

Accurate approximations to the potential $\varphi(x,0)$ in the head face plane for heads with underlayers have been given in [34]. For the differential head in the region $0 \le x < g$, an approximation which satisfies $\varphi_1^A(0,0)=0$ and $\varphi_1^A(g,0)=V$ is

$$\varphi_1^A(x,0)=\frac{Vx}{g}\Big[1-\frac{1}{2t}\sqrt{\frac{g^2-x^2}{6}}\Big(1-e^{-2t\sqrt{6/(g^2-x^2)}}\Big)\Big]. \tag{3.20}$$

In the element/shield gap $g+L<x<g+L+H$,

$$\varphi_2^A(x,0)=\varphi_1^A((g+L+H-x)g/H,0) \tag{3.21}$$

satisfies $\varphi_2^A(g+L,0)=V$ and $\varphi_2^A(g+L+H,0)=0$. For the dual stripe head

$$\varphi_3^A(x,0)=\varphi_1^A((x+g)/2,0)+\varphi_1^A((g-x)/2,0) \tag{3.22}$$

satisfies $\varphi_3^A(\pm g, 0) = V$ as required.

Using these approximations in

$$\varphi(x,y) = \frac{1}{2t}\sin\left[\frac{\pi y}{t}\right]\int_{-\infty}^{\infty}\frac{\varphi(u,0)}{\cosh\left[(u-x)\pi/t\right]-\cos\left[\pi y/t\right]}du\ ,0<y<t \qquad (3.23)$$

and differentiating prior to the integration gives approximate field components in region I where the recording medium lies. Figs. 24 and 25 give comparisons of the exact and approximate vertical fields for dual stripe and differential heads respectively, where the approximations are generally seen to be very accurate. The only area where there is a significant error in the approximation is between the MR elements for a dual stripe head. Here the actual vertical field reduction is greater than that given by the approximation. This gives confidence in the correctness of the exact field computations and indicates that the approximate solutions may be sufficient for many practical purposes.

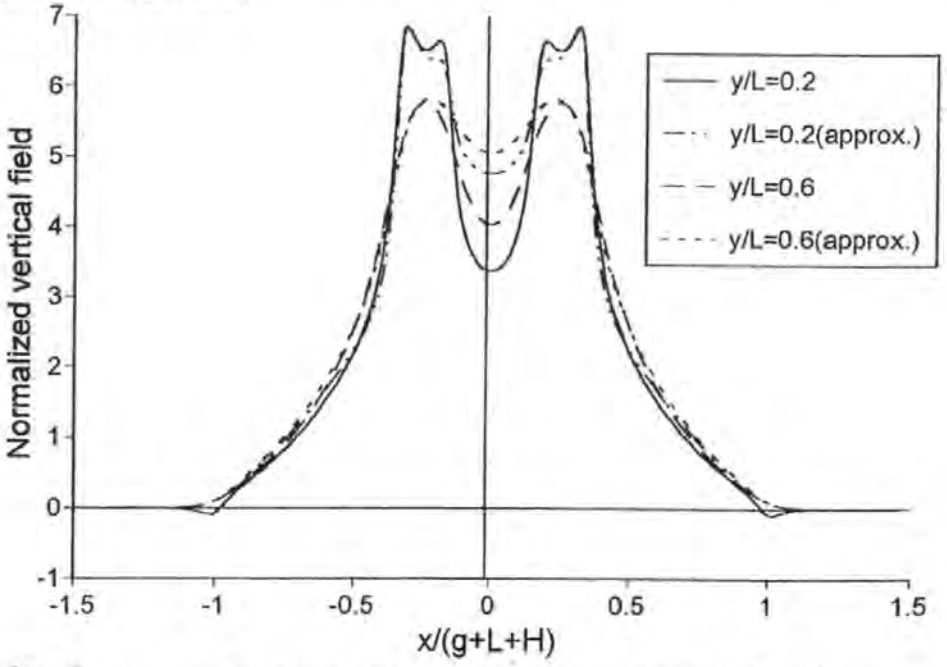

Figure 24. Comparison of the exact and approximate vertical field component for a dual stripe head with an underlayer, g/L=t/L=1.0, h/L=2.0

In [29] approximations are developed specifically for the horizontal fields of dual stripe and differential MR heads when no underlayer is present. They are

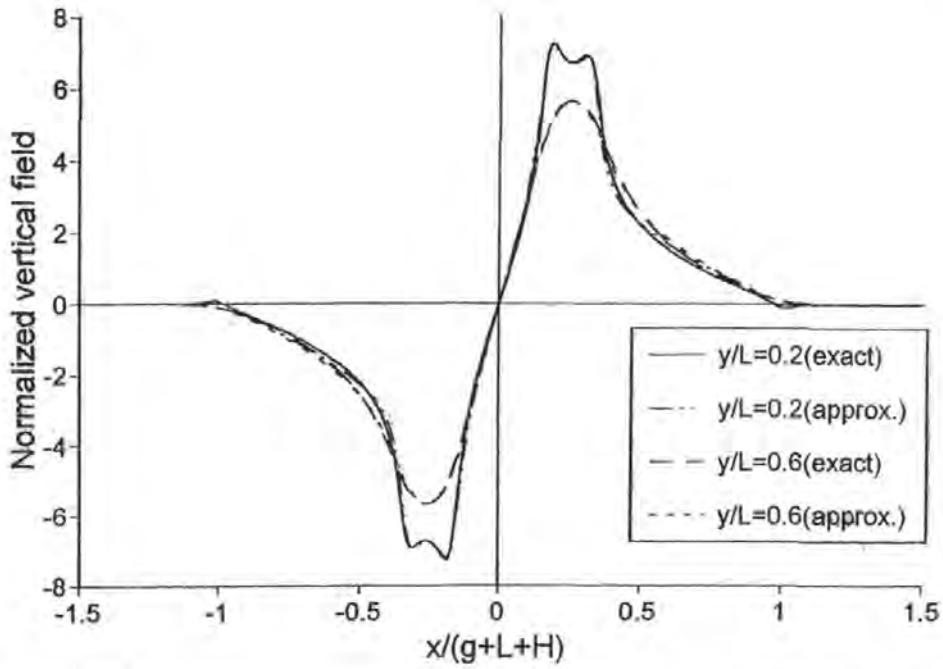

Figure 25. Comparison of the exact and approximate vertical field component for a differential head with an underlayer, g/L=t/L=1.0, h/L=2.0

based upon an equally weighted sum of the field assuming a linear variation in potential across any gaps (Karlqvist-style)[35] and the field of the equivalent 'thin' head (Westmijze-style)[36].

For the dual stripe head with no underlayer the approximate horizontal component of the magnetic field in the head face plane ($y = 0$) in the element/element and element/shield gaps is, for $x \geq 0$,

$$H_x^A(x,0) = \begin{cases} -\frac{1}{2}\frac{c_3 x}{\sqrt{(1-x^2)(x^2-b^2)(x^2-a^2)}} & 0 \leq x < b \\ \frac{1}{2}\left[\frac{1}{1-a} + \frac{c_3 x}{\sqrt{(1-x^2)(x^2-b^2)(x^2-a^2)}}\right] & a < x < 1 \end{cases} \tag{3.24}$$

where

$$c_3^{-1} = \int_a^1 \frac{x}{\sqrt{(1-x^2)(x^2-b^2)(x^2-a^2)}} dx. \tag{3.25}$$

Here, following the notation of [29], normalized coordinates have been taken, the correspondence with Fig. 15 being $1 \equiv g + L + H$ (the shield edge), $a \equiv g + L$ (the

outer edge of the MR element) and $b \equiv g$ (the inner edge of the MR element). The constant c_3^{-1} may be expressed as the complete elliptic integral of the first kind

$$c_3^{-1} = \frac{1}{\sqrt{1-b^2}} F\left(\sqrt{\frac{1-a^2}{1-b^2}}, \frac{\pi}{2}\right) . \tag{3.26}$$

For the differential head the corresponding results are,

$$H_x^A(x,0) = \begin{cases} \frac{1}{2}\left[\frac{1}{b} + \frac{c_4}{\sqrt{(1-x^2)(x^2-b^2)(x^2-a^2)}}\right] & 0 \le x < b \\ -\frac{1}{2}\left[\frac{1}{1-a} + \frac{c_4}{\sqrt{(1-x^2)(x^2-b^2)(x^2-a^2)}}\right] & a < x < 1 \end{cases} \tag{3.27}$$

where

$$c_4^{-1} = \int_a^1 \frac{1}{\sqrt{(1-x^2)(x^2-b^2)(x^2-a^2)}} dx. \tag{3.28}$$

Again, c_4^{-1} may be written as the elliptic integral

$$c_4^{-1} = \frac{1}{a\sqrt{1-b^2}} F\left(\frac{b\sqrt{1-a^2}}{a\sqrt{1-b^2}}, \frac{\pi}{2}\right) . \tag{3.29}$$

Both the horizontal and vertical field at any point in $y > 0$ may be determined from $H_x^A(x,0)$ [37] as

$$H_x^A(x,y) = \frac{y}{\pi} \int_{-\infty}^{\infty} \frac{H_x^A(u,0)}{(x-u)^2 + y^2} du \tag{3.30}$$

and

$$H_y^A(x,y) = \frac{1}{\pi} \int_{-\infty}^{\infty} \frac{(u-x) H_x^A(u,0)}{(x-u)^2 + y^2} du . \tag{3.31}$$

Of the various integral relationships available, these are the most convenient to use since $H_x(x,0)$ is zero on the faces of the MR elements and the shields and it is only necessary to integrate across the gaps. Figs. 26 and 27 show a comparison of the exact and approximate horizontal field components for the dual stripe and differential heads respectively where it can be seen that these approximations are generally extremely accurate.

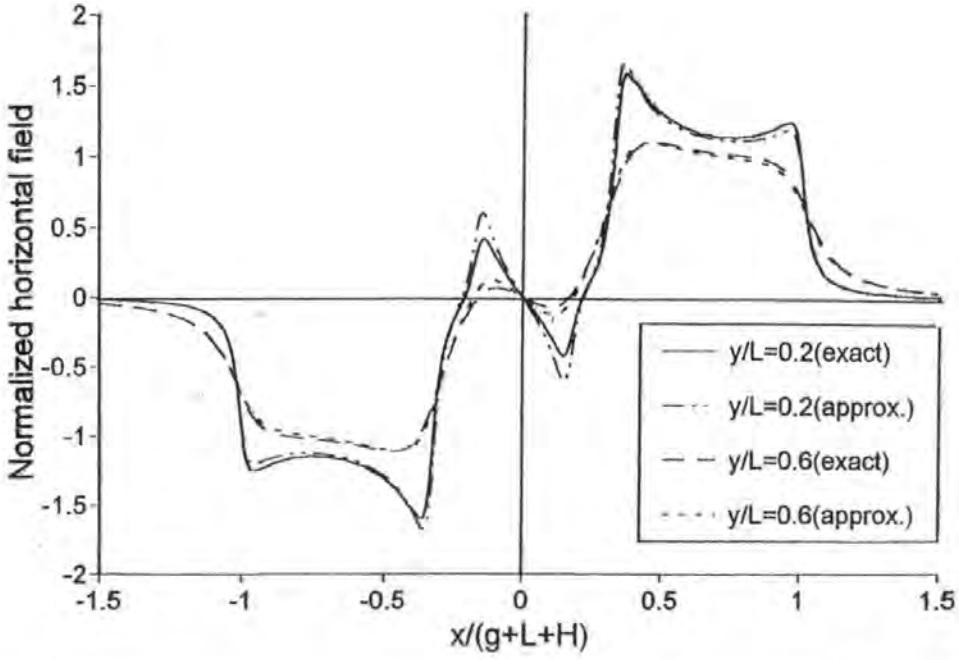

Figure 26. Comparison of the exact and approximate horizontal field component for a dual stripe head without an underlayer, g/L=1.0, h/L=2.0

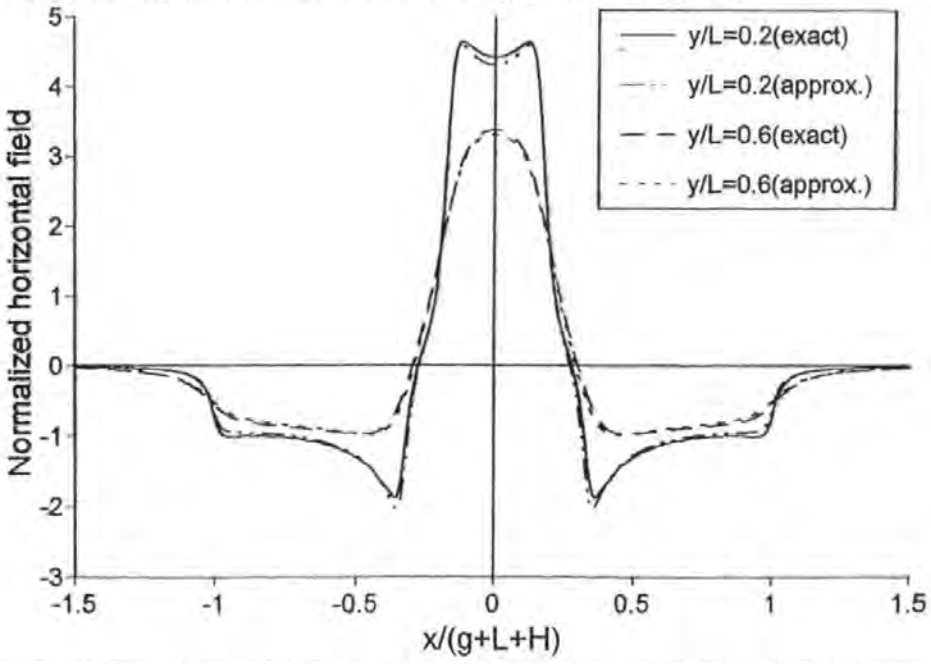

Figure 27. Comparison of the exact and approximate horizontal field component for a differential head without an underlayer, g/L=1.0, h/L=2.0

In [29] the accuracy of a similar approximation for a single-element MR head was demonstrated by comparison with the full theoretical solution but the double-element approximations could, at that time, only be tested against experimental results. However, it should be noted that even evaluation of the approximate fields is a non-trivial computational task due to the nature of the constants c_3 and c_4. This is true despite the new observation made here that c_3 and c_4 can be expressed as elliptic integrals has enabled efficient numerical software to be used.

3.6. Spectral Response Functions

As shown in Chapter 2, for the 2-D model of an MR sensor considered here, operating such that its response is linear, the reciprocity theorem gives the output voltage as the correlation integral [38]

$$e(\bar{x}) = C^{MR} \int_{y=d}^{d+\delta} \int_{x=-\infty}^{\infty} \mathbf{H}(x+\bar{x}, y) \cdot \mathbf{M}(x, y) dx dy. \tag{3.32}$$

Here C^{MR} is a constant, $\mathbf{H} = -\nabla\varphi$ is the magnetic field produced by the reciprocity potential φ, $\mathbf{M}$ is the recorded magnetization on a medium of thickness δ at a distance d from the plane $y = 0$ (Fig. 12) and $\bar{x}$ is the relative position of the medium and the head.

Taking the Fourier transform of (3.32) gives

$$\hat{e}(k) = C^{MR} \int_{d}^{d+\delta} \widehat{\mathbf{H}}(k, y) \cdot \widehat{\mathbf{M}}^{*}(k, y) dy \tag{3.33}$$

where $\widehat{\mathbf{H}}(k, y)$ is the Fourier transform of the field and $\widehat{\mathbf{M}}^{*}(k, y)$ is the complex conjugate of the transform of the magnetization. $\widehat{\mathbf{H}}(k, y)$ may be simply expressed in terms of $\widehat{\mathbf{H}}(k, 0)$, which is usually known as the spectral response function.

When an underlayer is present, the transformed horizontal and vertical fields are

$$\widehat{\mathbf{H}}(k, y) = \Big(\frac{\sinh[k(t-y)]}{\sinh[kt]} \widehat{H}_x(k, 0), \frac{\cosh[k(t-y)]}{\cosh[kt]} \widehat{H}_y(k, 0) \Big) \tag{3.34}$$

and

$$\widehat{H}_y(k, 0) = i \coth[kt] \widehat{H}_x(k, 0). \tag{3.35}$$

This simplifies to

$$\widehat{\mathbf{H}}(k,y) = e^{-ky}\widehat{\mathbf{H}}(k,0) \tag{3.36}$$

and

$$\widehat{H}_y(k,0) = i\widehat{H}_x(k,0) \tag{3.37}$$

in the case of no underlayer.

$\widehat{\mathbf{H}}(k,0)$ may be evaluated from $\widehat{\varphi}(k,0)$, the transform of the surface potential $\varphi(x,0)$, since

$$\widehat{H}_x(k,0) = -ik\widehat{\varphi}(k,0) \tag{3.38}$$

and

$$\widehat{H}_y(k,0) = k\coth[kt]\widehat{\varphi}(k,0) \tag{3.39}$$

with $\coth[kt]$ replaced by unity if there is no underlayer. This enables $\widehat{\mathbf{H}}(k,0)$ to be evaluated here in a particularly simple way. If, in region I, where the recording medium lies, $\varphi(x,y)$ is written in the form

$$\varphi(x,y) = \int_0^\infty D(k)\cos[kx]f(k,y)dk \tag{3.40}$$

where $f(k,y)$ is any function, then

$$\widehat{\varphi}(k,y) = \pi D(k)f(k,y). \tag{3.41}$$

Hence for the dual stripe head, from (3.6) with $\alpha = 0$,

$$\begin{aligned}\widehat{\varphi}^{++}(k,0) \;=\; & 2Vh\frac{\sin[k(g+L+h)]\sin[kh]}{(kh)^2} \\ & + \sum_{n=1}^{\infty} A_n 2(n-1/2)g(-1)^n\pi\frac{\cos[kg]}{(kg)^2-[(n-1/2)\pi]^2} \\ & + \sum_{n=1}^{\infty} B_n 4nh(-1)^{n+1}\pi\frac{\sin[k(g+L+h)]\sin[kh]}{(kh)^2-(n\pi)^2} \\ & + \sum_{n=1}^{\infty} C_n 4(n-1/2)h(-1)^n\pi\frac{\cos[k(g+L+h)]\cos[kh]}{(kh)^2-[(n-1/2)\pi]^2}.\end{aligned} \tag{3.42}$$

If

$$\varphi(x,y) = \int_0^\infty D(k)\sin[kx]f(k,y)dk \tag{3.43}$$

then

$$\widehat{\varphi}(k,y) = -i\pi D(k) f(k,y) \tag{3.44}$$

For the differential head, from (3.14) with $\alpha = 0$,

$$\begin{aligned}\widehat{\varphi}^{-+}(k,0) &= 2Vhi\frac{\cos[k(g+L+h)]\sin[kh]}{(kh)^2} - 2Vgi\frac{\sin[kg]}{(kg)^2} \\ &+ \sum_{n=1}^{\infty} A_n 2ng(-1)^{n+1} i\pi \frac{\sin[kg]}{(kg)^2-(n\pi)^2} \\ &+ \sum_{n=1}^{\infty} B_n 4nh(-1)^{n+1} i\pi \frac{\cos[k(g+L+h)]\sin[kh]}{(kh)^2-(n\pi)^2} \\ &+ \sum_{n=1}^{\infty} C_n 4(n-1/2)h(-1)^{n+1} i\pi \frac{\sin[k(g+L+h)]\cos[kh]}{(kh)^2-[(n-1/2)\pi]^2}\end{aligned} \tag{3.45}$$

The following figures show typical spectral responses, plotted as functions of $k(g+L+H)$. For heads with underlayers, the vertical component $\widehat{H}_y(k,0)$ is shown. From (3.35) the magnitude of the horizontal component only differs by a factor of $\coth[kt]$. When there is no underlayer, from (3.37), $\widehat{H}_x(k,0)$ and $\widehat{H}_y(k,0)$ have the same magnitude.

For a dual stripe head with an underlayer and a fixed shield to shield distance, Figs. 28 and 29 show the effect of varying the length (L) of the MR element and the inter-element gap ($G = 2g$). The position of the first null is principally determined by the dimension $2L+G$, the length of an 'equivalent' shielded single pole, which should be as small as possible. For a fixed $2L+G$, the gap (G) should be as small as possible. For example, the spectral response curves for $g : L : h : t = 0.5 : 1 : 2.25 : 1$ in Fig. 28 and for $g : L : h : t = 1 : 0.5 : 2.25 : 1$ in Fig. 29 show that, for a fixed $2L+G = 3$, the first null position for $g = 0.5$ is 8.7 compared with 7.2 for $g = 1$. It naturally follows that the highest frequency for the first null is produced when $G = 0$. For example, for a fixed $2L+G = 4$, the first null moves from 5.2 with $g : L : h : t = 0.5 : 1.5 : 2 : 1$ to 6.9 with $g : L : h : t = 0 : 2 : 2 : 1$ (the single pole), a shift of approximately 33%. This is consistent with a similar observation in [29] for a dual stripe head without an underlayer.

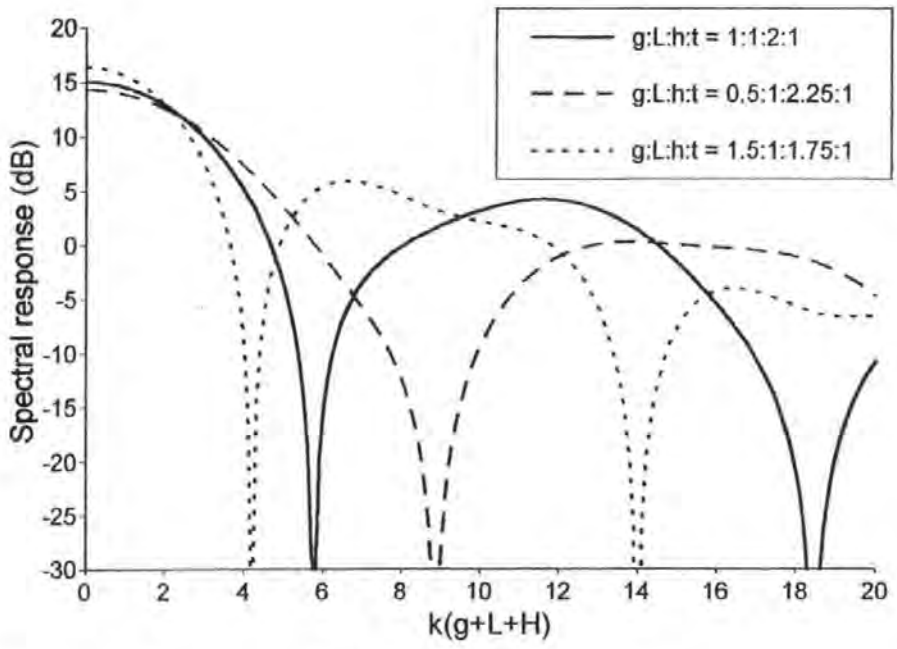

Figure 28. Spectral response of a dual stripe head with an underlayer, as the inter-element gap varies.

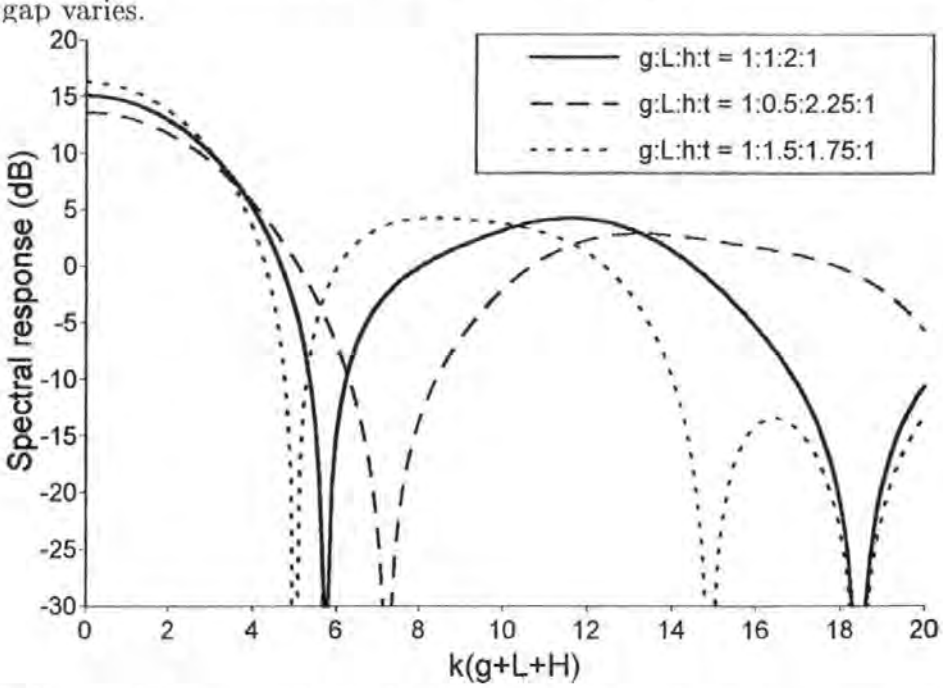

Figure 29. Spectral response of a dual stripe head with an underlayer, as the element length varies.

When no underlayer is present similar conclusions may be drawn. However, for identical head dimensions, the first null occurs at a slightly lower frequency without an underlayer and there is less variation in the position of this null as L and G vary. This is illustrated in Fig. 30, where the spectral response curves for a fixed $2L + G$ and a range of values G are plotted. As G reduces there is only a slight shift in the position of the first null towards higher frequencies and the minimum between the first and second nulls becomes more pronounced, eventually developing into a null as $G \rightarrow 0$, corresponding to a shielded single pole. Generally, the spectral response curves are more complicated when no underlayer is present, having more nulls and also minima beyond the first null.

For a differential head with an underlayer the head geometry is similar to that of a ring head and therefore the spectrum depends strongly on the gap, G, between the MR elements, as illustrated in Fig. 31. The dependence on the gap length (G), rather than the gap plus elements length ($2L + G$) that is the critical dimension for the dual stripe head, results in a first null for the differential head that is naturally higher than that of a dual stripe head of identical dimensions. This is confirmed by the solid curves in Figs. 29 and 31, for example, where identical head dimensions give first nulls of 5.8 and 13.0, respectively. Figs. 31 and 32 show that for a fixed gap G, a smaller pole length L produces the first null at a higher frequency, although as the ratio G/L decreases, head bumps occur before that first null. For example, a comparison of $g : L : h : t = 1.5 : 1 : 1.75 : 1$ in Fig. 31 with $g : L : h : t = 1.5 : 0.5 : 2 : 1$ in Fig. 32, for a fixed $G = 3$, shows that a pole length of $L = 1$ produces a first null of 9.7 whereas a pole length of $L = 0.5$ gives a first null position of 11.1.

Similar conclusions hold for the differential head when there is no underlayer present. However, the first null position changes only slightly and, as for the dual stripe head, the patterns are more complicated beyond the first null.

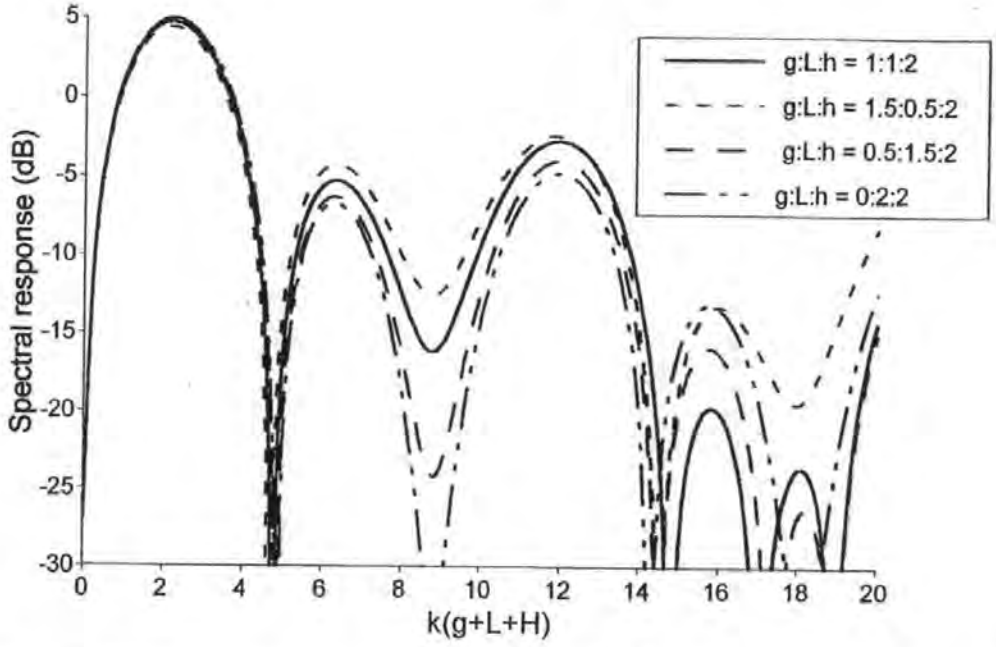

Figure 30. Spectral response of a dual stripe head without an underlayer, as the inter-element gap and the element length vary.

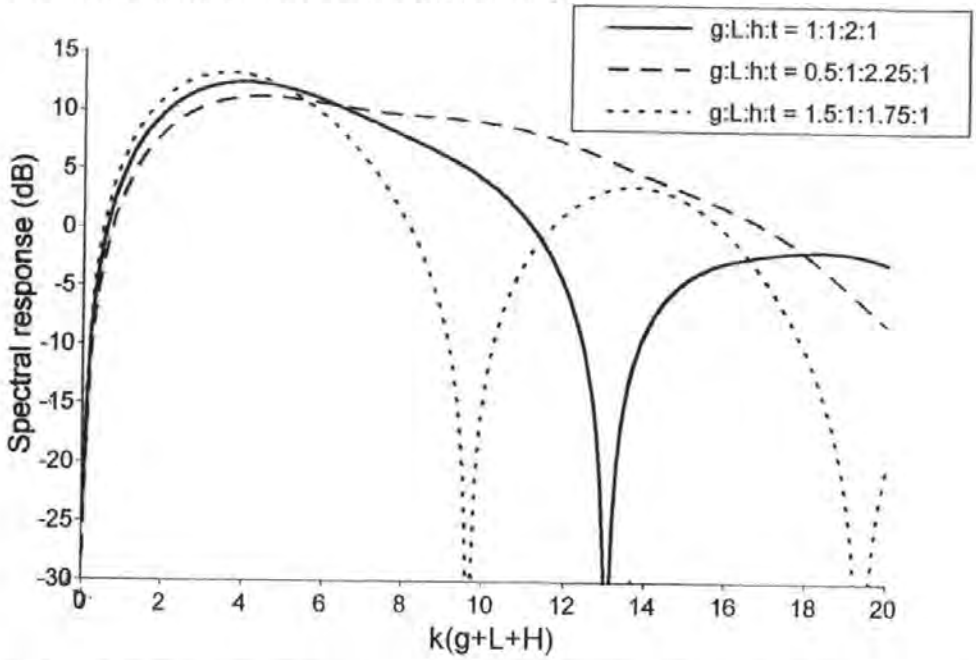

Figure 31. Spectral response of a differential head with an underlayer, as the inter-element gap varies.

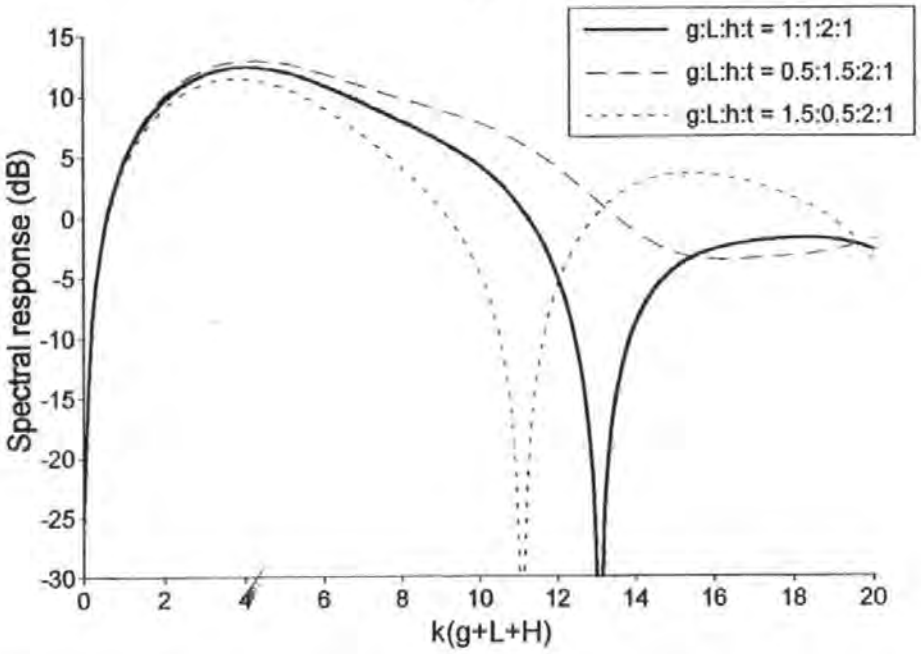

Figure 32. Spectral response of a differential head with an underlayer, as the inter-element gap and the element length vary.

3.7. Summary

In this chapter:

- The Fourier method is used to provide, for the first time, full analytic solutions for double-element shielded MR heads for both longitudinal and perpendicular recording.
- Representative Fourier coefficients and field plots are given.
- Previously published approximate solutions which are applicable to double-element heads are compared with the new exact solutions.
- Explicit spectral response functions are given and typical results are used to examine the dependence of the first null upon the dimensions of the head.

CHAPTER 4

A STUDY OF OUTPUT VOLTAGE FOR DOUBLE-ELEMENT SHIELDED MR HEADS

4.1. Introduction

In the derivation of the reciprocity principle presented in Chapter 2, the correlation integral

$$e(\bar{x}) = C^{MR} \int_{y=d}^{d+\delta} \int_{x=-\infty}^{\infty} \mathbf{H}(x+\bar{x}, y) \cdot \mathbf{M}(x, y) dx dy, \tag{4.1}$$

was developed to represent the output voltage for the generic 2-D model of a double-element shielded MR head shown in Fig. 12. In this chapter the integral is used to investigate the output voltage of such heads, both for perpendicularly recorded media in the presence of an underlayer and for longitudinally recorded media with no underlayer present. In digital recording the magnetization is changed in as short a distance as possible to enable the maximum number of transitions on a track. Ideally, the magnetization pattern would be that of a step change from its maximum value in one sense to its maximum value in the opposite sense. However, such a pattern is unrealistic and many of the features of the reproduce process are most adequately modelled by consideration of a magnetization distribution characterized by transitions of finite length. The hyperbolic tangent (tanh) is used here to model a single recorded transition on the medium as it has been suggested that this produces better agreement with experiment than the popular arctangent model [39]. In section 4.2 the hyperbolic tangent transition model is used, along with the surface potentials calculated in Chapter 3, to obtain expressions for the output pulse from a longitudinally recorded medium with no underlayer and from a perpendicularly recorded medium with an underlayer. Representative plots are presented and these are used to compare the accuracy of output voltage calculations using different numbers of coefficients from the corresponding Fourier series. In section 4.3, regression techniques are used to produce

a practical method for the generation of approximations to the first coefficient of the Fourier series. The approximate coefficients are shown to provide a convenient means for the generation of accurate approximations to the output voltage waveforms.

4.1.1. Output from a Longitudinally Recorded Medium with no Underlayer

For longitudinally recorded media the magnetization has an x component only, $\mathbf{M} = M_x\mathbf{i}$, and the output voltage for the 2-D model considered here is given by

$$e(\bar{x}) = C^{MR}\int_{y=d}^{d+\delta}\int_{x=-\infty}^{\infty} H_x(x+\bar{x},y)M_x(x,y)dx\,dy. \tag{4.2}$$

Calculation of the output voltage is performed by first taking the Fourier transform of (4.2), which can be done fully analytically for the magnetization considered here. This leads to integrands in the inverse Fourier transforms which decay to zero, as the Fourier variable tends to infinity, more rapidly than the integrands of (4.2) go to zero as $x \to \pm\infty$. Numerical evaluation of the relevant integrals is therefore considerably more efficient. Taking the Fourier transform of (4.2) gives

$$\hat{e}_x(k) = C^{MR}\int_{y=d}^{d+\delta} \widehat{H}_x(k,y)\widehat{M}_x^*(k)dy, \tag{4.3}$$

where $\widehat{M}_x^*(k)$ denotes the complex conjugate of the transform of the longitudinal component of the magnetization vector, which is now assumed to be constant through the medium thickness. With no underlayer present $\widehat{\mathbf{H}}(k,y) = e^{-ky}\widehat{\mathbf{H}}(k,0)$. Using this result in (4.3) and carrying out the integration produces

$$\hat{e}_x(k) = C^{MR}\widehat{H}_x(k,0)\frac{e^{-kd}}{k}(1-e^{-k\delta})\widehat{M}_x^*(k) \tag{4.4}$$

and since $\widehat{H}_x(k,0) = -ik\hat{\varphi}(k,0)$ the transformed output can be expressed as

$$\hat{e}_x(k) = C^{MR}[-ik\hat{\varphi}(k,0)]\frac{e^{-kd}}{k}(1-e^{-k\delta})\widehat{M}_x^*(k). \tag{4.5}$$

Expressions for $\hat{\varphi}(k,0)$, the transform of the surface potential for both the dual stripe head and the differential head are given in Chapter 3. They are

$$\hat{\varphi}^{++}(k,0) \;=\; 2Vh\frac{\sin[k(g+L+h)]\sin[kh]}{(kh)^2}$$

$$+\sum_{n=1}^{\infty} A_n 2(n-1/2)g(-1)^n\pi\frac{\cos[kg]}{(kg)^2-[(n-1/2)\pi]^2}$$
$$+\sum_{n=1}^{\infty} B_n 4nh(-1)^{n+1}\pi\frac{\sin[k(g+L+h)]\sin[kh]}{(kh)^2-(n\pi)^2}$$
$$+\sum_{n=1}^{\infty} C_n 4(n-1/2)h(-1)^n\pi\frac{\cos[k(g+L+h)]\cos[kh]}{(kh)^2-[(n-1/2)\pi]^2} \quad (4.6)$$

and

$$\widehat{\varphi}^{-+}(k,0) = 2Vhi\frac{\cos[k(g+L+h)]\sin[kh]}{(kh)^2} - 2Vgi\frac{\sin[kg]}{(kg)^2}$$
$$+\sum_{n=1}^{\infty} A_n 2ng(-1)^{n+1}i\pi\frac{\sin[kg]}{(kg)^2-(n\pi)^2}$$
$$+\sum_{n=1}^{\infty} B_n 4nh(-1)^{n+1}i\pi\frac{\cos[k(g+L+h)]\sin[kh]}{(kh)^2-(n\pi)^2}$$
$$+\sum_{n=1}^{\infty} C_n 4(n-1/2)h(-1)^{n+1}i\pi\frac{\sin[k(g+L+h)]\cos[kh]}{(kh)^2-[(n-1/2)\pi]^2}, \quad (4.7)$$

respectively.

A single recorded transition on the medium is modelled using the hyperbolic tangent. Thus,

$$M_x(x) = M_r \tanh\left[\frac{2x}{\pi a}\right] \quad (4.8)$$

where a denotes the transition parameter. Taking the complex conjugate of the Fourier sine transform and assuming a unit tanh transition gives

$$\widehat{M}_x^*(k) = 2i\int_0^{\infty}\tanh\left[\frac{2x}{\pi a}\right]\sin[kx]\,dx = \frac{i\pi^2 a}{2\sinh\left[\frac{\pi^2 ak}{4}\right]}. \quad (4.9)$$

The output voltage is given by the inverse Fourier transform of $\widehat{e}_x(k)$. For the dual stripe head the inverse Fourier cosine transform

$$e_x^{++}(\bar{x}) = \frac{1}{\pi}\int_{k=0}^{\infty}\widehat{e}_x^{++}(k)\cos[k\bar{x}]dk, \quad (4.10)$$

is appropriate and for the differential head the inverse sine transform

$$e_x^{-+}(\bar{x}) = \frac{i}{\pi}\int_{k=0}^{\infty}\widehat{e}_x^{-+}(k)\sin[k\bar{x}]dk. \quad (4.11)$$

is used. Thus for the dual stripe head the output pulse due to a single recorded transition is

$$e_x^{++}(\bar{x}) = C^{MR}\frac{\pi a}{2}\int_{k=0}^{\infty}\widehat{\varphi}^{++}(k,0)\frac{e^{-kd}(1-e^{-k\delta})}{\sinh\left[\frac{\pi^2 ak}{4}\right]}\cos\left[k\bar{x}\right]dk, \tag{4.12}$$

and the corresponding output pulse for the differential head is given by

$$e_x^{-+}(\bar{x}) = C^{MR}\frac{i\pi a}{2}\int_{k=0}^{\infty}\widehat{\varphi}^{-+}(k,0)\frac{e^{-kd}(1-e^{-k\delta})}{\sinh\left[\frac{\pi^2 ak}{4}\right]}\sin\left[k\bar{x}\right]dk. \tag{4.13}$$

4.1.2. Output from a Perpendicularly Recorded Medium with an Underlayer

For perpendicular recording the magnetization has a y component only, $\mathbf{M} = M_y\mathbf{j}$, and the output voltage is given by

$$e_y(\bar{x}) = C^{MR}\int_{y=d}^{d+\delta}\int_{x=-\infty}^{\infty}H_y(x+\bar{x},y)M_y(x,y)dx\,dy. \tag{4.14}$$

Using the Fourier transform convolution result this becomes

$$\widehat{e}_y(k) = C^{MR}\int_{y=d}^{d+\delta}\widehat{H}_y(k,y)\widehat{M}_y^*(k)dy. \tag{4.15}$$

Perpendicular recording commonly requires an underlayer, the presence of which generates the relationships

$$\widehat{H}_y(k,y) = \frac{\cosh\left[k(t-y)\right]}{\cosh\left[kt\right]}\widehat{H}_y(k,0) \tag{4.16}$$

and

$$\widehat{H}_y(k,0) = k\coth\left[kt\right]\widehat{\varphi}(k,0), \tag{4.17}$$

where $t = d+\delta$ and it has been assumed that the underlayer is immediately next to the recording medium. Using these in (4.15) gives

$$\widehat{e}_y(k) = C^{MR}\int_{y=d}^{d+\delta}k\frac{\cosh\left[k(t-y)\right]}{\sinh\left[kt\right]}\widehat{\varphi}(k,0)\widehat{M}_y^*(k)dy, \tag{4.18}$$

and performing the y integration produces

$$\widehat{e}_y(k) = C^{MR}\frac{\sinh\left[k\delta\right]}{\sinh\left[kt\right]}\widehat{\varphi}(k,0)\widehat{M}_y^*(k). \tag{4.19}$$

The perpendicular output voltages for each head configuration can be written as the inverse Fourier transforms of (4.19). For the tanh model (4.9) of a single perpendicular transition the output voltage for the dual stripe head with an underlayer is

$$e_y^{++}(\bar{x}) = -C^{MR}\frac{\pi a}{2}\int_{k=0}^{\infty}\widehat{\varphi}^{++}(k,0)\frac{\sinh[k\delta]}{\sinh[kt]\sinh[\frac{\pi^2 ak}{4}]}\sin[k\bar{x}]dk, \tag{4.20}$$

and for the differential head with an underlayer it is

$$e_y^{-+}(\bar{x}) = C^{MR}\frac{i\pi a}{2}\int_{k=0}^{\infty}\widehat{\varphi}^{-+}(k,0)\frac{\sinh[k\delta]}{\sinh[kt]\sinh[\frac{\pi^2 ak}{4}]}\cos[k\bar{x}]dk. \tag{4.21}$$

4.1.3. Results

Expressions (4.6) and (4.7) for $\widehat{\varphi}^{++}(k,0)$ and $\widehat{\varphi}^{-+}(k,0)$ each comprise a leading term plus three infinite series, for which the corresponding Fourier coefficients A_n, B_n and C_n must be computed. Determination of these coefficients is not straightforward, as discussed in Chapter 3, requiring the solution of three coupled infinite sets of linear simultaneous equations which contain highly oscillatory integrals. Once the calculation of the coefficients is completed however, $\widehat{\varphi}^{++}(k,0)$ and $\widehat{\varphi}^{-+}(k,0)$ may be evaluated by truncating each infinite series to some finite size n. The output voltages given by (4.12), (4.13), (4.20) and (4.21) are calculated by performing a numerical integration over the semi-infinite range of k.

Output calculations have been carried out for both the dual stripe head and the differential head with and without an underlayer present. For a broad range of ratios g/L and h/L it was found that the inclusion of more than 6 terms of each series usually resulted in very little change to the calculations. However when the element/shield gap is large, that is when $h/L > 3.0$ approximately, it becomes necessary to include more terms of each infinite series to obtain an accurate solution. Consequently when reference is made to an 'exact' output voltage in the results that follow it will be taken to mean the output voltage which was calculated by including sufficient terms of each series to ensure that the peak output voltage differs by less than 0.1 percent to that obtained by using one fewer term from each series. For most practical purposes however it will be seen that only the first coefficients A_1, B_1 and C_1 plus the leading terms of (4.6) and (4.7) would be needed.

Parameter values for the representative figures that are shown here for dual element heads were chosen in agreement with the experimental dual MR head dimensions given in [40]. Thus for a dual MR head with a shield/shield separation of 300nm the chosen scaled ratios $g : L : h : t : d : \delta : a = 1 : 1 : 2 : 4 : 2 : 2 : 1.28$ represent a head with an inter-element gap of $2g = 50$nm, elements of length $L = 25$nm, an element/shield separation of $2h = 100$nm, a flying height of $d = 50$nm and a recording medium of thickness $\delta = 50$nm. The transition parameter for such a head is $a = 32$nm and is taken to be independent of flying height. Fig. 33 compares the 'exact' output voltage pulse due to a longitudinal transition for the dual stripe head without an underlayer with the output calculated using the leading term only and with that calculated using the leading term plus the first term of each series. Fig. 34 shows the same comparison for the differential head without an underlayer. It is common for such heads [41] to first differentiate (4.13) in order to give the familiar single pulse shape rather than a dipolar pulse with two peaks of opposite sign and therefore Fig. 34 shows

$$d[e_x^{-+}(\bar{x})]/d\bar{x} = C^{MR}\frac{i\pi a}{2}\int_{k=0}^{\infty} k\hat{\varphi}^{-+}(k,0)\frac{\sinh[k\delta]}{\sinh[kt]\sinh[\frac{\pi^2 ak}{4}]}\sin[k\bar{x}]dk. \qquad (4.22)$$

Similarly [42], [43] for the dual stripe head with an underlayer, (4.20) is first differentiated to give a single pulse rather than a step-like (tanh) response.

$$-d[e_y^{++}(\bar{x})]/d\bar{x} = C^{MR}\frac{\pi a}{2}\int_{k=0}^{\infty} k\hat{\varphi}^{++}(k,0)\frac{\sinh[k\delta]}{\sinh[kt]\sinh[\frac{\pi^2 ak}{4}]}\cos[k\bar{x}]dk \qquad (4.23)$$

and the output is shown in Fig. 35. The output for a differential head with an underlayer does not require any prior manipulation and is shown in Fig. 36.

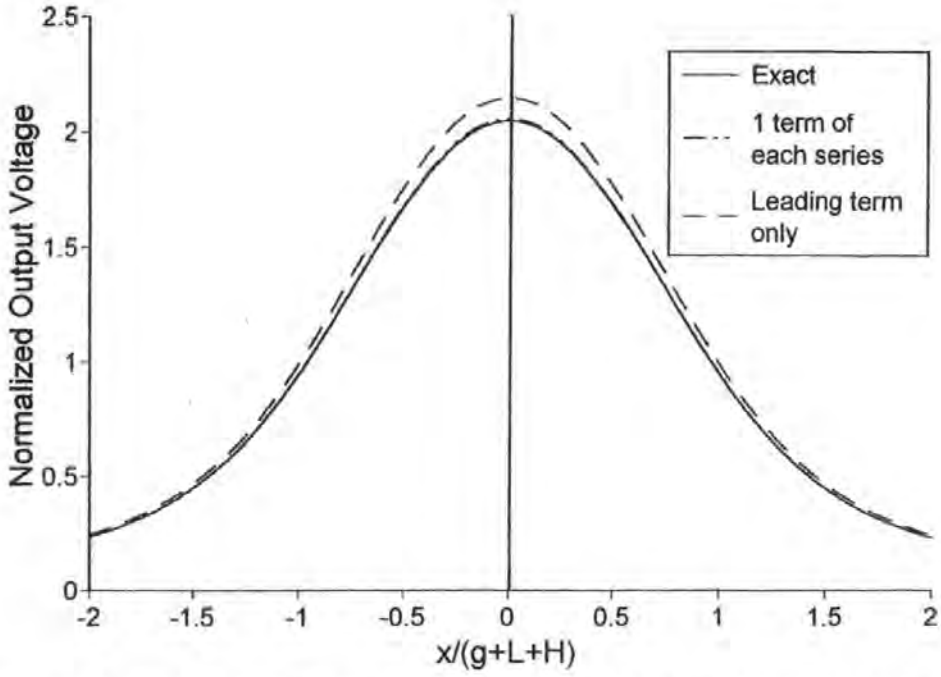

Figure 33. Output voltage pulse for a dual stripe head without an underlayer, g=1, L=1, h=2, a=1.28, δ=d=2.0

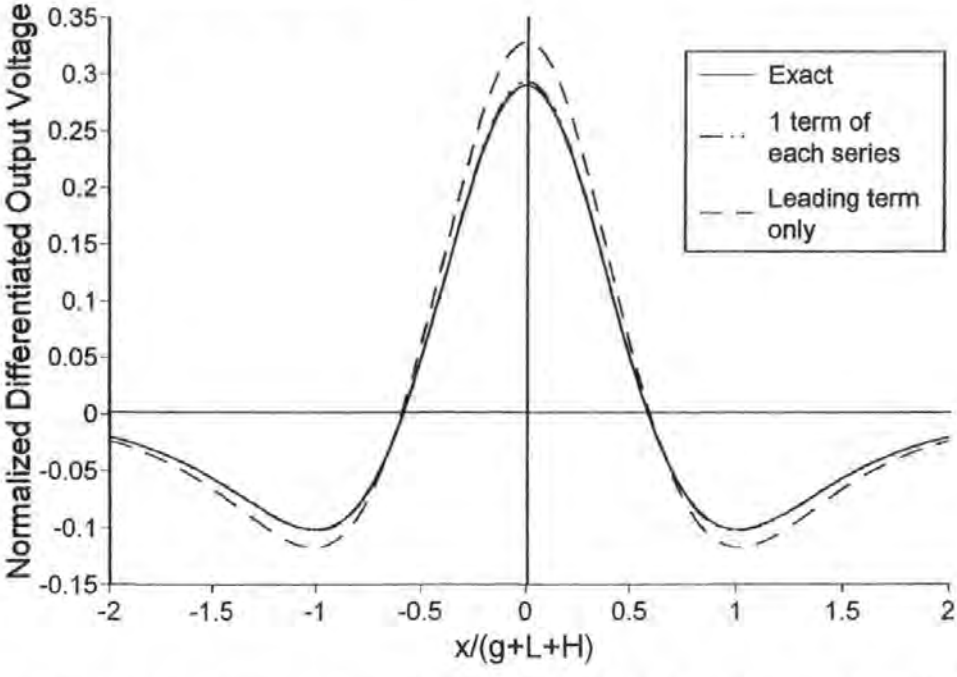

Figure 34. Output voltage pulse for a differential head without an underlayer, g=1, L=1, h=2, a=1.28, δ=d=2.0

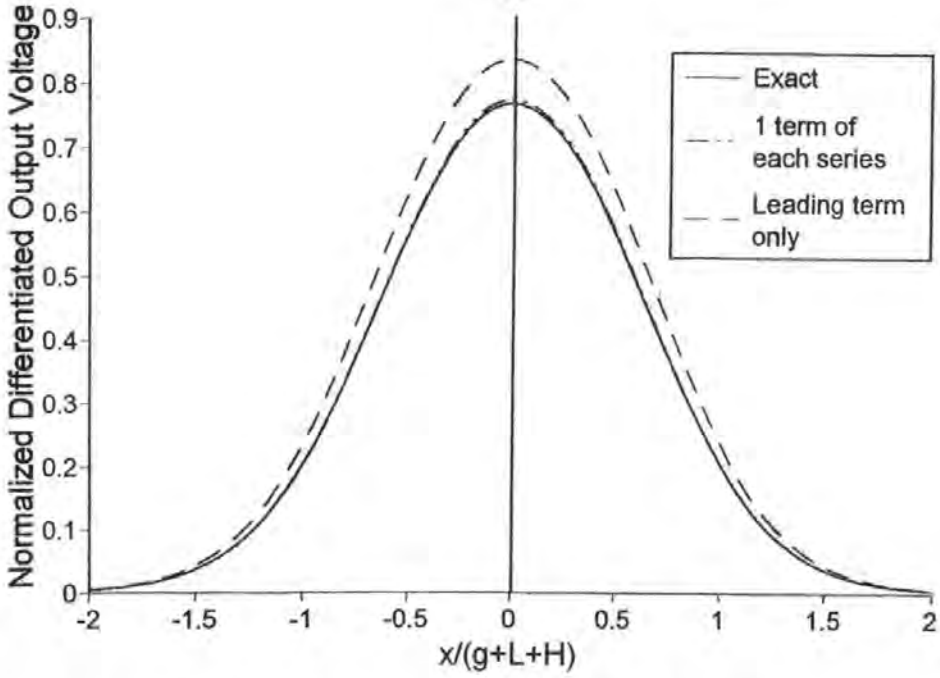

Figure 35. Output voltage pulse for a dual stripe head with an underlayer, t=4, g=1, L=1, h=2, a=1.28, δ=d=2.0

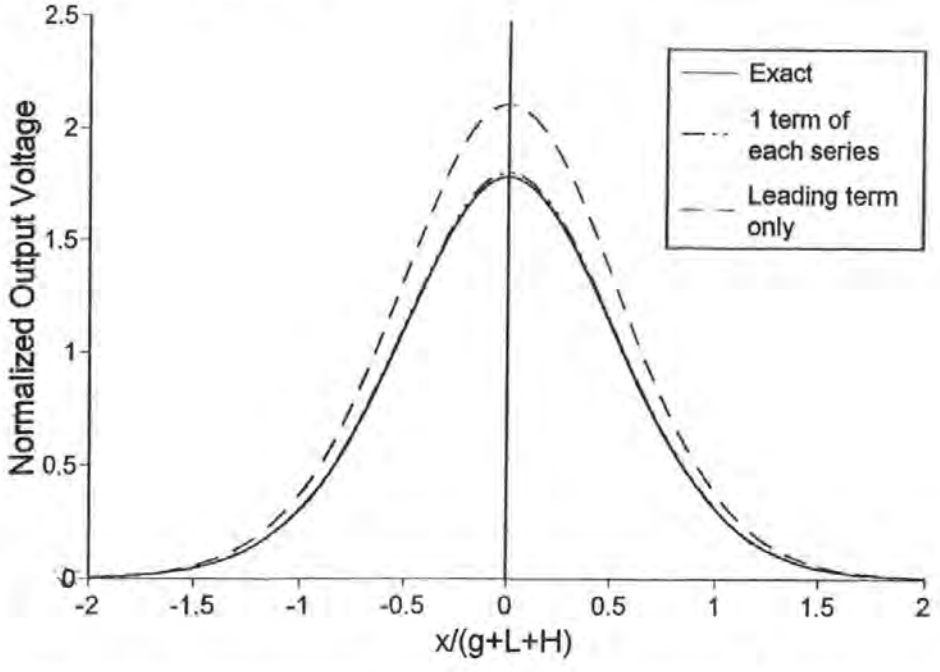

Figure 36. Output voltage pulse for a differential head with an underlayer, t=4, g=1, L=1, h=2, a=1.28, δ=d=2.0

4.2. Approximate Fourier Coefficients

4.2.1. Shielded Double-Element Head

The comparisons made in Figs 33-36 indicate that for most practical purposes the output calculations are sufficiently accurate if only the first (principal) term of the each infinite series is included. However, evaluation of even the first coefficients A_1, B_1 and C_1 involves the solution of large systems of linear equations. Therefore, to provide a more widely accessible method for the calculation of output voltages it is convenient to have approximations to the coefficients A_1, B_1 and C_1 thus avoiding the necessity to solve the associated systems of equations. Accurate coefficients A_1, B_1 and C_1 have been calculated for a wide range of typical head dimensions ($0 \leq g/L \leq 2.5, 0.5 \leq h/L \leq 5$) for the dual stripe and differential head both without an underlayer present. The data generated was used to fit bi-variate regression models [44] which approximate the coefficients for any head dimensions within the range stated above. Investigation of the data produced for both heads indicated that in each case a quadratic regression model of the form

$$A + B(g/L) + C(h/L) + D(g/L)(h/L) + E(g/L)^2 + F(h/L)^2 \tag{4.24}$$

was appropriate. For the dual stripe head without an underlayer the best fits are

$$\begin{aligned} A_1 &= 0.029 - 0.122(g/L) + 0.023(h/L) + 0.008(g/L)(h/L) + 0.018(g/L)^2 \\ &\quad -0.003(h/L)^2 \\ B_1 &= 0.044 + 0.002(h/L) \\ C_1 &= -0.017 + 0.009(g/L) - 0.022(h/L) + 0.001(g/L)(h/L) - 0.003(g/L)^2 \\ &\quad +0.002(h/L)^2. \end{aligned} \tag{4.25}$$

For the differential head without an underlayer the principal coefficients are given by

$$\begin{aligned} A_1 &= -0.087 - 0.016(g/L) + 0.004(h/L) + 0.002(g/L)(h/L) + 0.001(g/L)^2 \\ &\quad -0.001(h/L)^2 \end{aligned}$$

$$
\begin{aligned}
B_1 &= 0.045 - 0.014(g/L) + 0.018(h/L) - 0.006(g/L)(h/L) + 0.006(g/L)^2 \\
C_1 &= -0.051 + 0.044(g/L) - 0.069(h/L) + 0.01(g/L)(h/L) - 0.014(g/L)^2 \\
&\quad +0.004(h/L)^2.
\end{aligned}
\tag{4.26}
$$

Figs. 37 and 38 show typical output pulses obtained using these approximations compared with the 'exact' solutions and with those produced by including the leading terms only. Table 5 shows the percentage error in the approximated peak output voltage for the dual stripe head without an underlayer over the range of head dimensions that was used to generate the model. The average percentage error over $-2 \leq x/(g+L+h) \leq 2$ in the approximated output voltage for this head is given in Table 6.

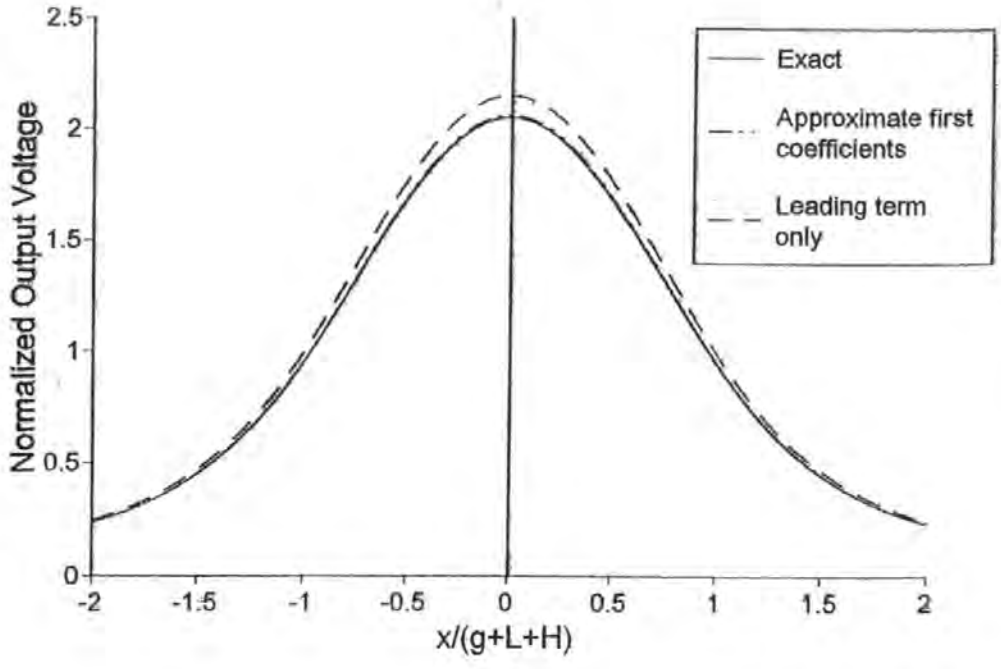

Figure 37. Output voltage pulse for a dual stripe head without an underlayer, g=1, L=1, h=2, a=1.28, δ=d=2.0

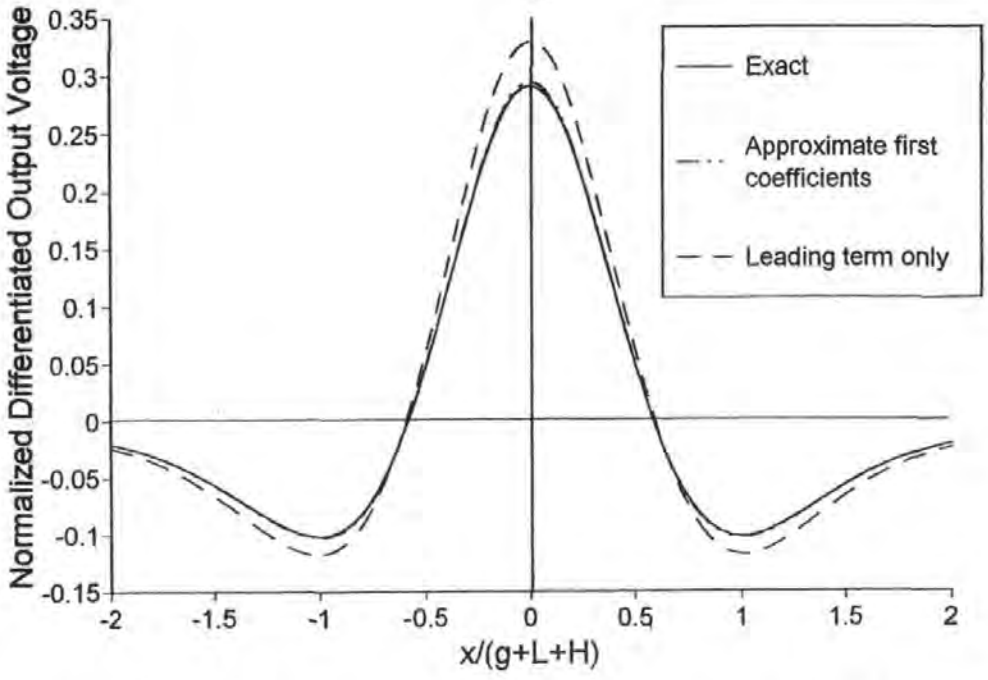

Figure 38. Output voltage pulse for a differential head without an underlayer, g=1, L=1, h=2, a=1.28, δ=d=2.0

g/L \ h/L	0.5	1.0	1.5	2.0	5.0
0.0	0.004	0.330	0.522	0.599	0.968
0.5	0.092	0.290	0.430	0.610	0.870
1.0	0.033	0.263	0.340	0.405	0.630
1.5	0.180	0.340	0.410	0.580	0.920
2.0	0.606	0.410	0.520	0.660	1.101

Table 5. Percentage error in peak output voltage calculated for a dual stripe head without an underlayer using approximated first terms only. L=1.0, a=1.28, δ=d=2.0.

It can be seen that the largest error occurs when the pole/pole and pole/shield separations are at their greatest ($g/L = 2.0$ and $h/L = 5.0$ respectively), when there is a 1.101 percent error in the peak output voltage and a 0.745 percent error in the average output voltage. Tables 7 and 8 show the same information for the differential head without an underlayer with the largest errors again occurring when the pole/shield separation is at its largest.

g/L \ h/L	0.5	1.0	1.5	2.0	5.0
0.0	0.021	0.309	0.479	0.506	0.352
0.5	0.116	0.270	0.370	0.440	0.380
1.0	0.287	0.242	0.294	0.302	0.313
1.5	0.470	0.210	0.300	0.290	0.570
2.0	0.576	0.380	0.510	0.610	0.745

Table 6. Average percentage error in output voltage calculated for a dual stripe head without an underlayer using approximated first terms only. L=1.0, a=1.28, δ=d=2.0

h/L / g/L	0.5	1.0	1.5	2.0	5.0
0.5	0.009	0.418	0.838	1.150	2.988
1.0	0.181	0.356	0.724	1.174	2.450
1.5	0.611	0.913	1.384	1.105	2.981
2.0	0.783	0.421	0.801	1.241	2.667
2.5	1.086	0.983	1.066	1.210	3.052

Table 7. Percentage error in peak output voltage calculated for a differential head without an underlayer using approximated first terms only. L=1.0, a=1.28, δ=d=2.0

h/L / g/L	0.5	1.0	1.5	2.0	5.0
0.5	0.038	0.394	0.780	0.823	6.207
1.0	0.131	0.291	0.761	0.980	2.152
1.5	0.318	0.563	1.360	1.012	2.662
2.0	0.715	0.367	0.711	1.113	2.214
2.5	0.880	0.772	0.842	0.982	3.430

Table 8. Average percentage error in output voltage calculated for a differential head without an underlayer using approximated first terms only. L=1.0, a=1.28, δ=d=2.0

Regression models were also obtained to approximate the first Fourier coefficients for the dual stripe and differential heads with an underlayer present. The range of head dimensions used was $0 \leq g/L \leq 2.5$, $0.5 \leq h/L \leq 5.0$ for the dual stripe head and $0.5 \leq g/L \leq 2.5$, $0.5 \leq h/L \leq 5.0$ for the differential head. The normalized head to underlayer separation parameter (t/L) was allowed to vary between 0.25 and 10, the latter being effectively equivalent to there being no underlayer present. The regression models for the heads in the presence of an underlayer were calculated with the assumption that the behaviour of the Fourier coefficients can be described by multiplying the corresponding models for each type of head without an underlayer given in (4.25) and (4.26) respectively, by a factor of $(1 + \alpha e^{\beta(t/L)})$. These models are particularly convenient since they reduce to the models (4.25) and (4.26) as t becomes large and so provide general models for all head configurations. The best fits for the dual stripe head in the presence of an underlayer are given by

$$\begin{aligned} A_1 &= (1 + 6.862e^{-0.558(t/L)}) \times (\text{model for } A_1 \text{ without an underlayer}) \\ B_1 &= (1 + 3.139e^{-0.913(t/L)}) \times (\text{model for } B_1 \text{ without an underlayer}) \\ C_1 &= (1 + 7.578e^{-0.390(t/L)}) \times (\text{model for } C_1 \text{ without an underlayer}). \end{aligned} \tag{4.27}$$

For the differential head with an underlayer the data is best fitted by

$$\begin{aligned} A_1 &= (1 + 3.007e^{-1.009(t/L)}) \times (\text{model for } A_1 \text{ without an underlayer}) \\ B_1 &= (1 + 2.007e^{-1.675(t/L)}) \times (\text{model for } B_1 \text{ without an underlayer}) \\ C_1 &= (1 + 2.495e^{-0.907(t/L)}) \times (\text{model for } C_1 \text{ without an underlayer}). \end{aligned} \tag{4.28}$$

Tables 9 and 10 show the percentage errors in the peak and average output voltage respectively for the dual stripe head with an underlayer using (4.27) to approximate the first Fourier coefficients. The same calculations using (4.28) for the differential head with an underlayer are presented in Tables 11 and 12.

h/L \ g/L	0.5	1.0	1.5	2.0	5.0
0.0	0.284	0.360	0.498	0.615	1.958
0.5	0.350	0.472	0.517	0.725	1.255
1.0	0.163	0.489	0.568	0.580	1.198
1.5	0.111	0.365	0.441	0.982	1.257
2.0	0.053	0.490	0.483	0.945	2.058

Table 9. Percentage error in peak output voltage calculated for a dual stripe head with an underlayer using approximated first terms only. L=1.0, a=1.28, t=4.0, δ=d=2.0

h/L \ g/L	0.5	1.0	1.5	2.0	5.0
0.0	0.117	0.331	0.658	0.776	2.059
0.5	0.206	0.881	0.559	1.026	1.357
1.0	0.160	0.626	0.625	0.678	1.332
1.5	0.195	0.567	0.511	1.154	1.244
2.0	0.207	0.522	0.599	0.912	1.861

Table 10. Average percentage error in output voltage calculated for a dual stripe head with an underlayer using approximated first terms only. L=1.0, a=1.28, t=4.0, δ=d=2.0

h/L / g/L	0.5	1.0	1.5	2.0	5.0
0.5	0.237	0.465	0.913	1.986	8.784
1.0	0.455	0.991	1.110	2.468	7.120
1.5	0.877	1.290	1.369	2.548	5.874
2.0	1.050	1.565	1.245	2.945	8.154
2.5	1.220	2.010	1.986	3.125	13.017

Table 11. Percentage error in peak output voltage calculated for a differential head with an underlayer using approximated first terms only. L=1.0, a=1.28, δ=d=2.0

h/L / g/L	0.5	1.0	1.5	2.0	5.0
0.5	0.280	0.732	1.026	1.956	5.512
1.0	0.551	1.121	1.089	2.663	3.222
1.5	0.912	1.306	1.380	2.315	4.356
2.0	1.563	1.303	1.699	2.010	10.123
2.5	1.687	1.327	2.041	2.113	14.706

Table 12. Average percentage error in output voltage calculated for a differential head with an underlayer using approximated first terms only. L=1.0, a=1.28, δ=d=2.0

The largest errors for both head types again occur when the pole/shield gap is at its greatest. The growing magnitude of the errors when the ratio h/L is increased beyond about 3.0 is a consequence of not including enough terms of each series rather than a deficiency in the model developed here to approximate the principal coefficients. In the case of the differential head with an underlayer taking $g/L = 2.5$ and $h/L = 5.0$ results in a error in the peak output voltage, when using only the first approximated terms of the series, of 14.7 percent. The error is only marginally reduced by using the accurately computed first coefficients in the calculation, when it is 12.9 percent. In order to achieve the level of accuracy defined here as the 'exact' output voltage it is necessary to include 10 terms of each infinite series. It should be noted that using the leading term only in the calculation of the peak output voltage for such a head would result in a 28.9 percent error. Output calculated using the approximated coefficients are plotted against the exact solution and the solution computed using only the leading term for both the dual stripe and differential heads, in Figs. 39 and 40 respectively.

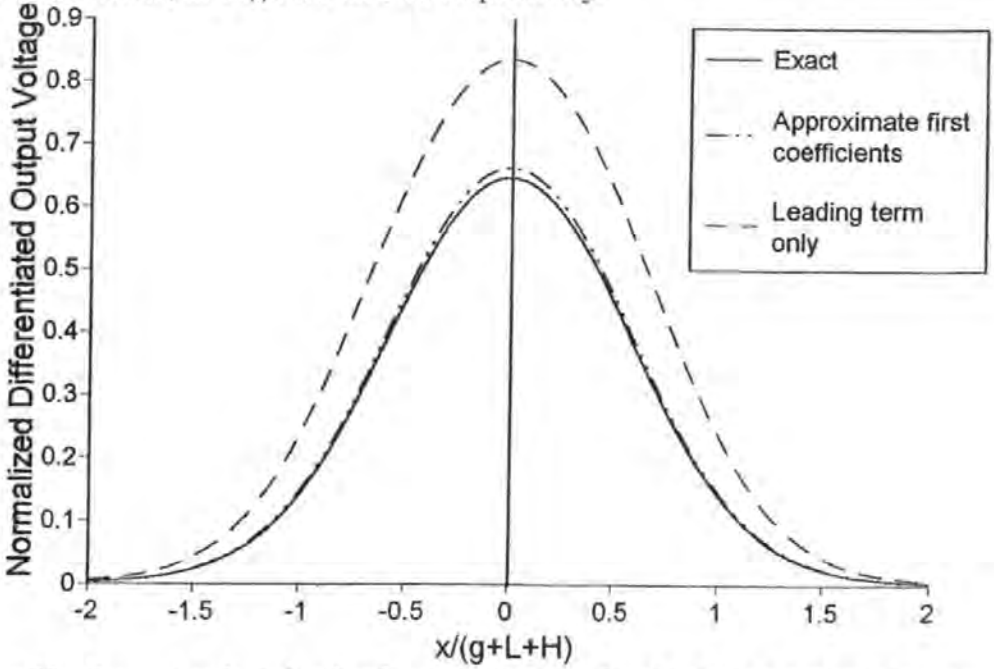

Figure 39. Output voltage pulse for a dual stripe head with an underlayer, t=4, g=1, L=1, h=2, a=1.28, δ=d=2.0

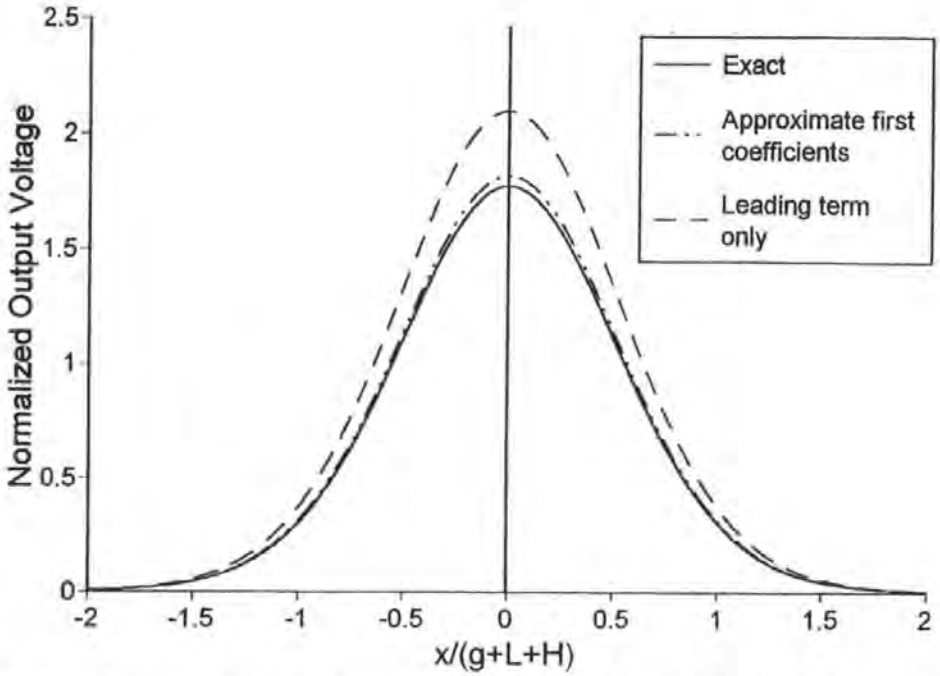

Figure 40. Output voltage pulse for a differential head with an underlayer, t=4, g=1, L=1, h=2, a=1.28, δ=d=2.0

4.2.2. Shielded Single Pole Head

Putting $g = 0$ reduces the geometry of the dual stripe head to the special case of a single, shielded pole head with pole length $2L$ and a pole/shield gap of $H = 2h$. Consequently, taking g to be equal to zero in expressions (4.12) and (4.20) produces expressions for the output voltage from a shielded pole head without an underlayer and with a longitudinally recorded medium and that from a shielded pole with an underlayer and with a perpendicularly recorded medium, respectively. The Fourier transform of the surface potential (4.6) which appears in expressions (4.12) and (4.20) is, with $g = 0$,

$$\begin{aligned}\widehat{\varphi}^{++}(k,0) &= 2Vh\frac{\sin[k(L+h)]\sin[kh]}{(kh)^2} \\ &\quad + \sum_{n=1}^{\infty} B_n 4nh(-1)^{n+1}\pi\frac{\sin[k(L+h)]\sin[kh]}{(kh)^2-(n\pi)^2} \\ &\quad + \sum_{n=1}^{\infty} C_n 4(n-1/2)h(-1)^{n}\pi\frac{\cos[k(L+h)]\cos[kh]}{(kh)^2-[(n-1/2)\pi]^2} \qquad (4.29)\end{aligned}$$

which is in agreement with the expression for $\widehat{\varphi}(k,0)$ for the shielded pole given in [17]. The above transform of the surface potential for the shielded pole head contains two infinite series of Fourier coefficients rather than the three infinite series that are present in (4.6) for the dual stripe head. This is because the series A_n originates from the solution to Laplace's equation in the region between the dual MR head elements and there is no such region in a shielded pole head. As a result, only B_1 and C_1 are needed from the regression model for the principal Fourier coefficients (4.27).

The output pulse obtained by using approximated coefficients B_1 and C_1, for a shielded pole head without an underlayer with a longitudinally recorded medium, is compared in Fig. 41 with the 'exact' solution and that given by using only the leading term of (4.29). For all of the representative figures for the single shielded pole head, a gap to pole length ratio of $h/L = 2.5$ was chosen. The percentage error of the peak output voltage (at $x = 0$) for these particular parameters, using the approximated coefficients, is less than 1 percent while the error produced by using the leading term only is almost 6 percent. Across the complete range of head parameters used in the model the approximated coefficients consistently produced errors which were less than 1 percent in the peak output while the leading term computations resulted in errors of up to 10 percent over the same range of parameters.

Fig. 42 shows the corresponding results for the output pulse for a shielded pole head with an underlayer and with a perpendicularly recorded medium. At $x = 0$ there is a percentage error in the peak output, using the approximated coefficients, of less than 0.5 percent while the error produced by using the leading term only gives an error of 11.2 percent. Over the range of head parameters the approximated coefficients produced errors of up to 1.7 percent in the peak output while the leading term resulted in errors as large as 17.7 percent.

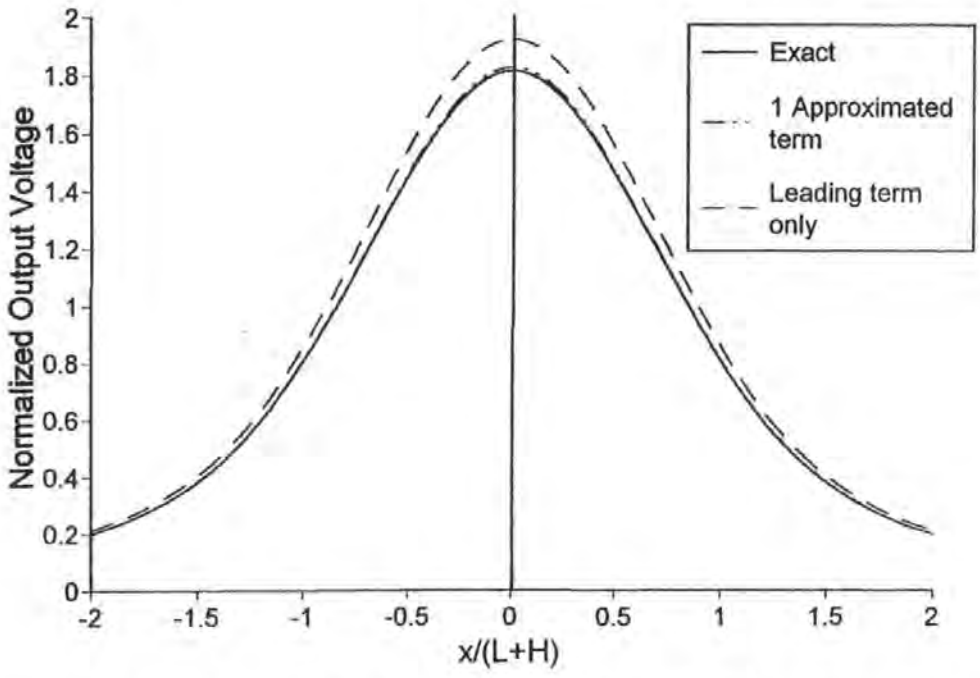

Figure 41. Output voltage pulse for a shielded pole head without an underlayer, L=1, h=2.5, a=1.28, δ=d=2.0

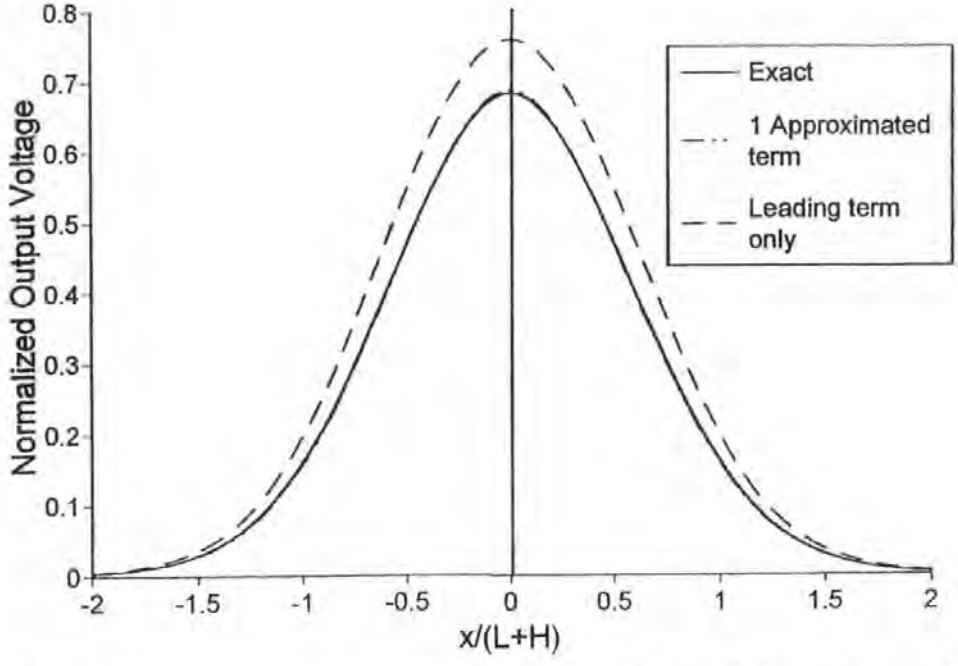

Figure 42. Output voltage pulse for a shielded pole head with an underlayer, t=4, L=1, h=2.5, a=1.28, δ=d=2.0

4.3. Summary

In this chapter the surface potentials of the double-element MR heads given in Chapter 3 have been considered in conjunction with a medium with a hyperbolic tangent magnetization pattern to calculate

- The output from a longitudinally recorded medium with no underlayer.
- The output from a perpendicularly recorded medium with an underlayer.

Also:

- It is shown that for most head geometries it is sufficient to use the first 6 coefficients from the Fourier series for a reliable approximation.
- A bivariate regression model is developed to provide a convenient method for the approximation of the first coefficient of the Fourier series.

CHAPTER 5

INTEGRALS ARISING IN MODELS OF SHIELDED MAGNETORESISTIVE HEADS

5.1. Introduction

Recently Aharoni [45] has given analytic results, in the form of rapidly convergent infinite series, for some of the integrals appearing in Chapter 3. In fact *all* the integrals given in Appendix B may be written either in terms of special functions or as rapidly convergent infinite series which provides an alternative and usually more efficient means of calculation than direct numerical integration. In this chapter it is shown how these results may be obtained, giving examples of each approach. Although all the analysis given in Chapter 3 was explicitly for dual stripe and differential double-element heads, a special case of the dual stripe head (with no inter-element gap , $g = 0$) is the shielded single pole head and appropriate results given here apply to that simpler geometry. Also, these results are applicable to all integrals required for the Fourier analysis of thin film heads with underlayers [46].

5.2. Integrals

5.2.1. Potential Integrals

The integrals required to compute the magnetic potential when an underlayer is present may be evaluated by contour integration, the appropriate contour being an infinitely large semi-circle in the upper-half complex plane. The trigonometric terms are written as the real parts of complex exponentials but care must be taken to ensure that these terms remain bounded on the semi-circular arc as its radius tends to infinity. This requires slightly different representations for different regions of the x variable and leads to different series in these regions. For example, for

$$I_n^{++} = \int_0^\infty \frac{\cos[kg]\cos[kx]}{(kg)^2 - [(n-1/2)\pi]^2} \frac{\sinh[k(t-y)]}{\sinh[kt]} dk, \tag{5.1}$$

consider

$$\int_C f(z)dz = \int_C \frac{\cos[zg]\cos[zx]}{(zg)^2 - [(n-1/2)\pi]^2} \frac{\sinh[z(t-y)]}{\sinh[zt]} dz \tag{5.2}$$

along a closed contour, C, consisting of the line along the x axis from -R to R and the semi-circle Γ above the x axis having this line as diameter as shown in Fig. 43 (the contour is actually coincident with the x axis but is shown separate for visual purposes).

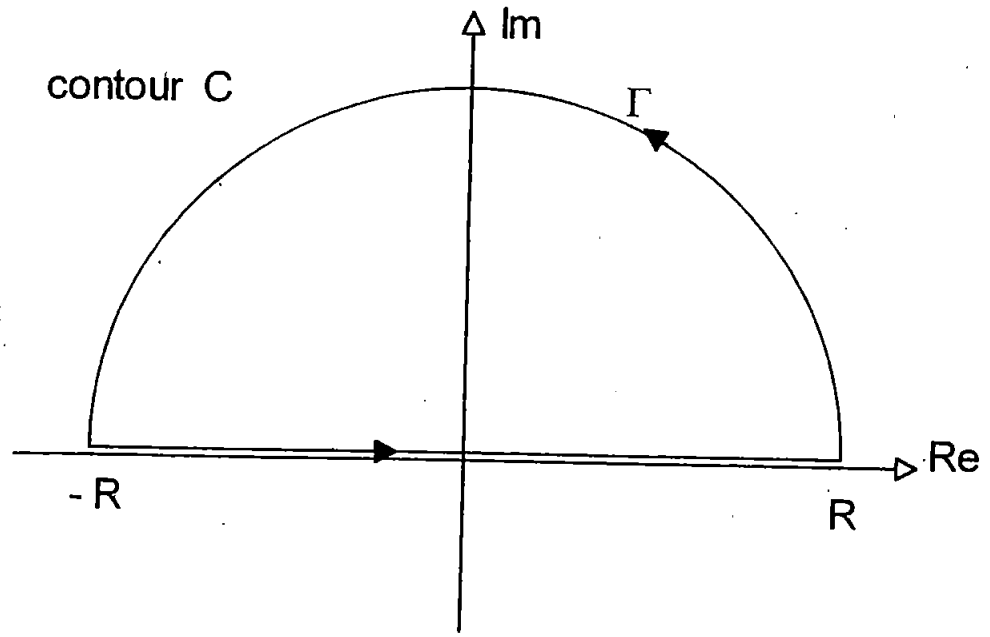

Figure 43. Semi-circular contour of integration.

When $x \leq g$ we write the product of the cosine terms as $0.5\mathrm{Re}[e^{i(g+x)z} + e^{i(g-x)z}] = 0.5[e^{-y(g+x)} + e^{-y(g-x)}]$, while if $x \geq g$ we take $0.5\mathrm{Re}[e^{i(g+x)z} + e^{i(x-g)z}] = 0.5[e^{-y(g+x)} + e^{-y(x-g)}]$. These representations ensure that $\int_\Gamma f(z)dz$ approaches zero as $\mathrm{R} \to \infty$. The poles due to the hyperbolic sine term lie on the positive imaginary

axis at integer multiples of π/t, and are enclosed by the contour. The poles that lie on the real axis at $z = \pm(n - 1/2)\pi/g$ are accommodated by modifying the contour using two semi-circular indents as shown in Fig. 44.

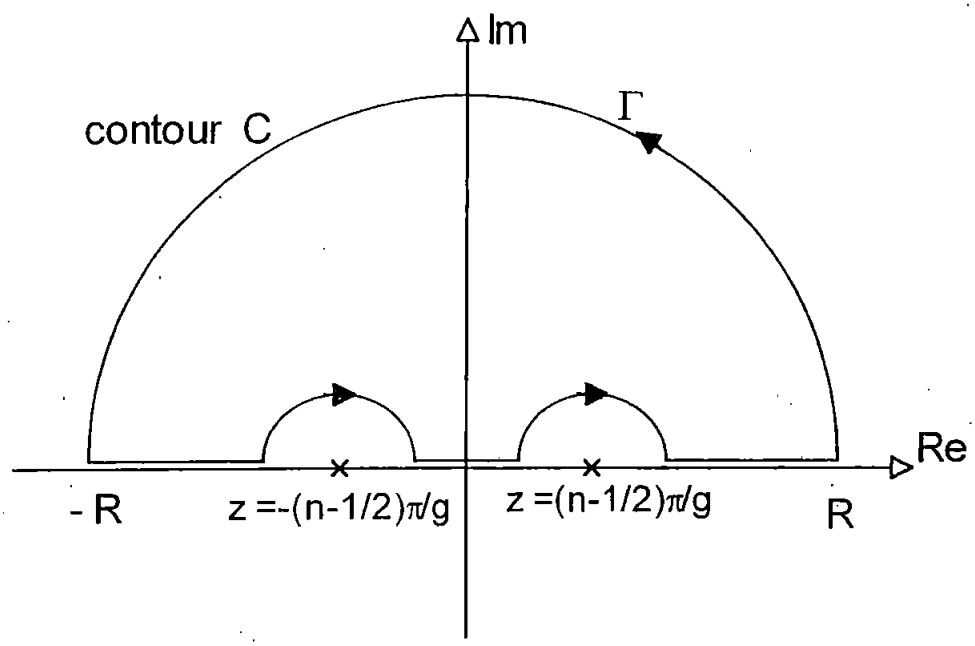

Figure 44. Indented semi-circular contour of integration.

The residue theorem then gives the result

$$\int_{k=-\infty}^{\infty} \frac{\cos[kg]\cos[kx]}{(kg)^2 - [(n-1/2)\pi]^2} \frac{\sinh[k(t-y)]}{\sinh[kt]} dk$$
$$= 2\pi i \sum \text{residues due to poles on imaginary axis}$$
$$+ \pi i \sum \text{residues due to poles on real axis} \qquad (5.3)$$

and since the integrand is an even function,

$$\int_{k=0}^{\infty} \frac{\cos[kg]\cos[kx]}{(kg)^2 - [(n-1/2)\pi]^2} \frac{\sinh[k(t-y)]}{\sinh[kt]} dk$$
$$= \pi i \sum \text{residues due to poles on imaginary axis}$$
$$+ \frac{\pi i}{2} \sum \text{residues due to poles on real axis.} \qquad (5.4)$$

Evaluating the residues gives the required results. For $x \le g$,

$$I_n^{++} = \frac{-t}{2\pi}\sum_{p=1}^{\infty}\frac{e^{-p\pi(g-x)/t}(1+e^{-2p\pi x/t})}{(pg)^2+[(n-1/2)t]^2}\sin\left[\frac{p\pi y}{t}\right] + \frac{(-1)^n\cos\left[(n-1/2)\pi x/g\right]}{2g(n-1/2)}\frac{\sinh\left[(n-1/2)\pi(t-y)/g\right]}{\sinh\left[(n-1/2)\pi t/g\right]} \qquad (5.5a)$$

and for $x \ge g$,

$$I_n^{++} = \frac{-t}{2\pi}\sum_{p=1}^{\infty}\frac{e^{-p\pi(x-g)/t}(1+e^{-2p\pi g/t})}{(pg)^2+[(n-1/2)t]^2}\sin\left[\frac{p\pi y}{t}\right]. \qquad (5.5b)$$

Similarly for

$$J_n^{++} = \int_0^{\infty}\frac{\sin\left[k(g+L+h)\right]\sin\left[kh\right]\cos\left[kx\right]}{(kh)^2-(n\pi)^2}\frac{\sinh\left[k(t-y)\right]}{\sinh\left[kt\right]}dk \qquad (5.6)$$

for $x \le g+L$,

$$J_n^{++} = \frac{t}{4\pi}\sum_{p=1}^{\infty}\frac{e^{-p\pi(g+L-x)/t}(e^{-2p\pi h/t}-1)(1+e^{-2p\pi x/t})}{(ph)^2+(nt)^2}\sin\left[\frac{p\pi y}{t}\right] + \begin{cases} 0 & \text{if } n \ne 0 \\ \frac{\pi}{2h}\left(\frac{t-y}{t}\right) & \text{if } n = 0\,, \end{cases} \qquad (5.7a)$$

for $g+L \le x \le g+L+H$,

$$J_n^{++} = \frac{t}{4\pi}\sum_{p=1}^{\infty}\left[\frac{e^{-p\pi(g+L+H-x)/t}(1+e^{-2p\pi x/t})-e^{-p\pi(x-g-L)/t}(1+e^{-2p\pi(g+L)/t})}{(ph)^2+(nt)^2}\right]\sin\left[\frac{p\pi y}{t}\right] - \begin{cases} \frac{1}{4nh}\frac{\sin\left[n\pi(x-g-L)/h\right]\sinh\left[n\pi(t-y)/h\right]}{\sinh\left[n\pi t/h\right]} & \text{if } n \ne 0 \\ \frac{\pi}{4h^2}(x-g-L-H)\left(\frac{t-y}{t}\right) & \text{if } n = 0 \end{cases} \qquad (5.7b)$$

and for $x \ge g+L+H$,

$$J_n^{++} = \frac{t}{4\pi}\sum_{p=1}^{\infty}\frac{e^{-p\pi(x-g-L-H)/t}(1-e^{-2p\pi(g+L+h)/t})(1-e^{-2p\pi h/t})}{(ph)^2+(nt)^2}\sin\left[\frac{p\pi y}{t}\right]. \qquad (5.7c)$$

When there is no underlayer the ratio of the two sinh terms in these integrals is replaced by e^{-ky} and the above contour integration approach is no longer suitable. It is not possible simply to let t tend to infinity in the above results and obtain series

representations for these potential integrals. By taking a large value for t and enough terms of the series, approximate results can be found but it is preferable to proceed differently. All the potential integrals may be evaluated in terms of

$$J(\alpha,\beta,\gamma,\delta)=\int_0^\infty \frac{\sin[\beta k]\sin[\gamma k]e^{-\delta k}}{k^2-\alpha^2}dk \tag{5.8}$$

and

$$K(\alpha,\beta,\gamma,\delta)=\int_0^\infty \frac{\cos[\beta k]\cos[\gamma k]e^{-\delta k}}{k^2-\alpha^2}dk. \tag{5.9}$$

These integrals may be evaluated using standard results. For example

$$\begin{aligned} J(\alpha,\beta,\gamma,\delta) &= \int_0^\infty \frac{\sin[\beta k]\sin[\gamma k]\,e^{-\delta k}}{k^2-\alpha^2}dk \\ &= \frac{1}{2}\left\{\int_0^\infty \frac{\cos[(\beta-\gamma)k]\,e^{-\delta k}}{k^2-\alpha^2}\,dk - \int_0^\infty \frac{\cos[(\beta+\gamma)k]\,e^{-\delta k}}{k^2-\alpha^2}\,dk\right\} \\ &= \frac{1}{2}\mathrm{Re}\left\{\int_0^\infty \frac{e^{-pk}}{k^2-\alpha^2}\,dk - \int_0^\infty \frac{e^{-qk}}{k^2-\alpha^2}\,dk\right\}, \end{aligned} \tag{5.10}$$

where $p=\delta-i(\beta-\gamma)$ and $q=\delta-i(\beta+\gamma)$.

For $\alpha,\beta,\gamma,\delta>0$ it may be shown that [47, 3.354.3],

$$\int_0^\infty \frac{e^{-\mu k}}{k^2-\alpha^2}\,dk=\frac{1}{2\alpha}\left[e^{\alpha\mu}\,\mathrm{E}_1(\alpha\mu)-e^{-\alpha\mu}\left[\mathrm{E}_1(-\alpha\mu)+i\pi\right]\right], \tag{5.11}$$

where $\mathrm{E}_1(z)$ is the complex exponential integral defined in Appendix A, which may be evaluated from a series expansion for 'small' arguments [48] and by Laguerre integration for 'large' arguments [49]. Using this result in (5.10) gives,

$$\begin{aligned} J(\alpha,\beta,\gamma,\delta) &= \frac{1}{4\alpha}\mathrm{Re}\left[e^{-\alpha p}\,\mathrm{E}_1(-\alpha p)-e^{\alpha p}\,\mathrm{E}_1(\alpha p)-e^{-\alpha q}\,\mathrm{E}_1(-\alpha q)+e^{\alpha q}\,\mathrm{E}_1(\alpha q)\right] \\ &\quad + i\pi\left[e^{-\alpha p}-e^{-\alpha q}\right] \\ &= \frac{1}{4\alpha}\mathrm{Re}\left[e^{-\alpha p}\,\mathrm{E}_1(-\alpha p)-e^{\alpha p}\,\mathrm{E}_1(\alpha p)-e^{-\alpha q}\,\mathrm{E}_1(-\alpha q)+e^{\alpha q}\,\mathrm{E}_1(\alpha q)\right] \\ &\quad + \frac{\pi}{2\alpha}e^{-\alpha\delta}\begin{cases}\cos[\alpha\beta]\sin[\alpha\gamma] & \text{if } \beta\geq\gamma \\ \sin[\alpha\beta]\cos[\alpha\gamma] & \text{if } \beta<\gamma,\end{cases} \end{aligned} \tag{5.12}$$

When $\alpha=0$, (5.10) may be evaluated using the result [47, 3.948.3]

$$\begin{aligned} \int_0^\infty \frac{e^{-\delta k}\left\{\cos[ak]-\cos[bk]\right\}}{k^2}\,dk &= \frac{\delta}{2}\log\left[\frac{a^2+\delta^2}{b^2+\delta^2}\right]+b\arctan\left[\frac{b}{\delta}\right] \\ &\quad -a\arctan\left[\frac{a}{\delta}\right], \end{aligned} \tag{5.13}$$

to give

$$J(0,\beta,\gamma,\delta) = \frac{\delta}{4}\log\left[\frac{(\beta-\gamma)^2+\delta^2}{(\beta+\gamma)^2+\delta^2}\right] + \left(\frac{\beta+\gamma}{2}\right)\arctan\left[\frac{\beta+\gamma}{\delta}\right] - \left(\frac{\beta-\gamma}{2}\right)\arctan\left[\frac{\beta-\gamma}{\delta}\right], \tag{5.14}$$

and for $\alpha,\delta>0$, $J(\alpha,\beta,\gamma,\delta)=J(\alpha,|\beta|,|\gamma|,\delta)\,\mathrm{sign}(\beta)\,\mathrm{sign}(\gamma)$. The results for (5.8) given in [14] are for the particular case of $\alpha\beta$ being an integer multiple of π and contain some typographical errors.

Using a similar approach for $K(\alpha,\beta,\gamma,\delta)$ produces, for $\alpha,\beta,\gamma,\delta>0$,

$$K(\alpha,\beta,\gamma,\delta) = \frac{1}{4\alpha}\mathrm{Re}\left[e^{-\alpha p}\,\mathrm{E}_1(-\alpha p) - e^{\alpha p}\,\mathrm{E}_1(\alpha p) + e^{-\alpha q}\,\mathrm{E}_1(-\alpha q) - e^{\alpha q}\,\mathrm{E}_1(\alpha q)\right] - \frac{\pi}{2\alpha}e^{-\alpha\delta}\begin{cases}\sin[\alpha\beta]\cos[\alpha\gamma] & \text{if } \beta\geq\gamma\\ \cos[\alpha\beta]\sin[\alpha\gamma] & \text{if } \beta<\gamma,\end{cases} \tag{5.15}$$

and for $\alpha,\delta>0$, $K(\alpha,\beta,\gamma,\delta)=K(\alpha,|\beta|,|\gamma|,\delta)$. Then, for example

$$\begin{aligned} I_n^{++} &= \int_{k=0}^{\infty}\frac{\cos[kg]\cos[kx]\,e^{-ky}}{(kg)^2-[(n-1/2)\pi]^2}dk \\ &= \frac{1}{g^2}\int_{k=0}^{\infty}\frac{\cos[kg]\cos[kx]\,e^{-ky}}{k^2-[(n-1/2)\pi/g]^2}dk \\ &= \frac{1}{g^2}K((n-1/2)\pi/g,x,g,y) \end{aligned} \tag{5.16}$$

and

$$\begin{aligned} J_n^{++} &= \int_{k=0}^{\infty}\frac{\sin[k(g+L+h)]\sin[kh]\cos[kx]\,e^{-ky}}{(kh)^2-(n\pi)^2}dk \\ &= \frac{1}{2h^2}\int_{k=0}^{\infty}\frac{\sin[k(g+L+h+x)]\sin[kh]\,e^{-ky}}{k^2-(n\pi/h)^2}dk \\ &\quad + \frac{1}{2h^2}\int_{k=0}^{\infty}\frac{\sin[k(g+L+h-x)]\sin[kh]\,e^{-ky}}{k^2-(n\pi/h)^2}dk \\ &= \frac{1}{2h^2}\Big[J(n\pi/h,g+L+h+x,h,y) \\ &\quad + J(n\pi/h,g+L+h-x,h,y)\Big]. \end{aligned} \tag{5.17}$$

By writing

$$\frac{\sinh[k(t-y)]}{\sinh[kt]} = \frac{e^{k[t-y]}-e^{-k[t-y]}}{e^{kt}-e^{-kt}}$$

$$
\begin{aligned}
&= \frac{e^{-ky} - e^{-k[2t-y]}}{1 - e^{-2kt}} \\
&= (e^{-ky} - e^{-k[2t-y]})(1 - e^{-2kt})^{-1} \\
&= (e^{-ky} - e^{-k[2t-y]})(1 + e^{-2kt} + e^{-4kt} + \dots) \\
&= \sum_{m=0}^{\infty} e^{-k[2mt+y]} - e^{-k[2(m+1)t-y]}, \qquad (5.18)
\end{aligned}
$$

all the potential integrals when there is an underlayer may alternatively be written as infinite series of the $J(\alpha, \beta, \gamma, \delta)$ and $K(\alpha, \beta, \gamma, \delta)$ functions. For example,

$$
I_n^{++} = \frac{1}{g^2} \sum_{m=0}^{\infty} K((n-1/2)\pi/g, x, g, 2mt + y) - K((n-1/2)\pi/g, x, g, 2(m+1)t - y) \qquad (5.19)
$$

and

$$
\begin{aligned}
J_n^{++} &= \frac{1}{2h^2} \sum_{m=0}^{\infty} J(n\pi/h, g + L + h + x, h, 2mt + y) \\
&\quad + J(n\pi/h, g + L + h - x, h, 2mt + y) \\
&\quad - J(n\pi/h, g + L + h + x, h, 2(m+1)t - y) \\
&\quad - J(n\pi/h, g + L + h - x, h, 2(m+1)t - y). \qquad (5.20)
\end{aligned}
$$

However, such series do not converge particularly fast and it is certainly preferable to use the series (5.5) and (5.7) derived previously.

5.2.2. Field Integrals

The field integrals when an underlayer is present cannot be evaluated directly using contour integration as in the previous section since the relevant complex functions do not tend to zero sufficiently fast on the semi-circular arc as its radius tends to infinity. However, they may be evaluated simply by differentiating the series for the potential. For example, $M_n^{++} = -\partial J_n^{++}/\partial x$ and $Q_n^{++} = -\partial J_n^{++}/\partial y$.

When there is no underlayer the series obtained above may be used with large values of t but it is better to treat these integrals directly, as for the potential integrals. All the field integrals may be written in terms of

$$
L(\alpha, \beta, \gamma, \delta) = \int_0^{\infty} \frac{k \sin[\beta k] \sin[\gamma k] e^{-\delta k}}{k^2 - \alpha^2} dk, \qquad (5.21)
$$

$$M(\alpha,\beta,\gamma,\delta) = \int_0^\infty \frac{k\sin[\beta k]\cos[\gamma k]e^{-\delta k}}{k^2-\alpha^2}dk \tag{5.22}$$

and

$$N(\alpha,\beta,\gamma,\delta) = \int_0^\infty \frac{k\cos[\beta k]\cos[\gamma k]e^{-\delta k}}{k^2-\alpha^2}dk. \tag{5.23}$$

To evaluate these integrals the same procedure is used as previously for the potential integrals (5.8) and (5.9). For example

$$\begin{aligned} L(\alpha,\beta,\gamma,\delta) &= \int_0^\infty \frac{k\sin[\beta k]\sin[\gamma k]\,e^{-\delta k}}{k^2-\alpha^2}dk \\ &= \frac{1}{2}\left\{\int_0^\infty \frac{k\cos[(\beta-\gamma)k]\,e^{-\delta k}}{k^2-\alpha^2}\,dk - \int_0^\infty \frac{k\cos[(\beta+\gamma)k]\,e^{-\delta k}}{k^2-\alpha^2}\,dk\right\} \\ &= \frac{1}{2}\mathrm{Re}\left\{\int_0^\infty \frac{ke^{-pk}}{k^2-\alpha^2}\,dk - \int_0^\infty \frac{ke^{-qk}}{k^2-\alpha^2}\,dk\right\}. \end{aligned} \tag{5.24}$$

where p and q are as defined earlier. The appropriate result [47, 3.354.4] in this case is

$$\int_0^\infty \frac{ke^{-\mu k}}{k^2-\alpha^2}\,dk = \frac{1}{2}\left[e^{\alpha\mu}\,\mathrm{E}_1(\alpha\mu) + e^{-\alpha\mu}\left[\mathrm{E}_1(-\alpha\mu) + i\pi\right]\right], \tag{5.25}$$

which produces, for $\alpha,\beta,\gamma,\delta > 0$,

$$\begin{aligned} L(\alpha,\beta,\gamma,\delta) &= \frac{1}{4}\mathrm{Re}\left[e^{-\alpha p}\,\mathrm{E}_1(-\alpha p) + e^{\alpha p}\,\mathrm{E}_1(\alpha p) - e^{-\alpha q}\,\mathrm{E}_1(-\alpha q) - e^{\alpha q}\,\mathrm{E}_1(\alpha q)\right] \\ &\quad + \frac{\pi}{2}e^{-\alpha\delta}\begin{cases} \cos[\alpha\beta]\sin[\alpha\gamma] & \text{if } \beta \geq \gamma \\ \sin[\alpha\beta]\cos[\alpha\gamma] & \text{if } \beta < \gamma. \end{cases} \end{aligned} \tag{5.26}$$

When $\alpha = 0$, the appropriate result [47, 3.948.2] is

$$\int_0^\infty \frac{e^{-\delta k}\left\{\cos[ak] - \cos[bk]\right\}}{k}\,dk = \frac{1}{2}\log\left[\frac{b^2+\delta^2}{a^2+\delta^2}\right], \tag{5.27}$$

from which it follows that

$$L(0,\beta,\gamma,\delta) = \frac{1}{4}\log\left[\frac{(\beta+\gamma)^2+\delta^2}{(\beta-\gamma)^2+\delta^2}\right] \tag{5.28}$$

and if not both of β and γ are positive, $L(\alpha,\beta,\gamma,\delta) = L(\alpha,|\beta|,|\gamma|,\delta)\,\mathrm{sign}(\beta)\,\mathrm{sign}(\gamma)$.

The integrals (5.22) and (5.23) may be treated similarly. For $\alpha,\beta,\gamma,\delta > 0$,

$$\begin{aligned} M(\alpha,\beta,\gamma,\delta) &= \frac{1}{4}\mathrm{Im}\left[e^{-\alpha p}\,\mathrm{E}_1(-\alpha p) + e^{\alpha p}\,\mathrm{E}_1(\alpha p) + e^{-\alpha q}\,\mathrm{E}_1(-\alpha q) + e^{\alpha q}\,\mathrm{E}_1(\alpha q)\right] \\ &\quad + \frac{\pi}{2}e^{-\alpha\delta}\begin{cases} \cos[\alpha\beta]\cos[\alpha\gamma] & \text{if } \beta \geq \gamma \\ -\sin[\alpha\beta]\sin[\alpha\gamma] & \text{if } \beta < \gamma, \end{cases} \end{aligned} \tag{5.29}$$

$$M(0,\beta,\gamma,\delta) = \frac{1}{2}\arctan\left[\frac{\beta+\gamma}{\delta}\right] + \frac{1}{2}\arctan\left[\frac{\beta-\gamma}{\delta}\right] \tag{5.30}$$

and if not both of β and γ are positive, $M(\alpha,\beta,\gamma,\delta) = M(\alpha,|\beta|,|\gamma|,\delta)\,\mathrm{sign}(\beta)$.

For $\alpha,\beta,\gamma,\delta > 0$,

$$\begin{aligned} N(\alpha,\beta,\gamma,\delta) &= \frac{1}{4}\mathrm{Re}\Big[e^{-\alpha p}\,\mathrm{E}_1(-\alpha p) + e^{\alpha p}\,\mathrm{E}_1(\alpha p) + e^{-\alpha q}\,\mathrm{E}_1(-\alpha q) + e^{\alpha q}\,\mathrm{E}_1(\alpha q)\Big] \\ &\quad -\frac{\pi}{2}e^{-\alpha\delta}\begin{cases} \sin[\alpha\beta]\cos[\alpha\gamma] & \text{if } \beta \geq \gamma \\ \cos[\alpha\beta]\sin[\alpha\gamma] & \text{if } \beta < \gamma \end{cases} \end{aligned} \tag{5.31}$$

and $N(\alpha,\beta,\gamma,\delta) = N(\alpha,|\beta|,|\gamma|,\delta)$. Then, for example,

$$\begin{aligned} L_n^{-+} &= \int_0^\infty \frac{k\sin[kg]\cos[kx]\,e^{-ky}}{(kg)^2-(n\pi)^2}dk \\ &= \frac{1}{g^2}M(n\pi/g,g,x,y) \end{aligned} \tag{5.32}$$

and

$$\begin{aligned} Q_n^{++} &= \int_{k=0}^\infty \frac{k\sin[k(g+L+h)]\sin[kh]\cos[kx]\,e^{-ky}}{(kh)^2-(n\pi)^2}dk \\ &= \frac{1}{2h^2}\int_{k=0}^\infty \frac{k\sin[k(g+L+h+x)]\sin[kh]\,e^{-ky}}{k^2-(n\pi/h)^2}dk \\ &\quad + \frac{1}{2h^2}\int_{k=0}^\infty \frac{k\sin[k(g+L+h-x)]\sin[kh]\,e^{-ky}}{k^2-(n\pi/h)^2}dk \\ &= \frac{1}{2h^2}\Big[L(n\pi/h,g+L+h+x,h,y) \\ &\quad + L(n\pi/h,g+L+h-x,h,y)\Big]. \end{aligned} \tag{5.33}$$

As for the potential integrals, by writing

$$\begin{aligned} \frac{\cosh[k(t-y)]}{\sinh[kt]} &= \frac{e^{k[t-y]}+e^{-k[t-y]}}{e^{kt}-e^{-kt}} \\ &= \frac{e^{-ky}+e^{-k[2t-y]}}{1-e^{-2kt}} \\ &= (e^{-ky}+e^{-k[2t-y]})(1-e^{-2kt})^{-1} \\ &= (e^{-ky}+e^{-k[2t-y]})(1+e^{-2kt}+e^{-4kt}+\dots) \\ &= \sum_{m=0}^\infty e^{-k[2mt+y]}+e^{-k[2(m+1)t-y]} \end{aligned} \tag{5.34}$$

all the field integrals, when there is an underlayer, may alternatively be written as infinite series of the $L(\alpha,\beta,\gamma,\delta)$, $M(\alpha,\beta,\gamma,\delta)$ and $N(\alpha,\beta,\gamma,\delta)$ functions. For example,

$$L_n^{-+} = \frac{1}{g^2}\sum_{m=0}^{\infty} M(n\pi/g, g, x, 2mt+y) - M(n\pi/g, g, x, 2(m+1)t-y) \qquad (5.35)$$

and

$$\begin{aligned} Q_n^{++} \;=\; & \frac{1}{2h^2}\sum_{m=0}^{\infty} L(n\pi/h, g+L+h+x, h, 2mt+y) \\ & +L(n\pi/h, g+L+h-x, h, 2mt+y) \\ & +L(n\pi/h, g+L+h+x, h, 2(m+1)t-y) \\ & +L(n\pi/h, g+L+h-x, h, 2(m+1)t-y). \end{aligned} \qquad (5.36)$$

But series derived in this way do not converge as fast as those obtained by differentiating series such as (5.5) and (5.7). Results for (5.21) and (5.22) are given in [14] when $\alpha\beta$ is an integer multiple of π. The result (5.33) with $n = 0$ and for the case of a single shielded pole ($g = 0$) has been given in [50] where the leading term only ($n = 0$) of the vertical field is computed.

5.2.3. Coefficient Integrals

The results given in [45] are for the integrals required to determine the coefficients in the Fourier expansions in the case of a head with an underlayer. An alternative derivation of those results is via complex contour integration, the appropriate contour again being an infinitely large semi-circle in the upper-half complex plane with the diameter being the real axis. The infinite series arise from the poles of $\sinh[zt]$ on the positive imaginary axis and the additional terms needed when $m = n$ are due to poles on the real axis. When no underlayer is present ($t = \infty$ and $\coth[kt]$ is replaced by unity) those expressions may be used to give reasonably accurate results if t is made sufficiently large and enough terms of the series are taken. However, a more reliable approach in this case is to write the integrals in terms of the sine and cosine integrals, $\mathrm{Si}(x)$ and $\mathrm{Ci}(x)$ respectively [48], e.g. I_{mn}^{-+} (apart from a factor of

g^2) was given in [9] for the three cases $m \neq n$ and $m, n \neq 0$; $m = n \neq 0$; $m \neq 0$ and $n = 0$. The other coefficient integrals may be evaluated similarly although they do lead to more complicated expressions. For example, for

$$J_{mn}^{-+} = \int_0^\infty \frac{k \cos[k(g+L+h)] \sin[kh] \sin[kg]}{[(kg)^2 - (m\pi)^2][(kh)^2 - (n\pi)^2]}\, dk \ , \tag{5.37}$$

the trigonometric terms in the numerator are written as the sum of cosine functions,

$$\begin{aligned}
&\cos[k(g+L+h)] \sin[kh] \sin[kg] \\
&= \frac{1}{2}\Big\{\sin[k(g+L+H)] - \sin[k(g+L)]\Big\} \sin[kg] \\
&= \frac{1}{4}\Big\{\cos[k(L+H)] + \cos[k(G+L)] - \cos[k(G+L+H)] - \cos[kL]\Big\} \ ,
\end{aligned} \tag{5.38}$$

and the remaining terms in the integrand are split using partial fractions,

$$\begin{aligned}
&\frac{k}{[(kg)^2 - (m\pi)^2][(kh)^2 - (n\pi)^2]} \\
&= \frac{1}{g^2h^2[(m\pi/g)^2 - (n\pi/h)^2]}\left\{\frac{k}{[k^2 - (m\pi/g)^2]} - \frac{k}{[k^2 - (n\pi/h)^2]}\right\} \\
&= \frac{1}{\pi^2[(mh)^2 - (ng)^2]}\left\{\frac{k}{[k^2 - (m\pi/g)^2]} - \frac{k}{[k^2 - (n\pi/h)^2]}\right\} .
\end{aligned} \tag{5.39}$$

Combining (5.35) and (5.36), allows J_{mn}^{-+} to be written as eight separate integrals, each of the form

$$P(\alpha, \beta) = \int_0^\infty \frac{k \cos[\beta k]}{\alpha^2 - k^2}\, dk \ . \tag{5.40}$$

For $\alpha, \beta > 0$ it may be shown that [47, 3.723.11],

$$P(\alpha, \beta) = \cos(\alpha\beta)\mathrm{Ci}(\alpha\beta) + \sin(\alpha\beta)\mathrm{Si}(\alpha\beta) \ , \tag{5.41}$$

which, for $mh \neq ng$ and $m, n \neq 0$, gives

$$J_{mn}^{-+} = \frac{1}{4\pi^2[(ng)^2 - (mh)^2]}[A - B] \ , \tag{5.42}$$

where

$$a_1 \ = \ m\pi(G+L)/g, \ a_2 = m\pi(L+H)/g, \ a_3 = m\pi(G+L+H)/g, \ a_4 = m\pi L/g,$$

$$
\begin{aligned}
b_1 &= n\pi(G+L)/h,\ b_2 = n\pi(L+H)/h,\ b_3 = n\pi(G+L+H)/h,\ b_4 = n\pi L/h,\\
A &= \cos(a_1)\mathrm{Ci}(a_1) + \sin(a_1)\mathrm{Si}(a_1) + \cos(a_2)\mathrm{Ci}(a_2) + \sin(a_2)\mathrm{Si}(a_2)\\
&\quad - \cos(a_3)\mathrm{Ci}(a_3) - \sin(a_3)\mathrm{Si}(a_3) - \cos(a_4)\mathrm{Ci}(a_4) - \sin(a_4)\mathrm{Si}(a_4),\\
B &= \cos(b_1)\mathrm{Ci}(b_1) + \sin(b_1)\mathrm{Si}(b_1) + \cos(b_2)\mathrm{Ci}(b_2) + \sin(b_2)\mathrm{Si}(b_2)\\
&\quad - \cos(b_3)\mathrm{Ci}(b_3) - \sin(b_3)\mathrm{Si}(b_3) - \cos(b_4)\mathrm{Ci}(b_4) - \sin(b_4)\mathrm{Si}(b_4). \qquad (5.43)
\end{aligned}
$$

For $mh = ng$ and $m \neq 0$, the trigonometric terms are written as the sum of four cosines as in (5.38). The other terms in the integrand are split using partial fractions

$$
\begin{aligned}
&\frac{k}{[(kg)^2 - (m\pi)^2][(kh)^2 - (mh\pi/g)^2]}\\
&= \frac{1}{g^2h^2}\left\{\frac{k}{[k^2 - (m\pi/g)^2][k^2 - (m\pi/g)^2]}\right\}\\
&= \frac{1}{4m\pi gh^2}\left\{\frac{1}{[k - (m\pi/g)]^2} - \frac{1}{[k + (m\pi/g)]^2}\right\} \qquad (5.44)
\end{aligned}
$$

which allows J^{-+}_{mn} to be expressed as the sum of eight separate integrals, each of the form

$$\int_0^\infty \frac{\cos[\beta k]}{(k \pm \alpha)^2}\, dk\,. \qquad (5.45)$$

Integration by parts on (5.45) produces

$$\pm\frac{1}{\alpha} - \beta\int_0^\infty \frac{\sin[\beta k]}{k \pm \alpha}\, dk\,. \qquad (5.46)$$

The integrals in (5.46) may be evaluated using standard results [47, 3.722.1, 3.722.5], for $\beta > 0$,

$$\int_0^\infty \frac{\sin[\beta k]}{k + \alpha}\, dk = \mathrm{Ci}(\alpha\beta)\sin(\alpha\beta) - \cos(\alpha\beta)\big[\mathrm{Si}(\alpha\beta) - \pi/2\big] \qquad (5.47)$$

and

$$\int_0^\infty \frac{\sin[\beta k]}{k - \alpha}\, dk = \cos(\alpha\beta)\big[\mathrm{Si}(\alpha\beta) + \pi/2\big] - \mathrm{Ci}(\alpha\beta)\sin(\alpha\beta)\,. \qquad (5.48)$$

Hence, for $mh = ng$ and $m \neq 0$,

$$
\begin{aligned}
J^{-+}_{mn} &= \frac{1}{8\pi mh^2g}\Big[(G+L)(\sin(a_1)\mathrm{Ci}(a_1) - \cos(a_1)\mathrm{Si}(a_1))\\
&\quad +(L+H)(\sin(a_2)\mathrm{Ci}(a_2) - \cos(a_2)\mathrm{Si}(a_2))\\
&\quad -(G+L+H)(\sin(a_3)\mathrm{Ci}(a_3) - \cos(a_3)\mathrm{Si}(a_3))\\
&\quad -L(\sin(a_4)\mathrm{Ci}(a_4) - \cos(a_4)\mathrm{Si}(a_4))\Big]. \qquad (5.49)
\end{aligned}
$$

For $m \neq 0$ and $n = 0$, the denominator is split using partial fractions,

$$\frac{k}{[(kg)^2 - (m\pi)^2][kh]^2} = \frac{1}{\pi m h^2}\left\{\frac{k}{[k^2 - (m\pi/g)^2]} - \frac{1}{k}\right\}. \tag{5.50}$$

The left-hand term within the braces is identical to that in (5.44) and is treated as previously. To proceed with the right-hand term the trigonometric functions in the numerator of the integrand are written as the difference of two products of sine functions,

$$\cos[k(g+L+h)]\sin[kh]\sin[kg] = \frac{1}{2}\Big\{\sin[k(g+L+H)]\sin[kg] - \sin[k(g+L)]\sin[kg]\Big\}, \tag{5.51}$$

which leads to two integrals of the form

$$R(\alpha,\beta) = \int_0^\infty \frac{\sin[\alpha k]\sin[\beta k]}{k}\, dk\,. \tag{5.52}$$

These integrals may be evaluated using the standard result [47, 3.741.1], for $\alpha, \beta > 0, \alpha \neq \beta$,

$$R(\alpha,\beta) = \frac{1}{4}\log\left(\frac{\alpha+\beta}{\alpha-\beta}\right)^2, \tag{5.53}$$

from which it follows that

$$J_{m0}^{-+} = \frac{1}{(2\pi m h)^2}\left[\log\left(\frac{(G+L)(L+H)}{L(G+L+H)}\right) - A\right]. \tag{5.54}$$

The results derived in this chapter allow very efficient computation of the integrals arising in exact Fourier method solutions, avoiding the need for numerical integration. They provide a reliable means of generating exact solutions and have proved particularly useful in the development and analysis of accurate approximations for a variety of different head configurations. For example, in [51] an approximation of the output of a shielded MR head for perpendicular media is presented and compared with the exact solution obtained by using the techniques given here and in [45]. Similarly, in [52] the results are used to evaluate the accuracy of a method for obtaining approximate field components for a variety of 2D perpendicular head geometries. In

[53] an alternative method for obtaining exact solutions for the magnetic potential for shielded pole heads is given, using non-orthogonal basis functions. The exact Fourier solution, using the results derived here, is again used to provide a measure of the accuracy of the results obtained.

5.3. Summary

In this chapter:

- The integrals arising in the two-dimensional models of shielded magnetoresistive heads presented in Chapter 3 are expressed either in terms of special functions or as rapidly convergent infinite series.
- In each case this provides an alternative and normally more efficient means of evaluation than direct numerical integration.

CHAPTER 6

CALCULATION OF THE SWITCHING CONSTANT OF MAGNETIC RECORDING MEDIA

6.1. Introduction

In this chapter the high speed switching behaviour of the following two different classes of magnetic recording media are investigated:

- modern thin film hard disk.
- single domain particulate recording tape.

The media are modelled by the use of suitable particle orientation distribution functions which are chosen to simulate the dynamic properties of each class. In section 6.2, an outline of high speed switching developments is given and a brief review of recent work of particular relevance to this thesis is presented. In section 6.3, the switching times for the media are computed by solving, numerically, the Landau-Lifshitz-Gilbert damped gyromagnetic precession equation detailed in Chapter 2. The results of these computations are then used, in section 6.4, to calculate the gyromagnetic switching constant of each media by utilizing the widely accepted expression developed by Thornley et al. [54] to describe the switching behaviour of various recording media. In section 6.5, the switching constants produced are discussed and compared with published experimental values for different media.

6.2. Overview of High Speed Switching

In rigid disk drives with thin film heads, data rates of 500 mega-bits per second are commonplace today. It is almost certain that 750 Mbit/s rate products will appear shortly and data rates of 1 Gbit/s (1000 Mbit/s) have already been reported

in development. In digital tape drives, the maximum data rates are considerably slower, being in the 100-200 Mbit/s range, because of the lower bit density capability and lower linear speed.

These developments have led to renewed interest in the high speed switching behavior of recording media. When the switching time is longer than, say, 5 nanoseconds, corresponding to a 200 Mbit/s rate, it is generally acknowledged that thermal energy has the major controlling influence on the switching behavior. The smaller the single domain magnetic particle or grain, the greater is the effect of thermal energy on switching. Media with small grains of low anisotropy material have coercivities that increase markedly with decreases in the switching time; such media are said to have 'high viscosity'.

On the other hand, when switching times are less than, say, 1 nanosecond, the process is predominantly controlled by gyro-magnetic precession, because there is too little time available for thermal energy to have an appreciable effect. In this regime, termed adiabatic, the switching time depends upon the damping constant, which converts the (Zeeman) magnetic energy of the electron spin system to thermal (hysteresis) energy in the lattice.

The first measurements of the adiabatic switching of (γ-Fe_2O_3) magnetic recording media were performed by Thornley et al. in the early 1970s [54]. They discovered that the switching behavior could be fitted well to the expression,

$$T_s = \frac{S_w}{H_a - H_0} \tag{6.1}$$

where T_s is the switching time, H_a is the applied field, H_0 is a threshold field and S_w is defined as the switching constant. The threshold field H_0 is related to both the anisotropy field and the coercivity of the medium.

The fact that a high (500 Oe) coercivity material such as γ-Fe_2O_3 had a well defined switching constant was, at the time, surprising. Previously, this behavior had been known only in the low (1-10 Oe) coercivity ferrite and thin Permalloy film materials used in the random access memories of early computers. Many authors have since commented upon the universality of the switching constant concept in both soft (low H_c) and hard (high H_c) magnetic materials [55].

More recently, He, Doyle and co-workers have extended the experimental technique of Thornley and have reported upon the switching constant of modern recording media, including metal particle (MP), metal evaporated (ME), barium ferrite and chromium dioxide tapes [56] and high coercivity thin films [57].

Despite all this activity on the switching constant of magnetic recording media, there does not appear to have been an attempt to calculate the switching constant directly from the damped gyro-magnetic precession equation, as is undertaken in this chapter.

Here the Gilbert form [10] of the damped gyro-magnetic equation is used to calculate the switching constant of two different classes of magnetic recording media. The first class is intended to simulate a modern thin film hard disk, where the individual single domain magnetic grains, though not oriented in the plane of the disk, all have their anisotropy axes lying in the plane of the disk. In other words, the easy axes of the grains are oriented at random in the plane of the disk. This arrangement of grains will be termed '2-D random'.

In the second class of media, meant to simulate a single domain particulate recording tape, the easy axes of the particles are partially oriented, with cylindrical symmetry, along a direction lying in the plane of the tape. Suitable angular distribution functions can be found in the literature; they are based upon numerical fits to, for example, the angular variation of the maximum remanence. Generally, a well-oriented tape will have greater than 90% of the particle easy axes lying within a cone of semi-angle 30° around the orientation direction. This arrangement of grains will be termed '3-D oriented'.

For both classes of media it is assumed that the individual grains or particles switch independently. That is to say, it is taken that both the magnetostatic interaction fields and exchange fields between the grains and particles may be ignored. As the coercivity and anisotropy field of modern media increase compared to the moment density, the omission of the magnetostatic interactions becomes an increasingly valid approximation. In thin film disks, inter-grain exchange coupling is kept low because it is known that such coupling reduces the signal-to-noise ratio

of the medium. In particulate tapes, exchange coupling between particles is unlikely because the individual particles are separated by the plastic binder system.

In both classes of media, the solution of the damped Gilbert equation is computed numerically, following the formalism of Gillette and Oshima [58], for the range of damping constants $0.2 \leq \alpha \leq 2.0$. Low damping constant solutions have a great deal of precession and long switching times. The critical damping constant, $\alpha = 1$, yields the shortest switching time with little precession.

In a recent paper, Mallinson [59] showed that when the applied field direction and the anisotropy axis of a single domain grain or particle were parallel, the damped Gilbert equation could be solved analytically. However, it has not been found possible to extend that analytical solution to the general case where the field direction and the anisotropy axis are not co-linear.

In the 2-D random thin film disk case the solution of the damped Gilbert equation is computed numerically for 100 sampled grain orientations from 0° to 90°. The switching time computed is the time taken for the slowest one of 90% of the grains' magnetization vectors to cross their uniaxial anisotropy hard equatorial planes. The individual grain switching times for the 2-D random set of grains are, of course, given equal weighting.

In the 3-D oriented tape case, the switching times are calculated with the appropriate weighting for the cylindrically symmetric array of particles.

The results of these calculations are displayed in two ways. First, the reciprocal of the switching time is plotted versus $H_a - H_k$, where H_k is the anisotropy field (2K/M for uniaxial magnetocrystalline and $M(N_\perp\text{-}N_{||})$ for uniaxial shape anisotropies). It will be noted that the resultant curves are very nearly straight lines, indicating that, indeed, a switching constant as defined above does exist. Second, switching constants, which are proportional to the reciprocal of the slopes of these curves, are plotted versus the damping constant α. It is found that not only are the calculated values of S_w in fairly good accord with the recent experimental results but also that the lowest values of S_w occur close to the critical value ($\alpha = 1$) of the damping constant.

6.3. Theoretical Model

Consider a single domain particle made of a magnetic material which has uniaxial magnetocrystalline anisotropy, a uniform magnetization $\mathbf{M}$, taken here to have a constant magnitude $M = 1000$, and an easy axis aligned with the z direction (Fig. 45). The choice of $M = 1000$ is arbitrary and although it does affect the 'reduced time', τ, defined after (6.3) and used in several of the figures, it has no effect upon the values of S_w calculated here using (6.8). The dynamic behavior of the particle's magnetization vector $\mathbf{M}$ is assumed to evolve in time as described by the Gilbert form [10] (L-L-G) of the Landau-Lifshitz equation:

$$\frac{d\mathbf{M}}{dt} = -\gamma(\mathbf{M} \times \mathbf{H}_T) + \frac{\alpha}{M}(\mathbf{M} \times \frac{d\mathbf{M}}{dt}) \tag{6.2}$$

where $\gamma \simeq 1.76 \times 10^7$ rad Oe^{-1} sec^{-1} is the magnetomechanical or gyromagnetic ratio and α is the phenomenological damping constant. $\mathbf{H}_T = (H_{Tx}, H_{Ty}, H_{Tz})$ is the vector sum of the effective anisotropy field, $\mathbf{H}_k = (H_{kx}, H_{ky}, H_{kz})$, and the external field, $\mathbf{H}_a = (H_{ax}, H_{ay}, H_{az})$, and it represents the total effective field acting on $\mathbf{M}$. The anisotropy may be thought of as a fictitious field $H_k \cos\theta$ acting in the easy axis direction, that is $\mathbf{H}_k = (0, 0, H_k \cos\theta)$, from which it follows that $\mathbf{H}_T = (H_{ax}, H_{ay}, H_{az} + H_k \cos\theta)$. Gillette and Oshima [58] showed that the L-L-G equation may be expressed, in the spherical polar coordinate system of Fig. 45, as the two coupled first order differential equations:

$$\begin{aligned} \sin\theta \frac{d\varphi}{d\tau} &= F_1 + \alpha F_2 \\ \frac{d\theta}{d\tau} &= F_2 - \alpha F_1, \end{aligned} \tag{6.3}$$

where

$$\begin{aligned} F_1 &= -\frac{H_{Tx}}{M}\cos\theta\cos\varphi - \frac{H_{Ty}}{M}\cos\theta\sin\varphi + \frac{H_{Tz}}{M}\sin\theta, \\ F_2 &= -\frac{H_{Tx}}{M}\sin\varphi + \frac{H_{Ty}}{M}\cos\varphi, \end{aligned}$$

and $\tau = M\gamma t/(1+\alpha^2)$ is the reduced time.

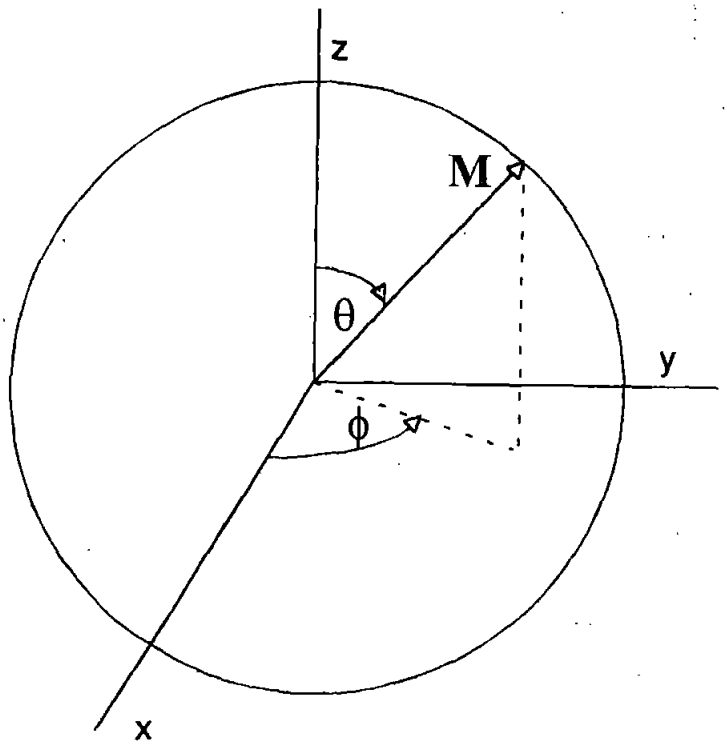

Figure 45. Coordinate system for a single grain.

Only in the case of the applied field and the anisotropy axis being co-linear, giving $F_2 = 0$, does it appear that an analytic solution to these equations can be found [59]. Numerical solutions to (6.3) have been computed [60], [61] by using numerical integration routines based on the Runge-Kutta method [62], as are the results here.

6.3.1. Thin Film Hard Disk Media

It has been shown [63] that the physical structure of longitudinal thin film media is realistically modeled by assuming that the uniaxial magnetocrystalline axes of the individual single domain grains are randomly distributed in the plane of the medium (2-D random). Each individual grain has its easy axis lying at an angle of between 0° and 90° to the applied field. This is shown in the schematic drawing of Fig. 46, in which the external field $\mathbf{H}_a$ is applied in the negative x direction and the

magnetizations M are aligned with the randomly distributed easy axes of the grains forming angles θ_p with the applied field. This is simulated by sampling 100 equally spaced angles between 0° and 90°. The switching time is then defined as the time taken for the slowest one of 90% of the magnetization vectors to achieve a polar angle of greater than 90°, at which time the removal of the applied field would result in 90% of the magnetization vectors precessing towards, and aligning with, the easy axis opposite to their initial direction.

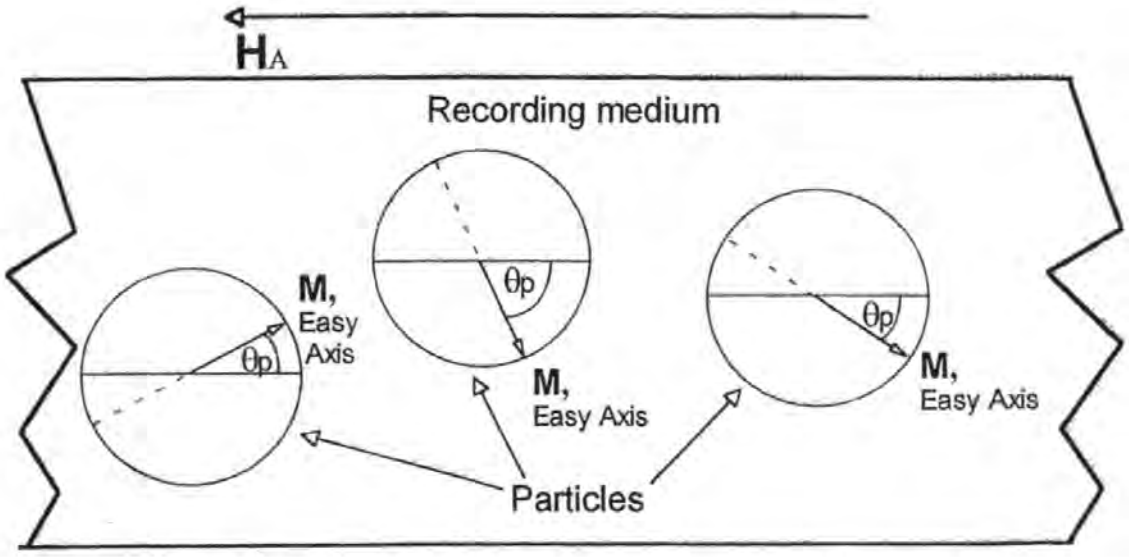

Figure 46. Randomly oriented grains in a thin film medium.

6.3.2. Single Domain Particle Recording Tape Media

In this class of media the particle easy axes are partially oriented in the longitudinal direction. Here we consider a medium in which 90% of the easy axes lie within a 60° cone centered about the longitudinal direction.

Bertram [64] has proposed that the orientation of the particle easy axes may be assumed to be distributed in the recording plane (the x, y plane where x is the longitudinal direction and y is the out-of-tape direction) by the function

$$f(\theta_p) = N_\beta \, e^{\beta \cos^2 \theta_p} \tag{6.4}$$

where N_β is a suitable normalization factor and β is the orientation parameter. Positive values of β represent media oriented to a greater (larger β) or lesser (smaller β) extent about the longitudinal direction. The case $\beta = 0$ represents 2-D random or unoriented media. The distribution function (6.4) is extended here to describe the particle orientation of magnetic tape media. Bate and Williams [65] have shown that the angular distribution of the particle easy axes in magnetic tape is cylindrically symmetric, to 'within about 10%', about the direction of orientation. A cylindrically symmetric 3-D representation, $g(\theta_p)$, of the 2-D distribution function (6.4) is obtained by taking the product of (6.4) and a spherical polar surface element and integrating over all azimuthal angles. This gives

$$g(\theta_p) = N_\beta \int_0^{2\pi} e^{\beta \cos^2 \theta_p} R^2 \sin \theta_p \, d\varphi = 2\pi R^2 e^{\beta \cos^2 \theta_p} \sin \theta_p \tag{6.5}$$

where R is the radius of the sphere and the normalization factor N_β is given by

$$N_\beta = \int_0^{2\pi} \int_0^{\pi/2} e^{\beta \cos^2 \theta_p} R^2 \sin \theta_p d\theta_p \, d\varphi = 2\pi R^2 \int_0^{\pi/2} e^{\beta \cos^2 \theta_p} \sin \theta_p d\theta_p \, . \tag{6.6}$$

Single domain particles within magnetic tape media are therefore assumed to be oriented according to the distribution function

$$g(\theta_p) = \frac{e^{\beta \cos^2 \theta_p} \sin \theta_p}{\int_0^{\pi/2} e^{\beta \cos^2 \theta_p} \sin \theta_p d\theta_p} \, . \tag{6.7}$$

In order to have 90% of the particle distribution oriented within 30° (the half cone angle) of the orientation direction, β must equal 9.89. This value of β is assumed hereafter.

As with 2-D random media, 100 equally spaced orientation angles between 0° and 90° are sampled, but each angular sample in this case is weighted by the distribution function (6.7). Again the switching time is then taken as the time for the slowest one of 90% of the normalized distribution to switch (cross the hard equatorial plane).

6.4. Results

When $\alpha < 1$, the dynamic behavior of a grain's magnetization vector is complex. For low values of α the magnetization vector tends to follow a damped orbit which carries it back and forth across the hard equatorial plane [56]. This behavior is illustrated in Fig. 47 where the percentage of switched grains in a 2-D random distribution is plotted against the reduced time, τ $(= M\gamma t/(1+\alpha^2))$, elapsed since the application of an external field. Results for the two cases $H_k = 1000$ Oe with $H_a = 2500$ Oe and $H_a = 4000$ Oe are shown and α is equal to 0.2. Here one reduced time unit, τ, corresponds to 0.0591 ns in actual time. Immediately following the introduction of the external switching field the magnetizations of the individual grains within the 2-D random distribution begin their forced precessional orbits across the hard plane and the percentage of switched grains increases rapidly until it reaches approximately 74% for $H_a - H_k = 1500$ Oe and approximately 71% for $H_a - H_k = 3000$ Oe. At this point (at about $\tau = 1.65$ and $\tau = 1.1$, respectively) more and more individual grains have magnetizations which, having successfully switched, are continuing in their forced orbits back across the hard plane leading to a net decrease in the percentage of grains switched thus creating a local maximum. The same effect produces further local maxima, although these are less pronounced as time passes.

One consequence of this behavior is illustrated in Fig. 48, where the reciprocal of the reduced switching time, τ_s, is plotted against $H_a - H_k$, for $H_k = 1000$ Oe with α again equal to 0.2. The disjointed linear form of the plot is due to the fact that, for $H_a - H_k < 3000$ Oe, more than 90% of the distribution has switched by the second local maximum (and therefore, by our definition, the medium has switched).

However, for $H_a - H_k \geq 3000$ Oe the second local maximum does not exceed the 90% threshold and switching is not achieved at that time. For $H_a - H_k \geq 3000$ Oe, the percentage of switched grains goes through a further local minimum before reaching 90% at the third attempt.

The discontinuous form of the plotted values in Fig. 48 is potentially a source of error when calculating the switching constant. For low values of α there are two

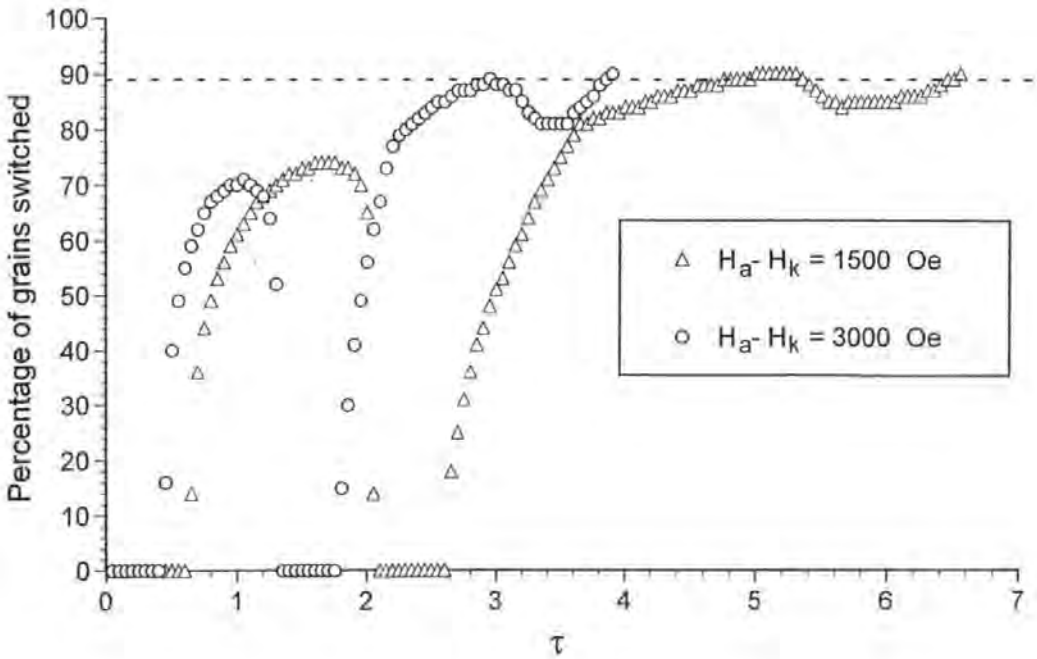

Figure 47. Percentage of grains switched at reduced time for 2-D random media with $\alpha = 0.2$, $H_k = 1000$ Oe, $H_a = 2500$ Oe and 4000 Oe.

separate line segments and therefore two slightly different values for the gradient of $1/\tau_s$ versus $H_a - H_k$ on which to base the calculation of S_w. For example, Fig. 48 shows that when $\alpha = 0.2$, the two line segments have gradients of 8.33×10^{-5} for $H_a - H_k \leq 2750$ Oe and 7.23×10^{-5} for $H_a - H_k \geq 3000$ Oe. Substituting these two values into the calculation

$$S_w = \frac{1}{\text{gradient}} \times \frac{1+\alpha^2}{M\gamma} \tag{6.8}$$

in turn, produces switching constants of 709 ns-Oe and 817 ns-Oe, respectively. This apparent ambiguity is resolved here by requiring that a medium is considered to be switched only if both the threshold value of 90% is achieved and the percentage will not drop below 90% at any subsequent time while the external field remains applied. This added criterion to the definition of switching has the effect of excluding the

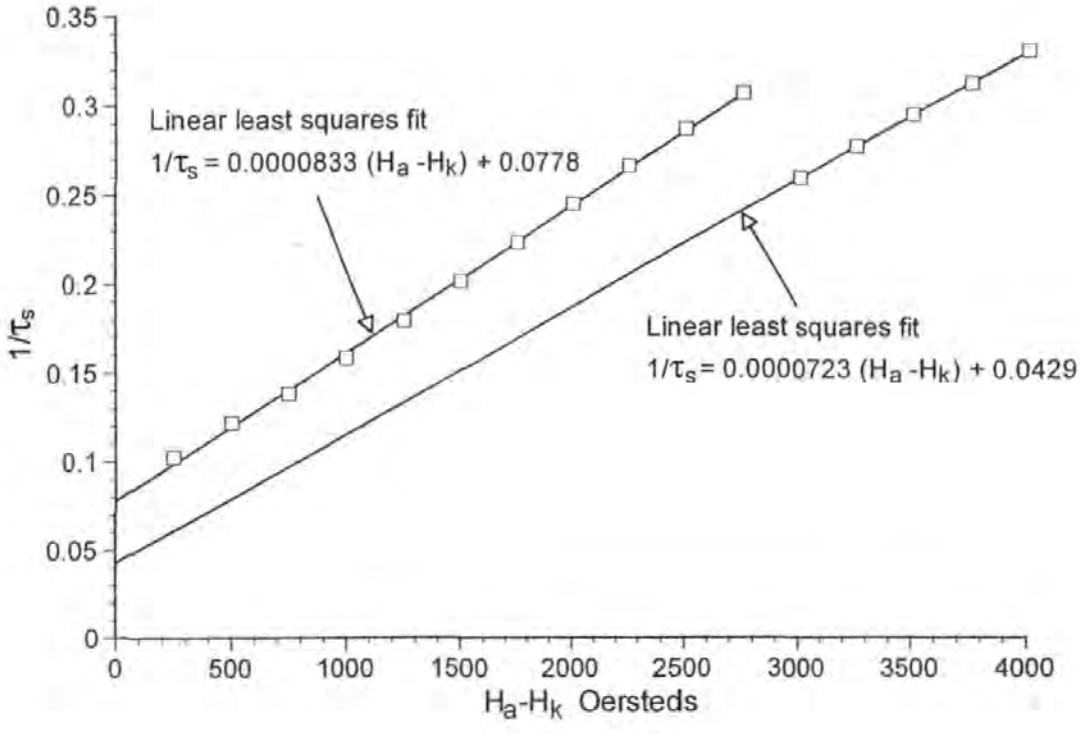

Figure 48. Variation of reciprocal of reduced switching time with $H_a - H_k$ for 2-D random media with $\alpha = 0.2$, $H_k = 1000$ Oe.

switching of media by the local maxima illustrated in Fig. 47. It follows that in the case of Fig. 48, the line segment for $H_a - H_k \geq 3000$ Oe is chosen and the resulting switching constant for 2-D random media with $\alpha = 0.2$ is given as 817 ns-Oe.

Fig. 49 shows $1/\tau_s$ plotted against $H_a - H_k$ for $H_k = 1000$ Oe with $\alpha = 1.0$ for 2-D random and 3-D oriented media. Here one reduced time unit corresponds to 0.114 ns. It is clear that the switching time is no longer affected by local maxima when $\alpha = 1.0$ since the plot produces a continuous single straight line for each class of media. The switching behavior for 2-D random media with $\alpha = 1.0$, $H_k = 1000$ Oe and $H_a = 3500$ Oe is shown in Fig. 50. In contrast to the $\alpha = 0.2$ case, the percentage of switched grains increases monotonically after the introduction of the switching field, with no local maxima to consider in the computation of the switching constant.

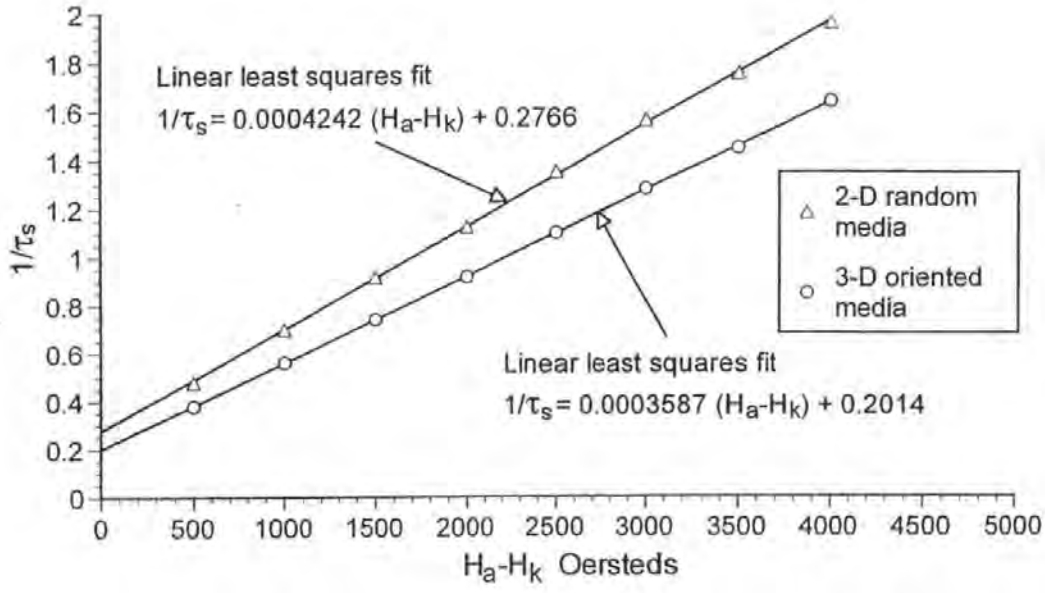

Figure 49. Variation of reciprocal of reduced switching time with $H_a - H_k$ for 2-D random and 3-D oriented media with $\alpha = 1.0$, $H_k = 1000$ Oe.

The switching constants for 2-D random and 3-D oriented media for $0.2 \leq \alpha \leq 2.0$ are plotted in Fig. 51, where it is observed that for each class of media, the minimum value of S_w occurs close to the critical value of $\alpha = 1.0$. Finally, the switching constants obtained for the two classes of media, for a range of values of α are given in Table 13.

6.5. Discussion

In the results presented above there are several points of interest. First, it is remarkable that the plots of the reciprocal of the reduced switching time, $1/\tau_s$, versus $H_a - H_k$ are essentially perfect straight lines. It should be noted that the appearance of the anisotropy field, H_k, in the theoretical (L-L-G) model rather than the related

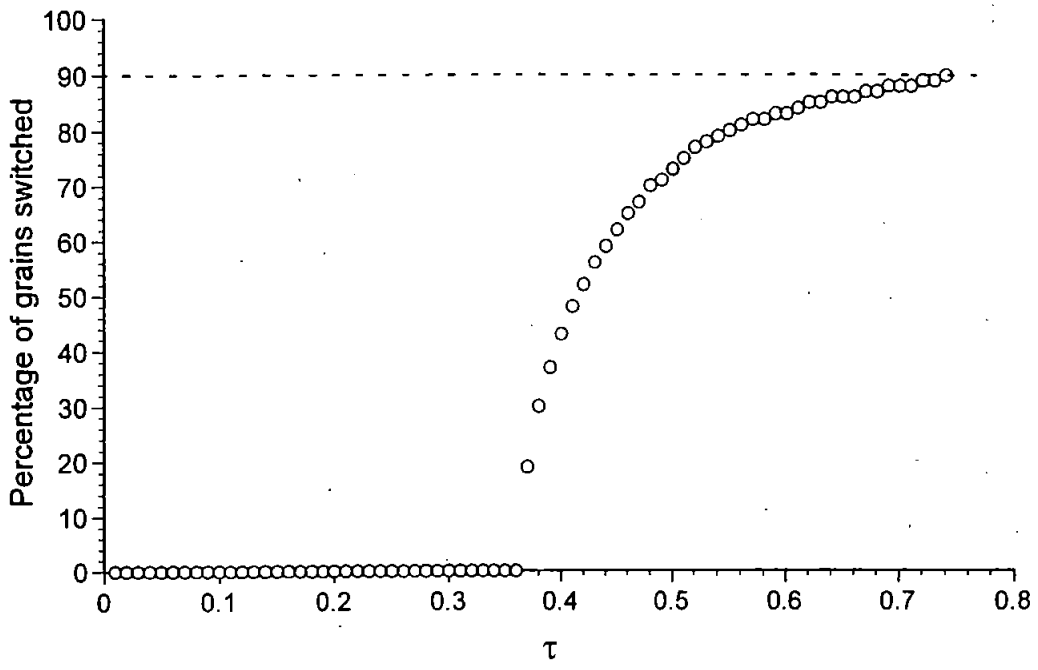

Figure 50. Percentage of grains switched at reduced time for 2-D random media with $\alpha = 1.0$, $H_k = 1000$ Oe and $H_a = 3500$ Oe.

threshold field, H_0, gives rise to lines which do not pass through the origin as predicted by (6.1). However, it is the slope of these lines only that is used in the calculation of the switching constants. Second, it is to be pointed out that the slopes of these straight lines, which are proportional to the reciprocals of the switching constants S_w, are independent of the value of the anisotropy field, H_k. The value of S_w depends only upon the damping parameter α and the orientation parameter β of the particle/grain ensemble. The lowest values of S_w, which give the fastest switching, occur at values of the damping parameter, α, approximately equal to unity in both oriented and unoriented arrays.

It is difficult to prove mathematically just why the $1/\tau_s$ versus $H_a - H_k$ curves are so linear. This is, principally, because the basic Gilbert equation does not admit an analytical solution except for the co-linear, perfectly oriented, case

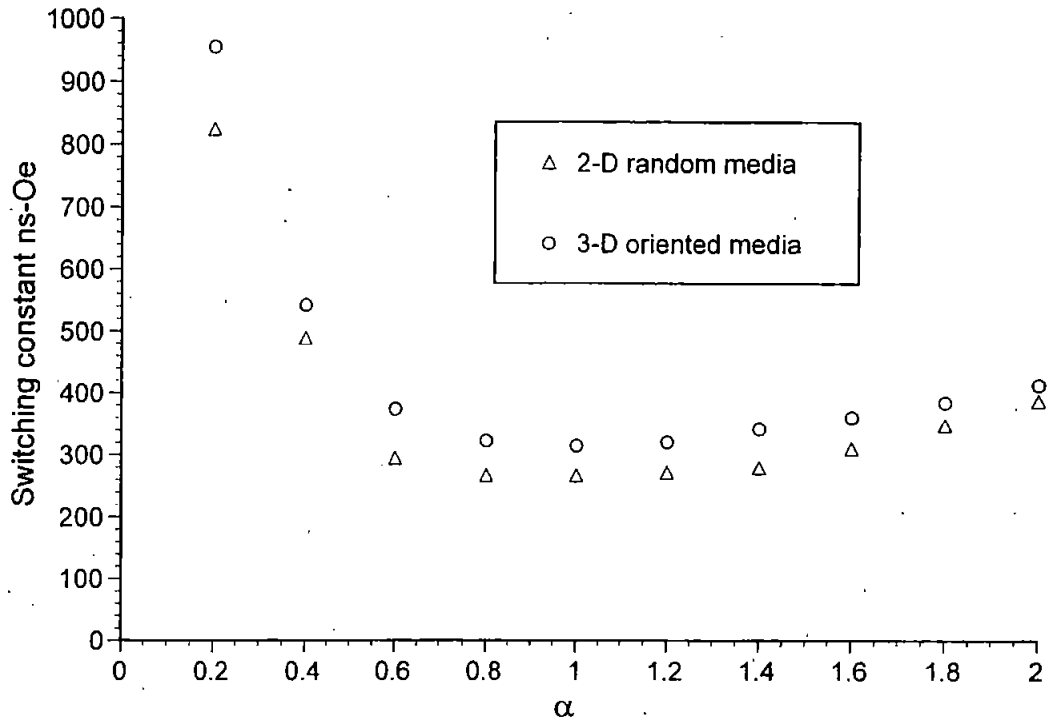

Figure 51. Variation of the switching constant with α for 2-D random and 3-D oriented media.

[59]. Moreover, the procedure used to determine the switching time of each grain is inherently non-linear.

In that very special case of a single spherical grain with the anisotropy easy axis co-linear with the applied field, the analytical solution for the time to switch from polar angle θ_1 to θ_2, given in [59], does give the approximate linear relationship

$$\frac{1}{T_s} \approx \frac{-\gamma\alpha}{1+\alpha^2} \; \frac{1}{\ln\left[\frac{\tan(\theta_1/2)}{\tan(\theta_2/2)}\right]} \; \left[(H_a - H_k) + H_k\left(1 - \frac{\ln\left[\frac{\sin(\theta_1)}{\sin(\theta_2)}\right]}{\ln\left[\frac{\tan(\theta_1/2)}{\tan(\theta_2/2)}\right]}\right)\right]. \tag{6.9}$$

When $\theta_2 = 90°$ this gives an approximate formula for a "switching constant" which depends on the initial orientation angle θ_1 as

$$S_w \approx -\frac{1+\alpha^2}{\gamma\alpha} \; \ln\left[\tan(\theta_1/2)\right]. \tag{6.10}$$

α	2-D random S_w (ns-Oe)	3-D oriented S_w (ns-Oe)
0.2	817	955
0.4	489	542
0.6	295	374
0.8	267	323
1.0	267	316
1.2	272	321
1.4	280	343
1.6	311	361
1.8	350	386
2.0	389	415

Table 13. Switching constants for 2-D random and 3-D oriented media for different values of α.

Unfortunately, this simple approximation cannot be used to calculate S_w for distributions of grains in which the anisotropy axes of the grains are not co-linear with the applied field.

The fact that the S_w's calculated here are independent of the value of H_k is best illustrated by example. In Fig. 52 the reciprocal reduced switching time, $1/\tau_s$, versus $H_a - H_k$ is shown for the 2-D random case with $\alpha = 1.0$, both for $H_k = 1000$ Oe and for $H_k = 2000$ Oe. For both values of H_k the slopes and, therefore, the S_w's are identical. It is to be understood, however, that if a field greater than 2000 Oe were to be applied, the material with the lower H_k would switch more rapidly than that with the higher H_k, because the switching time is inversely proportional to the 'excess' field, $H_a - H_k$.

It is to be realized that the values of S_w calculated here hold for all positive values of the excess field, $H_a - H_k$. Thus, for example, if $S_w = 500$ ns-Oe, excess fields of 50, 500 and 5000 Oe, which might be appropriate for materials such as Permalloy, γ-Fe_2O_3 tape and modern high coercivity recording media respectively, will produce

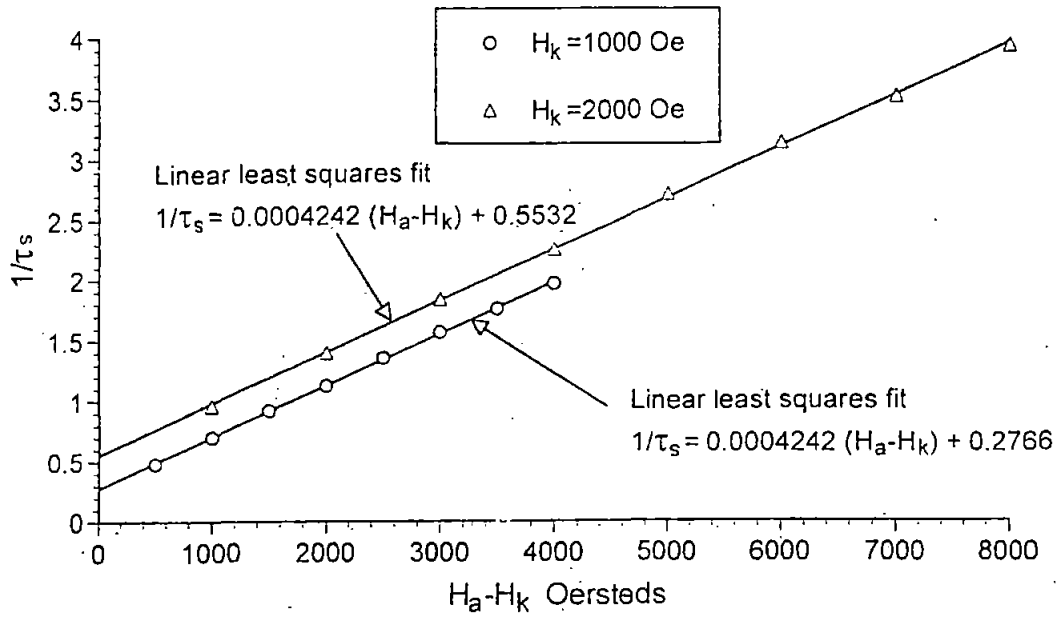

Figure 52. Variation of the reciprocal of reduced switching time with $H_a - H_k$ for 2-D random media with $\alpha = 1.0$, $H_k = 1000$ Oe and 2000 Oe.

switching times, T_s, of 10, 1 and 0.1 ns respectively. The analysis presented here applies equally to the switching of all classes of magnetic media.

In both the 2-D random and 3-D oriented cases, the lowest values of the computed switching constant occur close to a value of the damping parameter, α, equal to unity. This is not surprising because it has been understood for many years that the fastest Gilbert damped gyro-magnetic switching occurs when $\alpha = 1$. It is perhaps surprising, however, to see that the effect of orienting the grains/particles is to produce larger values of S_w and, therefore, slower switching.

Finally, the calculated values of S_w reported here may be compared with the published, experimentally measured, values. In a recent invited paper, He et al. report upon high-speed switching measurements in tapes as follows: Metal Particle tape 140 ns-Oe, Metal-Evaporated tape 190 ns-Oe, Barium Ferrite tape 240 ns-Oe,

Chromium Dioxide tape 222 ns-Oe, γ-Fe_2O_3(A) 87 ns-Oe and γ-Fe_2O_3(B) 160 ns-Oe [56]. In the present work the lowest value for 2-D random media is 267 ns-Oe and for 3-D oriented media is 316 ns-Oe. Ignoring the γ-Fe_2O_3(A) remarkably low value reported by He et al., the values computed here from the Gilbert equation are within a factor of two of the experimental values. In a recent paper, [57], Rizzo et al. report that a thin film with $H_c \approx 1000$ Oe, behaved adiabatically with a measured S_w of 373 ns-Oe. Again our computed values of S_w agree within a factor of two of the experimental.

There are several reasons that lead one to expect that the experimental values will be smaller than those computed. First, many of the high-speed switching experiments made use of a static bias field which is known to reduce the switching time and, concomitantly, the switching constant. For example, it has been shown recently that if the dc bias field is $0.5H_k$ and the applied field is $1.5H_k$, the switching time is reduced by 18% in the perfectly aligned case [58]. For lower applied fields, the reduction becomes greater. Second, in experimental work the current pulses which produce the dynamic switching field almost inevitably have non-negligible rise and fall times during which, of course, some particle/grain switching occurs. If this switching is not accounted for properly, the result is, again, lower apparent switching constants. Without mathematical justification, the traditional correction has been, over at least the last 40 years, to modify equation (6.1) to become $S_w = \int_T (H_a - H_k)dt$, where T is the time interval when $H_a \geq H_k$. In our computations the rise and fall times of the applied field are taken to be zero.

6.6. Summary

In this chapter:

- The Gilbert form of the Landau-Lifshitz equation has been solved numerically for an assembly of magnetic particles in order to calculate the switching constant of a magnetic recording medium.

- For each of two different classes of media a strong linear relation between the reciprocal of the switching time and the difference between the applied and anisotropy fields is illustrated.
- Theoretical calculations of the switching constant are shown to be in good agreement with published experimental values.

CHAPTER 7

THE FUTURE OF MAGNETIC INFORMATION STORAGE TECHNOLOGY

7.1. Introduction

The data storage industry continues to be driven by the need for low cost, high capacity, fast access and high data rate storage products. The primary memory (random access memory - RAM) of the modern computer, in which all of the immediate computational tasks are performed, is semiconductor based due mainly to its extremely fast access to and from the computer's processing elements. These semiconductor devices are volatile - they require power to maintain the integrity of the data. This feature of their operation often involves compromises in processing complexity, power supply requirements, writing data rate and cost, making them unsuitable as a method of secondary, non-removable on-line mass storage. The magnetic HDD is non-volatile and it remains the natural choice as a secondary or mass memory to store data to be used in, or resulting from, the computation process. Optical storage can provide an alternative to the magnetic HDD as a method of secondary storage in some circumstances. By virtue of its removability, it has become accepted as the preferred technology for many library type applications including; pre-recorded audio, pre-recorded video and software program distribution. However, aside from the removability issue, magnetic HDD storage is superior to optical storage in every respect for secondary storage purposes and there are no alternative technologies that are likely candidates to replace it over the next ten years, although it seems certain that there must be a deviation from traditional, longitudinal recording technology [66]. Since 1990, the start of the era of magnetoresistive technology, the compound growth rate of areal density with time, shown in Fig. 53, has been in the region of 60%.

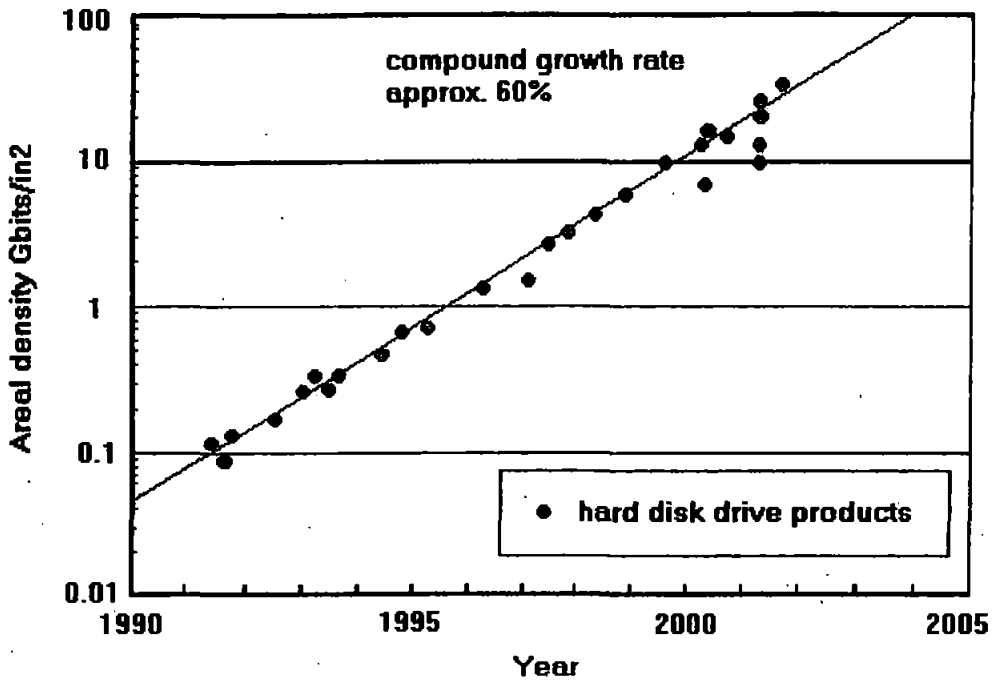

Figure 53. Growth rate of HDD areal density since 1990.

Section 7.2 discusses physical limitations that may prevent the achievement of such growth in the future, while section 7.3 outlines some of the innovative approaches that can be used to postpone the effects of perceived physical barriers.

7.2. Physical Limitations

Much of the progress in magnetic storage can be attributed to simple scaling. If the magnetic properties of the materials are constant, the field characteristics remain unchanged even if all the dimensions are scaled by the same factor. Therefore, to double the linear density and to double the track density (i.e. to quadruple the areal density), it is necessary to scale all of the dimensions by half. If the head/disk surface velocity remains unchanged the data rate is doubled. Clearly, progress due solely to scaling can not continue indefinitely, although there is still some scope for

further gains in this area. However, we are approaching physical dimensions and switching times in the media and the recording head at which the magnetic properties are different than they were for larger scale HDD's working at lower data rates. Higher data rates will reduce the switching time of the medium to the subnanosecond scale. Further research such as that presented in Chapter 6 is necessary to investigate the gyromagnetic and damping processes that set the intrinsic switching limit of the medium [67]. In addition, difficulties arise with head to disk spacings that are only an order of magnitude larger than an atomic diameter [68]. At these distances, there are a number of forces acting on the utrathin (1-2 nm) lubricant film due to the presence of a flying slider, including slider generated air pressure gradients and air shear [69]. As a result the lubricant film exhibits a thickness modulation during operation that influences the recording performance of the head [70].

Most researchers believe that the superparamagnetic effect will provide the first inelastic barrier to further progress using simple scaling methods [71]. Proper scaling demands that the individual particles in a bit cell decrease in size at the same rate as all of the other dimensions, so that the number of particles per bit cell remains constant. If the particle size is not scaled with each increase in areal density, the random nature of particle locations within each bit cell with respect to track and bit cell boundaries induces an unacceptable magnetic noise into the recording process. The average energy with which a particle's magnetization fluctuates is a very strong function of particle size, and this eventually leads to the loss of magnetic stability. Many of the early predictions of the maximum densities achievable before the effect becomes a fundamental problem have proved to be spectacularly inaccurate, suggesting figures as low as 7 Mb/in^2 [72]. More recently, Charap and Lu [73] predicted an ultimate limit of 36 Gbit/in^2 for longitudinal recording, based on the assumption of linear scaling and the bit aspect ratio (trackwidth/bit length) of 16:1. All of these suggested densities have been surpassed, with several demonstrations of recording densities beyond 100 Gbit/in^2 [74], [75]. However, more innovative methods are needed for the solutions of tomorrow and some of these are discussed in the next section.

7.3. Ultrahigh Density Magnetic Recording

7.3.1. Longitudinal Recording

There are a variety of materials and design changes that can be employed to postpone the effects of thermal instability. Recording media made from materials with a higher magnetic anisotropic density are a possibility, because the increase in anisotropy counters the reduction in volume of the grains in the scaling process. Unfortunately, this approach brings with it greater demands on the associated write field requirements. The write field improvements must then be brought about by design changes in the write head and the use of higher saturation magnetization materials for the write poles. The search for suitable candidates for write pole materials with even higher saturation magnetization density continues, but progress is slowing in this area and will ultimately limit the maximum achievable write field. Another approach is to reduce the bit cell aspect ratio (BAR), as this has been shown to result in a reduction of magnetic noise. A reduction of the BAR has been a feature common to high areal density demonstrations in recent years, resulting in ratios currently in the region of 6:1. As a result, future requirements to write and read extremely narrow tracks, and to understand the side writing/reading off-track characteristics of a head will become increasingly important and will require 3-dimensional models such as those presented in [76].

Recently, extremely high areal densities have been achieved [75] using media that consist of two magnetic layers that are antiferromagnetically coupled (AFC) through a non-magnetic layer, as shown in Fig 54. Both layers are magnetized, in anti-parallel direction, such that the effective magnetic thickness of the whole structure is given by the difference between the magnetic thickness of the two layers. The reduced effective magnetic thickness of the recording media allows a smaller transition parameter, while the augmented physical thickness of the structure leads to an improved thermal stability. The introduction of AFC media shows that it is possible to extend longitudinal recording beyond previously perceived limits [66].

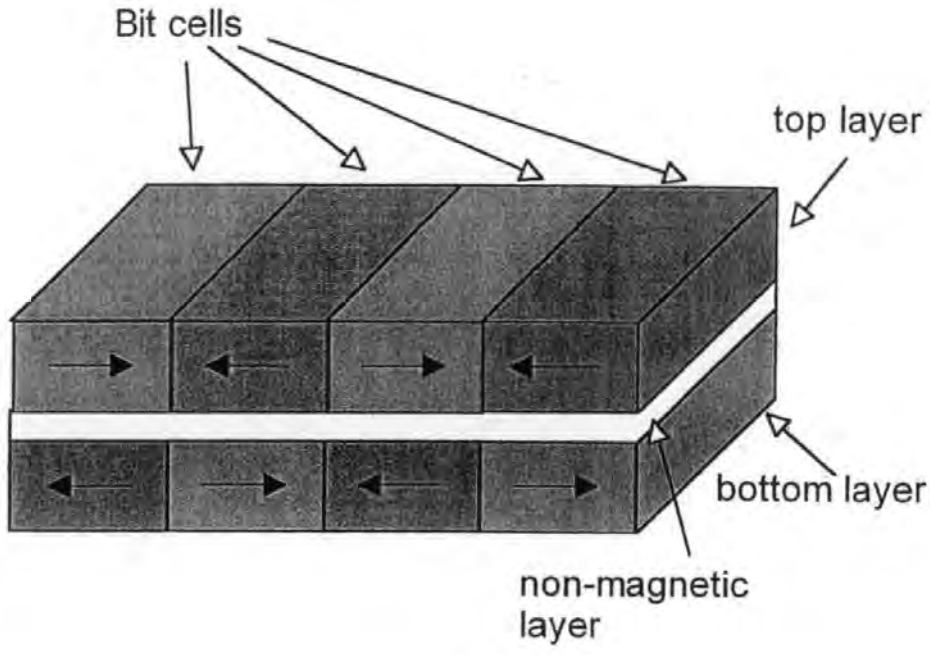

Figure 54. Antiferromagnetically coupled (AFC) media.

7.3.2. Perpendicular Recording

There is good reason to believe that perpendicular recording will offer improved thermal stability solutions over conventional, longitudinal recording systems. Bertram [6] has suggested a limiting density for perpendicular recording that is five times that of longitudinal recording. The use of media with a high permeability soft underlayer offers significant gains in the ability to write on higher coercivity materials and, in addition, the optimal thickness for perpendicular media is significantly larger than for longitudinal media. Thus, the volume per magnetic grain can be correspondingly larger without degrading the transition parameter. A recording system based upon a perpendicular media with a soft underlayer, along with a GMR read head and a write head with a wide gap between the write pole and collector pole is generally considered to be the main candidate to replace longitudinal recording [7],

[77]. Demonstrations of high density perpendicular recording over 60 Gbit/in^2 have been reported [78] and it seems likely that the industry goal of Terabit/in^2 recording will first be realized using perpendicular recording technology [79].

7.4. Summary

In this chapter:

- The physical phenomena that will prevent the evolutionary path of magnetic storage by scaling processes are reviewed.
- Some of the recent advances in recording media and head design that will prolong longitudinal recording are discussed.
- An outline of perpendicular recording and it's role in the realization of terabit/in^2 magnetic recording is given.

APPENDIX A

SPECIAL FUNCTIONS

All of the integrals quoted in Chapter 2 for the single pole head and many of those in Chapter 3 for double-element heads may be written in terms of special functions which provides a more efficient means of calculation than direct numerical integration. These special functions are defined as [46]:

$$\mathrm{Ei}(z) = -\mathrm{E}_1(-z) \tag{A.1}$$

and

$$\mathrm{E}_1(z) = \int_z^\infty \frac{e^{-t}}{t}\, dt = -\gamma - \ln(z) - \sum_{n-1}^{\infty} \frac{(-1)^n z^n}{nn!} \tag{A.2}$$

where γ is Euler's constant.

$$\overline{\mathrm{Ei}}(z) = \mathrm{Ei}(z) - i\pi\,. \tag{A.3}$$

The sine integral is

$$\mathrm{Si}(x) = \int_0^x \frac{\sin(t)}{t}\, dt \tag{A.4}$$

and the cosine integral is

$$\mathrm{Ci}(x) = -\int_x^\infty \frac{\cos(t)}{t}\, dt\,. \tag{A.5}$$

APPENDIX B

INTEGRALS REQUIRED

B.1. For $\varphi_I^{++}(x,y)$

$$I_n^{++} = \int_0^\infty \frac{\cos[kg]\cos[kx]}{(kg)^2 - [(n-1/2)\pi]^2} \frac{\sinh[k(t-y)]}{\sinh[kt]} dk \tag{B.1}$$

$$J_n^{++} = \int_0^\infty \frac{\sin[k(g+L+h)]\sin[kh]\cos[kx]}{(kh)^2 - (n\pi)^2} \frac{\sinh[k(t-y)]}{\sinh[kt]} dk \tag{B.2}$$

$$K_n^{++} = \int_0^\infty \frac{\cos[k(g+L+h)]\cos[kh]\cos[kx]}{(kh)^2 - [(n-1/2)\pi]^2} \frac{\sinh[k(t-y)]}{\sinh[kt]} dk \tag{B.3}$$

B.2. For the Equations (3.7) – (3.9)

$$I_{mn}^{++} = \int_0^\infty \frac{k\cos^2[kg]}{[(kg)^2 - [(m-1/2)\pi]^2][(kg)^2 - [(n-1/2)\pi]^2]} \coth[kt] dk \tag{B.4}$$

$$J_{mn}^{++} = \int_0^\infty \frac{k\sin[k(g+L+h)]\sin[kh]\cos[kg]}{[(kg)^2 - [(m-1/2)\pi]^2][(kh)^2 - (n\pi)^2]} \coth[kt] dk \tag{B.5}$$

$$K_{mn}^{++} = \int_0^\infty \frac{k\cos[k(g+L+h)]\cos[kh]\cos[kg]}{[(kg)^2 - [(m-1/2)\pi]^2][(kh)^2 - [(n-1/2)\pi]^2]} \coth[kt] dk \tag{B.6}$$

$$L_{mn}^{++} = \int_0^\infty \frac{k\sin^2[k(g+L+h)]\sin^2[kh]}{[(kh)^2 - (m\pi)^2][(kh)^2 - (n\pi)^2]} \coth[kt] dk \tag{B.7}$$

$$M_{mn}^{++} = \int_0^\infty \frac{k\cos[k(g+L+h)]\sin[k(g+L+h)]\cos[kh]\sin[kh]}{[(kh)^2 - (m\pi)^2][(kh)^2 - [(n-1/2)\pi]^2]} \coth[kt] dk \tag{B.8}$$

$$N_{mn}^{++} = \int_0^\infty \frac{k\cos^2[k(g+L+h)]\cos^2[kh]}{[(kh)^2 - [(m-1/2)\pi]^2][(kh)^2 - [(n-1/2)\pi]^2]} \coth[kt] dk \tag{B.9}$$

B.3. For the Magnetic Field Components

$$L_n^{++} = \int_0^\infty \frac{k\cos[kg]\sin[kx]}{(kg)^2 - [(n-1/2)\pi]^2} \frac{\sinh[k(t-y)]}{\sinh[kt]} dk \tag{B.10}$$

$$M_n^{++} = \int_0^\infty \frac{k\sin[k(g+L+h)]\sin[kh]\sin[kx]}{(kh)^2 - (n\pi)^2} \frac{\sinh[k(t-y)]}{\sinh[kt]} dk \tag{B.11}$$

$$N_n^{++} = \int_0^\infty \frac{k\cos[k(g+L+h)]\cos[kh]\sin[kx]}{(kh)^2 - [(n-1/2)\pi]^2} \frac{\sinh[k(t-y)]}{\sinh[kt]} dk \tag{B.12}$$

$$P_n^{++} = \int_0^\infty \frac{k\cos[kg]\cos[kx]}{(kg)^2 - [(n-1/2)\pi]^2} \frac{\cosh[k(t-y)]}{\sinh[kt]} dk \tag{B.13}$$

$$Q_n^{++} = \int_0^\infty \frac{k\sin[k(g+L+h)]\sin[kh]\cos[kx]}{(kh)^2 - (n\pi)^2} \frac{\cosh[k(t-y)]}{\sinh[kt]} dk \tag{B.14}$$

$$R_n^{++} = \int_0^\infty \frac{k\cos[k(g+L+h)]\cos[kh]\cos[kx]}{(kh)^2 - [(n-1/2)\pi]^2} \frac{\cosh[k(t-y)]}{\sinh[kt]} dk \tag{B.15}$$

B.4. For $\varphi_I^{-+}(x,y)$

$$I_n^{-+} = \int_0^\infty \frac{\sin[kg]\sin[kx]}{(kg)^2 - (n\pi)^2} \frac{\sinh[k(t-y)]}{\sinh[kt]} dk \tag{B.16}$$

$$J_n^{-+} = \int_0^\infty \frac{\cos[k(g+L+h)]\sin[kh]\sin[kx]}{(kh)^2 - (n\pi)^2} \frac{\sinh[k(t-y)]}{\sinh[kt]} dk \tag{B.17}$$

$$K_n^{-+} = \int_0^\infty \frac{\sin[k(g+L+h)]\cos[kh]\sin[kx]}{(kh)^2 - [(n-1/2)\pi)]^2} \frac{\sinh[k(t-y)]}{\sinh[kt]} dk \tag{B.18}$$

B.5. For the Equations (3.15) – (3.17)

$$I_{mn}^{-+} = \int_0^\infty \frac{k \sin^2 [kg]}{[(kg)^2 - (m\pi)^2][(kg)^2 - (n\pi)^2]} \coth [kt] dk \tag{B.19}$$

$$J_{mn}^{-+} = \int_0^\infty \frac{k \cos [k(g+L+h)] \sin [kh] \sin [kg]}{[(kg)^2 - (m\pi)^2][(kh)^2 - (n\pi)^2]} \coth [kt] dk \tag{B.20}$$

$$K_{mn}^{-+} = \int_0^\infty \frac{k \sin [k(g+L+h)] \cos [kh] \sin [kg]}{[(kg)^2 - (m\pi)^2][(kh)^2 - [(n-1/2)\pi]^2]} \coth [kt] dk \tag{B.21}$$

$$L_{mn}^{-+} = \int_0^\infty \frac{k \cos^2 [k(g+L+h)] \sin^2 [kh]}{[(kh)^2 - (m\pi)^2][(kh)^2 - (n\pi)^2]} \coth [kt] dk \tag{B.22}$$

$$M_{mn}^{-+} = M_{mn}^{++} \tag{B.23}$$

$$N_{mn}^{-+} = \int_0^\infty \frac{k \sin^2 [k(g+L+h)] \cos^2 [kh]}{[(kh)^2 - [(m-1/2)\pi]^2][(kh)^2 - [(n-1/2)\pi]^2]} \coth [kt] dk \tag{B.24}$$

B.6. For the Magnetic Field Components

$$L_n^{-+} = \int_0^\infty \frac{k \sin[kg] \cos[kx]}{(kg)^2 - (n\pi)^2} \frac{\sinh[k(t-y)]}{\sinh[kt]} dk \tag{B.25}$$

$$M_n^{-+} = \int_0^\infty \frac{k \cos[k(g+L+h)] \sin[kh] \cos[kx]}{(kh)^2 - (n\pi)^2} \frac{\sinh[k(t-y)]}{\sinh[kt]} dk \tag{B.26}$$

$$N_n^{-+} = \int_0^\infty \frac{k \sin[k(g+L+h)] \cos[kh] \cos[kx]}{(kh)^2 - [(n-1/2)\pi]^2} \frac{\sinh[k(t-y)]}{\sinh[kt]} dk \tag{B.27}$$

$$P_n^{-+} = \int_0^\infty \frac{k \sin[kg] \sin[kx]}{(kg)^2 - (n\pi)^2} \frac{\cosh[k(t-y)]}{\sinh[kt]} dk \tag{B.28}$$

$$Q_n^{-+} = \int_0^\infty \frac{k \cos[k(g+L+h)] \sin[kh] \sin[kx]}{(kh)^2 - (n\pi)^2} \frac{\cosh[k(t-y)]}{\sinh[kt]} dk \tag{B.29}$$

$$R_n^{-+} = \int_0^\infty \frac{k \sin[k(g+L+h)] \cos[kh] \sin[kx]}{(kh)^2 - [(n-1/2)\pi]^2} \frac{\cosh[k(t-y)]}{\sinh[kt]} dk \tag{B.30}$$

REFERENCES

[1] V. Poulsen, U.S. Patent 661,619. 13 November 1900.

[2] Y. Huai, J. Zhang, G. W. Anderson, N. Zhu, P. Zou, R. Kemshetti, D. Seagle, M. Lederman, M. Zhao, and L. C. Wang, "High sensitive spin valve heads with specular thin oxide capping layers", in *8th joint MMM-intermag Conf.*, vol. EB-14, San Antonio, TX, Jan 7-11, 2001, p.264.

[3] S. Iwasaki and K. Takemura, "An analysis for the cicular mode of magnetization in short wavelength recording", *IEEE Trans. Magn.*, MAG-11, pp. 1173-1175, Sept. 1975.

[4] S. Iwasaki and Y. Nakamura, "An analysis for magnetization mode for high density recording", *IEEE Trans Magn.*, MAG-13, pp. 1272-1277, Sept. 1977.

[5] D. Weller, et al., "High K_u materials approach to 100Gbits/in^2", *IEEE Trans. Magn.*, vol. 36, no. 1, pp.10-15, Dec. 2000.

[6] H. N. Bertram and M. Williams, "SNR and density limit estimates: a comparison of longitudinal and perpendicular recording", *IEEE Trans. Magn.*, vol. 36, no 1, pp. 4-9, Dec. 2000.

[7] R. W. Wood, J. J. Miles and T. Olson, "Recording technologies for one terabit per square inch systems", *IEEE Trans. Magn.*, vol. 38, no 4, pp. 1711-1718, July 2002.

[8] J. D. Jackson, *Classical Electrodynamics*, John Wiley and Sons, 1962.

[9] G. J. Y. Fan, "Analysis of a practical perpendicular head for digital purposes", *J. Appl. Phys.*, vol. 31, pp. 402S-403S, May 1960.

[10] T. L. Gilbert, "A Lagrangian formulation of the gyromagnetic equation of the magnetization field", *Phys. Rev.*, vol. 100, p. 1243, 1955.

[11] K. J. Binns and P. J. Lawrenson, *Analysis and Computation of Electric and Magnetic Field Problems*, Pergamon Press, Oxford, 1973.

[12] H. Muraoka and Y. Nakamura, "Quantification of perpendicular magnetic record-

ing with double layer media", *J. Magn. Jap.*, Vol. 21, No. S2, 1997.

[13] G. J. Y. Fan, "A study of the playback process of a magnetic ring head", *IBM J. Res. Devel.*, vol. 5, pp. 321-325, Oct. 1961.

[14] A. W. Baird, "An evaluation and approximation of the Fan equations describing magnetic fields near recording heads", *IEEE Trans. Magn.*, MAG-16, No. 5, pp. 1350-1352, Sept. 1980.

[15] H. L. Huang and H. Y. Deng, "Comparison of ring head and head write fields", *IEEE Trans. Magn.*, MAG-22, No. 5, pp. 1305-1309, Sept. 1986.

[16] D. T. Wilton, "Comparison of ring and pole head magnetic fields", *IEEE Trans. Magn.*, pp. 1229-1232, No. 3, May 1990.

[17] D. T. Wilton and D. J. Mapps, "An analysis of a shielded magnetic pole for perpendicular recording", *IEEE Trans. Magn.*, vol. 29, pp. 4182-4193, Nov. 1993.

[18] D. T. Wilton, "An analysis of the magnetic field of a ring head with a highly permeable underlayer", *IEEE Trans. Magn.*, vol. 27, pp. 3751-3755, July 1991.

[19] Numerical Algorithms Group Ltd, Fortran Library Manual, Oxford.

[20] C. D. Mee and E. D. Daniel, *Magnetic Recording Technology*,McGraw-Hill, 1995.

[21] L. Landau and E. Lifshitz, Phys. Z. Sowjet. 8, 153(1935); in Landau L. D. *Collected Papers.* edited by D. ter Haar (Gordon and Breach, New York, 1967) p. 101.

[22] J. C. Mallinson, "Damped gyromagnetic switching", *IEEE Trans. Magn.*, pp. 1976-1981, July 2000.

[23] D. J. Mapps, "Magnetoresistive sensors", *Sensors and Actuators*, vol. A59, pp. 9-19, 1997.

[24] J. C. Mallinson, *Magneto-Resistive Heads: Fundamentals and Applications*, San Diego: Academic Press, 1996.

[25] S. Iwasaki and N. Honda, "Strategy for implementation of perpendicular magnetic recording", *J. Mag. Soc. Japan*, vol. 21, no. S2, pp. 1-8, 1997.

[26] R. S. Indeck, J. H. Judy and S. Iwasaki, "A magnetoresistive gradiometer", *IEEE Trans. Magn.*, vol. MAG-24, pp. 2617-2619, Nov. 1988.

[27] H. S. Gill, V. W. Hesterman, G. J. Tarnopolski, L. T. Tran, P. D. Frank and H. Hamilton, "A Magnetoresistive gradiometer for detection of perpendicularly recorded transitions", *J. Appl. Phys.*, vol. 65, pp. 402-404, Jan. 1989.

[28] N. Smith, J Freeman, P. Koeppe and T. Carr, "Dual magnetoresistive head for very high density recording", *IEEE Trans. Magn.*, vol. MAG-28, pp. 2992-2994, Sept. 1992.

[29] Y. Zhang, S. Shtrikman and H. N. Bertram, "Playback pulse shapes and spectra for shielded MR heads", *IEEE Trans. Magn.*, vol. 33, pp. 1093-1103, Mar. 1997.

[30] D. T. Wilton and D. J. Mapps, "An analysis of a shielded magnetic pole for perpendicular recording", *IEEE Trans. Magn.*, vol. 29, pp. 4182-4193, Nov. 1993.

[31] E. Champion and H. N. Bertram, "The effect of MR head geometry on playback pulse shape and spectra", *IEEE Trans. Magn.*, vol. 31, pp. 2461-2470, July 1995.

[32] NAG Routine D01AKF, Numerical Algorithms Group, Oxford, UK.

[33] F. Z. Wang, L. N. He, D. J. Mapps, D. T. Wilton, W. W. Clegg and P. Robinson, "Keepered media reproduction with dual MR heads", *IEEE Trans. Magn.*, vol. 34, pp. 1982-1984, July 1998.

[34] D.T Wilton, H. A. Shute and D. J. Mapps, "Accurate approximation of fields and spectral response functions for perpendicular recording heads", *IEEE Trans. Magn.*, vol. 34, pp. 2172-2179, July 1999.

[35] O. Karlqvist, "Calculation of the magnetic field in the ferromagnetic layer of a magnetic drum", *Trans. Roy. Inst. Technol. Stockholm*, vol. 86, pp. 1-27, 1954.

[36] W. K. Westmijze, "Studies on magnetic recording. II field configuration around the gap and the gap-length formula", *Philips Res. Rep.*, vol. 8, pp. 161-183, June 1953.

[37] R. V. Churchill and J. W. Brown, *Complex Variables and Applications*, McGraw Hill, 1984.

[38] H. N. Bertram, *Theory of Magnetic Recording*, Cambridge University Press, Cambridge, UK., 1994.

[39] E. Champion and H. N. Bertram, "The effect of MR head geometry on playback pulse shape and spectra", *IEEE Trans. Magn.*, vol. 31, pp. 2461-2470, July 1995.

[40] Y. Zhang, S Shtrikman and H. N. Bertram, "Playback Pulse Shape and Spectra

for Shielded MR Heads", *IEEE Trans. Magn.*,vol. 33, pp. 1093-1103, Mar. 1997.

[41] N. Smith and S. W. Yuan "Micromagnetic Modeling of a Narrow-Track Dual Magnetoresistive Head", *IEEE Trans. Magn.*, vol. 30, pp. 388-393, Mar. 1994.

[42] H. Muraoka, H. Yamada and Y. Nakamura, "MR Head Reading Characteristics in Perpendicular Magnetic Recording", *IEEE Trans. Magn.*, vol. 32, pp. 3482-3484, Sept. 1996.

[43] H. Muraoka, H. Yamada, Y. Nakamura, I. Abe and K. Yazawa, "Resolution Enhancement of Shielded MR Heads for Perpendicular Magnetic Recording", *IEEE Trans. Magn.*, vol. 33, pp. 2929-2931, Sept. 1997.

[44] S-PLUS for Windows Professional Version 4.5, Release 1, April 1998, MathSoft, Inc.

[45] A. Aharoni, "Integrals used in magnetoresistive head modeling", *IEEE Trans. Magn.*, vol. 36, No 5, pp. 3879-3880, Sept. 2000.

[46] D. T. Wilton, D. J. Mapps and H. A. Shute, "Exact field calculations for conventional and graded magnetization thin film recording heads", *IEEE Trans. Magn.*, vol. 30, pp. 253-263, Mar. 1994.

[47] I. S. Gradshteyn and I. M. Ryzhik, *Tables of Integrals, Series and Products.* New York: Academic, 1993.

[48] M. Abramowitz and I. A. Stegun, *Handbook of Mathematical Functions.* New York: Dover, 1965.

[49] J. Todd, "Evaluation of the exponential integral for large complex arguments", *J. Res. NBS*, vol. 52, pp. 313-317, RP 2508, June 1954.

[50] H. Muraoka, Y. Sugita and Y. Nakamura, "Simplified expressions of shielded MR head response for double-layer perpendicular medium", *IEEE Trans. Magn.*, vol. 35, pp. 2235-2237, Sept. 1999.

[51] D. T. Wilton, H. A Shute, S. J. C. Brown and D. J. Mapps, "Approximation of shielded MR head output for perpendicular media", presented at PMRC 2000, Sendai, Japan, October 2000 and *J. Magn., Mater.,* 235, pp. 393-397, 2001.

[52] H. A. Shute, D. T. Wilton, D. McA McKirdy and D. J. Mapps, "Improved approximations for 2-D perpendicular recording heads", presented at NAPMRC 03, Monterey, Jan. 2003 and *IEEE Trans. Magn.*, vol. 39, no 4, pp. 2098-2102, 2003.

[53] H. A. Shute, D. T. Wilton, and D. McA McKirdy, "Magnetic potential for shielded pole heads using non-orthogonal basis functions", to be submitted to *IEEE Trans. Magn.*,

[54] R. F. M. Thornley and J. A. Williams, "Switching speeds in magnetic tapes", *IBM J. Res. Dev.*, pp. 576-578, Nov. 1974.

[55] G. T. Rado and H. Suhl, Eds., Magnetism, Vol. 2, Ch 10 and 11, Academic Press, New York, 1963.

[56] L. He, W. D. Doyle, L. Varga, H. Fujiwara and P. J. Flanders, "High speed switching in magnetic recording media", *J. Mag. and Mag. Mat.*, vol. 155, no. 3, pp. 6-12, 1996.

[57] N. D. Rizzo, T. J. Silva and A. B. Kos, "Nanosecond Magnetization Reversal in High Coercivity Thin Films", *IEEE Trans. Magn.*, vol. MAG-36, no. 1, pp. 159-165, Jan. 2000.

[58] P. R. Gillette and K. Oshima, "Magnetization reversal by rotation", *J. Appl. Phys.*, vol. 29, no. 3, pp. 529-531, Mar. 1958.

[59] J. C. Mallinson, "Damped gyromagnetic switching", *IEEE Trans. Magn.*, pp. 1976-1981, July 2000.

[60] L. He, W. D. Doyle and H. Fujiwara, "High speed coherent switching below the Stoner-Wohlfarth limit", *IEEE Trans. Magn.*, vol. 30, no. 6, pp. 4086-4088, Nov. 1994.

[61] L. He and W. D. Doyle, "A theoretical description of magnetic switching experiments in picosecond field pulses", *J. Appl. Phys.*, vol. 79, no. 8, pp. 6489-6491, Apr. 1996.

[62] NAG Routine D02BBF, Numerical Algorithms Group, Oxford, UK.

[63] K. E. Johnson, P. R. Ivett, D. R. Timmons, M. Mirzamaani, S. E. Lambert and T. Yogi, "The effect of Cr underlayer thickness on magnetic and structural properties of CoPtCr thin films", *J. Appl. Phys.*, vol. 67, no. 9, pp. 4686-4688, May 1990.

[64] H. N. Bertram, "Geometric effects in the magnetic recording process", *IEEE Trans. Magn.*, vol. MAG-20, no. 3, pp. 468-478, May 1984.

[65] G. Bate and J. A. Williams, "The cylindrical symmetry of the angular distribution of particles in magnetic tapes", *IEEE Trans. Magn.*, vol. MAG-14, no. 5, pp.

869-870, Sept. 1978.

[66] A. Moser, K. Takano, D. T. Margulies, M. Albrecht, Y. Sonobe, Y. Ikeda, S. Sun and E. E. Fullerton, "Magnetic recording: advancing into the future", *J. Appl. Phys.*, vol. 35, pp. 157-167R, Sept. 2002.

[67] A. F. Torabi, H. Zhou and H. N. Bartram, "Micromagnetic study of dynamic switching constant in film media", *J. Appl. Phys.*, vol. 87, no 9, pp. 5669-5671, May 2000.

[68] D. B. Bogy, W. Fong, B. H. Thornton, H. Zhu, H. M. Gross and C. S. Bhatia, "Some tribology and mechanics issues for 100 Gb/in^2 hard disk drive", *IEEE Trans. Magn.*, vol. 38, no 5, pp. 1879-1885, Sept. 2002.

[69] D. Kuo, X. Ma, H. Tang and J. Gui, "Effect of nonuniform lubricant distribution and de-wetting on head-disk dynamics", *IEEE Trans. Magn.*, vol. 37, no 4, pp. 1836-1838, July 2001.

[70] X. Ma, H. Tang, M. Stirniman and J. Gui, "Lubricant thickness modulation induced by head-disk dynamic interactions", *IEEE Trans. Magn.*, vol. 38, no 1, pp. 112-117, Jan. 2002.

[71] D. Weller and A. Moser, "Thermal effect limits in ultrahigh-density magnetic recording", *IEEE Trans. Magn.*, vol. 35, no 6, pp. 4423-4439, Nov. 1999.

[72] M. Wildmann, "Mechanical limitations in magnetic recording", *IEEE Trans. Magn.*, vol. 10, no 3, pp. 509-514, Sept. 1974.

[73] S. H. Charup, P-L. Lu and Y. He, "Thermal stability of recorded information at high densities", *IEEE Trans. Magn.*, vol. 33, pp. 978-983, Jan. 1997.

[74] A. Moser, C. T. Rettner, M. E. Best, E. E. Fullerton, D. Weller, M. Parker and M. Doer, "Writing and detecting bits at 100 Gbit/in^2 in longitudinal magnetic recording media", *IEEE Trans. Magn.*, vol. 36, no 5, pp. 2137- 2139, Sept. 2002.

[75] Z. Zhang, Y. C. Feng, T. Clinton, G. Badran, N-H. Yeh, G. Tarnopolsky, E. Girt, M. Munteanu, S. Harkness, H. Richter, T. Nolan, S. Hwang, G. Rauch, M. Ghaly, D. Larson, E. Singleton, V. Va'sko, J. Ho, F. Vee Kong, K. Duxstad and S. Slade, "Magnetic recording demonstration over 100 Gb/in^2", *IEEE Trans. Magn.*, vol. 38, no 5, pp. 1861- 1866, Sept. 2002.

[76] D. T. Wilton, D. McA, M. McKirdy, H. A. Shute, J. J. Miles and D. J. Mapps,

"Approximate 3-D head fields for perpendicular magnetic recording", *to be published.*

[77] S. Batra, "A perpendicular write head design for high-density recording", *IEEE Trans. Magn.*, vol. 38, no 1, pp. 157-162, Jan. 2002.

[78] F. H. Liu, K. Stoev, L. Leal, J. Wang, Y. Chen, S. Shi, H. C. Tong, M. Lederman and M. Re, "Advanced heads for perpendicular recording at high areal densities and high data rates", *IEEE Trans. Magn.*, vol. 38, no 1, pp. 151-156, Jan. 2002.

[79] M Mallary, A. Torabi and M. Benakli, "One terabit per square inch perpendicular recording conceptual design", *IEEE Trans. Magn.*, vol. 38, pp. 1719-1724, July 2002.

PUBLISHED PAPERS

Calculation of the Switching Constant of Magnetic Recording Media

Stephen J. C. Brown, John C. Mallinson, *Fellow, IEEE*, David T. Wilton, and Hazel A. Shute

Abstract—**We studied the dynamic switching time in two classes of media by considering two different particle orientation distribution functions. We calculated the switching constant directly from the Landau–Lifshitz–Gilbert equation of motion, which was chosen to simulate the dynamic properties of the media. A strong linear relation between the reciprocal of the switching time and the difference between the applied and anisotropy fields is illustrated. In media for which experimental results are available, the values we obtained here agree within a factor of 2.**

Index Terms—**Magnetic recording, magnetization switching, media.**

I. Introduction

IN RIGID disk drives with thin film heads, data rates of 500 Mb/s are commonplace today. It is almost certain that 750 Mb/s rate products will appear shortly and data rates of 1 Gb/s (1000 Mb/s) have already been reported in development. In digital tape drives, the maximum data rates are considerably slower, being in the 100–200 Mb/s range, because of the lower bit density capability and lower linear speed.

These developments have led to renewed interest in the high-speed switching behavior of recording media. When the switching time is longer than, say, 5 ns, corresponding to a 200 Mb/s rate, it is generally acknowledged that thermal energy has the major controlling influence on the switching behavior. The smaller the single domain magnetic particle or grain, the greater is the effect of thermal energy on switching. Media with small grains of low anisotropy material have coercivities that increase markedly with decreases in the switching time; such media are said to have "high viscosity."

On the other hand, when switching times are less than, say, 1 ns, the process is predominantly controlled by gyro-magnetic precession, because there is too little time available for thermal energy to have an appreciable effect. In this regime, termed adiabatic, the switching time depends upon the damping constant, which converts the (Zeeman) magnetic energy of the electron spin system to thermal (hysteresis) energy in the lattice.

The first measurements of the adiabatic switching of (γ-Fe_2O_3) magnetic recording media were performed by Thornley *et al.* in the early 1970s [1]. They discovered that the switching behavior could be fitted well to the expression

$$T_s = \frac{S_w}{H_a - H_0} \tag{1}$$

where T_s is the switching time, H_a is the applied field, H_0 is a threshold field, and S_w is defined as the switching constant. The threshold field H_0 is related to both the anisotropy field and the coercivity of the medium.

The fact that a high (500 Oe) coercivity material such as γ-Fe_2O_3 had a well-defined switching constant was, at the time, surprising. Previously, this behavior had been known only in the low (1–10 Oe) coercivity ferrite and thin permalloy film materials used in the random access memories of early computers. Many authors have since commented upon the universality of the switching constant concept in both soft (low H_c) and hard (high H_c) magnetic materials [2].

More recently, the experimental technique of Thornley has been extended in order to investigate the switching constant of modern recording media, including metal particle (MP), metal evaporated (ME), barium ferrite and chromium dioxide tapes [3], and high-coercivity thin films [4].

Despite all this activity on the switching constant of magnetic recording media, there does not appear to have been an attempt to calculate the switching constant directly from the damped gyro-magnetic precession equation. This paper addresses that calculation.

Here, the Gilbert form [5] of the damped gyro-magnetic equation is used to calculate the switching constant of two different classes of magnetic recording media. The first class is intended to simulate a modern thin-film hard disk, where the individual single domain magnetic grains, though not oriented in the plane of the disk, all have their anisotropy axes lying in the plane of the disk. In other words, the easy axes of the grains are oriented at random in the plane of the disk. This arrangement of grains will be termed "2-D random."

In the second class of media, meant to simulate a single-domain particulate recording tape, the easy axes of the particles are partially oriented, with cylindrical symmetry, along a direction lying in the plane of the tape. Suitable angular distribution functions can be found in the literature; they are based upon numerical fits to, for example, the angular variation of the maximum remanence. Generally, a well-oriented tape will have greater than 90% of the particle easy axes lying within a cone of semiangle 30° around the orientation direction. This arrangement of grains will be termed "3-D oriented."

For both classes of media, it is assumed that the individual grains or particles switch independently. That is to say, it

Manuscript received February 1, 2001; revised August 15, 2001.

S. J. C. Brown, D. T. Wilton and H. A. Shute are with the Department of Mathematics and Statistics and the Centre for Research in Information Storage Technology, University of Plymouth, Drake Circus, Plymouth, Devon PL4 8AA, U.K. (e-mail: dwilton@plymouth.ac.uk)

J. C. Mallinson is with Mallinson Magnetics Inc., Belmont, CA 94002 USA.

Publisher Item Identifier S 0018-9464(02)00392-8.

is taken that both the magnetostatic interaction fields and exchange fields between the grains and particles may be ignored. As the coercivity and anisotropy field of modern media increase compared to the moment density, the omission of the magnetostatic interactions becomes an increasingly valid approximation. In thin film disks, intergrain exchange coupling is kept low because it is known that such coupling reduces the signal-to-noise ratio of the medium. In particulate tapes, exchange coupling between particles is unlikely because the individual particles are separated by the plastic binder system.

In both classes of media, the solution of the damped Gilbert equation is computed numerically, following the formalism of Gillette and Oshima [6], for the range of damping constants $0.2 \leq \alpha \leq 2.0$. Low damping constant solutions have a great deal of precession and long switching times. The critical damping constant, $\alpha = 1$, yields the shortest switching time with little precession.

In a recent paper, Mallinson [7] showed that when the applied field direction and the anisotropy axis of a single domain grain or particle were parallel, the damped Gilbert equation could be solved analytically. However, it has not been found possible to extend that analytical solution to the general case where the field direction and the anisotropy axis are not colinear.

In the 2-D random thin-film disk case, the solution of the damped Gilbert equation is computed numerically for 100 sampled grain orientations from 0° to 90°. The switching time computed is the time taken for the slowest one of 90% of the grains' magnetization vectors to cross their uniaxial anisotropy hard equatorial planes. The individual grain switching times for the 2-D random set of grains are, of course, given equal weighting.

In the 3-D oriented tape case, the switching times are calculated with the appropriate weighting for the cylindrically symmetric array of particles.

The results of these calculations are displayed in two ways. First, the reciprocal of the switching time is plotted versus $H_a - H_k$, where H_k is the anisotropy field (2 K/M for uniaxial magnetocrystalline and $M(N_\perp - N_\parallel)$ for uniaxial shape anisotropies). It will be noted that the resultant curves are very nearly straight lines, indicating that, indeed, a switching constant as defined above does exist. Second, switching constants, which are proportional to the reciprocal of the slopes of these curves, are plotted versus the damping constant α. It is found that not only are the calculated values of S_w in fairly good accord with the recent experimental results but also that the lowest values of S_w occur close to the critical value ($\alpha = 1$) of the damping constant.

II. Theoretical Model

Consider a single domain particle made of a magnetic material which has uniaxial magnetocrystalline anisotropy, a uniform magnetization M, taken here to have a constant magnitude $M = 1000$, and an easy axis aligned with the z direction (Fig. 1). The choice of $M = 1000$ is arbitrary and although it does affect the "reduced time," τ, defined after (3) and used in several of the figures, it has no effect upon the values of S_w calculated here using (8). The dynamic behavior of the particle's

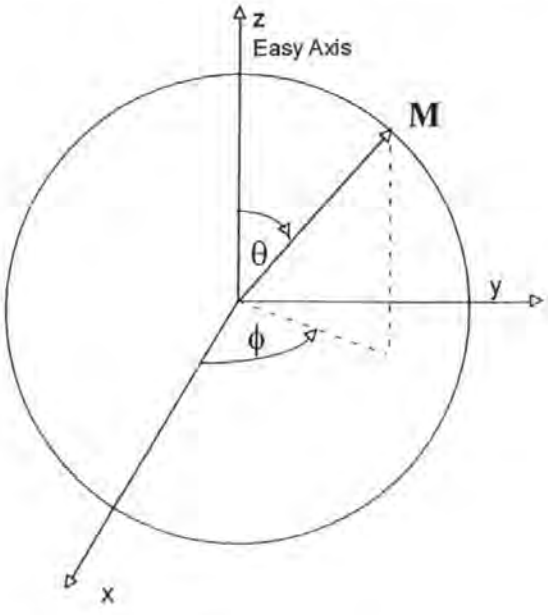

Fig. 1. Coordinate system for a single grain.

magnetization vector M is assumed to evolve in time as described by the Gilbert form [5] (L–L–G) of the Landau–Lifshitz equation:

$$\frac{d\mathbf{M}}{dt} = -\gamma(\mathbf{M} \times \mathbf{H}_T) + \frac{\alpha}{M}\left(\mathbf{M} \times \frac{d\mathbf{M}}{dt}\right) \tag{2}$$

where $\gamma \simeq 1.76 \times 10^7$ radOe^{-1}sec^{-1} is the magnetomechanical or gyromagnetic ratio and α is the phenomenological damping constant. $\mathbf{H}_T = (H_{Tx}, H_{Ty}, H_{Tz})$ is the vector sum of the effective anisotropy field, $\mathbf{H}_k = (H_{kx}, H_{ky}, H_{kz})$, and the external field, $\mathbf{H}_a = (H_{ax}, H_{ay}, H_{az})$, and it represents the total effective field acting on M. The anisotropy may be thought of as a fictitious field $H_k \cos\theta$ acting in the easy axis direction, that is $\mathbf{H}_k = (0, 0, H_k \cos\theta)$, from which it follows that $\mathbf{H}_T = (H_{ax}, H_{ay}, H_{az} + H_k \cos\theta)$. Gillette and Oshima [6] showed that the L–L–G equation may be expressed, in the spherical polar coordinate system of Fig. 1, as the two coupled first order differential equations:

$$\begin{aligned} \sin\theta \frac{d\varphi}{d\tau} &= F_1 + \alpha F_2 \\ \frac{d\theta}{d\tau} &= F_2 - \alpha F_1 \end{aligned} \tag{3}$$

where

$$F_1 = -\frac{H_{Tx}}{M}\cos\theta\cos\varphi - \frac{H_{Ty}}{M}\cos\theta\sin\varphi + \frac{H_{Tz}}{M}\sin\theta$$

$$F_2 = -\frac{H_{Tx}}{M}\sin\varphi + \frac{H_{Ty}}{M}\cos\varphi$$

and $\tau = M\gamma t/(1+\alpha^2)$ is the reduced time. Only in the case of the applied field and the anisotropy axis being colinear, giving $F_2 = 0$, does it appear that an analytic solution to these equations can be found [7]. Numerical solutions to (3) have been computed [8], [9] by using numerical integration routines based on the Runge–Kutta method [10], as are the results here.

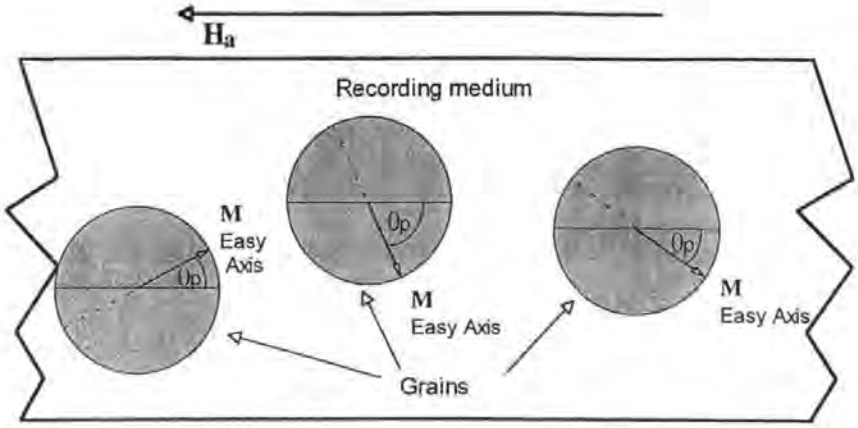

Fig. 2. Randomly oriented grains in a thin film medium.

A. Thin-Film Hard Disk Media

It has been shown [11] that the physical structure of longitudinal thin film media is realistically modeled by assuming that the uniaxial magnetocrystalline axes of the individual single domain grains are randomly distributed in the plane of the medium (2-D random). Each individual grain has its easy axis lying at an angle of between 0° and 90° to the applied field. This is shown in the schematic drawing of Fig. 2, in which the external field $\mathbf{H}_a$ is applied in the negative x direction and the magnetizations M are aligned with the randomly distributed easy axes of the grains forming angles θ_p with the applied field. This is simulated by sampling 100 equally spaced angles between 0° and 90°. The switching time is then defined as the time taken for the slowest one of 90% of the magnetization vectors to achieve a polar angle of greater than 90°, at which time the removal of the applied field would result in 90% of the magnetization vectors precessing toward, and aligning with, the easy axis opposite to their initial direction.

B. Single Domain Particle Recording Tape Media

In this class of media, the particle easy axes are partially oriented in the longitudinal direction. Here, we consider a medium in which 90% of the easy axes lie within a 60° cone centered about the longitudinal direction.

Bertram [12] has proposed that the orientation of the particle easy axes may be assumed to be distributed in the recording plane (the x, y plane where x is the longitudinal direction and y is the out-of-tape direction) by the function

$$f(\theta_p) = N_\beta \, e^{\beta \cos^2 \theta_p} \tag{4}$$

where N_β is a suitable normalization factor and β is the orientation parameter. Positive values of β represent media oriented to a greater (larger β) or lesser (smaller β) extent about the longitudinal direction. The case $\beta = 0$ represents 2-D random or unoriented media. The distribution function (4) is extended here to describe the particle orientation of magnetic tape media. Bate and Williams [13] have shown that the angular distribution of the particle easy axes in magnetic tape is cylindrically symmetric, to "within about 10%," about the direction of orientation. A cylindrically symmetric 3-D representation, $g(\theta_p)$, of the 2-D distribution function (4) is obtained by taking the product of (4) and a spherical polar surface element and integrating over all azimuthal angles. This gives

$$g(\theta_p) = N_\beta \int_0^{2\pi} e^{\beta \cos^2 \theta_p} R^2 \sin\theta_p \, d\varphi = 2\pi R^2 e^{\beta \cos^2 \theta_p} \sin\theta_p \tag{5}$$

where R is the radius of the sphere and the normalization factor N_β is given by

$$\begin{aligned} N_\beta &= \int_0^{2\pi} \int_0^{\pi/2} e^{\beta \cos^2 \theta_p} R^2 \sin\theta_p d\theta_p \, d\varphi \\ &= 2\pi R^2 \int_0^{\pi/2} e^{\beta \cos^2 \theta_p} \sin\theta_p d\theta_p. \end{aligned} \tag{6}$$

Single domain particles within magnetic tape media are, therefore, assumed to be oriented according to the distribution function

$$g(\theta_p) = \frac{e^{\beta \cos^2 \theta_p} \sin\theta_p}{\int_0^{\pi/2} e^{\beta \cos^2 \theta_p} \sin\theta_p d\theta_p}. \tag{7}$$

In order to have 90% of the particle distribution oriented within 30° (the half cone angle) of the orientation direction, β must equal 9.89. This value of β is assumed hereafter.

As with 2-D random media, 100 equally spaced orientation angles between 0° and 90° are sampled, but each angular sample in this case is weighted by the distribution function (7). Again the switching time is then taken as the time for the slowest one of 90% of the normalized distribution to switch (cross the hard equatorial plane).

III. Results

When $\alpha < 1$, the dynamic behavior of a grain's magnetization vector is complex. For low values of α, the magnetization vector tends to follow a damped orbit which carries it back and forth across the hard equatorial plane [3]. This behavior is illustrated in Fig. 3 where the percentage of switched grains in a 2-D random distribution is plotted against the reduced time, $\tau (= M\gamma t/(1+\alpha^2))$, elapsed since the application of an external field. Results for the two cases $H_k = 1000$ Oe with $H_a = 2500$ Oe and $H_a = 4000$ Oe are shown and α is equal to 0.2. Here, one reduced time unit, τ, corresponds to 0.0591 ns

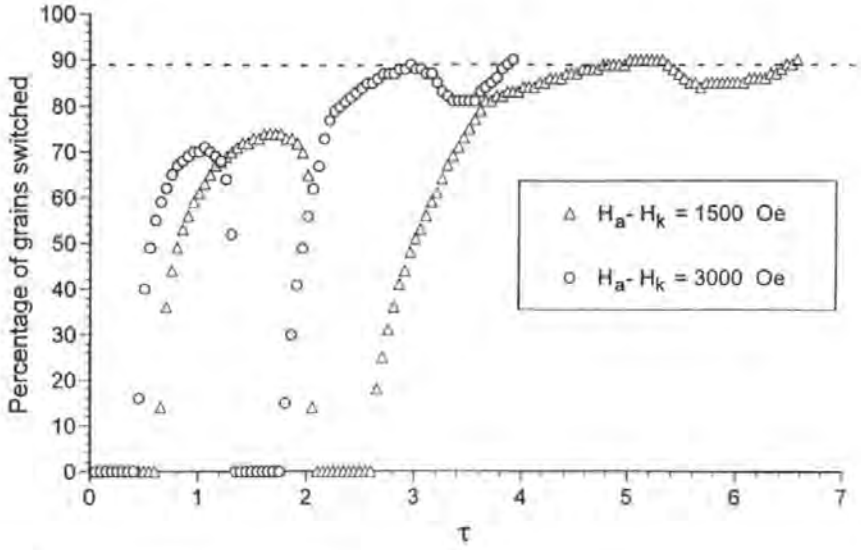

Fig. 3. Percentage of grains switched at reduced time for 2-D random media with $\alpha = 0.2$, $H_k = 1000$ Oe, $H_a = 2500$ Oe and 4000 Oe.

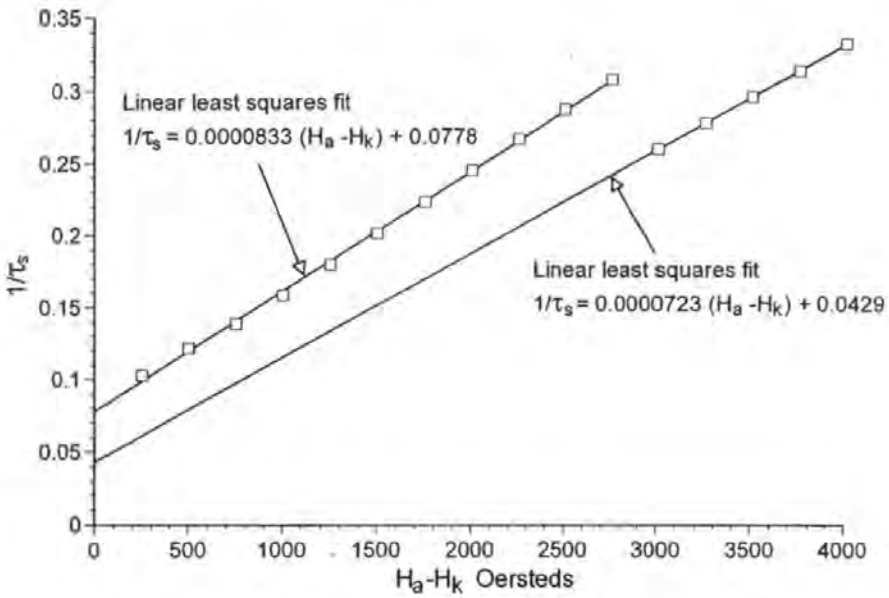

Fig. 4. Variation of reciprocal of reduced switching time with $H_a - H_k$ for 2-D random media with $\alpha = 0.2$, $H_k = 1000$ Oe.

in actual time. Immediately following the introduction of the external switching field the magnetizations of the individual grains within the 2-D random distribution begin their forced precessional orbits across the hard plane and the percentage of switched grains increases rapidly until it reaches approximately 74% for $H_a - H_k = 1500$ Oe and approximately 71% for $H_a - H_k = 3000$ Oe. At this point (at about $\tau = 1.65$ and $\tau = 1.1$, respectively), more and more individual grains have magnetizations which, having successfully switched, are continuing in their forced orbits back across the hard plane leading to a net decrease in the percentage of grains switched thus creating a local maximum. The same effect produces further local maxima, although these are less pronounced as time passes.

One consequence of this behavior is illustrated in Fig. 4, where the reciprocal of the reduced switching time, τ_s, is plotted against $H_a - H_k$, for $H_k = 1000$ Oe with α again equal to 0.2. The disjointed linear form of the plot is due to the fact that, for $H_a - H_k < 3000$ Oe, more than 90% of the distribution has switched by the second local maximum (and therefore, by our definition, the medium has switched). However, for $H_a - H_k \geq 3000$ Oe, the second local maximum does not exceed the 90% threshold and switching is not achieved at that time. For $H_a - H_k \geq 3000$ Oe, the percentage of switched grains goes through a further local minimum before reaching 90% at the third attempt.

The discontinuous form of the plotted values in Fig. 4 is potentially a source of error when calculating the switching constant. For low values of α, there are two separate line segments and therefore two slightly different values for the gradient of $1/\tau_s$ versus $H_a - H_k$ on which to base the calculation of S_w. For example, Fig. 4 shows that when $\alpha = 0.2$, the two line segments have gradients of 8.33×10^{-5} for $H_a - H_k \leq 2750$ Oe

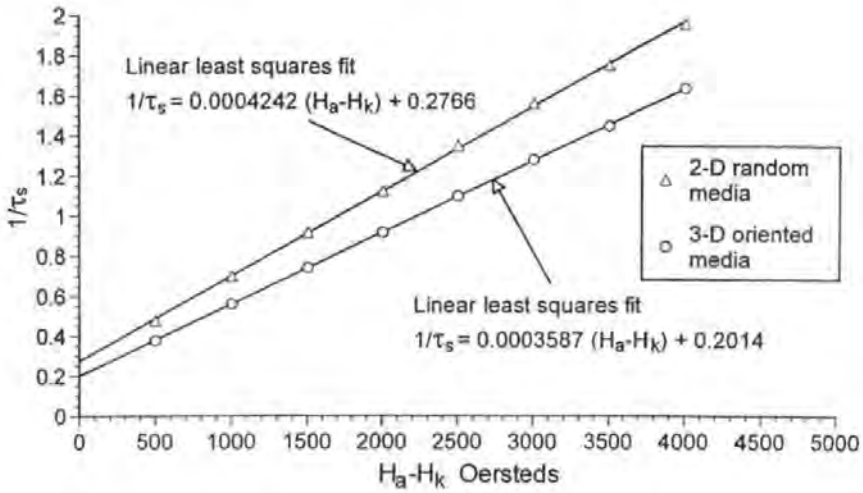

Fig. 5. Variation of reciprocal of reduced switching time with $H_a - H_k$ for 2-D random and 3-D oriented media with $\alpha = 1.0$, $H_k = 1000$ Oe.

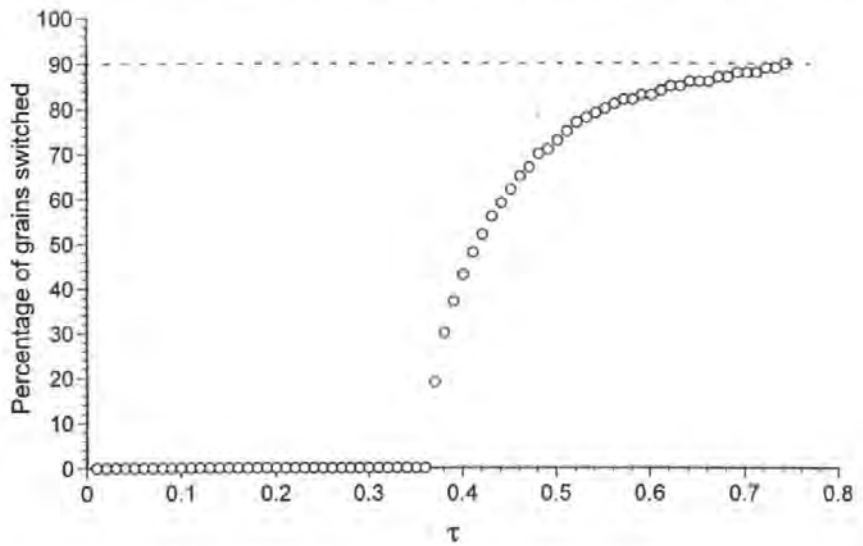

Fig. 6. Percentage of grains switched at reduced time for 2-D random media with $\alpha = 1.0$, $H_k = 1000$ Oe and $H_a = 3500$ Oe.

and 7.23×10^{-5} for $H_a - H_k \geq 3000$ Oe. Substituting these two values into the calculation

$$S_w = \frac{1}{\text{gradient}} \times \frac{1+\alpha^2}{M\gamma} \tag{8}$$

in turn, produces switching constants of 709 ns-Oe and 817 ns-Oe, respectively. This apparent ambiguity is resolved here by requiring that a medium is considered to be switched only if both the threshold value of 90% is achieved and the percentage will not drop below 90% at any subsequent time while the external field remains applied. This added criterion to the definition of switching has the effect of excluding the switching of media by the local maxima illustrated in Fig. 3. It follows that in the case of Fig. 4, the line segment for $H_a - H_k \geq 3000$ Oe is chosen and the resulting switching constant for 2-D random media with $\alpha = 0.2$ is given as 817 ns-Oe.

Fig. 5 shows $1/\tau_s$ plotted against $H_a - H_k$ for $H_k = 1000$ Oe with $\alpha = 1.0$ for 2-D random and 3-D oriented media. Here, the reduced time unit corresponds to 0.114 ns. It is clear that the switching time is no longer affected by local maxima when $\alpha = 1.0$ since the plot produces a continuous single straight line for each class of media. The switching behavior for 2-D random media with $\alpha = 1.0$, $H_k = 1000$ Oe and $H_a = 3500$ Oe is shown in Fig. 6. In contrast to the $\alpha = 0.2$ case, the percentage of switched grains increases monotonically after the introduction of the switching field, with no local maxima to consider in the computation of the switching constant.

The switching constants for 2-D random and 3-D oriented media for $0.2 \leq \alpha \leq 2.0$ are plotted in Fig. 7, where it is observed that for each class of media, the minimum value of S_w occurs close to the critical value of $\alpha = 1.0$. Finally, the switching constants obtained for the two classes of media, for a range of values of α are given in Table I.

IV. Discussion

In the results presented above, there are several points of interest. First, it is remarkable that the plots of the reciprocal of the reduced switching time, $1/\tau_s$, versus $H_a - H_k$ are essentially perfect straight lines. It should be noted that the appearance

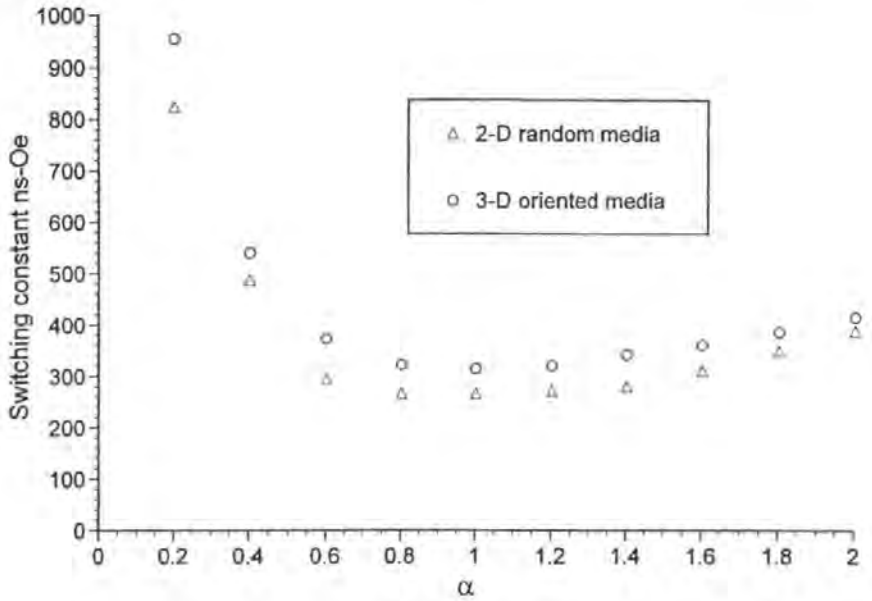

Fig. 7. Variation of the switching constant with α for 2-D random and 3-D oriented media.

TABLE I
SWITCHING CONSTANTS FOR 2-D RANDOM AND 3-D ORIENTED MEDIA FOR DIFFERENT VALUES OF α

α	2-D random S_w (ns-Oe)	3-D oriented S_w (ns-Oe)
0.2	817	955
0.4	489	542
0.6	295	374
0.8	267	323
1.0	267	316
1.2	272	321
1.4	280	343
1.6	311	361
1.8	350	386
2.0	389	415

f the anisotropy field, H_k, in the theoretical (L–L–G) model ther than the related threshold field, H_0, gives rise to lines hich do not pass through the origin. However, it is the slope of ese lines only that is used in the calculation of the switching nstants. Second, it is to be pointed out that the slopes of these raight lines, which are proportional to the reciprocals of the vitching constants S_w, are independent of the value of the isotropy field, H_k. The value of S_w depends only upon the mping parameter α and the orientation parameter β of the rticle/grain ensemble. The lowest values of S_w, which give e fastest switching, occur at values of the damping parameter, approximately equal to unity in both oriented and unoriented ays.

It is difficult to prove mathematically just why the $1/\tau_s$ versus $H_a - H_k$ curves are so linear. This is, principally, because the basic Gilbert equation does not admit an analytical solution except for the colinear, perfectly oriented, case [7]. Moreover, the procedure used to determine the switching time of each grain is inherently nonlinear.

In that very special case of a single spherical grain with the anisotropy easy axis colinear with the applied field, the analytical solution for the time to switch from polar angle θ_1 to θ_2, given in [7], does give the approximate linear relationship

$$\frac{1}{T_s} \approx \frac{-\gamma\alpha}{1+\alpha^2} \frac{1}{\ln\left[\frac{\tan(\frac{\theta_1}{2})}{\tan(\frac{\theta_2}{2})}\right]} \cdot \left[(H_a - H_k) + H_k\left(1 - \frac{\ln\left[\frac{\sin(\theta_1)}{\sin(\theta_2)}\right]}{\ln\left[\frac{\tan(\frac{\theta_1}{2})}{\tan(\frac{\theta_2}{2})}\right]}\right)\right]. \quad (9)$$

When $\theta_2 = 90°$, this gives an approximate formula for a "switching constant" which depends on the initial orientation angle θ_1 as

$$S_w \approx -\frac{1+\alpha^2}{\gamma\alpha} \ln\left[\tan\left(\frac{\theta_1}{2}\right)\right]. \quad (10)$$

Unfortunately, this simple approximation cannot be used to calculate S_w for distributions of grains in which the anisotropy axes of the grains are not colinear with the applied field.

The fact that the S_ws calculated here are independent of the value of H_k is best illustrated by example. In Fig. 8, the reciprocal reduced switching time, $1/\tau_s$, versus $H_a - H_k$ is shown for the 2-D random case with $\alpha = 1.0$, both for $H_k = 1000$ Oe and for $H_k = 2000$ Oe. For both values of H_k the slopes and, therefore, the S_ws are identical. It is to be understood, however,

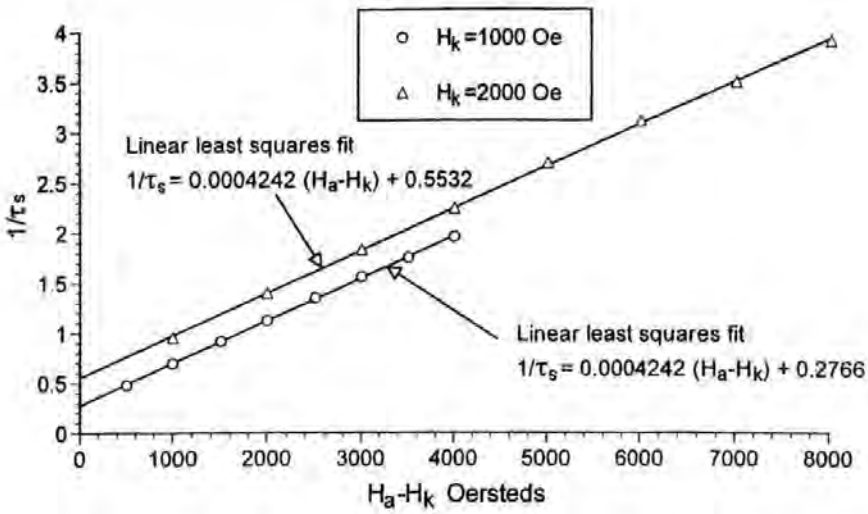

Fig. 8. Variation of the reciprocal of reduced switching time with $H_a - H_k$ for 2-D random media with $\alpha = 1.0$, $H_k = 1000$ Oe and 2000 Oe.

that if a field greater than 2000 Oe were to be applied, the material with the lower H_k would switch more rapidly than that with the higher H_k, because the switching time is inversely proportional to the "excess" field, $H_a - H_k$.

It is to be realized that the values of S_w calculated here hold for all positive values of the excess field, $H_a - H_k$. Thus, for example, if $S_w = 500$ ns-Oe, excess fields of 50, 500, and 5000 Oe, which might be appropriate for materials such as permalloy, γ-Fe_2O_3 tape and modern high coercivity recording media respectively, will produce switching times, T_s, of 10, 1, and 0.1 ns, respectively. The analysis presented here applies equally to the switching of all classes of magnetic medium.

In both the 2-D random and 3-D oriented cases, the lowest values of the computed switching constant occur close to a value of the damping parameter, α, equal to unity. This is not surprising because it has been understood for many years that the fastest Gilbert damped gyro-magnetic switching occurs when $\alpha = 1$. It is perhaps surprising, however, to see that the effect of orienting the grains/particles is to produce larger values of S_w and, therefore, slower switching.

Finally, the calculated values of S_w reported here may be compared with the published, experimentally measured, values. In a recent invited paper, He *et al.* report upon high-speed switching measurements in tapes as follows: Metal Particle tape 140 ns-Oe, Metal-Evaporated tape 190 ns-Oe, Barium Ferrite tape 240 ns-Oe, Chromium Dioxide tape 222 ns-Oe, γ-Fe_2O_3 (A) 87 ns-Oe and γ-Fe_2O_3 (B) 160 ns-Oe [3]. In the present work, the lowest value for 2-D random media is 267 ns-Oe and for 3-D oriented media is 316 ns-Oe. Ignoring the γ-Fe_2O_3 (A) remarkably low value reported by He *et al.*, the values computed here from the Gilbert equation are within a factor of 2 of the experimental values. In a recent paper [4], Rizzo *et al.* report that a thin film with $H_c \approx 1000$ Oe, behaved adiabatically with a measured S_w of 373 ns-Oe. Again our computed values of S_w agree within a factor of 2 of the experimental.

There are several reasons that lead one to expect that the experimental values will be smaller than those computed. First, many of the high-speed switching experiments made use of a static bias field which is known to reduce the switching time and, concomitantly, the switching constant. For example, it has been shown recently that if the dc bias field is $0.5H_k$ and the applied field is $1.5H_k$, the switching time is reduced by 18% in the perfectly aligned case [7]. For lower applied fields, the reduction becomes greater. Second, in experimental work the current pulses which produce the dynamic switching field almost inevitably have nonnegligible rise and fall times during which, of course, some particle/grain switching occurs. If this switching is not accounted for properly, the result is, again, lower apparent switching constants. Without mathematical justification, the traditional correction has been, over at least the last 40 years, to modify (1) to become $S_w = \int_T (H_a - H_k)dt$, where T is the time interval when $H_a \geq H_k$. In our computations the rise and fall times of the applied field are taken to be zero.

V. Conclusion

The Gilbert form of the Landau–Lifshitz equation has been solved numerically for an assembly of magnetic particles in order to calculate the switching constant of a magnetic recording medium. For each of two different classes of media, it has been found that an approximate theoretical linear relationship does exist between the reciprocal of the switching time and the difference between the applied and anisotropy fields. This is consistent with experimental observations. Theoretical calculations of the switching constant are in good agreement with published experimental values and this is considered to justify the omission here of the magnetostatic and exchange fields which undoubtedly exist in real media.

References

[1] R. F. M. Thornley and J. A. Williams, "Switching speeds in magnetic tapes," *IBM J. Res. Dev.*, pp. 576–578, Nov. 1974.

[2] G. T. Rado and H. Suhl, Eds., *Magnetism*. New York: Academic, 1963, vol. 2, ch. 10,11.

[3] L. He, W. D. Doyle, L. Varga, H. Fujiwara, and P. J. Flanders, "High speed switching in magnetic recording media," *J. Magn. Magn. Mater.*, vol. 155, no. 3, pp. 6–12, 1996.

[4] N. D. Rizzo, T. J. Silva, and A. B. Kos, "Nanosecond magnetization reversal in high coercivity thin films," *IEEE Trans. Magn.*, vol. 36, pp. 159–165, Jan. 2000.

[5] T. L. Gilbert, "A Lagrangian formulation of the gyromagnetic equation of the magnetization field," *Phys. Rev.*, vol. 100, p. 1243, 1955.
[6] P. R. Gillette and K. Oshima, "Magnetization reversal by rotation," *J. Appl. Phys.*, vol. 29, pp. 529–531, Mar. 1958.
[7] J. C. Mallinson, "Damped gyromagnetic switching," *IEEE Trans. Magn.*, vol. 36, pp. 1976–1981, July 2000.
[8] L. He, W. D. Doyle, and H. Fujiwara, "High speed coherent switching below the Stoner-Wohlfarth limit," *IEEE Trans. Magn.*, vol. 30, pp. 4086–4088, Nov. 1994.
[9] L. He and W. D. Doyle, "A theoretical description of magnetic switching experiments in picosecond field pulses," *J. Appl. Phys.*, vol. 79, pp. 6489–6491, Apr. 1996.
[10] "Numerical Algorithms Group ,", Oxford, U.K., NAG Routine D02BBF.
[11] K. E. Johnson, P. R. Ivett, D. R. Timmons, M. Mirzamaani, S. E. Lambert, and T. Yogi, "The effect of Cr underlayer thickness on magnetic and structural properties of CoPtCr thin films," *J. Appl. Phys.*, vol. 67, pp. 4686–4688, May 1990.
[12] H. N. Bertram, "Geometric effects in the magnetic recording process," *IEEE Trans. Magn.*, vol. MAG-20, pp. 468–478, May 1984.
[13] G. Bate and J. A. Williams, "The cylindrical symmetry of the angular distribution of particles in magnetic tapes," *IEEE Trans. Magn.*, vol. MAG-14, pp. 869–870, Sept. 1978.

tephen J. C. Brown received the M.Math. degree in mathematics in 1997 from ie University of Plymouth, U.K. He is currently working toward the Ph.D. degree in theoretical aspects of magnetic recording at the University of Plymouth.

ohn C. Mallinson (SM'74-F'82) was born in Bradford, U.K., on January 30, 932. He received the M.A. degree in natural philosophy (physics) from Uniersity College, Oxford, U.K., in 1953 and the D.Sc. degree in 1997.

He joined Amp., Inc., Harrisburg, PA, in 1954 to work on the theory and degn of all-magnetic logic elements. In 1962 he joined Ampex Corporation, Redood City, CA, where he held many positions concerned with the understanding nd development of magnetic recording systems. From 1976 to 1978, as Manger of High Bit Rate Recording in the Data Systems Division, he was conerned with the initial design of a 750 Mb/s digital recorder. From 1978 to 1985 e supervised the Magnetic Recording Technology Department, a multidisciinary group working in magnetic recording theory, high-density head fabricaon, coding and communications theory, and the exploration of advanced conepts in various areas of recording. In 1984 he was appointed Founding Director f the Center for Magnetic Recording Research at the University of California, an Diego. In 1990 he resigned his university position in order to pursue his reearch and consulting business interests. He is now President of Mallinson Magtics, Inc., Belmont, CA. He has published over 70 papers on a wide variety of eoretical topics in magnetic recording. he is the author of two textbooks, *The undations of Magnetic Recording* (New York: Academic, 1993) and *Magto-Resistive Heads: Fundamentals and Applications* (New York: Academic, 95).

Dr. Mallinson was an IEEE Magnetics Society Distinguished Lecturer in 83. In 1984 he was awarded the Alexander M. Poniatoff Award for "leadship in the theory and practice of magnetic recording."

David T. Wilton received the B.A. degree in mathematics from the University of York, U.K., in 1969 and the D.Phil. degree in numerical analysis from the University of Oxford, U.K., in 1974.

He spent three years at the University of Dundee, Scotland, and then three years with the Ministry of Defence working on dynamic fluid-structure interaction problems in underwater acoustics. Since 1978 he has been lecturing mathematics at the University of Plymouth. During 1987–1989, he spent two years at the City Polytechnic of Hong Kong. His main research interests are in numerical analysis and applied mathematics in the areas of electromagnetics and acoustics.

Hazel A. Shute received the B.Sc. degree in mathematical studies in 1992 and the Ph.D. degree in mathematical modeling in 1995, both from the University of Plymouth, U.K.

She is currently continuing her work on magnetic recording head read/write characteristics as a Postdoctoral Research Fellow at the University of Plymouth.

Analytic Solutions for Double-Element Shielded Magnetoresistive Heads

Stephen J. C. Brown, David T. Wilton, Hazel A. Shute, and Desmond J. Mapps

Abstract— **New analytic solutions are presented for idealized athematical models of double-element shielded magnetoresistive IR) magnetic recording heads. Two types of heads are consid-ed, represented by poles of either equal or opposite magnetic otentials, each in the presence of an infinitely permeable un-erlayer. The solutions for heads without underlayers are special ses of the more general results. Typical field plots and spectral sponse functions are given and comparisons are made with ublished approximate solutions.**

Index Terms— **Digital recording, magnetic fields, magnetic cording, magnetoresistive heads, mathematics.**

I. Introduction

MAGNETORESISTIVE (MR) heads are in common use today as reading sensors in the area of high density ngitudinal magnetic recording [1], [2]. It has also been ggested that MR heads are likely to have a strong influence the future development of perpendicular recording [3]. ouble-element heads offer advantages over single-element ads in terms of increased robustness against thermal spikes, e reduction of pulse amplitude asymmetry, and alleviating e electrical shorting to disk problem [1]. Various configu-tions of the two elements are possible, depending on the agnetization direction in each element due to the bias field, e directions of the sensing currents, and whether the output ltages are added or subtracted [4]–[6]. There are however ly two basic output pulse shapes, which, when the head sponse is linear, may be determined by assigning magnetic tentials to the two MR elements and applying the reciprocity inciple. The appropriate "reciprocity potentials" are either ual potentials on each pole or opposite potentials on each le [7]. The problem is then to solve Laplace's equation the magnetic scalar potential in the region exterior to elements. Here, new analyses are presented for both ssible potential distributions on the MR elements which are mmetrically placed between shields held at zero potential d are in the presence of a high permeability keeper layer zero potential.

An approximate solution for double-element heads has ently been proposed in [7]. The horizontal component of the face field in the gaps is taken as the equally weighted sum of a Karlqvist-type [8] approximation (linear potential variation and hence constant field across the gaps) and the exact field from a Westmijze-type [9] conformal mapping solution for infinitely thin MR elements and shields. This approximation is for a head above a medium with no underlayer. When an underlayer is present, approximations discussed in [10] are appropriate. These are based on a linear variation in potential between the MR element and the underlayer.

Full analytic solutions for such problems are possible using Fourier analysis or conformal mapping ideas while numerical approaches are usually based on finite difference, finite element, or boundary element methods. Here the Fourier method, first employed to study the magnetic field of a recording head by Fan [11] and extended in [12], is used as it is the only method which gives an explicit solution, although this is in the form of an infinite series whose coefficients must be calculated numerically. In the next section the method is briefly outlined and the magnetic potential and magnetic field results are given. Following [7], the name "dual stripe" refers to a head with MR elements at the same potential, while "differential" is used when the elements have opposite potential. The superscript "++" denotes results for the dual stripe head, while "−+" refers to the differential head. Solutions for both heads are given in the general case of an underlayer being present and for each head the simplifications in the special case of no underlayer are identified. In Section III, results of typical magnetic field calculations are presented, comparisons with approximate solutions are made, and spectral response results are given and discussed.

II. Magnetic Field

A. Dual Stripe MR Head with an Underlayer

The idealized mathematical model of a symmetrically shielded, double-element MR head is shown in Fig. 1. Two semi-infinite MR elements each of length L, and at the same potential V, are separated by a gap of $G = 2g$ and are perpendicular to and at a distance t from an infinite plane (the underlayer) at zero potential. The shields are semi-infinite in both the horizontal and vertical directions with element/shield gaps of $H = 2h$. The shields each have potential αV, although the case $\alpha = 0$ is of most practical interest. The shields, MR sensors and the underlayer are all assumed to have infinite permeability and the recorded medium has unit permeability. The magnetic potential φ satisfies Laplace's equation in the region below the underlayer and exterior to the elements and shields. By symmetry, only $x \geq 0$ needs to be considered, which is subdivided into regions I, II, and III as shown in

Manuscript received April 7, 1999; revised June 1, 1999.

S. J. C. Brown, D. T. Wilton, and H. A. Shute are with the School of thematics and Statistics and the Centre for Research in Information Storage hnology, University of Plymouth, Plymouth, Devon PL4 8AA, U.K. (e-l: sbrown@plymouth.ac.uk)

D. J. Mapps is with the School of Electronic, Communication and Electrical gineering and the Centre for Research in Information Storage Technology, versity of Plymouth, Plymouth, Devon PL4 8AA, U.K.

Publisher Item Identifier S 0018-9464(99)07353-7.

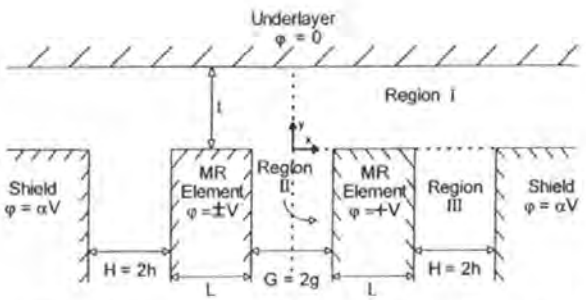

Fig. 1. Double-element shielded MR head: dual stripe head, $\varphi = +V$ on the left-hand element; differential head, $\varphi = -V$ on the left-hand element.

Fig. 1. The general solution of Laplace's equation in region I which is symmetric in x and zero at $y = t$ is

$$\varphi_{\mathrm{I}}^{++}(x, y) = \int_0^\infty D(k) \cos[kx] \sinh[k(t-y)]\, dk. \quad (1)$$

In region II the solution which is symmetric in x, takes the value $\varphi_{\mathrm{II}}^{++} = V$ at $x = g$ and has the correct behavior as $y \to -\infty$ is

$$\varphi_{\mathrm{II}}^{++}(x, y) = V + \sum_{n=1}^{\infty} A_n \cos[(n-1/2)\pi x/g] e^{(n-1/2)\pi y/g} \quad (2)$$

while in region III the appropriate solution is

$$\varphi_{\mathrm{III}}^{++}(x, y) = V[1 + (\alpha - 1)(x - g - L)/H] + \sum_{n=1}^{\infty} B_n \sin[n\pi(x - g - L - h)/h] e^{n\pi y/h} + \sum_{n=1}^{\infty} C_n \cos[(n-1/2)\pi(x - g - L - h)/h] \cdot e^{(n-1/2)\pi y/h}. \quad (3)$$

Matching the potential at $y = 0$

$$\varphi_{\mathrm{I}}^{++}(x, y) = \begin{cases} \varphi_{\mathrm{II}}^{++}(x, 0) & 0 \le x \le g \\ V & g \le x \le g + L \\ \varphi_{\mathrm{III}}^{++}(x, 0) & g + L \le x \le g + L + H \\ \alpha V & g + L + H \le x < \infty \end{cases} \quad (4)$$

and taking a Fourier cosine transform

$$F_c[f(x)] = \int_0^\infty \cos[\omega x] f(x)\, dx \quad (5)$$

gives $D(k)$ in terms of the Fourier coefficients A_n, B_n, and C_n and hence

$$\varphi_{\mathrm{I}}^{++}(x, y) = \frac{2Vh(1-\alpha)}{\pi} J_0^{++} + \frac{\alpha V(t-y)}{t} + \sum_{n=1}^{\infty} A_n 2(n-1/2)g(-1)^n I_n^{++} + \sum_{n=1}^{\infty} B_n 4nh(-1)^{n+1} J_n^{++} + \sum_{n=1}^{\infty} C_n 4(n-1/2)h(-1)^n K_n^{++}. \quad (6)$$

I_n^{++}, J_n^{++}, and K_n^{++} are integrals which are functions of x and y and are given in the Appendix.

Matching the potential gradient $\partial\varphi/\partial y$ at $y = 0$ in $0 \le x \le g$ and $g + L \le x \le g + L + H$, and using the orthogonality properties of the sine and cosine functions in (2) and (3) in their appropriate intervals, results in three coupled infinite sets of linear simultaneous equations for the coefficients A_n, B_n, and C_n

$$A_m + \sum_{n=1}^{\infty} A_n 4(n-1/2)g^2(-1)^{m+n} I_{mn}^{++} + \sum_{n=1}^{\infty} B_n 8ngh(-1)^{m+n+1} J_{mn}^{++} + \sum_{n=1}^{\infty} C_n 8(n-1/2)gh(-1)^{m+n} K_{mn}^{++} = \frac{4V(\alpha-1)gh}{\pi}(-1)^m J_{m0}^{++} + \frac{2V\alpha g}{t[(m-1/2)\pi]^2}(-1)^m \quad (7)$$

$$\sum_{n=1}^{\infty} A_n 4(n-1/2)gh(-1)^{m+n+1} J_{nm}^{++} + B_m + \sum_{n=1}^{\infty} B_n 8nh^2(-1)^{m+n} L_{mn}^{++} + \sum_{n=1}^{\infty} C_n 8(n-1/2)h^2(-1)^{m+n+1} M_{mn}^{++} = \frac{4V(\alpha-1)h^2}{\pi}(-1)^{m+1} L_{m0}^{++} \quad (8)$$

$$\sum_{n=1}^{\infty} A_n 4(n-1/2)gh(-1)^{m+n} K_{nm}^{++} + \sum_{n=1}^{\infty} B_n 8nh^2(-1)^{m+n+1} M_{nm}^{++} + C_m + \sum_{n=1}^{\infty} C_n 8(n-1/2)h^2(-1)^{m+n} N_{mn}^{++} = \frac{4V(\alpha-1)h^2}{\pi}(-1)^m M_{0m}^{++} + \frac{2V\alpha h}{t[(m-1/2)\pi]^2}(-1)^m \quad (9)$$

for $m = 1, 2, 3, \ldots$ in each case where the integrals I_{mn}^{++}, J_{mn}^{++}, K_{mn}^{++}, L_{mn}^{++}, M_{mn}^{++}, and N_{mn}^{++} are given in the Appendix. Normalized coefficients A_n/V, B_n/V, and C_n/V depend on the ratios g/L, h/L, and t/L.

The recording medium lies in region I and here the magnetic field components are

$$H_x^{++}(x, y) = -\frac{\partial \varphi_{\mathrm{I}}^{++}}{\partial x}(x, y) = \frac{2Vh(1-\alpha)}{\pi} M_0^{++} + \sum_{n=1}^{\infty} A_n 2(n-1/2)g(-1)^n L_n^{++} + \sum_{n=1}^{\infty} B_n 4nh(-1)^{n+1} M_n^{++}$$

$$+\sum_{n=1}^{\infty} C_n 4(n-1/2)h(-1)^n N_n^{++} \quad (10)$$

nd

$$H_y^{++}(x,y) = -\frac{\partial \varphi_I^{++}}{\partial y}(x,y)$$
$$= \frac{2Vh(1-\alpha)}{\pi} Q_0^{++} + \frac{\alpha V}{t}$$
$$+\sum_{n=1}^{\infty} A_n 2(n-1/2)g(-1)^n P_n^{++}$$
$$+\sum_{n=1}^{\infty} B_n 4nh(-1)^{n+1} Q_n^{++}$$
$$+\sum_{n=1}^{\infty} C_n 4(n-1/2)h(-1)^n R_n^{++} \quad (11)$$

here the integrals L_n^{++}, M_n^{++}, N_n^{++}, P_n^{++}, Q_n^{++}, and R_n^{++} re given in the Appendix.

The result given in [12] for a single element symmetrically laced between shields is consistent with the above more eneral result in regions I and III if the interelement separation istance G is set to zero.

Dual Stripe MR Head Without an Underlayer

The solution for the head shown in Fig. 1 with equal otentials but with no underlayer follows immediately from he previous solution as the special case of $t \to \infty$. In), $\sinh[k(t-y)]$ is replaced by e^{-ky} which leads to the presentation (6) for $\varphi_I^{++}(x,y)$ with $\sinh[k(t-y)]/\sinh[kt]$ each of the integrals I_n^{++}, J_n^{++}, and K_n^{++} becoming e^{-ky}. In the linear equations (7)–(9) the $\coth[kt]$ term in I_{mn}^{++}, J_{mn}^{++}, K_{mn}^{++}, L_{mn}^{++}, M_{mn}^{++}, and N_{mn}^{++} becomes unity. or the horizontal field $\sinh[k(t-y)]/\sinh[kt]$ becomes e^{-ky} each of L_n^{++}, M_n^{++}, and N_n^{++} and for the vertical field $\sinh[k(t-y)]/\sinh[kt]$ becomes e^{-ky} in each of P_n^{++}, Q_n^{++}, d R_n^{++}.

The result in [13] for a shielded single element is the rticular case of this solution when the interelement distance, is zero and $\alpha = 0$.

Differential MR Head with an Underlayer

For this head the geometry is shown in Fig. 1, with the tential on the left-hand MR element being $\varphi = -V$, that is, MR element potentials are equal in magnitude but opposite sign. In this case

$$\varphi_I^{-+}(x,y) = \int_0^{\infty} D(k)\sin[kx]\sinh[k(t-y)]\,dk \quad (12)$$

$$\varphi_{II}^{-+}(x,y) = \frac{Vx}{g} + \sum_{n=1}^{\infty} A_n \sin(n\pi x/g) e^{n\pi y/g} \quad (13)$$

$\varphi_{III}^{-+}(x,y)$ is as given in (3). Following the same method described in Section II-A leads to

$$\varphi_I^{-+}(x,y) = \frac{2Vh}{\pi}(\alpha-1)J_0^{-+} + \frac{2Vg}{\pi} I_0^{-+}$$
$$+\sum_{n=1}^{\infty} A_n 2ng(-1)^n I_n^{-+}$$
$$+\sum_{n=1}^{\infty} B_n 4nh(-1)^n J_n^{-+}$$
$$+\sum_{n=1}^{\infty} C_n 4(n-1/2)h(-1)^n K_n^{-+} \quad (14)$$

with I_n^{-+}, J_n^{-+}, and K_n^{-+} given in the Appendix.

The coefficients A_n, B_n, and C_n are obtained by solving

$$A_m + \sum_{n=1}^{\infty} A_n 4ng^2(-1)^{m+n} I_{mn}^{-+}$$
$$+\sum_{n=1}^{\infty} B_n 8ngh(-1)^{m+n} J_{mn}^{-+}$$
$$+\sum_{n=1}^{\infty} C_n 8(n-1/2)gh(-1)^{m+n} K_{mn}^{-+}$$
$$= \frac{4V(1-\alpha)gh}{\pi}(-1)^m J_{m0}^{-+} + \frac{4Vg^2}{\pi}(-1)^{m+1} I_{m0}^{-+} \quad (15)$$

$$\sum_{n=1}^{\infty} A_n 4ngh(-1)^{m+n} J_{nm}^{-+} + B_m$$
$$+\sum_{n=1}^{\infty} B_n 8nh^2(-1)^{m+n} L_{mn}^{-+}$$
$$+\sum_{n=1}^{\infty} C_n 8(n-1/2)h^2(-1)^{m+n} M_{mn}^{-+}$$
$$= \frac{4V(1-\alpha)h^2}{\pi}(-1)^m L_{m0}^{-+} + \frac{4Vgh}{\pi}(-1)^{m+1} J_{0m}^{-+} \quad (16)$$

$$\sum_{n=1}^{\infty} A_n 4ngh(-1)^{m+n} K_{nm}^{-+}$$
$$+\sum_{n=1}^{\infty} B_n 8nh^2(-1)^{m+n} M_{nm}^{-+} + C_m$$
$$+\sum_{n=1}^{\infty} C_n 8(n-1/2)h^2(-1)^{m+n} N_{mn}^{-+}$$
$$= \frac{4V(1-\alpha)h^2}{\pi}(-1)^m M_{0m}^{-+} + \frac{4Vgh}{\pi}(-1)^{m+1} K_{0m}^{-+} \quad (17)$$

for $m = 1, 2, 3, \ldots$ in each case where the integrals are given in the Appendix. The magnetic field components in region I are

$$H_x^{-+}(x,y) = -\frac{2Vh}{\pi}(\alpha-1)M_0^{-+} - \frac{2Vg}{\pi} L_0^{-+}$$
$$-\sum_{n=1}^{\infty} A_n 2ng(-1)^n L_n^{-+}$$
$$-\sum_{n=1}^{\infty} B_n 4nh(-1)^n M_n^{-+}$$
$$-\sum_{n=1}^{\infty} C_n 4(n-1/2)h(-1)^n N_n^{-+} \quad (18)$$

and

$$H_y^{-+}(x, y) = \frac{2Vh}{\pi}(\alpha - 1)Q_0^{-+} + \frac{2Vg}{\pi}P_0^{-+} + \sum_{n=1}^{\infty} A_n 2ng(-1)^n P_n^{-+} + \sum_{n=1}^{\infty} B_n 4nh(-1)^n Q_n^{-+} + \sum_{n=1}^{\infty} C_n 4(n-1/2)h(-1)^n R_n^{-+} \quad (19)$$

where the integrals are given in the Appendix. Here, if $L \to \infty$, the geometry becomes that of a ring head with an underlayer and the solution in regions I and II reduces to that given in [14].

D. Differential MR Head Without an Underlayer

Again, this solution is a special case of the previous one with $t \to \infty$. In (12) $\sinh[k(t-y)]$ is replaced by e^{-ky} giving e^{-ky} in each of I_n^{-+}, J_n^{-+}, and K_n^{-+} in place of $\sinh[k(t-y)]/\sinh[kt]$ for the representation (14). In (15)–(17) the $\coth[kt]$ term in each of I_{mn}^{-+}, J_{mn}^{-+}, K_{mn}^{-+}, L_{mn}^{-+}, M_{mn}^{-+}, and N_{mn}^{-+} becomes unity. For the integrals L_n^{-+}, M_n^{-+}, and N_n^{-+} in the horizontal field, $\sinh[k(t-y)]/\sinh[kt]$ becomes e^{-ky} as does $\cosh[k(t-y)]/\cosh[kt]$ in the integrals P_n^{-+}, Q_n^{-+}, and R_n^{-+} for the vertical field. Here, if $L \to \infty$, the solution for a ring head without an underlayer [15] is obtained in regions I and II.

III. Results

A. Magnetic Field Calculations

The normalized Fourier coefficients A_n/V, B_n/V, and C_n/V for the dual stripe head and differential head, in each case with an underlayer present, satisfy the three coupled infinite systems of linear algebraic equations (7)–(9) and (15)–(17), respectively. For each head configuration the three coupled infinite systems may be solved approximately by restricting each system to some finite size N, the normalized coefficients satisfying the resulting $3N \times 3N$ square system. The integrals appearing within the coupled systems and the other integrals appearing in the Appendix have been evaluated using numerical integration [16], since it has not yet proved possible to find closed form analytic expressions for them. This places a restriction on the size of N it has been possible to consider. All coefficients reproduced in this paper were computed using coupled systems truncated to a size of 60 $\times$ 60 ($N = 20$).

Table I shows the first six normalized coefficients A_n/V, B_n/V, and C_n/V for the dual stripe head with an underlayer present with $\alpha = 0$, $g : L : t = 1 : 1 : 1$ and a range of gap ratios h/L. As the pole to pole gap width, G, of the dual stripe head decreases the geometry approaches that of a shielded single pole head with an underlayer [12], providing a useful measure of the accuracy of the coefficients given in Table I. A comparison of the coefficients obtained using the dual stripe head analysis with $g = 0$ with those obtained for the shielded pole head in [12] confirms the expected correspondence, with coefficients which agree to at least three decimal places. Consequently this is the expected level of accuracy for the coefficients given in Table I and the other tables in this paper.

TABLE I
Coefficients A_n/V, B_n/V, and C_n/V for a Dual Stripe Head with an Underlayer with $\alpha = 0$, $g : L : t = 1 : 1 : 1$ and Computed with $N = 20$

h/L	0.5	1.0	1.5	2.0	2.5
A_1/V	-0.4116	-0.4111	-0.4109	-0.4108	-0.4108
A_2/V	0.0572	0.0571	0.0570	0.0570	0.0570
A_3/V	-0.0232	-0.0231	-0.0231	-0.0231	-0.0231
A_4/V	0.0128	0.0128	0.0128	0.0128	0.0128
A_5/V	-0.0083	-0.0083	-0.0083	-0.0083	-0.0083
A_6/V	0.0058	0.0058	0.0058	0.0058	0.0058
B_1/V	0.0504	0.0670	0.0866	0.1058	0.1233
B_2/V	-0.0166	-0.0209	-0.0261	-0.0315	-0.0369
B_3/V	0.0085	0.0106	0.0130	0.0155	0.0181
B_4/V	-0.0053	-0.0065	-0.0079	-0.0094	-0.0109
B_5/V	0.0038	0.0045	0.0054	0.0064	0.0074
B_6/V	-0.0027	-0.0033	-0.0040	-0.0047	-0.0054
C_1/V	-0.1138	-0.2059	-0.2756	-0.3277	-0.3674
C_2/V	0.0156	0.0287	0.0401	0.0506	0.0603
C_3/V	-0.0063	-0.0116	-0.0162	-0.0203	-0.0242
C_4/V	0.0035	0.0064	0.0089	0.0112	0.0133
C_5/V	-0.0023	-0.0042	-0.0058	-0.0072	-0.0085
C_6/V	0.0016	0.0029	0.0041	0.0051	0.0060

Table II shows the first six normalized coefficients for the differential head with an underlayer present with $\alpha = 0$, $g : L : t = 1 : 1 : 1$ and a range of gap ratios h/L. As the pole length L of the differential head with an underlayer increases relative to the head to medium separation t, the geometry approaches that of the idealized model of a ring head with an underlayer [14]. For ratios of $L/t > 5$ agreement with the coefficients for a ring head with an underlayer [14] is to about three decimal places. The normalized coefficients for the dual stripe head and differential head without an underlayer present are shown in Tables III and IV, respectively.

Representative horizontal and vertical field components for the dual stripe head and the differential head, both with an underlayer present, are shown in Figs. 2–5, in each case all distances have been normalized by half of the shield to shield gap $g + L + H$. Typical head dimension ratios of $g : L : h : t = 1 : 1 : 2 : 1$ have been chosen in line with experimental head dimensions given in [7] and [17]. Figs. 6–9 show the corresponding field components for the dual stripe head and differential head without an underlayer present.

TABLE II
OEFFICIENTS A_n/V, B_n/V, AND C_n/V FOR A DIFFERENTIAL HEAD WITH AN NDERLAYER WITH $\alpha = 0$, $g : L : t = 1 : 1 : 1$, AND COMPUTED WITH $N = 20$

h/L	0.5	1.0	1.5	2.0	2.5
A_1/V	-0.1330	-0.1328	-0.1327	-0.1326	-0.1326
A_2/V	0.0414	0.0414	0.0414	0.0414	0.0414
A_3/V	-0.0210	-0.0210	-0.0210	-0.0210	-0.0210
A_4/V	0.0129	0.0129	0.0129	0.0129	0.0129
A_5/V	-0.0089	-0.0089	-0.0089	-0.0089	-0.0089
A_6/V	0.0065	0.0065	0.0065	0.0065	0.0065
B_1/V	0.0502	0.0667	0.0863	0.1056	0.1231
B_2/V	-0.0165	-0.0208	-0.0260	-0.0315	-0.0369
B_3/V	0.0085	0.0105	0.0130	0.0155	0.0181
B_4/V	-0.0053	-0.0065	-0.0079	-0.0095	-0.0110
B_5/V	0.0037	0.0045	0.0054	0.0064	0.0074
B_6/V	-0.0027	-0.0033	-0.0040	-0.0047	-0.0054
C_1/V	-0.1136	-0.2059	-0.2756	-0.3277	-0.3674
C_2/V	0.0155	0.0287	0.0402	0.0507	0.0604
C_3/V	-0.0063	-0.0116	-0.0162	-0.0204	-0.0243
C_4/V	0.0035	0.0064	0.0090	0.0113	0.0134
C_5/V	-0.0023	-0.0042	-0.0058	-0.0072	-0.0086
C_6/V	0.0016	0.0029	0.0041	0.0051	0.0060

TABLE III
EFFICIENTS A_n/V, B_n/V, AND C_n/V FOR A DUAL STRIPE HEAD WITHOUT N UNDERLAYER WITH $\alpha = 0$, $g : L = 1 : 1$, AND COMPUTED WITH $N = 20$

h/L	0.5	1.0	1.5	2.0	2.5
A_1/V	-0.1259	-0.1074	-0.0949	-0.0856	-0.0784
A_2/V	0.0187	0.0157	0.0138	0.0124	0.0114
A_3/V	-0.0076	-0.0064	-0.0056	-0.0051	-0.0047
A_4/V	0.0042	0.0035	0.0031	0.0028	0.0026
A_5/V	-0.0027	-0.0023	-0.0020	-0.0018	-0.0017
A_6/V	0.0019	0.0016	0.0014	0.0013	0.0012
B_1/V	0.0444	0.0461	0.0474	0.0486	0.0495
B_2/V	-0.0148	-0.0152	-0.0154	-0.0157	-0.0160
B_3/V	0.0077	0.0079	0.0080	0.0081	0.0082
B_4/V	-0.0048	-0.0049	-0.0050	-0.0051	-0.0051
B_5/V	0.0033	0.0034	0.0035	0.0035	0.0036
B_6/V	-0.0025	-0.0025	-0.0026	-0.0026	-0.0026
C_1/V	-0.0198	-0.0312	-0.0391	-0.0450	-0.0497
C_2/V	0.0029	0.0045	0.0056	0.0064	0.0072
C_3/V	-0.0012	-0.0018	-0.0023	-0.0026	-0.0029
C_4/V	0.0006	0.0010	0.0013	0.0015	0.0016
C_5/V	-0.0004	-0.0006	-0.0008	-0.0009	-0.0010
C_6/V	0.0003	0.0005	0.0006	0.0007	0.0007

or each head configuration, average field component values a range of distances ($0.2 \leq y/L \leq 0.8$) from the

TABLE IV
COEFFICIENTS A_n/V, B_n/V, AND C_n/V FOR A DIFFERENTIAL HEAD WITHOUT AN UNDERLAYER WITH $\alpha = 0$, $g : L = 1 : 1$, AND COMPUTED WITH $N = 20$

h/L	0.5	1.0	1.5	2.0	2.5
A_1/V	-0.0990	-0.0962	-0.0946	-0.0936	-0.0928
A_2/V	0.0327	0.0319	0.0314	0.0312	0.0310
A_3/V	-0.0169	-0.0165	-0.0163	-0.0162	-0.0161
A_4/V	0.0105	0.0103	0.0102	0.0101	0.0101
A_5/V	-0.0073	-0.0071	-0.0070	-0.0070	-0.0070
A_6/V	0.0054	0.0053	0.0052	0.0052	0.0052
B_1/V	0.0463	0.0518	0.0573	0.0623	0.0669
B_2/V	-0.0154	-0.0171	-0.0188	-0.0206	-0.0223
B_3/V	0.0080	0.0088	0.0097	0.0105	0.0114
B_4/V	-0.0050	-0.0055	-0.0060	-0.0065	-0.0070
B_5/V	0.0035	0.0038	0.0041	0.0045	0.0048
B_6/V	-0.0026	-0.0028	-0.0030	-0.0033	-0.0036
C_1/V	-0.0497	-0.0818	-0.1051	-0.1230	-0.1375
C_2/V	0.0071	0.0123	0.0166	0.0204	0.0237
C_3/V	-0.0029	-0.0050	-0.0068	-0.0085	-0.0099
C_4/V	0.0016	0.0028	0.0038	0.0047	0.0055
C_5/V	-0.0010	-0.0018	-0.0024	-0.0030	-0.0036
C_6/V	0.0007	0.0013	0.0017	0.0021	0.0025

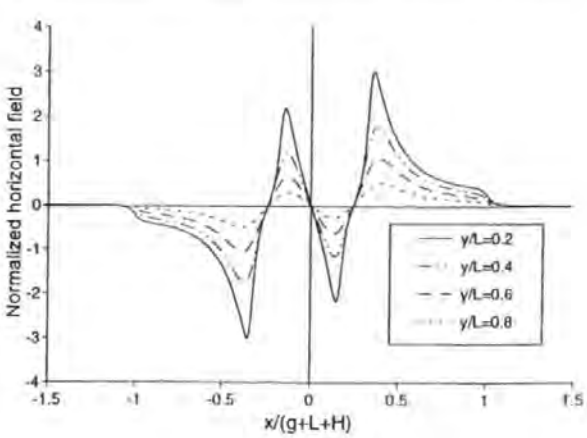

Fig. 2. Horizontal field component for a dual stripe head with an underlayer. $g : L : h : t = 1 : 1 : 2 : 1$.

head surface were computed, successively including more coefficients from the infinite series thus providing a measure of the number of coefficients needed to ensure accurate results. For both types of head with an underlayer, the average vertical field component values calculated using only the first coefficient of the series are within approximately 3% of the values obtained using 20 coefficients, the two coefficient results are within about 1%, the four coefficient results are within 0.3% and the ten coefficient computations agree to about 0.04%. Similar computations for each head without an underlayer reveal average horizontal components for the one, two, four, and ten coefficients computations that agree to approximately 1.5, 0.5, 0.2, and 0.04%, respectively, with the 20 coefficient results. Hence, it is possible in many

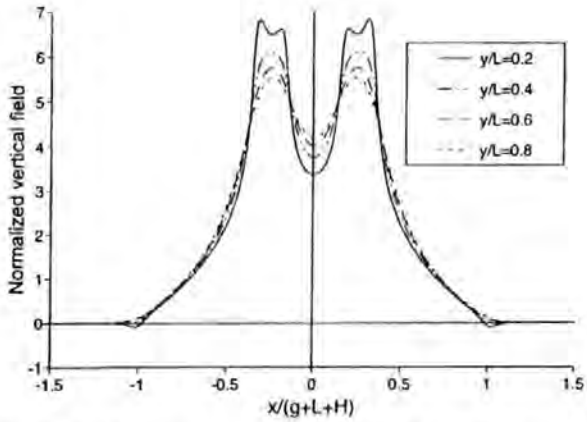

Fig. 3. Vertical field component for a dual stripe head with an underlayer, $g : L : h : t = 1 : 1 : 2 : 1$.

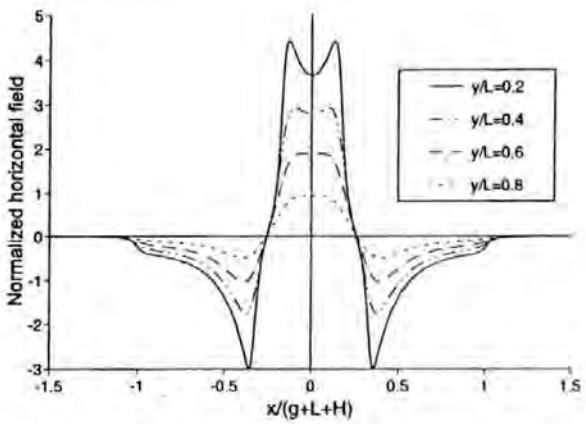

Fig. 4. Horizontal field component for a differential head with an underlayer, $g : L : h : t = 1 : 1 : 2 : 1$.

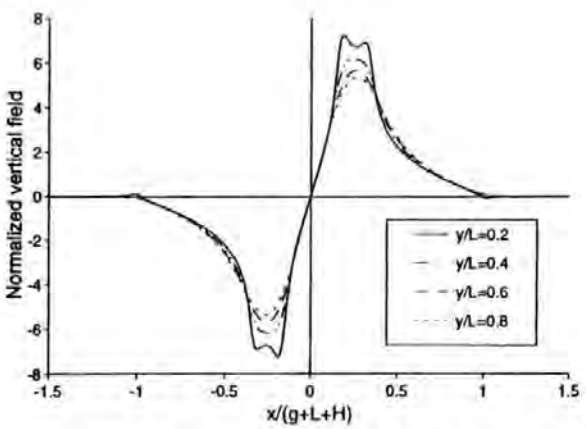

Fig. 5. Vertical field component for a differential head with an underlayer, $g : L : h : t = 1 : 1 : 2 : 1$.

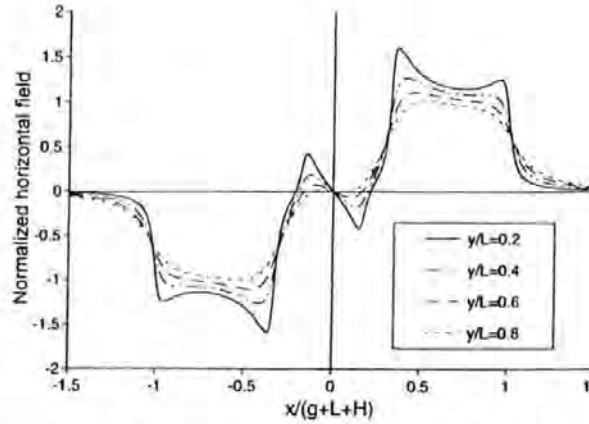

Fig. 6. Horizontal field component for a dual stripe head without an underlayer, $g : L : h = 1 : 1 : 2$.

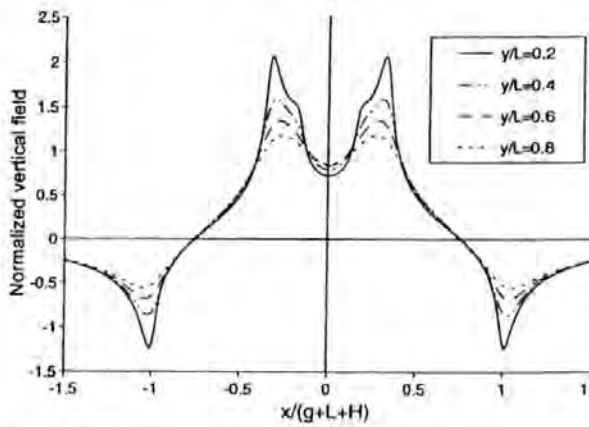

Fig. 7. Vertical field component for a dual stripe head without an underlayer, $g : L : h = 1 : 1 : 2$.

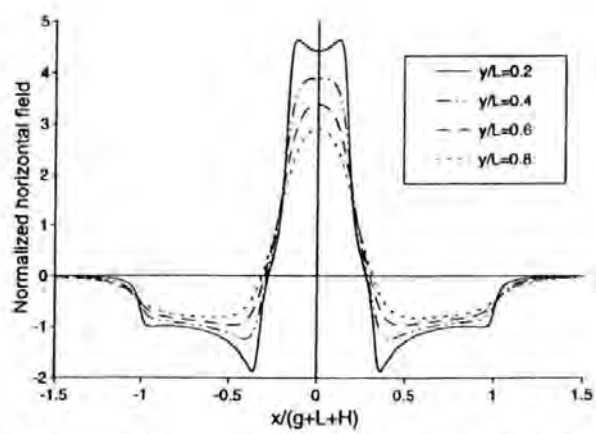

Fig. 8. Horizontal field component for a differential head without an underlayer, $g : L : h = 1 : 1 : 2$.

circumstances to obtain sufficiently good approximations by utilizing only the first few coefficients of the infinite series. All of the results presented here were obtained by truncating the appropriate infinite series to ten terms.

Figs. 2–9 clearly show how the presence of an underlayer gives an enhanced peak value for the vertical component of the magnetic field in comparison with that of the horizontal component. Moreover, the vertical field maintains a high value as the distance from the head increases while the horizontal field, as expected, decays rapidly to zero. With no underlayer the peak horizontal and vertical fields are of comparable magnitude and the decay in each component with distance from the head is similar. The shield, the edge of which is at $x/(g + L + H) = 1$, is seen here to be significantly less effective in reducing the fields to zero in the gap region than when an underlayer is present.

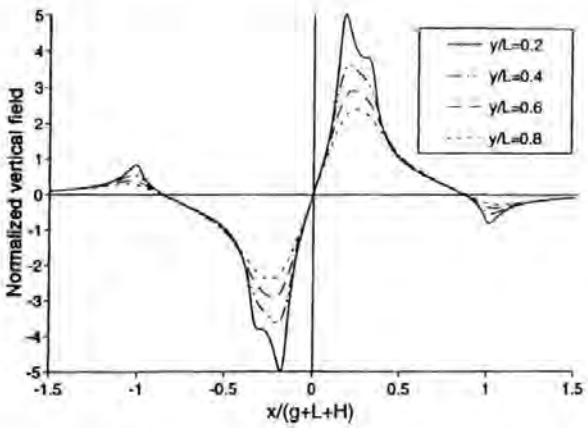

g. 9. Vertical field component for a differential head without an underlayer, $g : L : h = 1 : 1 : 2$.

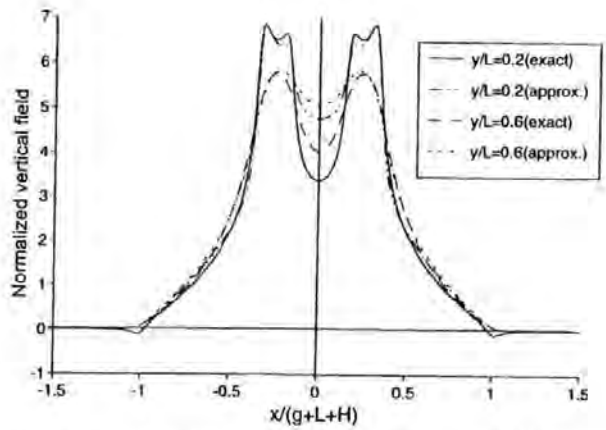

Fig. 10. Comparison of the exact and approximate vertical field component for a dual stripe head with an underlayer, $g : L : h : t = 1 : 1 : 2 : 1$.

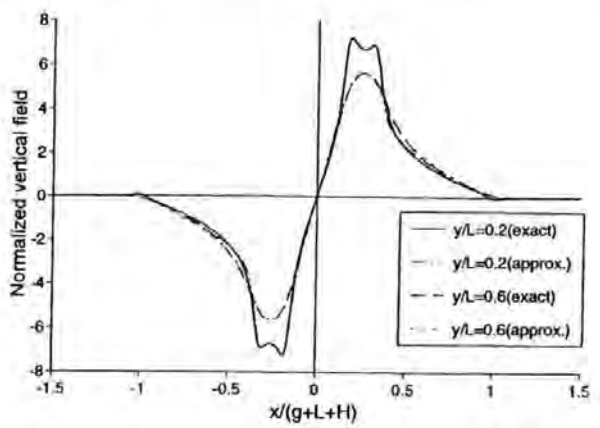

Fig. 11. Comparison of the exact and approximate vertical field component for a differential head with an underlayer, $g : L : h : t = 1 : 1 : 2 : 1$.

It is perhaps contrary to expectation that above the edges the MR elements for the dual stripe head in the region ose to the head face plane ($y/L < 0.6$ approximately, for e particular dimensions chosen), the peak horizontal field is gnificantly higher when an underlayer is present (Fig. 2) than hen there is no underlayer (Fig. 6). At any particular height, e magnetic potential varies similarly in each case, being eatest in front of the MR elements, lower between the ele- ents, and decaying to zero toward the shields (see [7, Fig. 11] r $y = 0$ and no underlayer). Although the potential is lower region I when an underlayer is present than when there is no derlayer, this reduction is greater above the element/element p and that part of each element/shield gap near the element, an above the two elements. This results in a higher horizontal ld (potential gradient) in these regions and in particular ove the edges of the elements, as shown in Fig. 2.

Comparison with Approximate Results

In Section II a full explicit solution for the magnetic ld of double-element shielded heads is given. Although ly a small number of terms is required to give excellent curacy, it is necessary to first compute the harmonic efficients A_n, B_n, and C_n. For many practical purposes approximate solution is acceptable, as exemplified by Karlqvist approximations to the field components of ring head, which, despite their known limitations, have ved popular for over 35 years. Here, previously published proximations which are applicable to double-element heads compared with the new exact solutions.

Close approximations to the potential $\varphi(x, 0)$ in the head e plane for heads with underlayers have been given in]. For the differential head in the region $0 \le x \le g$, an roximation which satisfies $\varphi_1^A(0, 0) = 0$ and $\varphi_1^A(g, 0) =$ is

$$(x, 0) = \frac{Vx}{g}\left[1 - \frac{1}{2t}\sqrt{\frac{g^2 - x^2}{6}}\left(1 - e^{-2t\sqrt{6/(g^2-x^2)}}\right)\right]. \tag{20}$$

he element/shield gap $g + L \le x \le g + L + H$

$$\varphi_2^A(x, 0) = \varphi_1^A((g + L + H - x)g/H, 0) \tag{21}$$

satisfies $\varphi_2^A(g + L, 0) = V$ and $\varphi_2^A(g + L + H, 0) = 0$. For the dual stripe head

$$\varphi_3^A(x, 0) = \varphi_1^A((x + g)/2, 0) + \varphi_1^A((g - x)/2, 0) \tag{22}$$

satisfies $\varphi_3^A(\pm g, 0) = V$ as required.

Using these approximations in

$$\varphi(x, y) = \frac{1}{2t}\sin\left[\frac{\pi y}{t}\right] \cdot \int_{-\infty}^{\infty} \frac{\varphi(u, 0)}{\cosh[(u - x)\pi/t] - \cos[\pi y/t]}\, du, \quad 0 < y < t \tag{23}$$

and differentiating prior to the integration gives approximate field components in region I where the recording medium lies. Figs. 10 and 11 give comparisons of the exact and approximate vertical fields for dual stripe and differential heads, respectively, where the approximations are generally seen to be very accurate. The only area where there is a significant error in the approximation is between the MR elements for a dual stripe head. Here the actual vertical field reduction is greater than that given by the approximation. This gives confidence in the correctness of the exact field computations and indicates that the approximate solutions may be sufficient for many practical purposes.

In [7] approximations are developed specifically for the horizontal fields of dual stripe and differential MR heads when no underlayer is present. They are based upon an equally weighted sum of the field assuming a linear variation in potential across any gaps (Karlqvist-style) and the field of the equivalent "thin" head (Westmijze-style).

For the dual stripe head with no underlayer the approximate horizontal component of the magnetic field in the head face plane ($y = 0$) in the element/element and element/shield gaps is, for $x \geq 0$

$$H_x^A(x, 0) = \begin{cases} -\dfrac{1}{2} \dfrac{c_3 x}{\sqrt{(1-x^2)(x^2-b^2)(x^2-a^2)}} \\ \qquad 0 \leq x < b \\ \dfrac{1}{2}\left[\dfrac{1}{1-a} + \dfrac{c_3 x}{\sqrt{(1-x^2)(x^2-b^2)(x^2-a^2)}}\right] \\ \qquad a < x < 1 \end{cases} \tag{24}$$

where

$$c_3^{-1} = \int_a^1 \frac{x}{\sqrt{(1-x^2)(x^2-b^2)(x^2-a^2)}}\, dx. \tag{25}$$

Here, following the notation of [7], normalized coordinates have been taken, the correspondence with Fig. 1 being $1 \equiv g + L + H$ (the shield edge), $a \equiv g + L$ (the outer edge of the MR element), and $b \equiv g$ (the inner edge of the MR element). The constant c_3^{-1} may be expressed as the complete elliptic integral of the first kind

$$c_3^{-1} = \frac{1}{\sqrt{1-b^2}} F\left(\sqrt{\frac{1-a^2}{1-b^2}}, \frac{\pi}{2}\right). \tag{26}$$

For the differential head the corresponding results are

$$H_x^A(x, 0) = \begin{cases} \dfrac{1}{2}\left[\dfrac{1}{b} + \dfrac{c_4}{\sqrt{(1-x^2)(x^2-b^2)(x^2-a^2)}}\right] \\ \qquad 0 \leq x < b \\ -\dfrac{1}{2}\left[\dfrac{1}{1-a} + \dfrac{c_4}{\sqrt{(1-x^2)(x^2-b^2)(x^2-a^2)}}\right] \\ \qquad a < x < 1 \end{cases} \tag{27}$$

where

$$c_4^{-1} = \int_a^1 \frac{1}{\sqrt{(1-x^2)(x^2-b^2)(x^2-a^2)}}\, dx. \tag{28}$$

Again, c_4^{-1} may be written as the elliptic integral

$$c_4^{-1} = \frac{1}{a\sqrt{1-b^2}} F\left(\frac{b\sqrt{1-a^2}}{a\sqrt{1-b^2}}, \frac{\pi}{2}\right). \tag{29}$$

Both the horizontal and vertical field at any point in $y > 0$ may be determined from $H_x^A(x, 0)$ [18] as

$$H_x^A(x, y) = \frac{y}{\pi} \int_{-\infty}^{\infty} \frac{H_x^A(u, 0)}{(x-u)^2 + y^2}\, du \tag{30}$$

and

$$H_y^A(x, y) = \frac{1}{\pi} \int_{-\infty}^{\infty} \frac{(u-x) H_x^A(u, 0)}{(x-u)^2 + y^2}\, du. \tag{31}$$

Of the various integral relationships available, these are the most convenient to use since $H_x(x, 0)$ is zero on the faces of the MR elements and the shields and it is only necessary to integrate across the gaps. Figs. 12 and 13 show a comparison of the exact and approximate horizontal field components for the dual stripe and differential heads, respectively, where it can be seen that these approximations are generally extremely accurate. In [7] the accuracy of a similar approximation for a single-element MR head was demonstrated by comparison with the full theoretical solution but the double-element approximations could, at that time, only be tested against experimental results. However, it should be noted that even evaluation of the approximate fields is a nontrivial computational task, due to the nature of the constants c_3 and c_4. This is true despite the new observation made here that c_3 and c_4 can be expressed as elliptic integrals which has enabled efficient numerical software to be used.

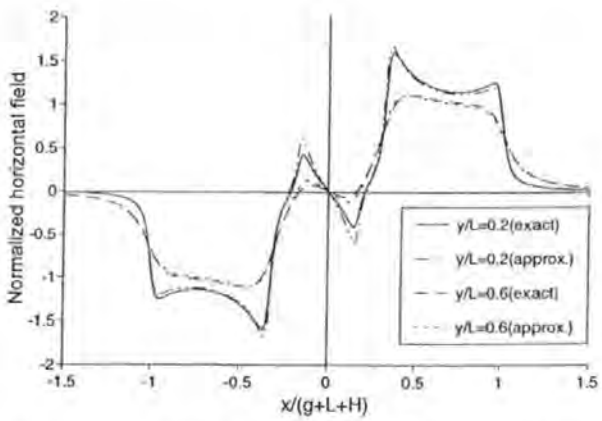

Fig. 12. Comparison of the exact and approximate horizontal field component for a dual stripe head without an underlayer, $g : L : h = 1 : 1 : 2$.

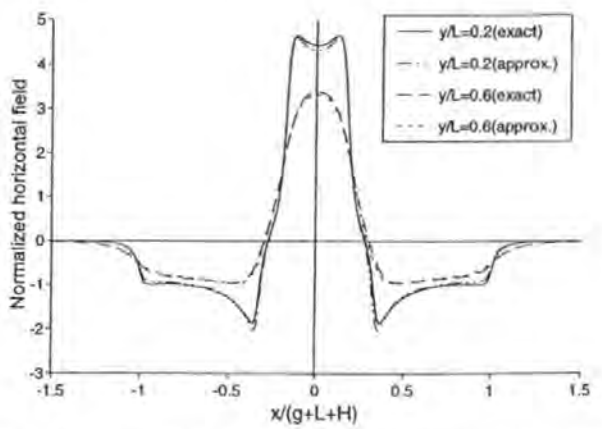

Fig. 13. Comparison of the exact and approximate horizontal field component for a differential head without an underlayer, $g : L : h = 1 : 1 : 2$.

C. Spectral Response Functions

For the two-dimensional model of an MR sensor considered here, operating such that its response is linear, the reciprocity theorem gives the output voltage as the correlation integral [19]

$$e(\overline{x}) = C^{\mathrm{MR}} \int_{y=d}^{d+\delta} \int_{x=-\infty}^{\infty} \mathbf{H}(x + \overline{x}, y) \cdot \mathbf{M}(x, y)\, dx\, dy. \tag{32}$$

Here C^{MR} is a constant dependent on various material and geometric properties of the head, $\mathbf{H} = -\nabla\varphi$ is the magnetic field produced by the reciprocity potential φ, $\mathbf{M}$ is the recorded magnetization on a medium of thickness δ at a distance d from the plane $y = 0$ (Fig. 1), and $\bar{x}$ is the relative position of the medium and the head.

Taking the Fourier transform of (32) gives

$$\tilde{e}(k) = C^{MR} \int_d^{d+\delta} \hat{\mathbf{H}}(k, y) \cdot \hat{\mathbf{M}}^*(k, y)\, dy \tag{33}$$

where $\hat{\mathbf{H}}(k, y)$ is the Fourier transform of the field and $\hat{\mathbf{M}}^*(k, y)$ is the complex conjugate of the transform of the magnetization. $\hat{\mathbf{H}}(k, y)$ may be simply expressed in terms of $\hat{\mathbf{H}}(k, 0)$, which is usually known as the spectral response function or the surface field spectrum.

When an underlayer is present, the transformed horizontal and vertical fields are

$$\hat{\mathbf{H}}(k, y) = \left(\frac{\sinh[k(t-y)]}{\sinh[kt]}\hat{H}_x(k, 0), \frac{\cosh[k(t-y)]}{\cosh[kt]}\hat{H}_y(k, 0)\right) \tag{34}$$

and

$$\hat{H}_y(k, 0) = i \coth[kt]\hat{H}_x(k, 0). \tag{35}$$

This simplifies to

$$\hat{\mathbf{H}}(k, y) = e^{-ky}\hat{\mathbf{H}}(k, 0) \tag{36}$$

and

$$\hat{H}_y(k, 0) = i\hat{H}_x(k, 0) \tag{37}$$

in the case of no underlayer.

$\hat{\mathbf{H}}(k, 0)$ may be evaluated from $\hat{\varphi}(k, 0)$, the transform of the surface potential $\varphi(x, 0)$, since

$$\hat{H}_x(k, 0) = -ik\hat{\varphi}(k, 0) \tag{38}$$

and

$$\hat{H}_y(k, 0) = k \coth[kt]\hat{\varphi}(k, 0) \tag{39}$$

with $\coth[kt]$ replaced by unity if there is no underlayer. This enables $\hat{\mathbf{H}}(k, 0)$ to be evaluated here in a particularly simple way. If, in region I, where the recording medium lies, $\varphi(x, y)$ is written in the form

$$\varphi(x, y) = \int_0^\infty D(k) \cos[kx] f(k, y)\, dk \tag{40}$$

then

$$\hat{\varphi}(k, y) = \pi D(k) f(k, y). \tag{41}$$

Hence for the dual stripe head, from (6) with $\alpha = 0$

$$\begin{aligned}\hat{\varphi}^{++}(k, 0) &= 2Vh\frac{\sin[k(g+L+h)]\sin[kh]}{(kh)^2} \\ &+ \sum_{n=1}^{\infty} A_n 2(n-1/2)g(-1)^n\pi \frac{\cos[kg]}{(kg)^2 - [(n-1/2)\pi]^2} \\ &+ \sum_{n=1}^{\infty} B_n 4nh(-1)^{n+1}\pi \frac{\sin[k(g+L+h)]\sin[kh]}{(kh)^2 - (n\pi)^2} \\ &+ \sum_{n=1}^{\infty} C_n 4(n-1/2)h(-1)^n\pi \frac{\cos[k(g+L+h)]\cos[kh]}{(kh)^2 - [(n-1/2)\pi]^2}.\end{aligned} \tag{42}$$

If

$$\varphi(x, y) = \int_0^\infty D(k)\sin[kx] f(k, y)\, dk \tag{43}$$

then

$$\hat{\varphi}(k, y) = -i\pi D(k) f(k, y). \tag{44}$$

For the differential head, from (14) with $\alpha = 0$

$$\begin{aligned}\hat{\varphi}^{-+}(k, 0) &= 2Vhi\frac{\cos[k(g+L+h)]\sin[kh]}{(kh)^2} - 2Vgi\frac{\sin[kg]}{(kg)^2} \\ &+ \sum_{n=1}^{\infty} A_n 2ng(-1)^{n+1} i\pi \frac{\sin[kg]}{(kg)^2 - (n\pi)^2} \\ &+ \sum_{n=1}^{\infty} B_n 4nh(-1)^{n+1} i\pi \frac{\cos[k(g+L+h)]\sin[kh]}{(kh)^2 - (n\pi)^2} \\ &+ \sum_{n=1}^{\infty} C_n 4(n-1/2)h(-1)^{n+1} i\pi \\ &\cdot \frac{\sin[k(g+L+h)]\cos[kh]}{(kh)^2 - [(n-1/2)\pi]^2}.\end{aligned} \tag{45}$$

The following figures show typical spectral responses, plotted as functions of $k(g + L + H)$. For heads with underlayers, the vertical component $\hat{H}_y(k, 0)$ is shown. From (35) the magnitude of the horizontal component only differs by a factor of $\coth[kt]$. When there is no underlayer, from (37), $\hat{H}_x(k, 0)$ and $\hat{H}_y(k, 0)$ have the same magnitude.

For a dual stripe head with an underlayer and a fixed shield to shield distance, Figs. 14 and 15 show the effect of varying the interelement gap ($G = 2g$) and the length (L) of the MR element. The position of the first null is principally determined by the dimension $2L + G$, the length of an "equivalent" shielded single pole, which should be as small as possible. For a fixed $2L + G$, it can be seen that G should be as small as possible, with $G = 0$ giving the highest frequency for the first null. For example, the first null moves from 5.2 with $g : L : h : t = 0.5 : 1.5 : 2 : 1$ to 6.9 with $g : L : h : t = 0 : 2 : 2 : 1$ (the single pole), a shift of approximately 33%. This is consistent with a similar observation in [7] for a dual stripe head without an underlayer.

When no underlayer is present similar conclusions may be drawn. However, for identical head dimensions, the first null occurs at a slightly lower frequency without an underlayer and there is less variation in the position of this null as L and G vary. This is illustrated in Fig. 16, where the spectral response curves for a fixed $2L+G$ and a range of values G are plotted. As G reduces there is only a slight shift in the position of the first null toward higher frequencies and the minimum between the first and second nulls becomes more pronounced, eventually developing into a null as $G \to 0$, corresponding to a shielded single pole. Generally, the spectral response curves

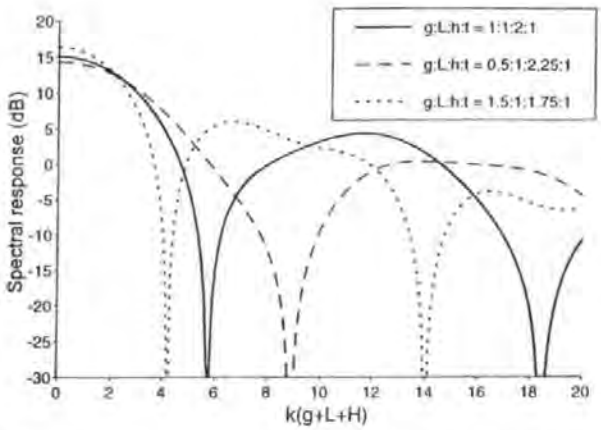

Fig. 14. Spectral response of a dual stripe head with an underlayer, as the interelement gap varies.

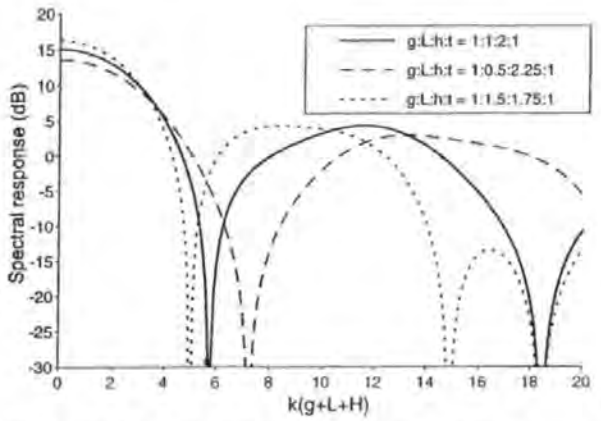

Fig. 15. Spectral response of a dual stripe head with an underlayer, as the element length varies.

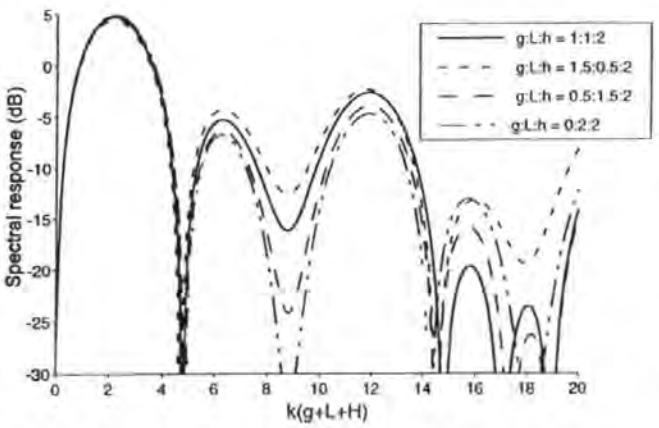

Fig. 16. Spectral response of a dual stripe head without an underlayer, as the interelement gap and the element length vary.

are more complicated when no underlayer is present, having more nulls and also minima beyond the first null.

For a differential head with an underlayer, the spectrum depends strongly on the gap G between the MR elements, as shown in Fig. 17. The differential head naturally has its first null at a much higher frequency than does the dual stripe head of identical dimensions. Figs. 17 and 18 show that for a fixed gap G, a smaller pole length L produces the first null at a

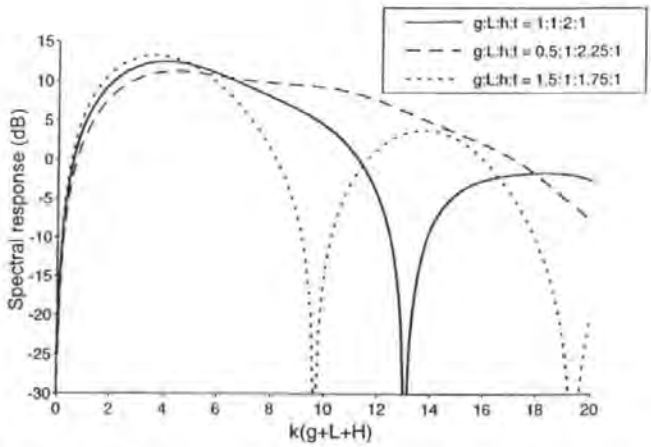

Fig. 17. Spectral response of a differential head with an underlayer, as the interelement gap varies.

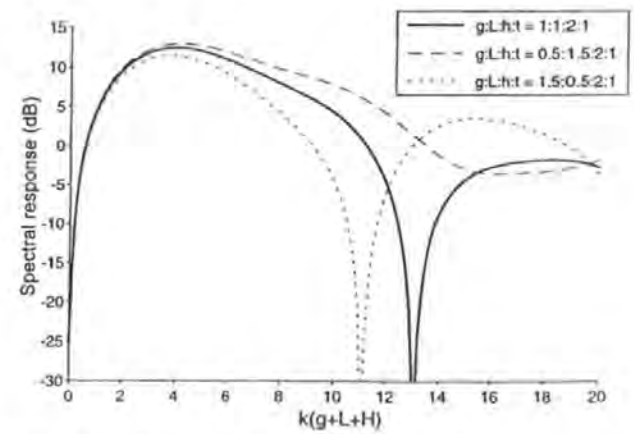

Fig. 18. Spectral response of a differential head with an underlayer, as the interelement gap and the element length vary.

higher frequency, although as the ratio G/L decreases, head bumps occur before that first null.

Similar conclusions hold when there is no underlayer. For the same dimensions the first null position changes by only a small amount to a higher frequency and, as for the dual stripe head, the patterns are more complicated beyond the first null.

IV. Conclusions

The Fourier method has been used to provide, for the first time, full analytic solutions for double-element shielded MR heads for both longitudinal and perpendicular recording. Representative Fourier coefficients and field plots have been given. Comparisons with recently published approximate solutions have shown that these approximate solutions may be sufficiently accurate for certain practical purposes. However, such approximations are not necessarily easy to evaluate and if their use is being considered, it would be prudent to check their accuracy against the exact solution for any particular head dimensions under consideration. Also, it has been noted that although all field plots given here used ten terms of each series, considerably fewer terms are needed in most circumstances. Explicit spectral response functions have been given and typical results have indicated the dependence of the first null upon the dimensions of the head.

APPENDIX
INTEGRALS REQUIRED

. For $\varphi_1^{++}(x, y)$

$$I_n^{++} = \int_0^\infty \frac{\cos[kg]\cos[kx]}{(kg)^2 - [(n-1/2)\pi]^2} \frac{\sinh[k(t-y)]}{\sinh[kt]}\,dk$$

$$J_n^{++} = \int_0^\infty \frac{\sin[k(g+L+h)]\sin[kh]\cos[kx]}{(kh)^2 - (n\pi)^2} \cdot \frac{\sinh[k(t-y)]}{\sinh[kt]}\,dk$$

$$K_n^{++} = \int_0^\infty \frac{\cos[k(g+L+h)]\cos[kh]\cos[kx]}{(kh)^2 - [(n-1/2)\pi]^2} \cdot \frac{\sinh[k(t-y)]}{\sinh[kt]}\,dk.$$

. For (7)–(9)

See (46) shown at the bottom of the page.

. For the Magnetic Field Components

$$L_n^{++} = \int_0^\infty \frac{k\cos[kg]\sin[kx]}{(kg)^2 - [(n-1/2)\pi]^2} \frac{\sinh[k(t-y)]}{\sinh[kt]}\,dk$$

$$M_n^{++} = \int_0^\infty \frac{k\sin[k(g+L+h)]\sin[kh]\sin[kx]}{(kh)^2 - (n\pi)^2} \cdot \frac{\sinh[k(t-y)]}{\sinh[kt]}\,dk$$

$$N_n^{++} = \int_0^\infty \frac{k\cos[k(g+L+h)]\cos[kh]\sin[kx]}{(kh)^2 - [(n-1/2)\pi]^2} \cdot \frac{\sinh[k(t-y)]}{\sinh[kt]}\,dk$$

$$P_n^{++} = \int_0^\infty \frac{k\cos[kg]\cos[kx]}{(kg)^2 - [(n-1/2)\pi]^2} \frac{\cosh[k(t-y)]}{\sinh[kt]}\,dk$$

$$Q_n^{++} = \int_0^\infty \frac{k\sin[k(g+L+h)]\sin[kh]\cos[kx]}{(kh)^2 - (n\pi)^2} \cdot \frac{\cosh[k(t-y)]}{\sinh[kt]}\,dk$$

$$R_n^{++} = \int_0^\infty \frac{k\cos[k(g+L+h)]\cos[kh]\cos[kx]}{(kh)^2 - [(n-1/2)\pi]^2} \cdot \frac{\cosh[k(t-y)]}{\sinh[kt]}\,dk.$$

D. For $\varphi_1^{-+}(x, y)$

$$I_n^{-+} = \int_0^\infty \frac{\sin[kg]\sin[kx]}{(kg)^2 - (n\pi)^2} \frac{\sinh[k(t-y)]}{\sinh[kt]}\,dk$$

$$J_n^{-+} = \int_0^\infty \frac{\cos[k(g+L+h)]\sin[kh]\sin[kx]}{(kh)^2 - (n\pi)^2} \cdot \frac{\sinh[k(t-y)]}{\sinh[kt]}\,dk$$

$$K_n^{-+} = \int_0^\infty \frac{\sin[k(g+L+h)]\cos[kh]\sin[kx]}{(kh)^2 - [(n-1/2)\pi)]^2} \cdot \frac{\sinh[k(t-y)]}{\sinh[kt]}\,dk.$$

E. For (15)–(17)

$$I_{mn}^{-+} = \int_0^\infty \frac{k\sin^2[kg]}{[(kg)^2 - (m\pi)^2][(kg)^2 - (n\pi)^2]} \cdot \coth[kt]\,dk$$

$$J_{mn}^{-+} = \int_0^\infty \frac{k\cos[k(g+L+h)]\sin[kh]\sin[kg]}{[(kg)^2 - (m\pi)^2][(kh)^2 - (n\pi)^2]} \cdot \coth[kt]\,dk$$

$$K_{mn}^{-+} = \int_0^\infty \frac{k\sin[k(g+L+h)]\cos[kh]\sin[kg]}{[(kg)^2 - (m\pi)^2][(kh)^2 - [(n-1/2)\pi]^2]} \cdot \coth[kt]\,dk$$

$$L_{mn}^{-+} = \int_0^\infty \frac{k\cos^2[k(g+L+h)]\sin^2[kh]}{[(kh)^2 - (m\pi)^2][(kh)^2 - (n\pi)^2]} \cdot \coth[kt]\,dk$$

$$M_{mn}^{-+} = M_{mn}^{++}$$

$$N_{mn}^{-+} = \int_0^\infty \frac{k\sin^2[k(g+L+h)]\cos^2[kh]}{[(kh)^2 - [(m-1/2)\pi]^2][(kh)^2 - [(n-1/2)\pi]^2]} \cdot \coth[kt]\,dk.$$

F. For the Magnetic Field Components

$$L_n^{-+} = \int_0^\infty \frac{k\sin[kg]\cos[kx]}{(kg)^2 - (n\pi)^2} \frac{\sinh[k(t-y)]}{\sinh[kt]}\,dk$$

$$M_n^{-+} = \int_0^\infty \frac{k\cos[k(g+L+h)]\sin[kh]\cos[kx]}{(kh)^2 - (n\pi)^2} \cdot \frac{\sinh[k(t-y)]}{\sinh[kt]}\,dk$$

$$I_{mn}^{++} = \int_0^\infty \frac{k\cos^2[kg]}{[(kg)^2 - [(m-1/2)\pi]^2][(kg)^2 - [(n-1/2)\pi]^2]} \coth[kt]\,dk$$

$$J_{mn}^{++} = \int_0^\infty \frac{k\sin[k(g+L+h)]\sin[kh]\cos[kg]}{[(kg)^2 - [(m-1/2)\pi]^2][(kh)^2 - (n\pi)^2]} \coth[kt]\,dk$$

$$K_{mn}^{++} = \int_0^\infty \frac{k\cos[k(g+L+h)]\cos[kh]\cos[kg]}{[(kg)^2 - [(m-1/2)\pi]^2][(kh)^2 - [(n-1/2)\pi]^2]} \coth[kt]\,dk$$

$$L_{mn}^{++} = \int_0^\infty \frac{k\sin^2[k(g+L+h)]\sin^2[kh]}{[(kh)^2 - (m\pi)^2][(kh)^2 - (n\pi)^2]} \coth[kt]\,dk$$

$$M_{mn}^{++} = \int_0^\infty \frac{k\cos[k(g+L+h)]\sin[k(g+L+h)]\cos[kh]\sin[kh]}{[(kh)^2 - (m\pi)^2][(kh)^2 - [(n-1/2)\pi]^2]} \coth[kt]\,dk$$

$$N_{mn}^{++} = \int_0^\infty \frac{k\cos^2[k(g+L+h)]\cos^2[kh]}{[(kh)^2 - [(m-1/2)\pi]^2][(kh)^2 - [(n-1/2)\pi]^2]} \coth[kt]\,dk. \quad (46)$$

$$N_n^{-+} = \int_0^\infty \frac{k \sin[k(g+L+h)] \cos[kh] \cos[kx]}{(kh)^2 - [(n-1/2)\pi]^2} \cdot \frac{\sinh[k(t-y)]}{\sinh[kt]}\, dk$$

$$P_n^{-+} = \int_0^\infty \frac{k \sin[kg] \sin[kx]}{(kg)^2 - (n\pi)^2} \frac{\cosh[k(t-y)]}{\sinh[kt]}\, dk$$

$$Q_n^{-+} = \int_0^\infty \frac{k \cos[k(g+L+h)] \sin[kh] \sin[kx]}{(kh)^2 - (n\pi)^2} \cdot \frac{\cosh[k(t-y)]}{\sinh[kt]}\, dk$$

$$R_n^{-+} = \int_0^\infty \frac{k \sin[k(g+L+h)] \cos[kh] \sin[kx]}{(kh)^2 - [(n-1/2)\pi]^2} \cdot \frac{\cosh[k(t-y)]}{\sinh[kt]}\, dk.$$

ACKNOWLEDGMENT

The authors would like to thank J. C. Mallinson for useful discussions on this work.

REFERENCES

[1] J. C. Mallinson, *Magneto-Resistive Heads: Fundamentals and Applications.* San Diego, CA: Academic, 1996.
[2] D. J. Mapps, "Magnetoresistive sensors," *Sens. Actuators*, vol. A59, pp. 9–19, 1997.
[3] S. Iwasaki and N. Honda, "Strategy for implementation of perpendicular magnetic recording," *J. Magn. Soc. Japan*, vol. 21, no. S2, pp. 1–8, 1997.
[4] R. S. Indeck, J. H. Judy, and S. Iwasaki, "A magnetoresistive gradiometer," *IEEE Trans. Magn.*, vol. MAG-24, pp. 2617–2619, Nov. 1988.
[5] H. S. Gill, V. W. Hesterman, G. J. Tarnopolski, L. T. Tran, P. D. Frank, and H. Hamilton, "A magnetoresistive gradiometer for detection of perpendicularly recorded transitions," *J. Appl. Phys.*, vol. 65, pp. 402–404, Jan. 1989.
[6] N. Smith, J. Freeman, P. Koeppe, and T. Carr, "Dual magnetoresistive head for very high density recording," *IEEE Trans. Magn.*, vol. MAG-28, pp. 2992–2994, Sept. 1992.
[7] Y. Zhang, S. Shtrikman, and H. N. Bertram, "Playback pulse shapes and spectra for shielded MR heads," *IEEE Trans. Magn.*, vol. 33, pp. 1093–1103, Mar. 1997.
[8] O. Karlqvist, "Calculation of the magnetic field in the ferromagnetic layer of a magnetic drum," *Trans. Roy. Inst. Technol. Stockholm*, vol. 86, pp. 1–27, 1954.
[9] W. K. Westmijze, "Studies on magnetic recording—II: Field configuration around the gap and the gap-length formula," *Philips Res. Rep.*, vol. 8, pp. 161–183, June 1953.
[10] D. T. Wilton, H. A. Shute, and D. J. Mapps, "Accurate approximation of fields and spectral response functions for perpendicular recording heads," *IEEE Trans. Magn.*, vol. 35, pp. 2172–2179, July 1999.
[11] G. J. Y. Fan, "Analysis of a practical perpendicular head for digital purposes," *J. Appl. Phys.*, vol. 31, pp. 402S–403S, May 1960.
[12] D. T. Wilton and D. J. Mapps, "An analysis of a shielded magnetic pole for perpendicular recording," *IEEE Trans. Magn.*, vol. 29, pp. 4182–4193, Nov. 1993.
[13] E. Champion and H. N. Bertram, "The effect of MR head geometry on playback pulse shape and spectra," *IEEE Trans. Magn.*, vol. 31, pp. 2461–2470, July 1995.
[14] D. T. Wilton, "An analysis of the magnetic field of a ring head with a highly permeable underlayer," *IEEE Trans. Magn.*, vol. 27, pp. 3751–3755, July 1991.
[15] G. J. Y. Fan, "A study of the playback process of a magnetic ring head," *IBM J. Res. Devel.*, vol. 5, pp. 321–325, Oct. 1961.
[16] NAG Routine D01AKF, Numerical Algorithms Group, Oxford, U.K.
[17] F. Z. Wang, L. N. He, D. J. Mapps, D. T. Wilton, W. W. Clegg, and P. Robinson, "Keepered media reproduction with dual MR heads," *IEEE Trans. Magn.*, vol. 34, pp. 1982–1984, July 1998.
[18] R. V. Churchill and J. W. Brown, *Complex Variables and Applications.* New York: McGraw-Hill, 1984.
[19] H. N. Bertram, *Theory of Magnetic Recording.* Cambridge, U.K.: Cambridge Univ. Press, 1994.

Stephen J. C. Brown received the M.Math. degree in mathematics in 1997 from the University of Plymouth, England. He is currently working toward the Ph.D. degree in theoretical aspects of magnetic recording at the University of Plymouth.

David T. Wilton received the B.A. degree in mathematics from the University of York, England, in 1969 and the D.Phil. degree in numerical analysis from the University of Oxford, England, in 1974.

He spent three years at the University of Dundee, Scotland, and then three years with the Ministry of Defence working on dynamic fluid-structure interaction problems in underwater acoustics. Since 1978, he has been lecturing mathematics at the University of Plymouth. During 1987–1989, he spent two years at the City Polytechnic of Hong Kong. His main research interests are in numerical analysis and applied mathematics in the areas of electromagnetics and acoustics.

Hazel A. Shute received the B.Sc. degree in mathematical studies in 1992 and the Ph.D. degree in mathematical modeling in 1995, both from the University of Plymouth, England.

She is currently continuing her work on magnetic recording head read/write characteristics as a postdoctoral Research Fellow at the University of Plymouth.

Desmond J. Mapps received the B.Eng. degree in electrical engineering in 1966 and the Ph.D. degree in magnetics in 1969, both from the University of Wales, Cardiff.

From 1969 to 1973, he researched computer memories in industry before joining the University of Plymouth, U.K. He is now a SONY Professor of Electronic Engineering and Head of the Centre for Research in Information Storage Technology at the University.

Dr. Mapps is a Fellow of the U.K. Institute of Physics and a Fellow of the U.K. Institution of Electrical Engineers.

Integrals Arising in Models of Shielded Magnetoresistive Heads

David T. Wilton, Stephen J. C. Brown, Hazel A. Shute, and Desmond J. Mapps, *Member, IEEE*

***Abstract*—Integrals arising in two-dimensional models of shielded magnetoresistive heads are expressed either in terms of special functions or as rapidly convergent infinite series. In each case, form of expression provides an alternative and normally more efficient means of evaluation than direct numerical integration.**

***Index Terms*—Fourier integrals, magnetic fields, magnetic recording, magnetoresistive heads.**

I. Introduction

RECENTLY, Aharoni [1] has given analytic results, in the form of rapidly convergent infinite series, for some of the integrals appearing in [2]. In fact, *all* thintegrals given in the Appendix of [2] may be written either in terms of special functions or as rapidly convergent infinite series which provides an alternative and usually more efficient means of calculation than direct numerical integration. Here we indicate briefly how these results may be obtained, giving examples of each approach. The detail given should be sufficient for the interested reader to derive similar expressions for the remaining integrals. Although all the analysis given in [2] was explicitly for dual-stripe and differential double-element heads, a special case of the dual-stripe head (with the interelement gap length, g, zero) is the shielded single-pole head and appropriate results given here apply to that simpler geometry. Also, these results are applicable to all integrals required for the Fourier analysis of thin-film heads with underlayers [3]. The notation of [2] will be used here without being redefined.

II. Integrals

A. Coefficient Integrals

The results given in [1] are for the integrals required to determine the coefficients in the Fourier expansions in the case of a head with an underlayer. An alternative derivation of those results is via complex contour integration, the appropriate contour being an infinitely large semicircle in the upper-half complex plane with the diameter being the real axis. The infinite series arise from the poles of $\sinh[zt]$ on the positive imaginary axis and the additional terms needed when $m = n$ are due to poles on the real axis. When no underlayer is present ($t = \infty$ and $\coth[kt]$ is replaced by unity), those expressions may be used to give reasonably accurate results if t is made sufficiently large and enough terms of the series are taken. However, a more reliable approach in this case is to write the integrals in terms of the sine and cosine integrals, $\mathrm{Si}(x)$ and $\mathrm{Ci}(x)$, respectively [4]; e.g., I_{mn}^{-+} (apart from a factor of g^2) was given in [5] for the three cases $m \neq n$ and $m, n \neq 0$; $m = n \neq 0$; $m \neq 0$ and $n = 0$. The other coefficient integrals may be evaluated similarly although they do lead to more complicated expressions. For example, for

$$J_{mn}^{-+} = \int_0^\infty \frac{k \cos[k(g+L+h)] \sin[kh] \sin[kg]}{[(kg)^2 - (m\pi)^2][(kh)^2 - (n\pi)^2]}\, dk \quad (1)$$

let $H = 2h$, $G = 2g$ and

$$\begin{aligned}
a_1 &= m\pi(G+L)/g & a_2 &= m\pi(L+H)/g \\
a_3 &= m\pi(G+L+H)/g & a_4 &= m\pi L/g \\
b_1 &= n\pi(G+L)/h & b_2 &= n\pi(L+H)/h \\
b_3 &= n\pi(G+L+H)/h & b_4 &= n\pi L/h \\
A &= \cos(a_1)\mathrm{Ci}(a_1) + \sin(a_1)\mathrm{Si}(a_1) + \cos(a_2)\mathrm{Ci}(a_2) \\
&\quad + \sin(a_2)\mathrm{Si}(a_2) - \cos(a_3)\mathrm{Ci}(a_3) - \sin(a_3)\mathrm{Si}(a_3) \\
&\quad - \cos(a_4)\mathrm{Ci}(a_4) - \sin(a_4)\mathrm{Si}(a_4) \\
B &= \cos(b_1)\mathrm{Ci}(b_1) + \sin(b_1)\mathrm{Si}(b_1) + \cos(b_2)\mathrm{Ci}(b_2) \\
&\quad + \sin(b_2)\mathrm{Si}(b_2) - \cos(b_3)\mathrm{Ci}(b_3) - \sin(b_3)\mathrm{Si}(b_3) \\
&\quad - \cos(b_4)\mathrm{Ci}(b_4) - \sin(b_4)\mathrm{Si}(b_4). \quad (2)
\end{aligned}$$

For $mh \neq ng$ and $m, n \neq 0$

$$J_{mn}^{-+} = \frac{1}{4\pi^2[(ng)^2 - (mh)^2]}[A - B]. \quad (3)$$

For $mh = ng$ and $m \neq 0$

$$\begin{aligned}
J_{mn}^{-+} = \frac{1}{8\pi m h^2 g} &[(G+L)(\sin(a_1)\mathrm{Ci}(a_1) - \cos(a_1)\mathrm{Si}(a_1)) \\
&+ (L+H)(\sin(a_2)\mathrm{Ci}(a_2) - \cos(a_2)\mathrm{Si}(a_2)) \\
&- (G+L+H)(\sin(a_3)\mathrm{Ci}(a_3) \\
&- \cos(a_3)\mathrm{Si}(a_3)) - L(\sin(a_4)\mathrm{Ci}(a_4) \\
&- \cos(a_4)\mathrm{Si}(a_4))]. \quad (4)
\end{aligned}$$

For $m \neq 0$ and $n = 0$

$$J_{m0}^{-+} = \frac{1}{(2\pi m h)^2}\left[\log\left(\frac{(G+L)(L+H)}{L(G+L+H)}\right) - A\right]. \quad (5)$$

To derive (3)–(5), the denominator of the integrand is split using partial fractions, the numerator is written as either two or four

Manuscript received August 9, 2000.

D. T. Wilton, S. J. C. Brown, and H. A. Shute are with the Department of Mathematics and Statistics and the Centre for Research in Information Storage Technology, University of Plymouth, Plymouth, Devon, PL4 8AA, U.K. (e-mail: dwilton@plymouth.ac.uk).

D. J. Mapps is with the Department of Communication and Electronic Engineering and the Centre for Research in Information Storage Technology, University of Plymouth, Plymouth, Devon, PL4 8AA, U.K.

Publisher Item Identifier S 0018-9464(01)00606-9.

separate trigonometric terms as appropriate, integration by parts is employed for (4) and then standard results [6] are used.

B. Potential Integrals

The integrals required to compute the magnetic potential when an underlayer is present may be evaluated by contour integration, the appropriate contour again being the semicircle described previously for the coefficient integrals. The trigonometric terms are written as the real parts of complex exponentials but care must be taken to ensure that these terms remain bounded on the semicircular arc as its radius tends to infinity. This requires slightly different representations for different regions of the x variable and leads to different series in these regions. For example, for

$$I_n^{++} = \int_0^\infty \frac{\cos[kg]\cos[kx]}{(kg)^2 - [(n-1/2)\pi]^2} \cdot \frac{\sinh[k(t-y)]}{\sinh[kt]}\, dk \quad (6)$$

when $x \le g$ we write the product of the cosine terms as $0.5\mathrm{Re}[e^{i(g+x)z} + e^{i(g-x)z}]$, while if $x \ge g$ we take $0.5\mathrm{Re}[e^{i(g+x)z} + e^{i(x-g)z}]$.

Then for $x \le g$

$$I_n^{++} = \frac{-t}{2\pi} \sum_{p=1}^{\infty} \frac{e^{-p\pi(g-x)/t}(1+e^{-2p\pi x/t})}{(pg)^2 + [(n-1/2)t]^2} \sin\left[\frac{p\pi y}{t}\right] + \frac{(-1)^n \cos[(n-1/2)\pi x/g]}{2g(n-1/2)} \cdot \frac{\sinh[(n-1/2)\pi(t-y)/g]}{\sinh[(n-1/2)\pi t/g]} \quad (7a)$$

and for $x \ge g$

$$I_n^{++} = \frac{-t}{2\pi} \sum_{p=1}^{\infty} \frac{e^{-p\pi(x-g)/t}(1+e^{-2p\pi g/t})}{(pg)^2 + [(n-1/2)t]^2} \sin\left[\frac{p\pi y}{t}\right]. \quad (7b)$$

Similarly for

$$J_n^{++} = \int_0^\infty \frac{\sin[k(g+L+h)]\sin[kh]\cos[kx]}{(kh)^2 - (n\pi)^2} \cdot \frac{\sinh[k(t-y)]}{\sinh[kt]}\, dk \quad (8)$$

we have for $x \le g + L$

$$J_n^{++} = \frac{t}{4\pi} \sum_{p=1}^{\infty} \frac{e^{-p\pi(g+L-x)/t}(e^{-2p\pi h/t}-1)(1+e^{-2p\pi x/t})}{(ph)^2 + (nt)^2} \cdot \sin\left[\frac{p\pi y}{t}\right] + \begin{cases} 0, & \text{if } n \neq 0 \\ \dfrac{\pi}{2h}\left(\dfrac{t-y}{t}\right), & \text{if } n = 0 \end{cases} \quad (9a)$$

for $g + L \le x \le g + L + H$ see (9b) at the bottom of the page and for $x \ge g + L + H$ see (9c) at the bottom of the page.

When there is no underlayer, the ratio of the two sinh terms in these integrals is replaced by e^{-ky} and the above contour integration approach is no longer suitable. As is the case for the coefficient integrals, it is not possible simply to let t tend to infinity in the above results and obtain series representations for these potential integrals. By taking a large value for t and enough terms of the series, approximate results can be found, but it is preferable to proceed differently. All the potential integrals may be evaluated in terms of

$$M(\alpha, \beta, \gamma, \delta) = \int_0^\infty \frac{\sin[\beta k]\sin[\gamma k]e^{-\delta k}}{k^2 - \alpha^2}\, dk \quad (10)$$

and

$$P(\alpha, \beta, \gamma, \delta) = \int_0^\infty \frac{\cos[\beta k]\cos[\gamma k]e^{-\delta k}}{k^2 - \alpha^2}\, dk. \quad (11)$$

For $\alpha, \beta, \gamma, \delta > 0$ it may be shown that [6]

$$M(\alpha, \beta, \gamma, \delta) = \frac{1}{4\alpha}\mathrm{Re}\left[e^{-\alpha p}\mathrm{E}_1(-\alpha p) - e^{\alpha p}\mathrm{E}_1(\alpha p) - e^{-\alpha q}\mathrm{E}_1(-\alpha q) + e^{\alpha q}\mathrm{E}_1(\alpha q)\right] + \frac{\pi}{2\alpha}e^{-\alpha\delta}\begin{cases}\cos[\alpha\beta]\sin[\alpha\gamma], & \text{if } \beta \ge \gamma \\ \sin[\alpha\beta]\cos[\alpha\gamma], & \text{if } \beta < \gamma\end{cases} \quad (12)$$

$$J_n^{++} = \frac{t}{4\pi} \sum_{p=1}^{\infty} \left[\frac{e^{-p\pi(g+L+H-x)/t}(1+e^{-2p\pi x/t}) - e^{-p\pi(x-g-L)/t}(1+e^{-2p\pi(g+L)/t})}{(ph)^2 + (nt)^2}\right] \sin\left[\frac{p\pi y}{t}\right] - \begin{cases} \dfrac{1}{4nh}\dfrac{\sin[n\pi(x-g-L)/h]\sinh[n\pi(t-y)/h]}{\sinh[n\pi t/h]}, & \text{if } n \neq 0 \\ \dfrac{\pi}{4h^2}(x-g-L-H)\left(\dfrac{t-y}{t}\right), & \text{if } n = 0 \end{cases} \quad (9b)$$

$$J_n^{++} = \frac{t}{4\pi} \sum_{p=1}^{\infty} \frac{e^{-p\pi(x-g-L-H)/t}(1-e^{-2p\pi(g+L+h)/t})(1-e^{-2p\pi h/t})}{(ph)^2 + (nt)^2} \sin\left[\frac{p\pi y}{t}\right] \quad (9c)$$

$$M(0,\beta,\gamma,\delta) = \frac{\delta}{4}\log\left[\frac{(\beta-\gamma)^2+\delta^2}{(\beta+\gamma)^2+\delta^2}\right] + \left(\frac{\beta+\gamma}{2}\right)\arctan\left[\frac{\beta+\gamma}{\delta}\right] - \left(\frac{\beta-\gamma}{2}\right)\arctan\left[\frac{\beta-\gamma}{\delta}\right] \quad (13)$$

and for $\alpha, \delta > 0$, $M(\alpha,\beta,\gamma,\delta) = M(\alpha,|\beta|,|\gamma|,\delta)\,\mathrm{sign}(\beta)\,\mathrm{sign}(\gamma)$. The results for (10) given in [7] are for the particular case of $\alpha\beta$ being an integer multiple of π and contain some typographical errors.

For $\alpha, \beta, \gamma, \delta > 0$

$$P(\alpha,\beta,\gamma,\delta) = \frac{1}{4\alpha}\,\mathrm{Re}\left[e^{-\alpha p}\mathrm{E}_1(-\alpha p) - e^{\alpha p}\mathrm{E}_1(\alpha p) + e^{-\alpha q}\,\mathrm{E}_1(-\alpha q) - e^{\alpha q}\mathrm{E}_1(\alpha q)\right] - \frac{\pi}{2\alpha}e^{-\alpha\delta}\begin{cases}\sin[\alpha\beta]\cos[\alpha\gamma], & \text{if } \beta \geq \gamma\\ \cos[\alpha\beta]\sin[\alpha\gamma], & \text{if } \beta < \gamma\end{cases} \quad (14)$$

and for $\alpha, \delta > 0$, $P(\alpha,\beta,\gamma,\delta) = P(\alpha,|\beta|,|\gamma|,\delta)$. In (12) and (14), $p = \delta - i(\beta-\gamma)$, $q = \delta - i(\beta+\gamma)$, and $\mathrm{E}_1(z)$ is the complex exponential integral which may be evaluated from a series expansion for "small" arguments [4] and by Laguerre integration for "large" arguments [8].

Then, for example

$$I_n^{++} = \frac{1}{g^2}P((n-1/2)\pi/g, x, g, y) \quad (15)$$

and

$$J_n^{++} = \frac{1}{2h^2}\left[M(n\pi/h, g+L+h+x, h, y) + M(n\pi/h, g+L+h-x, h, y)\right]. \quad (16)$$

By writing

$$\frac{\sinh[k(t-y)]}{\sinh[kt]} = \sum_{m=0}^{\infty}\left(e^{-k[2mt+y]} - e^{-k[2(m+1)t-y]}\right) \quad (17)$$

all the potential integrals when there is an underlayer may alternatively be written as infinite series of the $M(\alpha,\beta,\gamma,\delta)$ and $P(\alpha,\beta,\gamma,\delta)$ functions. For example

$$I_n^{++} = \frac{1}{g^2}\sum_{m=0}^{\infty}\left[P((n-1/2)\pi/g, x, g, 2mt+y) - P((n-1/2)\pi/g, x, g, 2(m+1)t-y)\right] \quad (18)$$

and

$$J_n^{++} = \frac{1}{2h^2}\sum_{m=0}^{\infty}\left[M(n\pi/h, g+L+h+x, h, 2mt+y) + M(n\pi/h, g+L+h-x, h, 2mt+y) - M(n\pi/h, g+L+h+x, h, 2(m+1)t-y) - M(n\pi/h, g+L+h-x, h, 2(m+1)t-y)\right]. \quad (19)$$

However, such series do not converge particularly fast and it is certainly preferable to use the series (7) and (9) derived previously.

C. Field Integrals

The field integrals when an underlayer is present cannot be evaluated directly using contour integration as in the previous sections since the relevant complex functions do not tend to zero sufficiently fast on the semicircular arc as its radius tends to infinity. However, they may be evaluated simply by differentiating the series for the potential. For example, $M_n^{++} = -\partial J_n^{++}/\partial x$ and $Q_n^{++} = -\partial J_n^{++}/\partial y$.

When there is no underlayer, the series obtained above may be used with large values of t, but it is better to treat these integrals directly, as for the potential integrals. All the field integrals may be written in terms of

$$J(\alpha,\beta,\gamma,\delta) = \int_0^{\infty}\frac{k\sin[\beta k]\sin[\gamma k]e^{-\delta k}}{k^2-\alpha^2}\,dk \quad (20)$$

$$K(\alpha,\beta,\gamma,\delta) = \int_0^{\infty}\frac{k\sin[\beta k]\cos[\gamma k]e^{-\delta k}}{k^2-\alpha^2}\,dk \quad (21)$$

and

$$L(\alpha,\beta,\gamma,\delta) = \int_0^{\infty}\frac{k\cos[\beta k]\cos[\gamma k]e^{-\delta k}}{k^2-\alpha^2}\,dk. \quad (22)$$

For $\alpha, \beta, \gamma, \delta > 0$

$$J(\alpha,\beta,\gamma,\delta) = \tfrac{1}{4}\,\mathrm{Re}\left[e^{-\alpha p}\mathrm{E}_1(-\alpha p) + e^{\alpha p}\mathrm{E}_1(\alpha p) - e^{-\alpha q}\,\mathrm{E}_1(-\alpha q) - e^{\alpha q}\mathrm{E}_1(\alpha q)\right] + \frac{\pi}{2}e^{-\alpha\delta}\begin{cases}\cos[\alpha\beta]\sin[\alpha\gamma], & \text{if } \beta \geq \gamma\\ \sin[\alpha\beta]\cos[\alpha\gamma], & \text{if } \beta < \gamma\end{cases} \quad (23)$$

$$J(0,\beta,\gamma,\delta) = \frac{1}{4}\log\left[\frac{(\beta+\gamma)^2+\delta^2}{(\beta-\gamma)^2+\delta^2}\right] \quad (24)$$

and if not both of β and γ are positive, $J(\alpha,\beta,\gamma,\delta) = J(\alpha,|\beta|,|\gamma|,\delta)\,\mathrm{sign}(\beta)\,\mathrm{sign}(\gamma)$.

For $\alpha, \beta, \gamma, \delta > 0$

$$K(\alpha,\beta,\gamma,\delta) = \tfrac{1}{4}\,\mathrm{Im}\left[e^{-\alpha p}\mathrm{E}_1(-\alpha p) + e^{\alpha p}\mathrm{E}_1(\alpha p) + e^{-\alpha q}\,\mathrm{E}_1(-\alpha q) + e^{\alpha q}\mathrm{E}_1(\alpha q)\right] + \frac{\pi}{2}e^{-\alpha\delta}\begin{cases}\cos[\alpha\beta]\cos[\alpha\gamma], & \text{if } \beta \geq \gamma\\ -\sin[\alpha\beta]\sin[\alpha\gamma], & \text{if } \beta < \gamma\end{cases} \quad (25)$$

$$K(0,\beta,\gamma,\delta) = \frac{1}{2}\arctan\left[\frac{\beta+\gamma}{\delta}\right] + \frac{1}{2}\arctan\left[\frac{\beta-\gamma}{\delta}\right] \quad (26)$$

and if not both of β and γ are positive, $K(\alpha,\beta,\gamma,\delta) = K(\alpha,|\beta|,|\gamma|,\delta)\,\mathrm{sign}(\beta)$.

For $\alpha, \beta, \gamma, \delta > 0$

$$L(\alpha,\beta,\gamma,\delta) = \tfrac{1}{4}\,\mathrm{Re}\left[e^{-\alpha p}\mathrm{E}_1(-\alpha p) + e^{\alpha p}\mathrm{E}_1(\alpha p) + e^{-\alpha q}\mathrm{E}_1(-\alpha q) + e^{\alpha q}\mathrm{E}_1(\alpha q)\right] - \frac{\pi}{2}e^{-\alpha\delta}\begin{cases}\sin[\alpha\beta]\cos[\alpha\gamma], & \text{if } \beta \geq \gamma\\ \cos[\alpha\beta]\sin[\alpha\gamma], & \text{if } \beta < \gamma\end{cases} \quad (27)$$

and $L(\alpha, \beta, \gamma, \delta) = L(\alpha, |\beta|, |\gamma|, \delta)$. In (23), (25), and (27), p and q are as defined earlier. Then, for example

$$L_n^{-+} = \frac{1}{g^2} K(n\pi/g, g, x, y) \tag{28}$$

and

$$Q_n^{++} = \frac{1}{2h^2} [J(n\pi/h, g + L + h + x, h, y) + J(n\pi/h, g + L + h - x, h, y)]. \tag{29}$$

As for the potential integrals, by writing

$$\frac{\cosh[k(t-y)]}{\sinh[kt]} = \sum_{m=0}^{\infty} \left(e^{-k[2mt+y]} + e^{-k[2(m+1)t-y]} \right) \tag{30}$$

all the field integrals, when there is an underlayer, may alternatively be written as infinite series of the $J(\alpha, \beta, \gamma, \delta)$, $K(\alpha, \beta, \gamma, \delta)$, and $L(\alpha, \beta, \gamma, \delta)$ functions. For example

$$L_n^{-+} = \frac{1}{g^2} \sum_{m=0}^{\infty} [K(n\pi/g, g, x, 2mt + y) - K(n\pi/g, g, x, 2(m + 1)t - y)] \tag{31}$$

and

$$\begin{aligned} Q_n^{++} = \frac{1}{2h^2} \sum_{m=0}^{\infty} & [J(n\pi/h, g+L+h+x, h, 2mt+y) \\ & + J(n\pi/h, g+L+h-x, h, 2mt+y) \\ & + J(n\pi/h, g+L+h+x, h, 2(m+1)t-y) \\ & + J(n\pi/h, g+L+h-x, h, 2(m+1)t-y)]. \end{aligned} \tag{32}$$

But series derived in this way do not converge as fast as those obtained by differentiating series such as (7) and (9). Results for (20) and (21) are given in [7] when $\alpha\beta$ is an integer multiple of π. The result (32) with $n = 0$ and for the case of a single shielded pole ($g = 0$) has been given in [9] where the leading term only ($n = 0$) of the vertical field is computed. It is observed in [9] that the summations required for the "with underlayer" integrals, due to using (17) and (30), arise from representing these potential and field contributions as combinations of reflections in the plane of the underlayer surface of the fields of equivalent "without underlayer" heads. Although this insight is instructive, for evaluation it is preferable to use the much more rapidly convergent series derived here through contour integration.

REFERENCES

[1] A. Aharoni, "Integrals used in magnetoresistive head modeling," *IEEE Trans. Magn.*, vol. 36, pp. 3879–3880, Sept. 2000.

[2] S. J. C. Brown, D. T. Wilton, H. A. Shute, and D. J. Mapps, "Analytic solutions for double-element shielded magnetoresistive heads," *IEEE Trans. Magn.*, vol. 35, pp. 4339–4350, Sept. 1999.

[3] D. T. Wilton, D. J. Mapps, and H. A. Shute, "Exact field calculations for conventional and graded magnetization thin film recording heads," *IEEE Trans. Magn.*, vol. 30, pp. 253–263, Mar. 1994.

[4] M. Abramowitz and I. A. Stegun, *Handbook of Mathematical Functions*. New York: Dover, 1965.

[5] G. J. Y. Fan, "Analysis of a practical perpendicular head for digital purposes," *J. Appl. Phys.*, vol. 31S, pp. 402S–403S, May 1960.

[6] I. S. Gradshteyn and I. M. Ryzhik, *Tables of Integrals, Series and Products*. San Diego, CA: Academic, 2000.

[7] A. W. Baird, "An evaluation and approximation of the Fan equations describing magnetic fields near recording heads," *IEEE Trans. Magn.*, vol. MAG-16, pp. 1350–1351, Sept. 1980.

[8] J. Todd, "Evaluation of the exponential integral for large complex arguments," *J. Res. Natl. Bur. Stand.*, vol. 52, pp. 313–317, June 1954.

[9] H. Muraoka, Y. Sugita, and Y. Nakamura, "Simplified expressions of shielded MR head response for double-layer perpendicular medium," *IEEE Trans. Magn.*, vol. 35, pp. 2235–2237, Sept. 1999.

David T. Wilton received the B.A. degree in mathematics from the University of York, York, U.K., in 1969 and the D.Phil. degree in numerical analysis from the University of Oxford, Oxford, U.K., in 1974.

He spent three years at the University of Dundee, Dundee, Scotland, and then three years with the Ministry of Defence working on dynamic fluid-structure interaction problems in underwater acoustics. Since 1978, he has been lecturing mathematics at the University of Plymouth, Plymouth, U.K. During 1987–1989, he spent two years at the City Polytechnic of Hong Kong. His main research interests are in numerical analysis and applied mathematics in the areas of electromagnetics and acoustics.

Stephen J. C. Brown received the M.Math. degree in mathematics in 1997 from the University of Plymouth, Plymouth, U.K. He is currently working toward the Ph.D. degree in theoretical aspects of magnetic recording at the University of Plymouth.

Hazel A. Shute received the B.Sc. degree in mathematical studies in 1992 and the Ph.D. degree in mathematical modeling in 1995, both from the University of Plymouth, Plymouth, U.K.

She is currently continuing her work on magnetic recording head read/write characteristics as a Postdoctoral Research Fellow at the University of Plymouth.

Desmond J. Mapps (M'99) received the B.Eng. degree in electrical engineering in 1966 and the Ph.D. degree in magnetics in 1969, both from the University of Wales, Cardiff, U.K.

From 1969 to 1973, he researched computer memories in industry before joining the University of Plymouth, Plymouth, U.K. He is now Professor of Electronic Engineering and Head of the Centre for Research in Information Storage Technology at the University.

Prof. Mapps is a Fellow of the U.K. Institute of Physics and a Fellow of the U.K. Institution of Electrical Engineers.

ELSEVIER

Journal of Magnetism and Magnetic Materials 235 (2001) 393–397

Journal of magnetism and magnetic materials

www.elsevier.com/locate/jmmm

Approximation of shielded MR head output for perpendicular media

D.T. Wilton[a,*], H.A. Shute[a], S.J.C. Brown[a], D.J. Mapps[b]

[a] *Department of Mathematics and Statistics, Centre for Research in Information Storage Technology, University of Plymouth, Drake Circus, Plymouth, Devon PL4 8AA, UK*

[b] *Department of Communication and Electronic Engineering, Centre for Research in Information Storage Technology, University of Plymouth, Plymouth, Devon PL4 8AA, UK*

Abstract

Output results are presented for a shielded MR head reading from a double-layer, perpendicular medium. The integrals required for an exact Fourier solution are given as rapidly convergent series. An approximation is used to provide accurate PW_{50} and D_{50} results over a wide range of practical head dimensions. Simple, approximate PW_{50} and D_{50} formulae are derived and their range of validity discussed.

Keywords: Magnetoresistive heads; Perpendicular recording; Replay characteristics; Approximate formulae

1. Introduction

Predictions of the response of shielded magnetoresistive (MR) heads using two-dimensional models based on Fourier analysis have been found to agree well with experimental results [1,2]. Two problems in applying such models are the numerical evaluation of the integrals occurring in the infinite series that arise and the need to determine the coefficients of these series, which depend on the particular head geometry. Here, both of these issues are discussed. All integrals required for the magnetic potential and the components of the magnetic field are given as rapidly convergent series, which offer a considerably more efficient means of evaluation than direct numerical integration. However, an alternative approach is to use approximations that do not require either the computation of Fourier coefficients or the evaluation of series of integrals. Such an approximation is considered here and its high accuracy is demonstrated by comparison with the full series solution for the output response of a single shielded MR element reading from a double-layer perpendicular medium. Also, simple approximate PW_{50} and D_{50} formulae are derived based on the leading (linear) term of the full Fourier solution and their range of application is discussed and illustrated.

2. Exact results

Fig. 1 shows the geometry under consideration. A single MR element of length $2L$ and at unit potential is symmetrically placed between shields at zero potential. The pole-shield gaps are each $2g$, the medium of thickness δ is a distance d from the pole and $t = d + \delta$. Fourier analysis may be used

*Corresponding author. Fax: +44-1752-232780.

E-mail address: dwilton@plymouth.ac.uk (D.T. Wilton).

0304-8853/01/$ - see front matter
PII: S0304-8853(01)00395-X

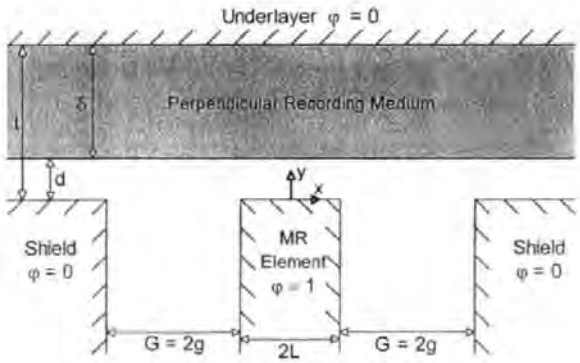

Fig. 1. Shielded MR head.

to solve Laplace's equation for the magnetic potential φ in the region between the pole, shields and underlayer [3]. The potential in $0 \leqslant y \leqslant t$ is given by

$$\varphi(x,y) = \frac{2g}{\pi} J_0 - 4g(-1)^n \sum_{n=1}^{\infty} [B_n n J_n - C_n (n - \tfrac{1}{2}) K_n] \quad (1)$$

with,

$$J_n = \int_0^{\infty} \frac{\sin[k(L+g)]\sin[kg]\cos[kx]}{(kg)^2 - (n\pi)^2} \times \frac{\sinh[k(t-y)]}{\sinh[kt]}\,dk, \quad (2)$$

$$K_n = \int_0^{\infty} \frac{\cos[k(L+g)]\cos[kg]\cos[kx]}{(kg)^2 - [(n-\tfrac{1}{2})\pi]^2} \times \frac{\sinh[k(t-y)]}{\sinh[kt]}\,dk, \quad (3)$$

where the Fourier coefficients B_n and C_n are determined by solving an infinite set of simultaneous equations whose coefficients have been given in Ref. [4] as rapidly convergent infinite series. Using complex contour integration, the integrals J_n and K_n may be expressed similarly. The appropriate contour is an infinitely large semi-circle in the upper half complex plane with the diameter being the real axis. The trigonometric terms are written as the real parts of complex exponentials with care being taken to ensure that these terms remain bounded on the semi-circular arc as its radius tends to infinity. This requires different representations for different regions of the x variable and leads to different series in thes regions. For $x \leqslant L$,

$$J_n = \frac{t}{4\pi} \sum_{p=1}^{\infty} \frac{e^{-p\pi(L-x)/t}(e^{-2p\pi g/t} - 1)(1 + e^{-2p\pi x/t})}{(pg)^2 + (nt)^2} \times \sin[p\pi y/t] + \begin{cases} 0, & \text{if } n \neq 0 \\ \dfrac{\pi}{2g}\left(\dfrac{t-y}{t}\right), & \text{if } n = 0, \end{cases} \quad (4a$$

for $L \leqslant x \leqslant L + G$,

$$J_n = \frac{t}{4\pi} \sum_{p=1}^{\infty} [e^{-p\pi(L+G-x)/t}(1 + e^{-2p\pi x/t}) - e^{-p\pi(x-L)/} \times (1 + e^{-2p\pi L/t})]\sin[p\pi y/t]/[(pg)^2 + (nt)^2] - \begin{cases} \dfrac{1}{4ng} \dfrac{\sin[n\pi(x-L)/g]\sinh[n\pi(t-y)/g]}{\sinh[n\pi t/g]}, \\ \quad \text{if } n \neq 0 \\ \dfrac{\pi}{4g^2}(x - L - G)\left(\dfrac{t-y}{t}\right), \\ \quad \text{if } n = 0 \end{cases} \quad (4b$$

and for $x \geqslant L + G$,

$$J_n = \frac{t}{4\pi} \sum_{p=1}^{\infty} \frac{e^{-p\pi(x-L-G)/t}(1 - e^{-2p\pi(L+g)/t})(1 - e^{-2p\pi g/t}}{(pg)^2 + (nt)^2} \times \sin[p\pi y/t]. \quad (4c$$

For $x \leqslant L$,

$$K_n = -\frac{t}{4\pi} \sum_{p=1}^{\infty} \frac{e^{-p\pi(L-x)/t}(1 + e^{-2p\pi g/t})(1 + e^{-2p\pi x/t}}{(pg)^2 + [(n-\tfrac{1}{2})t]^2} \times \sin[p\pi y/t], \quad (5a$$

for $L \leqslant x \leqslant L + G$

$$K_n = -\frac{t}{4\pi} \sum_{p=1}^{\infty} [e^{-p\pi(L+G-x)/t}(1 + e^{-2p\pi x/t}) + e^{-p\pi(x-L)/t}(1 + e^{-2p\pi L/t})] \times \sin[p\pi y/t]/[(pg)^2 + [(n-\tfrac{1}{2})t]^2] - \frac{1}{4(n-\tfrac{1}{2})g} \times \frac{\sin[(n-\tfrac{1}{2})\pi(x-L)/g]\sinh[(n-\tfrac{1}{2})\pi(t-y)/g]}{\sinh[(n-\tfrac{1}{2})\pi t/g]}, \quad (5b)$$

and for $x \geq L + G$

$$K_n = -\frac{t}{4\pi}\sum_{p=1}^{\infty}\frac{e^{-p\pi(x-L-G)/t}(1+e^{-2p\pi(L+g)/t})(1+e^{-2p\pi g/t})}{(pg)^2+[(n-\frac{1}{2})t]^2} \times \sin[p\pi y/t]. \quad (5c)$$

The vertical field $H_y(x,y)$ may be obtained by differentiating Eqs. (1), (4) and (5). These series are much more rapidly convergent than the series given in Ref. [2] for the leading term of $H_y(x,y)$, which is $-2g(\partial J_0/\partial y)/\pi$ in our notation. These new results allow very efficient evaluation of the potential and field and avoid the need for numerical integration.

When the MR sensor is operating such that its response is linear, the output voltage may be given by the reciprocity theorem as the correlation integral

$$e_y(\bar{x}) = C^{MR}\int_{y=d}^{t}\int_{x=-\infty}^{\infty} H_y(x+\bar{x},y)M_y(x)\,dx\,dy, \quad (6)$$

where C^{MR} is a constant, $M_y(x)$ is the recorded magnetisation on the medium, assumed to be constant through the medium thickness, and $\bar{x}$ is the relative position of the medium and the head. Rather than work directly with Eq. (6), it is preferable first to take the Fourier transform of Eq. (6), which can be done analytically for the magnetisation considered here, and compute the output voltage as an inverse Fourier transform. The integrand then converges rapidly to zero allowing efficient numerical integration or approximate results to be derived. Expressing the result in terms of $\hat{\varphi}(k,0)$, the transform of $\varphi(x,0)$, and performing the y integration gives

$$\hat{e}_y(k) = C^{MR}\hat{\varphi}(k,0)\frac{\sinh[k(t-d)]}{\sinh[kt]}\hat{M}_y^*(k). \quad (7)$$

Assuming a unit tanh transition model, $M_y(x) = \tanh[2x/(\pi a)]$, where a denotes the transition parameter, and differentiating the output to produce a single pulse rather than a step-like response, gives

$$E(\bar{x}) = \frac{d}{d\bar{x}}e_y(\bar{x}) = -C^{MR}\frac{\pi a}{2} \times \int_0^{\infty}\frac{k\hat{\varphi}(k,0)\sinh[k(t-d)]}{\sinh[kt]\sinh[\pi^2 ak/4]}\cos[k\bar{x}]\,dk, \quad (8)$$

where $\hat{\varphi}(k,0)$ is easily derived from Eq. (1) and involves no further integration [3]. For the case of an 'ideal' transition ($a = 0$), Eq. (8) reduces to $-2C^{MR}\varphi(\bar{x},d)$.

3. Approximate results

A common approximation used in head field calculations is to assume a linear variation in magnetic potential across pole-shield gaps which, for perpendicular recording, only provides accurate results for small shield-shield spacing [2]. An alternative approximation is based on a linear variation in potential between the MR element and the underlayer [5]. This gives an approximation to $\varphi(x,0)$ in pole-shield gaps in the form of an integral which can be evaluated as a rapidly convergent series and results in an explicit spectral response function $\hat{\varphi}(k,0)$ [5]. Common characterisations of the high frequency response of a particular head and medium combination are PW_{50} and D_{50}. PW_{50} is the width of a single output pulse at half its amplitude and D_{50} is the density at which the amplitude of the output from a sequence of magnetisation reversals drops to half that of a single transition. Fig. 2 shows typical PW_{50} results for two different underlayer distances and media thicknesses ($t = 100$ nm, $d = 50$ nm and $t = 50$ nm, $d = 25$ nm) with: MR element length −20 nm; shield-shield spacing −50 to 400 nm; transition length −10 nm. In each case, the exact results based on the accurate Fourier solution are shown together with results assuming the usual approximation (linear in the gaps). The results using the new approximation are shown as square symbols and they are seen to be an excellent match to the exact results over the whole range of shield-shield spacings, in contrast to the limited range of applicability of the linear approximation. Fig. 3

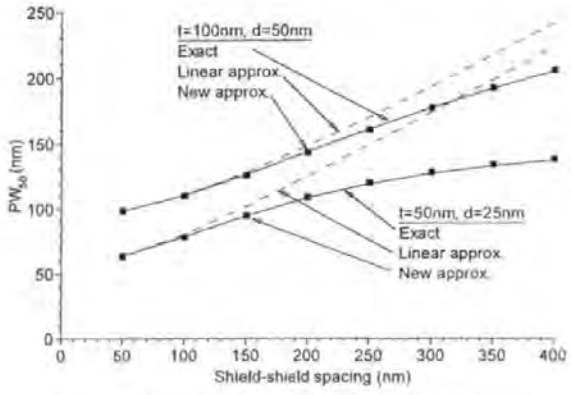

Fig. 2. Variation of PW_{50} with shield–shield spacing.

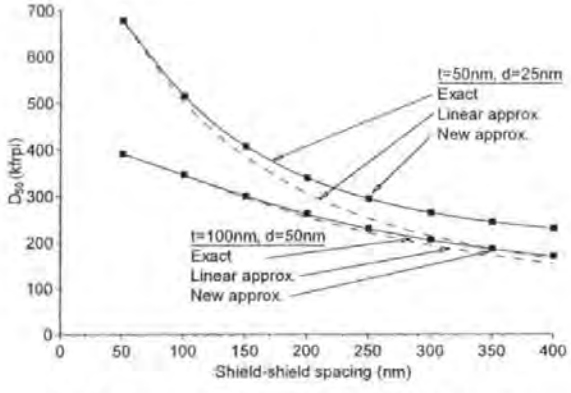

Fig. 3. Variation of D_{50} with shield–shield spacing.

shows D_{50} results for the same geometries (with ideal transitions). Here the linear approximation for $t = 100\,\text{nm}$, $d = 50\,\text{nm}$ is fairly good but not for $t = 50\,\text{nm}$, $d = 25\,\text{nm}$ and in each case, the new approximation is again excellent. These results indicate that this new approximation can be used with confidence to investigate the effect of head and medium dimensions and transition lengths on head output.

4. Approximate PW_{50} and D_{50} formulae

Simple PW_{50} and D_{50} formulae may be obtained by approximating Eq. (8) under the assumption of a linear potential across the pole-shield gaps, for which

$$\hat{\varphi}(k,0) \approx 2\sin[k(L+g)]\sin[kg]/(k^2 g). \tag{9}$$

Using the exponential approximations $\sin[x]/x \approx \exp[-x^2/6], x/\sinh[x] \approx \exp[-x^2/6]$ which are valid for small x and the rational approximation $\sinh[\alpha x]/\sinh[x] \approx 6\alpha/[6 + (1-\alpha^2)x^2)]$ which is valid for $0.6 \leqslant \alpha \leqslant 0.8$ leads to

$$E(\bar{x}) \propto \int_0^\infty \frac{e^{-k^2\beta^2}}{k^2+\gamma^2}\cos[k\bar{x}]\,dk, \tag{10}$$

where $\beta^2 = [(L+g)^2 + g^2 + \pi^4 a^2/16]/6$ and $\gamma^2 = 6/[d(2t-d)]$. This integral can be evaluated in terms of the error function (erf) as

$$E(\bar{x}) \propto \frac{\pi}{4\gamma} e^{\beta^2\gamma^2}\{2\cosh[\bar{x}\gamma] - e^{-\bar{x}\gamma}\,\mathrm{erf}[\beta\gamma - \frac{\bar{x}}{2\beta}] - e^{\bar{x}\gamma}\,\mathrm{erf}[\beta\gamma + \frac{\bar{x}}{2\beta}]\}. \tag{11}$$

PW_{50} is found by equating $E(\bar{x}_{50}) = E(0)/2$ to give the non-linear equation

$$1 - \mathrm{erf}[\theta] = 2\cosh[y_{50}] - e^{-y_{50}}\mathrm{erf}[\theta - y_{50}/(2\theta)] - e^{y_{50}}\mathrm{erf}[\theta + y_{50}/(2\theta)], \tag{12}$$

where $y_{50} = \bar{x}_{50}\gamma$ and $\theta = \beta\gamma$. Solving Eq. (12) numerically for y_{50} with θ in the range $0.1(0.1)2$ gives an almost linear variation of y_{50} with θ which can be best fitted by $y_{50} \approx 1.53\theta + 0.61$ and hence

$$PW_{50} \approx 1.25\sqrt{(L+g)^2 + g^2 + \pi^4 a^2/16} + 0.50\sqrt{d(2t-d)}. \tag{13}$$

The D_{50} density may be found using the 'simplified' analysis in Ref. [6, p. 157] where it is assumed that at D_{50} the waveform is approximately sinusoidal. This requires $E(0) = 4k_{50}\hat{E}(k_{50})/\pi$ to be solved for $k_{50} = \pi D_{50}$. This equation is

$$\pi(1 - \mathrm{erf}[\theta])e^{\theta^2}/8 = u_{50}e^{-u_{50}^2\theta^2}/(u_{50}^2 + 1), \tag{14}$$

where $u_{50} = k_{50}/\gamma$. Solving Eq. (14) numerically for u_{50} with θ in the range $0.1(0.1)3$ gives an almost linear variation of $1/u_{50}$ with θ which can be best fitted by $1/u_{50} \approx 0.67\theta + 0.30$ to give

$$D_{50} \approx \{0.86\sqrt{(L+g)^2 + g^2 + \pi^4 a^2/16} + 0.38\sqrt{d(2t-d)}\}^{-1}. \tag{15}$$

The accuracy achievable is shown in Figs. 4 and 5 where PW_{50} and D_{50} results for $t = 75\,\text{nm}$, $d = 25\,\text{nm}$, $L = 10\,\text{nm}$ and a range of shield-shield spacings are given. Also shown are results for the

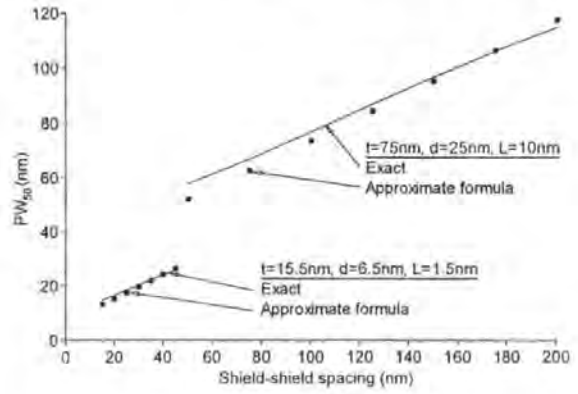

Fig. 4. Approximate PW_{50} formula.

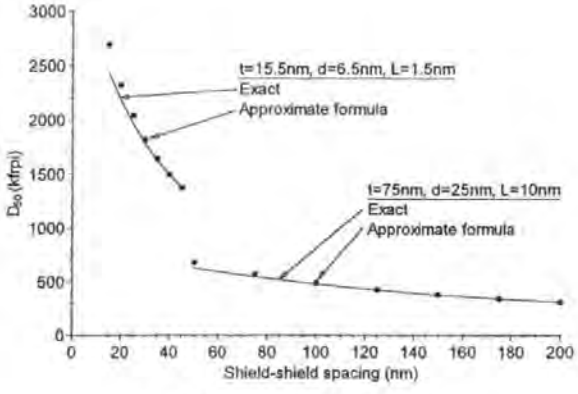

Fig. 5. Approximate D_{50} formula.

dimensions given in Ref. [7] for a possible future system operating at 1 Terabit/in^2 ($t = 15.5$ nm, $d = 6.5$ nm and $L = 1.5$ nm). In each case a zero ($a = 0$) transition length has been taken, which is the most severe test of the approximations. These formulae are only appropriate for $0.2 \leqslant d/t \leqslant 0.4$ and when the linear potential approximation is valid, say for a shield–shield spacing of less than twice the underlayer distance (t). However, as can be seen in Fig. 4 for example, this range is extended because this approximate formula underestimates the linear approximation which itself overestimates the true PW_{50}.

The above analysis is similar to that in Ref. [8] for longitudinal recording by a shielded MR head. However, in the perpendicular case the resulting formulae are less accurate, partly due to the presence of a ratio of sinh terms. This ratio decays to zero less rapidly than the corresponding $\exp[-k(d + \delta/2)]$ term in the longitudinal case, making approximation of Eq. (8) more difficult. Also this ratio requires approximating. The more simple exponential approximation of $\sinh[\alpha x]/\sinh[x] \approx \alpha \exp[-x^2(1 - \alpha^2)/6]$ has the advantage of giving a perfect Gaussian pulse but the resulting formulae are not sufficiently accurate. Better approximations in terms of exponentials do not appear to lead to analytic PW_{50} and D_{50} formulae. Also, the linear potential approximation is less accurate for perpendicular than longitudinal recording and unfortunately the new potential approximation used here is not convenient for deriving PW_{50} and D_{50} approximations.

5. Conclusions

For a shielded MR head, expressions have been given which avoid the need for expensive numerical integration in the full Fourier solution. An approximation has been used to provide very accurate output results for a double-layer perpendicular medium over a wide range of practical head dimensions. Simple PW_{50} and D_{50} formulae have been derived which are useful over a more limited range of dimensions. Although the results presented here are explicitly for single element MR reading heads, the ideas extend to inductive pole heads and to double element MR heads [3].

References

[1] H. Muraoka, Y. Nakamura, J. Mag. Soc. Jpn. 21 (S2) (1997) 157.
[2] H. Muraoka, Y. Sugita, Y. Nakamura, IEEE Trans. Magn. 35 (1999) 2235.
[3] S.J.C. Brown, D.T. Wilton, H.A. Shute, D.J. Mapps, IEEE Trans. Magn. 35 (1999) 4339.
[4] A. Aharoni, IEEE Trans. Magn. 36 (2000) 3879.
[5] D.T. Wilton, H.A. Shute, D.J. Mapps, IEEE Trans. Magn. 35 (1999) 2172.
[6] H.N. Bertram, Theory of Magnetic Recording, Cambridge Univ. Press, Cambridge, UK, 1994.
[7] R. Wood, IEEE Trans. Magn. 36 (2000) 36 and personal communication.
[8] Y. Zhang, S. Shtrikman, H.N. Bertram, IEEE Trans. Magn. 33 (1997) 1093.